Two-Phase Flow Measurement using Fast X-ray Line Detector System

Kyle Song

Dissertation submitted to the faculty of the Virginia Polytechnic Institute and State University in partial fulfillment of the requirements for the degree of

Doctor of Philosophy
In
Nuclear Engineering

Yang Liu, Chair
Mark A. Pierson
Thomas E. Diller
Guohua Cao
Heng Xiao

September 25th, 2019
Blacksburg, VA

Keywords: Algebraic Reconstruction Technique, Filter-Back-projection, Tomography, Two-Phase Flow, Void Fraction, X-ray

Copyright 2019, Kyle Song

Two-Phase Flow Measurement using Fast X-ray Line Detector System

Kyle Song

ABSTRACT

Void fraction is an essential parameter for understanding the interfacial structure, and heat and mass transfer mechanisms in various gas-liquid flow systems. It becomes critically important to accurately measure void fraction as advanced high fidelity two-phase flow models require high-quality validation data. However, void fraction measurement remains a challenging task to date due to the complexity and rapid-changing characteristic of the gas-liquid boundary flow structure. This study aims to develop an advanced void fraction measurement system based on x-ray and fast line detector technologies. The dissertation has covered the major components necessary to develop a complete measurement system. Spectral analysis of x-ray attenuation in two-phase flow has been performed, and a new void fraction model is developed based on the analysis. The newly developed pixel-to-radial conversion algorithm is capable of converting measured void fraction along with the detector array to the radial distribution in a circular pipe for a wide range of void fraction conditions. The x-ray system attains the radial distributions of key measurable factors such as void fraction and gas velocity. The data are compared with the double-sensor conductivity probe and gas flowmeter for various flow conditions. The results show reasonable agreements between the x-ray and the other measurement techniques. Finally, various 2-D tomography algorithms are implemented for the non-axisymmetric two-phase flow reconstruction. A comprehensive summary of classical absorption tomography for the two-phase flow study is provided. An in-depth sensitivity study is carried out using synthetic bubbles, aiming to investigate the effect of various uncertainty factors such as background noise, off-center shift, void profile effect, etc. The sensitivity study provides a general guideline for the performance of existing 2-D reconstruction algorithms.

Two-Phase Flow Measurement using Fast X-ray Line Detector System

Kyle Song

GENERAL AUDIENCE ABSTRACT

Gas-liquid flow phenomenon exists in an extensive range of natural and engineering systems, for example, hydraulic pipelines in a nuclear reactor, heat exchanger, pump cavitation, and boilers in the gas-fired power stations. Accurate measurement of the void fraction is essential to understand the behaviors of the two-phase flow phenomenon. However, measuring void fraction distribution in two-phase flow is a difficult task due to its complex and fast-changing interfacial structure. This study developed a comprehensive suite of the non-intrusive x-ray measurement techniques, and a pixel-to-radial conversion algorithm to process the line- and time-averaged void fraction information. The newly developed algorithm, called the Area-based Onion-Peeling (ABOP) method, can convert the pixel measurement to the radial void fraction distribution, which is more useful for studying and modeling axisymmetric flows. Various flow conditions are measured and evaluated for the benchmarking of the algorithm. Finally, classical 2-D reconstruction algorithms are investigated for the void fraction measurement in non-axisymmetric flows. A comprehensive summary of the performance of these algorithms for a two-phase flow study is provided. An in-depth sensitivity study using synthetic bubbles has been performed to examine the effect of uncertainty factors and to benchmark the algorithms for the non-axisymmetric flows.

Acknowledgments

I deliberate my sincere gratitude to my advisor, Professor Yang Liu, who has the patients and the substance of a genius for his guidance over the past five years. It had been a great honor to work with such a diligent and brilliant person. Without his guidance and persistent advising, this dissertation would not have been possible.

Special thanks to Professor Mark Pierson, for his dedication to the Nuclear Engineering Program and NRC fellowship grant throughout my entire Ph.D. program. I want to thank my committee members, Profesor Thomas Diller, Guohua Cao, Yunhui Zhu, and Heng Xiao for supportive recommendations and constructive criticisms in the preliminary exam and throughout my researches in Virginia Tech.

The valuable assistance of my colleagues and friends in research group MFTL, Dewei Wang, and Yucheng Fu are gratefully appreciated for their efforts and time in helping me with the experiments reported in this dissertation. The financial support of the NRC is gratefully acknowledged. Gratitude should be extended as well to my friend Yangkun Song, who has offered much assistance during my stay at Virginia Tech.

The last paragraph is reserved for my family. I must express my thankfulness for their unconditional support and long-lasting love. My sincerest thanks should be present to my mother, Lina Hong. She is the most important person in my life. I could not have been successful without her prayers and blessings. Her love, inspiration, and embracement give me the courage to reach this milestone in my life.

Table of Contents

List of Figures vii
List of Tables xi
1 Introduction 1
1.1 Research Background 1
1.2 Dissertation Objective 4
1.3 Dissertation Outline 5
2 Polychromatic X-ray Energy Measurement 7
2.1 Introduction 7
2.2 Experimental Setup 10
2.3 Measurement Principle 14
2.4 Photon to Electron Conversion 20
2.5 Sample two-phase flow result 27
2.6 Summary 33
3 Pixel to Radial Conversion Algorithm 35
3.1 Introduction 35
3.2 Experimental Conditions 39
3.3 Methodology 43
3.3.1 Area-based onion-peeling 43
3.3.3 Modified fan-beam onion-peeling method 48
3.4 Algorithm Benchmark with Synthetic Bubble Sensitivity Study 52
3.4.1: Pixel resolution 53
3.4.2 Mesh size effect 55
3.4.3 Added background noise effect 57
3.4.4 Off-center shift effect 59
3.4.5 Investigate radial conversion with different void profile 61
3.5 Sample Two-phase Flow Radial Conversion result and Probe Benchmark 65
3.5.1 Flow measurement using the x-ray densitometer system 65
3.5.2 Double-sensor Conductivity Probe benchmarking 68
3.5.3 Pixel to Radial conversion Result 69
3.5.4 Gas velocity measurement 71

3.5.5 Area averaged quantities: superficial gas velocity 75
3.6 Summary 76
4 Non-axisymmetric Geometry Reconstruction 77
4.1 Introduction 77
4.2 Experimental Setup 88
4.3 2-D Reconstruction Algorithm 91
4.3.1 Description of the Radon transform 92
4.3.2 Geometry of the parallel-beam system 95
4.3.3 Description of the Fan-beam System 97
4.3.4 Description of the filtered back-projection method 102
4.3.5 Description of the algebraic tomography 106
4.3.6.Description of the Iterative Reconstructive Method: 109
4.3.7 Attenuation images to void fraction 112
4.4 Synthetic Bubble Sensitivity Study 117
4.4.1 Limited viewing angle 118
4.4.2 Resolution effect 123
4.4.3 Background noise effect 126
4.4.4 Off-center shift effect 129
4.4.5 Different void profiles 132
4.5 Experimental Result 136
4.5.1 Phantom geometry test 136
4.5.2 Two-phase flow experiment 140
4.5.3 DP transducer and Spectral model benchmark 144
4.6 Summary 146
5. Conclusion and Recommendations 148
References 150

List of Figures

Fig. 2-1: Overall process of x-ray photon attenuation and energy conversion process in the typical x-ray measurement system. 8
Fig. 2-2: Schematic of the 25.4 mm I.D. air-water two-phase flow test facility. 12
Fig. 2-3: Schematic of the bubble injector design. 13
Fig. 2-4: (a) Schematic of the x-ray system; (b) picture taken from the outside with a test pipe inserted; (c) detector array arrangement. 13
Fig. 2-5: (a) Front and (b) top view of typical void fraction measurement using an x-ray densitometry system with a linear detector array. 14
Fig. 2-6: Linear attenuation coefficients of air, water, acrylic, and aluminum over x-ray energy up to 50 keV. Data from the National Institute of Standards and Technology (NIST) are used to generate this figure [45]. 15
Fig. 2-7: Polychromatic x-ray emission spectrum of a tungsten anode target, with 1 mA filament current, 50 kV tube voltage, at 0.25 m from the source. (a) Initial spectrum and those after penetrating various Acrylic thicknesses; and (b) spectra with different water thicknesses. 17
Fig. 2-8: Schematic of the calibration test to determine photon to electron conversion factor f_{conv}. 20
Fig. 2-9: For the center pixel, (a) comparison between measured void fraction and that predicted by Eq. (2-12); (b) the relative error of void fraction (α) and a liquid fraction (1-α) based on Eq. (2-12). 22
Fig. 2-10: The detector conversion factor f_{conv} for the center pixel obtained from the calibration test. 23
Fig. 2-11: For the center pixel, (a) Comparison between the measured voltage and that predicted by Eq.(2-14) with a conversion factor given by Eq.(2-14); (b) Relative error of the predicted void fraction and liquid fraction based on Eqs. (2-9) and (2-14), and measured voltage. 25
Fig. 2-12: (a) Relationship between the void fraction and detector voltage response for selected pixels for the 25.4 mm I.D. test pipe. (b) Comparison between the predicted voltage and experimental data when the 25.4 mm I.D. test section is filled with water and air. 26
Fig. 2-13: Synthetic 2-D images from the x-ray signals obtained from the 1-D detector array for (a) bubbly flow, jg = 0.16, jf = 0.69 m/s, and (b) slug flow, jg = 0.25, jf = 0.52 m/s. 28
Fig. 2-14: Void fraction distribution along the pixel location. (a) Bubbly flow, jg=0.16 m/s, jf=0.69 m/s. (b) Slug flow, jg=0.30 m/s, jf=0.52 m/s. 29
Fig. 2-15: (a) definition of the angles for the nth pixel. (b) coverage area (in red) of the nth pixel. 30
Fig. 2-16: X-ray signals obtained from upstream and downstream detector arrays, (a) bubbly flow; and (b) slug flow. 31
Fig. 2-17: Gas velocity distribution along the pixel, (a) bubbly flow; and (b) slug flow. 32
Fig. 3-1: Concept of 1-D line-averaged measurement in the axisymmetric flow system. The absorption length weights the measured value contributed by the test object placed on the path of line sight of the measurement (LOS). 36

Fig. 3-2: Illustration of fan-beam to parallel-beam rebinning. (a) projected region resulted from the fan-beam projection; (b) Re-binned parallel-beam rays and the equivalent projected resolution. 38
Fig. 3-3: A general overview of the proposed method.....39
Fig. 3-4: (a) Schematic of the vertical two-phase flow test facility; (b) Two-phase flow injector design; gas-sparger and water injector at the bottom of the test loop.....41
Fig. 3-5: Typical air-water two-phase flow images recorded by the x-ray system. From top to bottom, the bubbly, slug, churn-annular, and annular flow regime are visualized.....42
Fig. 3-6: Definition of the segment angles and the x-ray scanned pixel area (SPA) ABCD for the i_{th} pixel location. 45
Fig. 3-7: Definition of the partitioned area (PA) for the i_{th} pixel and j_{th} partitioned circular ring.47
Fig. 3-8: Definition of the modified fan-beam onion-peeling (FBOP) method. 52
Fig. 3-9: Reconstructed radial void fraction profile for (a) 0.1mm mode; (b) 0.4mm mode; (c) 1.6 mm mode. 54
Fig. 3-10: Reconstructed radial profile from the different mesh-size interval (a) 0.1mm mode; (b) 0.4 mm mode; (c) 1.6mm mode 56
Fig. 3-11: Impact from the added background noise effect (left column) vs. improved reconstruction (right column) (a) 0.1mm mode; (b) 0.4 mm mode; (c) 1.6mm mode. 58
Fig. 3-12: Sample case of off-centered pipe location. (a) The test section is located 0.5 mm Off-center in the positive y-direction in the measurement domain; (b) Difference between the spectrum distribution in the detector response: centered vs. shifted geometry. 60
Fig. 3-13: Reconstructed radial profile influenced by the off-center shift effect, (a) 0.1mm mode; (b) 1.6 mm mode.....61
Fig. 3-14: Reconstructed radial distribution for the various void profile with clean function. 63
Fig. 3-15: Reconstructed radial distribution for the various void profile with added random noise effect.....64
Fig. 3-16: Void fraction distribution along the pixel location (a) Run 1; (b) Run 2; (c) Run 3; (d) Run 4; (e) Run 5; (f) Run 6.....67
Fig. 3-17: Working principles of a double-sensor conductivity probe. 69
Fig. 3-18: Reconstructed radial profile from the pixel measurement using ABOP, FBOP, existing Abel deconvolution method, and probe benchmarking data. 70
Fig. 3-19: X-ray signals obtained from the upstream and downstream detector arrays. Sample signals extracted from (a) Run2- bubbly flow; and (b) Run3-slug flow. 72
Fig. 3-20: Gas velocity distribution along the pixel, (a) Run2; (b) Run3; (c) Run4;. (d) Run5; and (e) Run6. 73
Fig. 3-21: Reconstructed radial gas velocity, (a) Run2; (b) Run3; (c) Run4;. (d) Run5; and (e) Run6. 74
Fig. 4-1: Illustration of Radon transform (left figure) and the sinogram in the Fourier space (right figure). 80
Fig. 4-2: Illustration of discrete formulation for the CAT problem. The red square represents an area of interest. The specific attenuation length of i_{th} projection-ray (blue ray) passing through specific j_{th} voxel denoted as $\vec{\mu}^{v}$ 83
Fig. 4-3: Simple 2x2 tomography problem of the ART algorithm with one iteration. 84

Fig. 4-4: (a) Experimental arrangement of the x-ray tomography setting, (b) Two-phase flow air injector design. 90
Fig. 4-5: Illustration of the x-ray fan projection and the measured location, $z / D_h = 47.4$. 90
Fig. 4-6: Schematic of the x-ray system with high precision turntable tomography setting. 91
Fig. 4-7: Flowchart of the 2-D reconstruction algorithm. 92
Fig. 4-8: X-ray projections in the measurement plane. (a) Projections are carried out at a rotational angle θ; (b) Geometry of the parallel-beam system. 94
Fig. 4-9: Geometry of parallel-beam system. (a) Parallel-beam in the (x,y) coordinate system; (b) geometric relationship between the fixed system and the moving system. 96
Fig. 4-10: Fan-beam system. (a) three-dimensional view of the frame of the reference; (b) Basic parameters of the fan-beam geometry 98
Fig. 4-11: Illustration of rotating fan-beam geometry; (a) specific fan-beam projection made at an angle $\theta_{fan}^{k=1}$; (b) a projection made at an angle $\theta_{fan}^{k=2}$ 100
Fig. 4-12: Reconstruction method with re-sorting process; (a) Fan-beam and parallel-beam system geometrical; (b) re-sorting reconstruction method process for the fan-beam system. 101
Fig. 4-13: Sample reconstructed object using the back-projection method. 103
Fig. 4-14: Sample reconstructed object using a filtered back-projection method. 104
Fig. 4-15: Representation of simple algebraic tomographic problem. 106
Fig. 4-16: (a) Forward projection (FP) operation in the algebraic reconstruction method; (b) Back-projection (BP) operation in the algebraic reconstruction method. 108
Fig. 4-17: Three different variations of projection kernels used in the algebraic tomography. (a) Line kernel; (b) Joseph's kernel; (c) Strip kernel. 109
Fig. 4-18: Illustration of Ways to improve the reconstruction result by applying the minimum constraint. 111
Fig. 4-19: Sample illustration of the overall attenuation process of x-ray energy before and after passing through a two-phase flow structure. 113
Fig. 4-20: Generated synthetic image for the three reference data for the void fraction formulation. 118
Fig. 4-21: Arranged sinogram from the limited number of viewing angles. 119
Fig. 4-22: Reconstructed 2-D void fraction image using FBP and ART method. Each column indicates the number of projection data set. (a) Reconstructed void fraction profile using the FBP method and Ram-Lark filtering; (b) Reconstructed void fraction profile using the SIRT iteration method. 120
Fig. 4-23: Void fraction profile for the center-line x-axis. Each column indicates the number of projection data set used. (a) Reconstructed void fraction profile using the FBP method and Ram-Lark filtering; (b) Reconstructed void fraction profile using the various algebraic iteration methods. 121
Fig. 4-24: Void fraction difference between the actual void fraction value and reconstructed profile. Each column indicates the number of projection data set. Void fraction difference resulted from (a) FBP reconstruction; (b) algebraic iteration-based method. 122
Fig. 4-25: Void fraction distribution and the void fraction difference, $\Delta\alpha$, of the centerline x-axis resulted from 0.4mm and 0.8 mm pixel resolution mode, (a) Void fraction profile of FBP

method; (b) Void fraction profile of ART method; (c) $\Delta\alpha$ of FBP method; (d) $\Delta\alpha$ of ART method. 125
Fig. 4-26: Reconstructed 2-D image where the background noise within ±3% influences projection data. Reconstructed image of the (a) FBP method; (b) SIRT method. 127
Fig. 4-27: Void fraction profile of the centerline x-axis, (a) FBP method; (b) algebraic iteration methods. Distribution of void fraction difference, $\Delta\alpha$, of the centerline x-axis, (a) FBP method; (d) algebraic iteration methods. 128
Fig. 4-28: Illustration of the Off-center source location in the global coordinate system in the measurement domain. (a) Ideal case; (b) Off-center source location shift. 130
Fig. 4-29: The reconstructed 2-D image of the (a) FBP method; (b) SIRT reconstruction. 130
Fig. 4-30: Void fraction profile of the centerline x-axis of the (a) FBP method; (b) algebraic iteration methods. The void fraction difference, $\Delta\alpha$, of the centerline x-axis of the (c) FBP reconstruction; (d) algebraic iteration-based method. 131
Fig. 4-31: The reconstructed 2-D image of the attenuation coefficient. 133
Fig. 4-32: Reconstructed void profile of the centerline x-axis, (a) Single-step; (b) Ellipsoid; (c) Uniform; (d) Gaussian distribution. 134
Fig. 4-33: Void fraction difference, $\Delta\alpha$, of the centerline x-axis, (a) Single-step; (b) Ellipsoid; (c) Uniform; (d) Gaussian distribution. 135
Fig. 4-34: The reconstructed 2-D image of a phantom geometry. 137
Fig. 4-35: The reconstructed 2-D image of a phantom with a two 6.3mm cylindrical rod. 138
Fig. 4-36: The reconstructed 2-D image of a phantom with a two-6.3mm and one-3.2mm cylindrical rod. 139
Fig. 4-37: The attenuation profile of the phantom with three acrylic cylindrical rods. 140
Fig. 4-38: (a) Attenuation profile of the three reference data of the centerline x-axis; (b) Illustration of measurement uncertainty if air reference data is neglected in void fraction formulation. 142
Fig. 4-39: The reconstructed void fraction distribution of each flow condition listed in Table 16. (a) Bubbly flow, j_g=0.033m/s, j_f=0.463m/s; (b) Bubbly flow, j_g=0.060m/s, j_f=0.463m/s; (c) Slug flow, j_g=0.190m/s, j_f=0.042m/s; (d) Slug flow, j_g=0.284m/s, j_f=0.084m/s; 143
Fig. 4-40: The reconstructed 2-D void fraction image of each flow condition listed in Table 16. (a) Bubbly flow, j_g=0.033m/s, j_f=0.463m/s; (b) Bubbly flow, j_g=0.060m/s, j_f=0.463m/s; (c) Slug flow, j_g=0.190m/s, j_f=0.042m/s; (d) Slug flow, j_g=0.284m/s, j_f=0.084m/s; 144
Fig. 4-41: The time and line-averaged void fraction distribution along the detector pixel determined by the Spectral model. 145

List of Tables

Table 1: Summary of two-phase flow measurement using x-ray densitometry or CT imaging method in the literature.....9
Table 2: Area-averaged data from the x-ray and flowmeter measurement.....33
Table 3: Summary of pixel to a radial flow distribution for two-phase flow application in the literature.....37
Table 4: Mean absolute percent error.....65
Table 5: Flow Condition.....68
Table 6: Area-averaged data from the x-ray, radial conversion, and flowmeter measurement ...75
Table 7: Summary of 2-D tomographic reconstruction for two-phase flow available in the literature. 77
Table 8: Summary and comparison between algorithms used for TAS.....88
Table 9: trigonometric relationship.....95
Table 10: Relationship between the polar coordinate system and the fixed and moving coordinate system.....97
Table 11: List of the absolute void error and area-averaged quantity error resulted from the limited angular projection data set.....123
Table 12: List of the absolute void error and the area-averaged quantity errors of the 0.4mm and 0.8mm pixel resolution mode. 125
Table 13: List of the absolute void error and area-averaged quantity error due to the background noise effect.....128
Table 14: List of the absolute void error and area-averaged quantity error due to the off-center shift effect.....131
Table 15: List of the absolute void error and area-averaged quantity error of the different synthetic bubble void profile. 135
Table 16: Flow condition 142
Table 17: Relative error of the area-averaged quantity measured by different measurement technique.....146

1 Introduction

1.1 Research Background

Measuring the void fraction in a gas-liquid two-phase flow system is an important but challenging task due to the complex and fast-moving interfacial structures. The void fraction measurement is becoming progressively critical as the advancement of the high-fidelity Computational Fluid Dynamics (CFD) model. It is sufficient enough to develop the conventional two-phase flow models and codes with the one-dimensional two-phase flow parameters. However, CFD models frequently require local information such as two-dimensional or three-dimensional void fraction distribution. Advanced computational models cannot be critically evaluated without high-quality data; thus, their applications in realistic engineering problems will be cruelly restricted [1,2].

Both intrusive and non-intrusive techniques have been developed for two-phase flow measurements. Known intrusive techniques include local multi-sensor probe [3], optical probe [4], wire-mesh sensors [5–7], and constant temperature anemometry (CTA) [8]. Several techniques, such as four-sensor probes [9,10], conductivity probes [11], and optical probes [11,12] have been widely used to measure local void fraction or gas-velocity of two-phase flows [3,4,13,14]. These local measurement techniques have shown excellent measurement precision due to micro size sensor tip, which is about 10μm or smaller. However, local measurement techniques are not efficient because it only measures a single point at a time. Also, the local measurement method requires an extended sampling period to acquire the time-averaged information. The wire-mesh sensor [5–7] is another known intrusive method for void fraction measurement. The wire-mesh technique is capable of obtaining a limited number of discrete measurement points in a cross-sectional area simultaneously at a high frame rate. However, the electrical wires could cause unwanted substantial flow interference in the flow field, which is much higher when compared to the four-sensor probes. Also, the local void fraction information is sensitive to signal magnitude, which is subject to various noises in a two-phase flow.

Non-intrusive techniques can be divided into an invasive or non-invasive method. A well-known non-intrusive but invasive technique is electrical capacitance tomography (ECT) [15].

Other variations are electrical resistance imaging (ERI) or electrical resistance tomography (ERT) [16]. These non-intrusive but invasive techniques carry a limited number of electrodes. Therefore, measurement results have a relatively low spatial resolution, and the measurement accuracy is highly dependent on the flow regime. The high-speed camera is an imaging-based measurement technique, which is non-intrusive and non-invasive. The imaging-based method has been established in recent years for a two-phase flow measurement [17]. High-speed imaging has a substantial benefit from the high pixel resolution and fast frame rate. However, high-speed imaging techniques are restricted to low void fraction flows, such as bubbly flows. An alternative method for two-phase flow measurement is the radiation attention technique. The radiation measurement technique is a non-intrusive and non-invasive method. Gamma-ray systems often transmit much higher radiation energy, therefore, suitable for the complex flow systems with a high-pressure flow such as a heated rod-bundle geometry setting [18,19]. However, significant drawbacks exist in gamma-ray systems such as low spatial resolution and slower data acquisition rate than an equivalent x-ray based system [18–21].

Depending on the x-ray source and detector array arrangement, x-ray based systems deliver substantial advantages when compared with the measurement methods described above. X-rays are non-intrusive and non-invasive techniques; thus, the measurement eliminates undesired flow disturbance to individual bubbles. Since x-ray based measurement does not require physical contact with the flow, it is insensitive to the temperature or pressure of two-phase flows. In contrast with the high-speed camera, the x-ray measurement is not restricted by the test section geometry, the optical properties of the wall, or fluid. The x-ray attenuation technique shows less dependence on flow regimes than the ECT or ERT; therefore, it covers a wide range of flow regimes. The wide selection of the x-ray tubes and radiation detector sensors also provides many flexible designs for different research applications.

Typically the x-ray beam forms either a cone-beam or fan-beam projection. From the x-ray projection, the line-averaged information is recorded by individual pixels on the detector screen. With this line averaged data, one may extract the essential quantities such as void fraction or bubble velocity, which are essential parameters to study two-phase flow behavior. A non-time-resolved x-ray system is capable of measuring time and line-averaged void fraction, but not instantaneous values [18]. This line-averaged void fraction does not contain information about individual bubbles. For example, a series of line projections do not provide sufficient details of

the bubble information unless the system contains multiple sources and utilizes the tomography setting [19,20]. Also, most of the x-ray systems are not capable of resolving the energy spectrum of the x-ray beam. In general, an x-ray system involves the conversion from x-ray photons to visible photons, and from visible photons to electric signals. The detailed conversion processes must be investigated for measurement accuracy.

In the case of a complex flow system, the operating power of the x-ray source requires a high photon energy source, typically 150 KeV or higher. Such powerful x-ray sources produce high-level radiation, which requires a significant shielding around the system, as well as shielding around the measurement port. This configuration is often non-portable, which limits the availability or flexibility of the system if various locations need to be measured. High power systems often have large system dimensions, are relatively heavy due to the shielding material. Thus, this limits the mobility of the system and makes it impractical to relocate to various measurement locations to perform detail two-phase flow measurement. Also, the photon detectors equipped in the high power systems often composed of crystal-based scintillators or the combination of both high-speed imaging device and image intensifier, which further limits the mobility and flexibility of the measurement units.

Additional challenges are involved in using the x-ray based systems for void fraction measurement in two-phase flow applications. Typical x-ray source generates a polychromatic beam, which is a wide range of energy spectrum [21]. The conventional log model is a known void fraction formulation used for the x-ray attenuation measurement technique. However, measurement resulted from the polychromatic x-ray may cause significant uncertainty, since the conventional log model assumed constant x-ray energy and constant attenuation coefficient. Due to the x-ray's polychromatic characteristics, one must thoroughly analyze the ranges of the x-ray energy used in the measurement. Depending on the detector screen arrangement, the x-ray beam illuminates a form of a cone-beam or fan-beam. However, forward projection only measures the time and line-averaged attenuation value; thus, measured information does not provide local void fraction information. One must further process the pixel measurement to obtain the local or radial void fraction distribution of the flow field.

In the case of the non-axisymmetric flow geometry, such as a rectangular test section, the void fraction or velocity distribution is no longer axisymmetric. A 2-D tomographic reconstruction method is a suitable choice for reconstructing the void fraction distribution in such systems.

In the tomography imaging application, one can reconstruct the flow field from the multiple projections where signal acquisition is obtained from various angular directions [22]. For a two-phase flow application, one can reconstruct the flow field distribution without measuring the extensive viewing angle if the projection data set is substantial enough. Some of the tomography application for two-phase flows are tomographic PIV for flow velocity [23], and x-ray imaging for void fraction, or gas velocity distribution [6,17,19,24–27].

To overcome many challenges described above, this dissertation presents a relative compact and fast x-ray system design with the x-ray tube at 50kV and 1mA. The photodetector arrays used in the system consist of a thin scintillator layer and photodiode, which captures the attenuated x-ray photon and converts into an electron for voltage generation. This x-ray detector unit is capable of adjusting the sensitivity level and amplification of voltage output. All of the measurement components are assembled into a single enclosure, which makes it a relatively compact and light-weighted system. Thus, the system is capable of measuring the various port location of a two-phase flow loop. A polychromatic x-ray energy measurement model has been integrated for the two-phase flow measurement, in which the algorithm takes account of the beam hardening effect and modifies the energy spectrum of x-ray photons after penetrating test objects.

The x-ray system is also capable of rotating around a non-axisymmetric flow geometry after it is mounted on a high precision turntable. With the single source projection and the linear detector arrangement, the system is capable of capturing the time, and line averaged projection at a given viewing angle. The sinogram data set arranged from the multiple angular projections can be further processed to reconstruct the 2-D flow distribution in a rectangular test section. The existing CT reconstruction algorithms should be suited for recovering the void fraction distribution in a rectangular cross-sectional plane. This dissertation will investigate these algorithms and provide general guidelines for two-phase flow measurement.

1.2 Dissertation Objective

The presented research in this dissertation aims to develop a set of algorithms for various void fraction measurements using the x-ray attenuation technique. The presented algorithms consist of three parts, and their primary objectives are described below:

Part 1: Forward Projection Processing

a) Improve measurement accuracy using the spectral model developed by Song and Liu [28];
b) Evaluate the forward projection algorithm with the prediction model and experimental data;
c) Investigate measurement accuracy using the proposed algorithm and the existing log model.

Part 2: Pixel to Radial Conversion Algorithm

a) Develop a conversion algorithm capable of convert the line and time-averaged pixel measurement to radial void fraction or gas velocity distribution;
b) Conduct the sensitivity study using synthetic bubbles under the various uncertainty factors and analyze the conversion performance,
c) Evaluate the radial conversion result with the actual experimental data;

Part 3: 2-D Tomography Algorithm

a) Investigate absorption-based tomography imaging technique for the two-phase flow application and perform a comprehensive sensitivity study using a synthetic bubble;
b) Evaluate the reconstruction algorithm with synthetic image and experiment data in a non-axisymmetric geometry setting.

1.3 Dissertation Outline

In Chapter 2, the spectral model, calibration test, and conversion factor are described in the measurement methodology section. The x-ray energy spectrum study, photon to electron conversion, and detector conversion efficiency will be addressed by a calibration test. The performance of the spectral model is assessed by the prediction result and the measured two-phase flow data. The newly developed pixel to radial conversion algorithm is proposed to reconstruct the fan-beam projection measurement. The proposed algorithm combines the spectral model, calibration test, and conversion factor to yield robust and improve the measurement accuracy. The developed algorithm is extended to the pixel to radial gas velocity distribution as well.

Followed by Chapter 2, the spectral model is extended to estimate the void fraction in the two-phase flows with various liquid and gas flow rates in Chapter 3. The two-phase flow experiment is performed in a circular test-section with an inner diameter of 25.4mm. In this

experiment, the test facility runs air-water vertical flows. The compact and fast x-ray system is used to record the two-phase flow at a rate of 1000Hz. The line and time-averaged information of various flow conditions are analyzed with the spectral model. This forward projection data is then converted to radial void fraction distribution using a newly developed algorithm. The radial conversion parameters are compared with the double sensor probe measurement and flow-meter reading.

In Chapter 4, the 2-D CT methods are integrated into the two-phase flow measurement. There are two general classes of algorithms to perform two-dimensional reconstruction, either by analytical or algebraic-iteration methods. In this chapter, the 2-D reconstruction algorithms are integrated to deliver a comprehensive void fraction distribution in two-phase flows. Various CT algorithms have been studied for the two-phase flow image reconstruction.

The contents in Chapter 2 are based on the published work done by the author in the Ph.D. period:

K. Song, Y. Liu, "A compact x-ray system for two-phase flow measurement", Meas. Sci. Technol. 29 (2018) 025305 [28].

2 Polychromatic X-ray Energy Measurement

2.1 Introduction

X-ray based densitometry or tomography system has been extensively used in extracting the two-phase flow parameters such as void fraction or bubble velocity [6,24,29–31]. The x-ray based measurement methods are non-intrusive and non-invasive, thus will not cause any flow disturbance. Compared with optical imaging systems, the x-ray is restricted by the test section material composition, the shape of the test section walls, or the optical quality of fluids. The measurement accuracy of the x-ray system shows less dependence on flow regimes than the electrical capacitance tomography or electrical resistance tomography. The related researches are listed in Table 1.

For the two-phase flow application, the x-ray attenuation measurement methods are widely used. As an x-ray beam penetrates through the test object, x-ray photons are attenuated, scattered, or absorbed in the test object, therefore, resultant photons become less [32]. This behavior is known as the attenuation of x-ray and mathematically formulated by Beer-Lambert [33]. One can express the x-ray beam intensity after it penetrates through a homogeneous object with an overall depth L in the following equation:

$$I(L) = I_o e^{-\mu \cdot L} \tag{2.1}$$

Here, I_o is the initial intensity and μ is the attenuation coefficient of the object. The attenuation coefficient is energy-dependent in general. However, this equation is valid only with constant energy or with a constant attenuation coefficient. In general, the x-ray energy exhibits polychromatic characteristics, which is a wide range of energy spectrum [34,35]. Unless one uses beam synchronizer or significant pre-beam hardening, the above equation can not be used directly for estimating the attenuated polychromatic x-ray beam. Other challenges are involved with x-ray energy detection since most of the x-ray detectors are not energy-resolved. Many detector systems are photo-detector units, which means the detector system captures attenuated x-ray photons. This photo-detector system converts captured photon into a visible light then generates the electrons, which finally outputs voltage signals and displays the signals in the user interface in the operating

workstation unit. The concept of the overall x-ray photon to voltage conversion process is shown in *Fig. 2-1*.

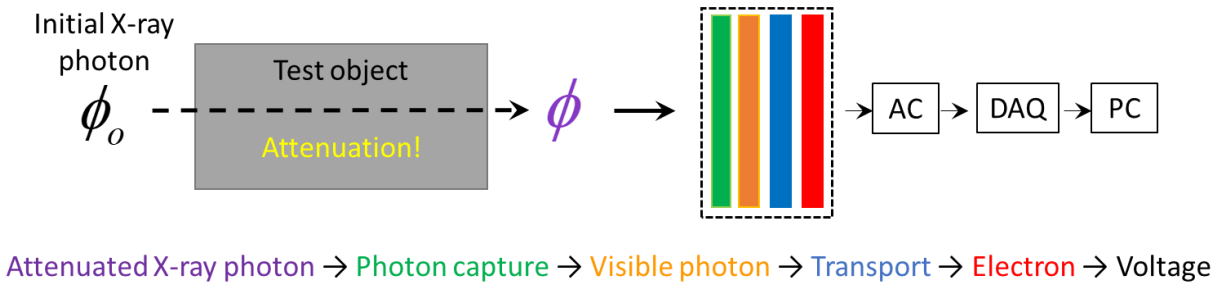

Fig. 2-1: Overall process of x-ray photon attenuation and energy conversion process in the typical x-ray measurement system.

In the literature, Inoue *et al.* [36] used both an x-ray densitometer and an x-ray Computed Tomography (CT) scanner to measure the void fraction distribution in a simulated full-scale Boiling Water Reactor (BWR) fuel assembly. It takes 15 seconds and 60 seconds for the CT scanner and densitometer, respectively, to perform one measurement. Therefore, these systems can measure the time-averaged void fraction, but not the instant values. In the literature of Coutier-Delgosha *et al.* [37] used the Advanced Photon Source (APS) at Argonne National Laboratory (ANL) to measure cavitation flows. The detector contains a scintillator which converts x-ray to visible light and a high-speed camera. With a high-intensity x-ray source (10^{12} photons/s on the test sample), the authors could take high-speed images of the flow at 10,000 fps. Mudde [38] designed a system consisting of three x-ray tubes and three corresponding scintillator detector arrays. Using this system, bubbles larger than 2.5~3 cm in a 23 cm diameter fluidized-bed could be measured, with a frame rate of 250 fps. Fischer *et al.* [39] have developed an x-ray CT system using a scanning electron beam and a circular detector. The system could measure two-phase flow at 1000 fps or higher with a spatial resolution of about 1.5 mm. Mäkiharju *et al.* [40] used a 150 kV x-ray tube, an image intensifier, and a high-speed camera to measure a 21 cm thick water tunnel. The system achieves a spatial resolution of 0.46 mm per pixel and a frame rate of 1000 fps.

It is noted that in the researches described above, the x-ray source has relatively high photon energy in the range of 150 keV or higher. These high-energy x-ray sources are capable of apply pre-beam hardening and only use a high energy range. Therefore, one can assume the

attenuation coefficient is linear or constant in the high-level energy spectrum interval. Also, the detectors used in the above studies, such as large scintillation crystal, or the combination of image intensifier and high-speed camera limits the mobility and flexibility of the measurement systems. Also, these powerful x-ray sources require a significant shielding around the test section and the measurement system.

To overcome these challenges, a novel measurement model has been established for the system, which takes account of the polychromatic energy spectrum of x-ray photons and the beam hardening effect. An improved measurement accuracy has been accomplished with the proposed model when compared with the conventional log model that has been widely used in the literature. With a fast x-ray system and newly developed spectral model, void fraction and velocity distributions are measured for a bubbly and slug flow in a 25.4 mm I.D. air-water two-phase flow test loop. The measured superficial gas velocities are then compared with the gas flowmeter for both conditions.

In the following, the experiment setup consisting of a round pipe and the x-ray system will be described. Then the details of the spectral model will be presented.

Table 1: Summary of two-phase flow measurement using x-ray densitometry or CT imaging method in the literature.

Two-Phase Flow Investigators	Operating Energy	X-ray Beam	Flow Geometry	# of Detector Pixels	Detector Geometry	Scan Rage	Flow Condition
Barthel (2015) [41]	150 keV (max)	Fan-Beam	Round Pipe (50 mm I.D.)	432x1	Semi-Circular	1000-5000 Hz	j_g= 0.038 m/s j_f= 1.017 m/s
Prasser (2005) [7]	160 keV (max)	Fan-Beam	Round Pipe (42 mm I.D.)	256x1	Semi-Circular	263 Hz	j_g= 0.02- 0.4 m/s j_f= 0.69 m/s
Mäkiharju (2013) [40]	150 keV (max)	Cone-Beam	Rectangular (210mm x 210mm)	Tri-Field Intensifier with 1.92 million pixels	2-D Flat-Panel	1000 Hz	j_g =0.38 to 1.86 m/s
Hori (2000) [42]	150keV (max)	Cone-Beam	Round Pipe (300mm I.D.), 3x3 Rod Bundle (12.6 mm Rod pitch)	584	Circular-Ring	2000 Hz	j_g= 0.5 m/s j_f= 0.5 m/s
Stutz (2003) [30]	160 keV (max)	Fan-Beam	Venturi-type Test Section (520 mm long, 44 mm wide, 50 mm high)	24x1	Linear Array	1000 Hz	j_g=6 to 10 m/s
Hubers (2005) [43]	200 keV (max)	Cone-Beam	Round Tube (0.13 to 15.88 mm)	1388(H)× 1024(V)	2-D Flat-Panel	10-60 Hz	j_g=3,10,18 cm/s
Mudde (2011) [38]	150 keV (max)	Fan-Beam	Fluidized Bed (230 mm I.D.)	32x1	Linear Array	2500 Hz	j_g= 0.6 m/s
Xin (2017) [18]	59.5 keV (max)	Fan-Beam	Round Pipe (82 mm I.D.)	82x1	Linear Array	33 Hz	Stratified, Annular Flow

2.2 Experimental Setup

The schematic of the two-phase flow test loop is shown in *Fig. 2-2*. The facility is designed for air-water two-phase up-flow at room temperature and atmospheric pressure. The 3 m tall circular test section is made of transparent acrylic pipes. The test section has an inner diameter (I.D.) of 25.4 mm and a wall thickness of 6.35 mm. A variable speed centrifugal pump (Grundfos CRNE 10-12) is used to deliver the desired water flow rate to the circular test section from a water storage tank. Airflow is supplied by the building compressed air line and regulated by a pressure regulator. Air-water mixture leaving the circular test section is separated by gravity in the storage tank. The water circulates through the loop and air is vented to the atmosphere. The loop also has a bypass line to provide additional control of the flow rate, and it also helps stabilize the flow rate in the test section.

Fig. 2-3 shows the schematic of the bubble injector design, at which air and water are mixed before entering the test section. The injector consists of a sparger tube which has a porous metal section (10-micron pore size) near the top. Air is injected from the inside of the sparger tube. Secondary water flow is sent to the annulus region between the sparger tube and the outer Acrylic tube, as shown in the figure. This water flow is used to shear off the bubbles generated on the outer surface of the sparger tube. The secondary water flow rate can be controlled by a ball valve and a flow meter to ensure that the desired bubble size is generated at the test section inlet. The two-phase mixture then enters a larger chamber where it mixes with the primary flow. The primary water flow enters the chamber through three branch pipes separated by 120° angles. This bubble injector design can provide symmetric and uniform bubble distribution at the test section inlet. The total water flow rate in the test section is controlled by the valves located on the primary flow line. Two-magnetic water flow meters (Toshiba Model LF654, 12.7 mm, and 50.8 mm) are used to measure the total water flow rate entering the test section. This combination could provide an accuracy of less than ± 1% of the actual reading over a wide range of flow rates up to 240 GPM. Four gas flow meters based on the laminar differential pressure flow technology (Cole-Parmer EW series), are used to measure the airflow rate entering the test section. These flow meters can measure airflow from 0-500 standard liter per minute (SLPM) with an accuracy of ± 1% of the actual reading. The test section is also equipped with other instruments, including pressure gauges,

thermocouples, and a high precision differential pressure transducer (Yokogawa EJA110A). Various flow regimes spanning from bubbly to annular could be obtained in the test section by controlling the air and water flow rates. In this study, bubbly and slug flows will be measured by the x-ray system.

Fig. 2-4 shows the schematic of the compact x-ray densitometry system manufactured by En'Urga Inc. As can be seen, it consists of an x-ray tube, three linear detector arrays, high voltage power supply, and controlling and data acquisition electronics in a single lead-shielded compact enclosure. The outside dimension of the enclosure is 62cm×32cm×46cm. Since the lead-shielded enclosure blocks most of the x-ray photons, an additional shielded room is not required for this system. The compact system can be flexibly installed at various locations of a test loop, or be used to measure various test loops. The other advantage of the developed system is that the relative distance between the x-ray source and the detector array is fixed. Therefore, calibration and alignment work is not necessary when measurement location changes. Once the enclosure is in place, no additional parts need to be installed. Only three cables coming out of the enclosure need to be connected. One is connected to the standard 110v AC wall outlet. The other two cables are connected to a personal computer (PC) which are used to control the system and perform data acquisition task.

The x-ray tube (Oxford Jupiter 5000) used in this work has a tungsten target and a focal spot size of 50 μm. The peak voltage can be adjusted between 10-50 kV, and the maximum beam current is up to 1 mA. A low attenuation, 127 μm thick beryllium window is used at the exit of the tube to reduce the absorption and ensure a high transmission rate of low energy photons. The conical beam generated by the tube forms a 23° angle. The tube is designed for continuous operation and thus has excellent stability during the test performed in this work.

Two sets of detectors have been manufactured, one with 0.1 mm wide pixels and the other with 0.4 mm wide pixels. They have similar overall dimensions and can be used with the x-ray system interchangeably. The 0.4 mm detector is used in this work. Detector system panel can be seen in Fig. *2-4*c, where the detector consists of two horizontal linear arrays placed 2.0 cm apart along the flow direction. Note that the vertical array shown in the figure is not used in this study. The center array is about 15.4 cm wide and is located at the same elevation as the x-ray source, whereas the downstream array is about 10.2 cm wide. Each array has uniformly distributed pixels of 0.4 mm in width and 0.6 mm in height. In total, there are 384 and 256 pixels in the center and

downstream arrays, respectively. The detector used in this work has a scintillator layer (Gd_2O_2S:Tb), which converts x-ray photons into visible light. The visible photons are then converted into electric signals by the CMOS photodiode. The electric charges generated in each pixel are amplified by a charge amplifier feedback capacitor and are then output to the data acquisition (DAQ) system.

A software with a graphical user interface (GUI) can be used to control the settings of the x-ray tube (tube current, peak voltage, *etc.*), the linear detector array (sensitivity, resolution, *etc.*), and collect and analyze detector signals. The signal acquisition rate is fixed at 1000 Hz for each pixel in this study. This rate is sufficiently fast to resolve the fast-moving bubbles. At the same time, it gives enough exposure time for each frame to ensure adequate contrast between gas and liquid. In addition, two different charge amplifier feedback capacitances can be selected to achieve the desired output level depending on void fraction conditions.

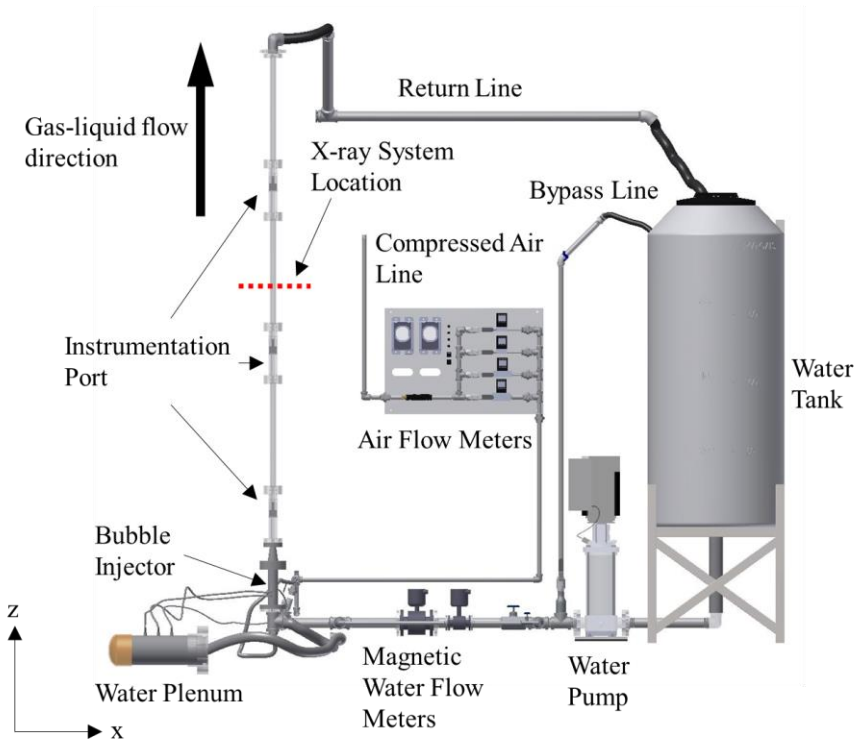

Fig. 2-2: Schematic of the 25.4 mm I.D. air-water two-phase flow test facility.

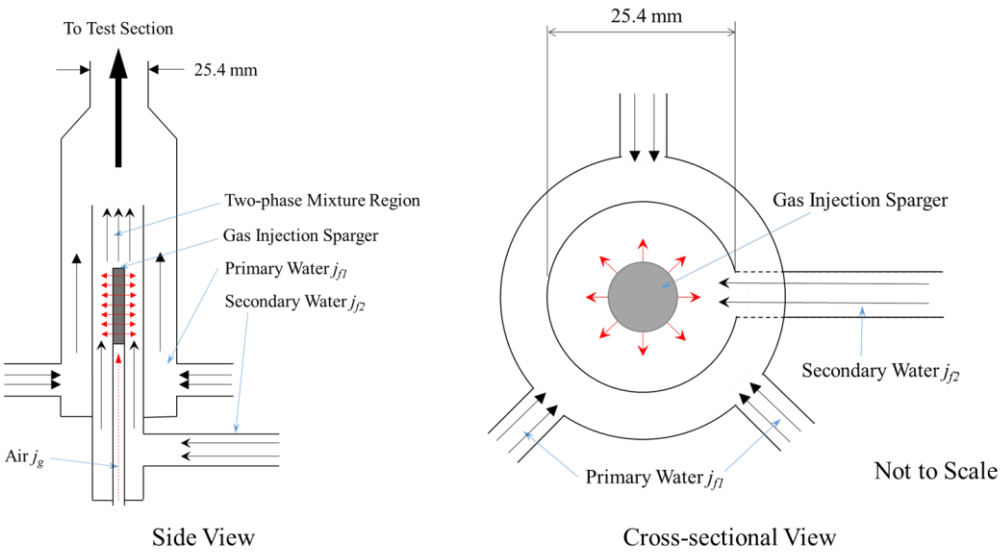

Fig. 2-3: Schematic of the bubble injector design.

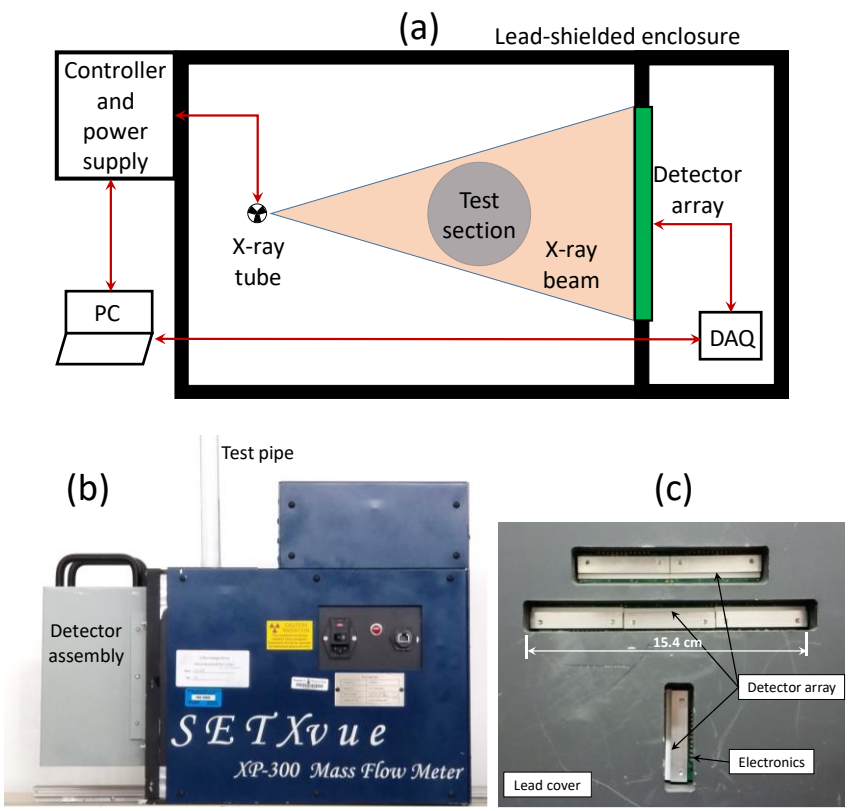

Fig. 2-4: (a) Schematic of the x-ray system; (b) picture taken from the outside with a test pipe inserted; (c) detector array arrangement.

2.3 Measurement Principle

In this section, the measuring principle of the x-ray densitometry system with a polychromatic x-ray source is introduced. *Fig. 2-5* illustrates a typical experimental arrangement of two-phase flow measurement with a linear detector array. A circular pipe of wall thickness δ is placed between the x-ray source and the detector array. The source can be considered as a point in this study due to its relatively small focal spot size (50 μm). For the sample beam shown in *Fig. 2-5*(b), it forms an arbitrary angle θ with the x-axis. To simplify the discussion, it is assumed that there is only one bubble in its path. Once it is generated, the beam will penetrate the air between the source and the pipe, front pipe wall, front liquid section, gas bubble, rear liquid section, rear pipe wall, and the air space between the pipe and the detector before it reaches the detector array. The attenuated x-ray beam is then detected by the detector pixel.

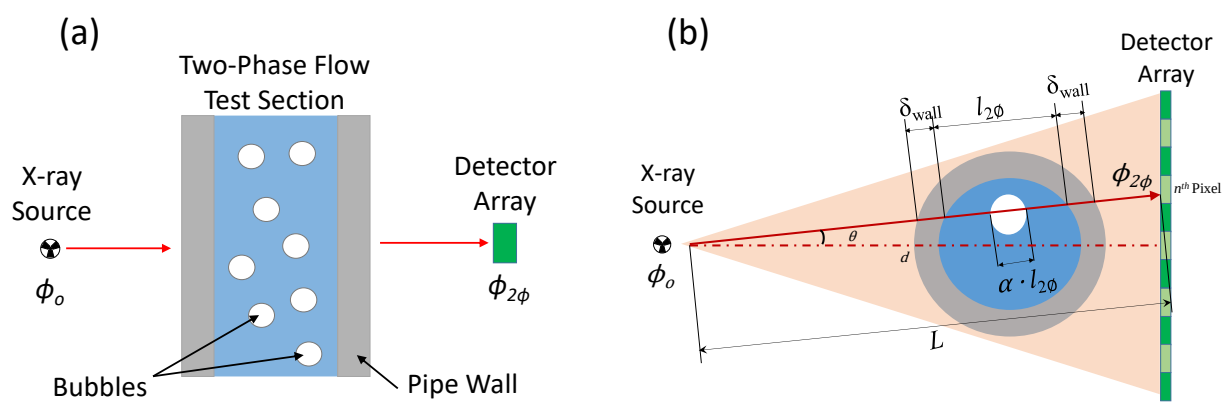

Fig. 2-5: (a) Front and (b) top view of typical void fraction measurement using an x-ray densitometry system with a linear detector array.

Over the x-ray energy range considered here (0~50keV), the attenuation coefficients of water, air, and acrylic show significant variations with photon energy, as shown in *Fig. 2-6*. It can also be seen that the attenuation coefficient of air is smaller than a water or acrylic wall by about three orders of magnitude over the entire energy range concerned here. Therefore, the attenuation in the air space can be neglected in this work. Based on the Beer-lambert law[44], one can estimate the photon flux at the pixel location as follows:

$$\dot{\phi}_{2\phi}(E,\theta) = \frac{\dot{\phi}_0(E,\theta)}{L^2} \cdot e^{-\left[l_{2\phi}(\theta)\cdot\mu_{2\phi}+2\cdot\delta_{wall}(\theta)\cdot\mu_p\right]} \tag{2.2}$$

where, $\dot{\phi}_0$ is the incident photon flux (or fluence rate) generated by the x-ray tube; $\dot{\phi}_0(E,\theta)dE$ represents the number of photons within energy interval [E, E+dE], passing through a unit area that is 1 m away from the source along the θ-angle direction per unit time; $\dot{\phi}_{2\phi}(E,\theta)$ is the photon flux at the pixel location; $\mu_{2\phi}$ is the linear attenuation coefficient of two-phase mixture; μ_p is the linear attenuation coefficient of the test section wall; $l_{2\phi}$ is the chord length along the beam, which is also the overall transmitted depth in the two-phase mixture; δ_{wall} is the wall thickness along the beam; and L is the distance in meter from the x-ray source to the detector pixel.

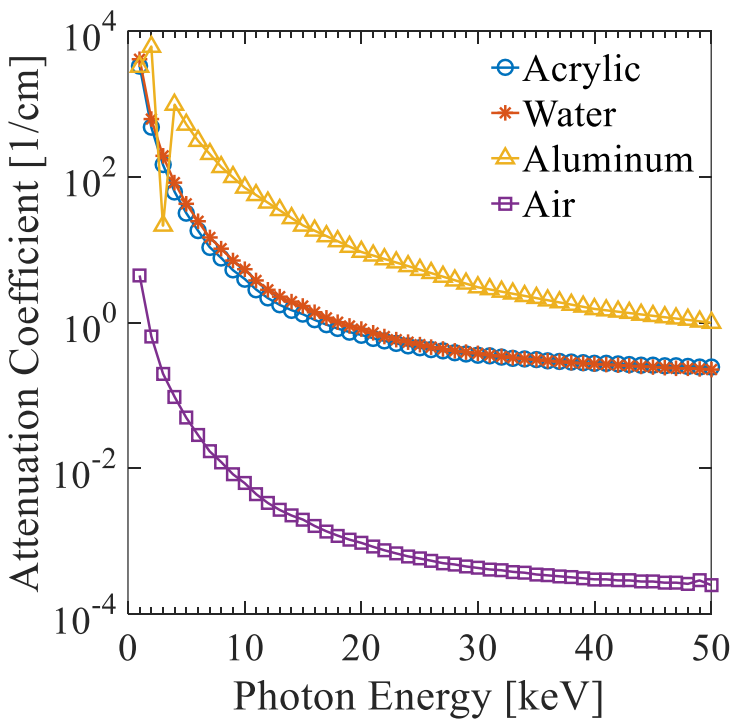

Fig. 2-6: Linear attenuation coefficients of air, water, acrylic, and aluminum over x-ray energy up to 50 keV. Data from the National Institute of Standards and Technology (NIST) are used to generate this figure [45].

The linear attenuation coefficient of the two-phase mixture can be given by:

$$\mu_{2\phi} = \alpha \cdot \mu_g + (1-\alpha) \cdot \mu_f \tag{2.3}$$

Here, α is the line-averaged void fraction along the beam; μ_f is the linear attenuation coefficient of liquid, and μ_g is the attenuation coefficient of gas. The distance between the source and detector pixel L can be expressed as:

$$L = \frac{d}{\cos\theta} \tag{2.4}$$

Here, d is the distance between the x-ray source and the center of the detector array.

Combining Eq.(2.3) with Eq.(2.4), one can express the photon flux after penetrating the two-phase mixture as:

$$\dot{\phi}_{2\phi}(E,\theta) = \frac{\dot{\phi}_0(E,\theta)\cos^2\theta}{d^2} \cdot e^{-\left[\alpha \cdot l_{2\phi}(\theta)\cdot\mu_g + (1-\alpha)\cdot l_{2\phi}(\theta)\cdot\mu_f + 2\cdot\delta_{wall}(\theta)\cdot\mu_p\right]} \tag{2.5}$$

The number of photons within energy interval [E, $E+dE$] received by the pixel in a single exposure can be given as:

$$\begin{aligned}\psi_{2\phi}(E,\theta) &= \dot{\phi}_{2\phi}(E,\theta)A_{pixel}\cos\theta\delta t \\ &= \frac{\dot{\phi}_0(E,\theta)A_{pixel}\cos^3\theta\delta t}{d^2} \cdot e^{-\left[\alpha \cdot l(\theta)\cdot\mu_g + (1-\alpha)\cdot l(\theta)\cdot\mu_f + 2\cdot\delta_{wall}(\theta)\cdot\mu_p\right]}.\end{aligned} \tag{2.6}$$

Here δt is the exposure time; A_{pixel} is the effective detection area of a single pixel.

In general, x-ray photons are produced by bombarding an anode target metal with high-speed electrons accelerated by high voltage cathode [46]. When incident electrons are decelerated near the target atoms (also called Bremsstrahlung interaction), the loss of kinetic energy is emitted as photons of equal energy. If the bombarding electrons have sufficient energy, they can eject an electron out of the innermost shell of a target atom. As a consequence, electrons from higher energy states drop down to fill the lower-energy vacancy, and x-ray photons with characteristic energies determined by the energy level difference are emitted. Typically photons generated by an x-ray tube exhibit polychromatic characteristics, *i.e.*, the x-rays have a wide range of energies, including the continuous spectrum generated by Bremsstrahlung and sharp spikes due to characteristic emissions.

After x-ray photons are generated in the target material, they have to go through the tube window, Acrylic pipe wall, and water in the test section before they reach the detector. These materials have different attenuation coefficients for different energies, as illustrated in *Fig. 2-6*. The x-ray spectrum will be modified every time the photons go through a specific layer of material. Fig. 6a shows the sample spectrum coming out of a 50 kV tube and that after going through acrylic

with various thicknesses. *Fig. 2-7* shows the spectrum with different thicknesses of water up to 50 mm. Here the x-ray spectrum is generated using SpecCalc [47], and a 127μm thick barium window is assumed at the exit of the tube. For both acrylic and water, it is seen that as material thickness increases, photon counts decrease over the entire spectrum. However, lower energy photons are attenuated at a faster rate due to the higher attenuation coefficient. This uneven attenuation has resulted in a change of the shape of the spectrum, also known as the beam-hardening effect. In general, the peak energy and the average energy becomes higher as material thickness increases.

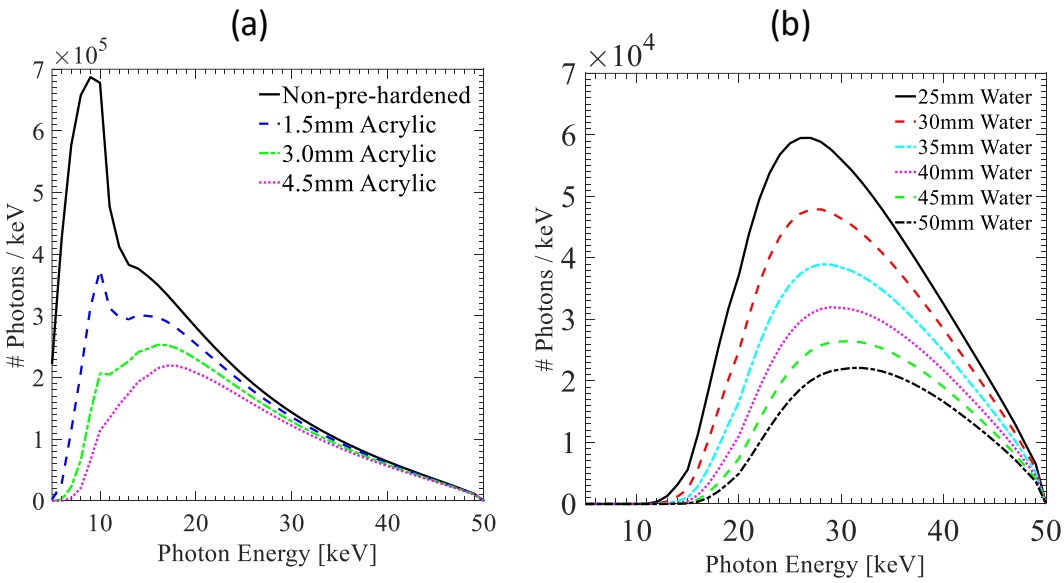

Fig. 2-7: Polychromatic x-ray emission spectrum of a tungsten anode target, with 1 mA filament current, 50 kV tube voltage, at 0.25 m from the source. (a) Initial spectrum and those after penetrating various Acrylic thicknesses; and (b) spectra with different water thicknesses.

A typical non-energy-resolving detector such as the one used in this work does not measure the photon fluence or energy intensity values. Instead, the detector system converts x-ray photons into visible light for detection by the photodiode embedded in the detector. Mäkiharju *et al.* [40] proposed that the signal level of an x-ray intensifier system is proportional to the total energy deposited in the detector pixel. Image intensifier's detection efficiency must be known to perform this calculation. In general, detection efficiency has a strong dependence on x-ray energy and is

very difficult to obtain. The detector used in this work has a scintillator layer which converts x-ray photons into a visible range. Then visible photons are converted into electric signals by the complementary metal-oxide-semiconductor (CMOS) detectors. To accurately determine the overall energy conversion efficiency, one needs to know not only the efficiency of the scintillator but also the efficiency of the CMOS detector, as well as the noises or signal losses introduced during photon transport from the scintillator to the CMOS pixel.

It is reported in the literature that the Gd_2O_2S:Tb scintillator used in this work has an average conversion efficiency of around 15% [48,49]. However, the variation with photon energy has not been reported. The efficiency of the CMOS detector varies with the frequency or wavelength of visible light photons. Such data is not available for the detector used in this work. Therefore, it is generally not practical to establish a detector response model based on the total energy deposition and the energy conversion efficiency of the detector. Note that even though Mäkiharju *et al.* [40] has proposed a model based on energy conversion efficiency, they did not use the model to perform the calculation as such information is not available. Instead, they assumed that the error induced by the x-ray spectrum can be neglected by pre-hardening the polychromatic beam.

In this work, to obtain a relation between the detector response and x-ray photon fluence, the scintillator efficiency, detector efficiency, and photon transport process are lumped into one parameter, the detector conversion factor f_{conv}. This parameter represents the number of electrons generated in the CMOS detector for each x-ray photon received. It should depend on x-ray energy as both scintillator and CMOS efficiencies are photon-energy dependent. Considering Eq.(2.6), the total electric charge generated in the CMOS pixel can be calculated as follows:

$$\begin{aligned} Q &= \frac{1}{6.242\times10^{18}}\int_0^{E_{\max}} \psi_{2\phi}(E,\theta)\cdot f_{conv}(E)\,dE \\ &= \frac{A_{pixel}\cos^3\theta\delta t}{6.242\times10^{18}\,d^2}\int_0^{E_{\max}} \dot{\phi}_0(E,\theta)\cdot e^{-\left[\alpha\cdot l(\theta)\cdot\mu_g+(1-\alpha)\cdot l(\theta)\cdot\mu_f+2\cdot\delta_{wall}(\theta)\cdot\mu_p\right]}\cdot f_{conv}(E)\,dE \end{aligned} \tag{2.7}$$

Here, Q is the electric charge measured in coulomb; E_{max} is the peak voltage of the x-ray tube. The final voltage output by the detector V can be given by:

$$V = \frac{Q}{C_f} \tag{2.8}$$

Here, C_f is the charge amplifier feedback capacitance. Combining Eq.(2.7) and Eq.(2.8), the output voltage of the pixel can be written as:

$$V = \frac{A_{pixel}\cos^3\theta\delta t}{6.242\times10^{18}d^2C_f}\int_0^{E_{\max}}\dot{\phi}_0(E,\theta)\cdot e^{-\left[\alpha\cdot l(\theta)\cdot\mu_g+(1-\alpha)\cdot l(\theta)\cdot\mu_f+2\cdot\delta_{wall}(\theta)\cdot\mu_p\right]}\cdot f_{conv}(E)\,dE \tag{2.9}$$

Here, note that the attenuation coefficients μ_g, μ_f and μ_p all depend on x-ray energy. If these values are relatively uniform over the energy spectrum of consideration, Eq.(2.9) can be simplified as:

$$V = \frac{A_{pixel}\cos^3\theta\delta t}{6.242\times10^{18}d^2C_f}e^{-\left[\alpha\cdot l(\theta)\cdot\mu_g+(1-\alpha)\cdot l(\theta)\cdot\mu_f+2\cdot\delta_{wall}(\theta)\cdot\mu_p\right]}\int_0^{E_{\max}}\dot{\phi}_0(E,\theta)\cdot f_{conv}(E)\,dE \tag{2.10}$$

In another case, if photons have a narrow spectrum, or being monochromatic (such as gamma-ray), Eq.(2.9) can be simplified as:

$$V = \frac{A_{pixel}\cos^3\theta\delta t}{6.242\times10^{18}d^2C_f}f_{conv}(E)\dot{\phi}_0(E,\theta)\cdot e^{-\left[\alpha\cdot l(\theta)\cdot\mu_g+(1-\alpha)\cdot l(\theta)\cdot\mu_f+2\cdot\delta_{wall}(\theta)\cdot\mu_p\right]} \tag{2.11}$$

In either case, one can derive the following equation for the void fraction measured by the pixel:

$$\alpha = \frac{\ln V_{2\phi}-\ln V_{fo}}{\ln V_{go}-\ln V_{fo}} \tag{2.12}$$

where, $V_{2\phi}$ is the voltage output for a two-phase mixture, V_{fo} is the voltage output for the test section full of liquid, or when $\alpha = 0$, and V_{go} is the voltage output for the test section full of gas, or when $\alpha = 1$. The above equation has been widely used to estimate the void fraction for x-ray and gamma-ray CT/densitometry systems [18,27,39,40,50].

The x-ray beam generated from x-ray tubes exhibits polychromatic characteristics. The detector system used in this study does not resolve the polychromatic energy spectrum. It is also noted that the attenuation coefficients μ_g, μ_f and μ_p show a strong dependence on photon energy over the energy range studied here. Under these conditions, it may introduce significant uncertainties if Eq.(2.12) is directly used to calculate void fraction. To investigate this effect, Eq.(2.9) should be analyzed, and the photon to electron conversion factor f_{conv} should be determined for various energy levels.

2.4 Photon to Electron Conversion

The detector conversion factor, f_{conv}, lumps together the effect of three light transport and conversion processes including the conversion from x-ray photon into a visible photon, visible photon transport, and conversion of a visible photon into an electron. The conversion factor should be a function of x-ray energy as the efficiencies of these separate processes typically depend on energy. A calibration experiment is performed to quantify the overall conversion efficiency and its dependence on photon energy. In this experiment, an acrylic container (115 mm L × 115mm W × 65 mm H) is placed between the x-ray source and detector array, which are arranged vertically as illustrated in *Fig. 2-8*. The water of known volume is injected into the container with a syringe to achieve the desired water depth. Then, the x-ray system is turned on, and the voltage signals from the detector array are recorded for the given water volume. The water depth can be calculated based on the injected volume and the cross-sectional area of the container. The same process is repeated for water depths ranging from 8 mm to 38 mm with a 1 mm increment. This thickness range could cover the total depth of the Acrylic wall and water when the 25.4 mm I.D. test section is full of air or water.

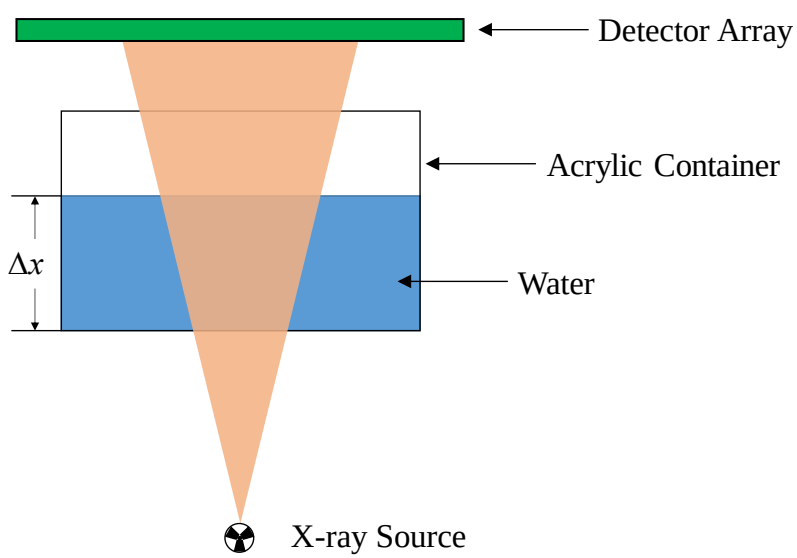

Fig. 2-8: Schematic of the calibration test to determine photon to electron conversion factor f_{conv}.

To facilitate the discussion, the smallest and largest water depths, *i.e.*, 8 mm and 38 mm are used to represent 0 and 100% void fraction values, respectively. The other water depths between these two can be normalized to obtain a void fraction value between 0 and 1. For a given water depth, Eq.(2.12) can be used to estimate the void fraction based on the voltage output from the detector. Fig. 8a shows the comparison between the void fraction calculated by the actual water depth and that by Eq.(2.12) based on the measured voltage signals from the center pixel (pixel #192). *Fig. 2-9*(b) shows the relative error of the void fraction predicted by Eq.(2.12). As can be seen in the figure, the log model presented in the equation generally underestimates the true void fraction. The relative error could be as high as −15% at the low void fraction end. The magnitude of relative error decreases with increasing void fraction. However, close to unity void fraction, two-phase flow is likely falling into the annular flow regime. In that case, the x-ray system is essentially measuring the liquid fraction $1-\alpha$, or film thickness, which is an important parameter to characterize the annular flow. Though the relative error of void fraction is small, the relative error of liquid fraction or film thickness could be very large at the unity void fraction end since the absolute value of these quantities are small. It can be seen from Fig. 8b that the relative error in $1-\alpha$ reaches nearly 40% for void fraction values of 0.9 or higher. From the above discussion, it is concluded that the measurement uncertainty based on Eq.(2.12) could be very large near the zero or unity void fraction values. Even at a void fraction of 0.5, the relative error of void fraction is about 10%.

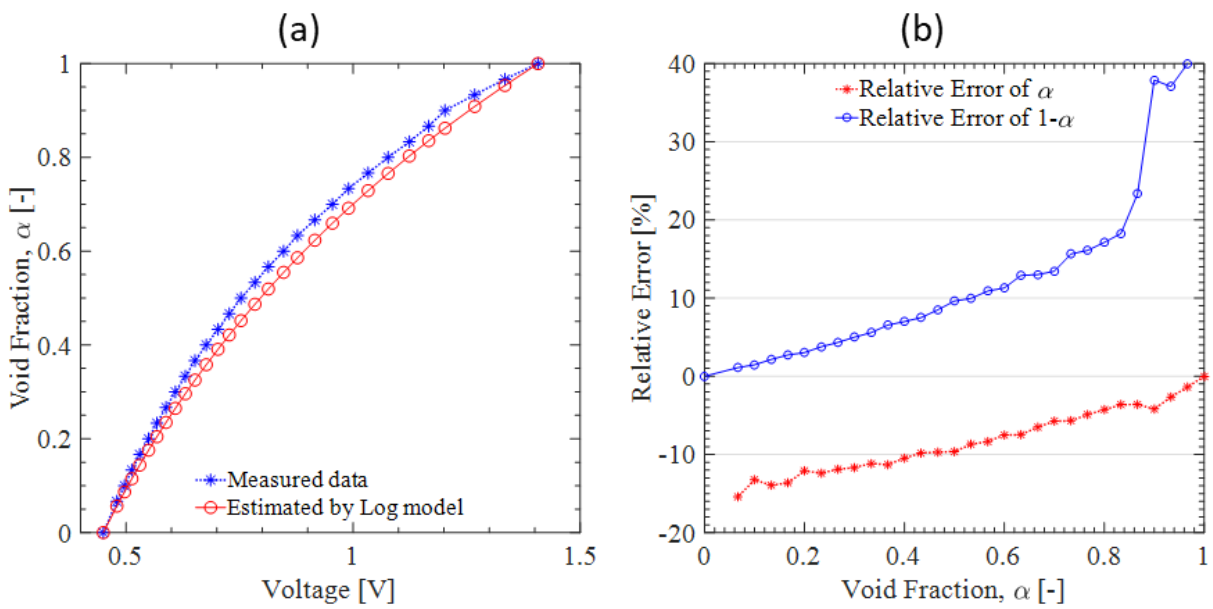

Fig. 2-9: For the center pixel, (a) comparison between measured void fraction and that predicted by Eq. (2-12); (b) the relative error of void fraction (α) and a liquid fraction (1-α) based on Eq. (2-12).

In this study, various polynomial functions (linear, quadratic, and cubic) have been tested for the detector conversion factor f_{con}. From Eq.(2.9), one can predict the absolute voltage output from the detector based on a given conversion factor model and measured void fraction values in the calibration test. The difference between the predicted and the recorded voltages can be compared to evaluate the accuracy of the given model. One can then vary the model coefficients and select the best model that gives the smallest discrepancy between the predicted and recorded voltages. From this optimization process, the following cubic function model has given the best prediction of the test results for all the detector pixels:

$$f_{conv}(E) = a \cdot E^3 + b \cdot E^2 + cE \tag{2.13}$$

where, E is the photon energy in keV; a, b and c are coefficients which should be determined for each pixel based on the calibration data.

A sample result for the center pixel is provided in *Fig. 2-10*. In this case, the detector conversion factor is given by:

$$f_{conv}(E) = 0.09994E^2 - 4.09E + 80.2 \tag{2.14}$$

As can be seen, the conversion factor increases monotonically with photon energy. When a higher energy photon strikes on the detector, more electrons will be generated. Qualitatively, this is consistent with the fact that a higher energy photon should deposit more energy in the detector compared with a low energy photon. The results reveal that the conversion factor does not increase linearly with photon energy. High energy photons tend to generate more electrons per unit energy deposited.

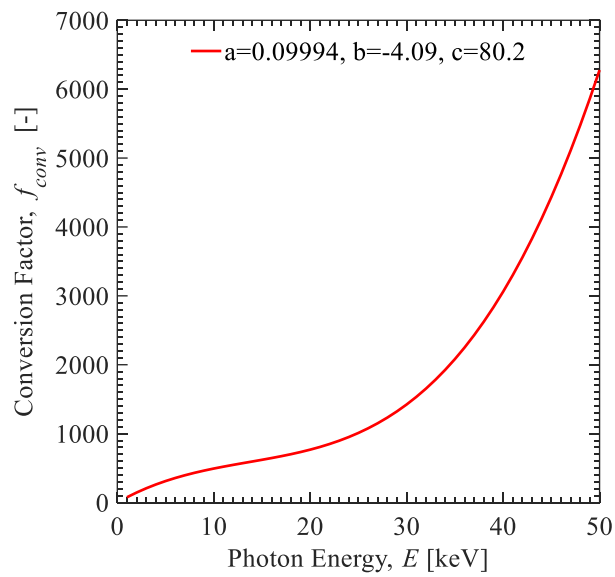

Fig. 2-10: The detector conversion factor f_{conv} for the center pixel obtained from the calibration test.

Essentially, Eq.(2.9) and Eq.(2.14) provide a one-to-one mapping from void fraction to detector response. There are two applications of this mapping. First, one can calculate the voltage response of the detector pixel for a given void fraction condition. The predicted voltage results of the calibration test are shown in Fig. 10a, together with the recorded voltage values during the test. As seen in the figure, the predicted voltage values show an excellent agreement with the experimental data for void fraction ranging from zero to unity. The other application of Eq.(2.9) and Eq.(2.14) is to predict void fraction based on measured voltage values. Eq.(2.9) involves the integration of a complex function of void fraction, thus an explicit expression of the void fraction

may not be available. However, the conversion from voltage to void fraction can be done numerically using a pre-generated curve such as that shown in Fig. 10a. Taking the measured voltage in the calibration test as input, the corresponding void fraction can be predicted. Fig. *2-11*(b) shows the relative error of predicted void fraction and liquid fraction. The relative error of void fraction is within ±2% for all data points. For liquid fraction, all points expect two are within ±2.5% error. The maximum liquid fraction error is 10.3% when $\alpha = 0.9$, or $1-\alpha = 0.1$. The mean absolute percentage error (MAPE) is 0.49% and 0.99% for void fraction and liquid fraction measurement, respectively. This is a significant improvement of the prediction accuracy compared with the similar results predicted by the log model, as shown in Fig. *2-9*(b).

Considering that each detector pixel may vary slightly during the manufacturing process, the above optimization steps have been carried out for each individual pixel in the detector. The conversion factor for an individual pixel can be fitted with a similar polynomial function, as shown in Eq.(2.13), with slightly varying coefficients. Once these conversion factors are obtained, the void fraction measured by individual pixels can be predicted by Eq.(2.9) following a similar approach described above. The pixels that are relevant to the 25.4 mm I.D. test pipe ranges from 110 to 272. For these pixels, the maximum absolute relative error of void fraction measurement is 4.39% among all the data points obtained in the calibration test. The overall MAPE is 0.28%, and more than 96.8% of all data points have an error of less than 2%. For liquid fraction measurement, the maximum absolute relative error is 7.09% among all data points. The overall MAPE is 0.39%, and more than 95.7% of all data points have an error below 2%.

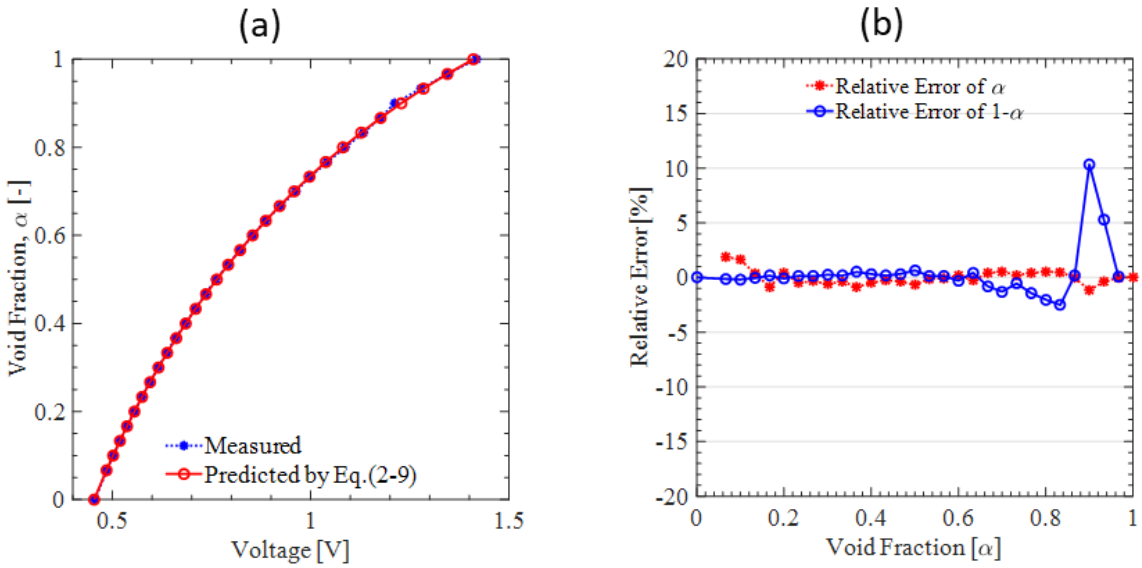

Fig. 2-11: For the center pixel, (a) Comparison between the measured voltage and that predicted by Eq.(2-14) with a conversion factor given by Eq.(2-14); (b) Relative error of the predicted void fraction and liquid fraction based on Eqs. (2-9) and (2-14), and measured voltage.

It is noted that the conversion factor f_{con} is an intrinsic property of the detector pixels, and it does not depend on the object placed in the x-ray system. Therefore, the same conversion factor obtained from the calibration test can be applied to the 25.4 mm circular test section as well. Since the geometry of the circular test section is different from that of the calibration test, additional steps should be taken to establish the relationship between the void fraction and voltage response from the detector pixels. From Fig. *2-4*, it can be seen that each pixel measures the line-averaged void fraction along the chord length formed by the x-ray beam and the inner pipe wall. For each pixel, one can calculate the corresponding chord length $l_{2\phi}$ and the wall-length δ_{wall} based on the given locations of the x-ray source, detector, and test pipe. The angle θ between the beam and the horizontal axis can also be determined from these geometrical parameters. Using Eq.(2.9), one can then predict the voltage response for various void fractions along the x-ray beam. Fig.11a illustrates the predicted results for three different pixels, the center one, and the 20th and 30th pixels from the center. As can be seen, each pixel shows a different curve, which should be caused by the difference in angle θ, chord length $l_{2\phi,}$ and the conversion factor f_{con} of these different pixels.

For the circular test pipe, the voltage response at zero and unity void fractions can be obtained by filling the test section with 100% water and air, respectively. Fig. 11b shows the comparison between the test results and predicted voltage signals over the pixel range covered by the test pipe. As can be seen, the prediction and experimental data agree with each other very well. This result further demonstrates the applicability of Eq.(2.9) for the prediction of detector response. It also indicates that the conversion factor obtained from the calibration test will yield an accurate measurement of void fraction in the 25.4 mm I.D. circular test section. During the actual test with a two-phase mixture flowing inside the pipe, the measured voltage from each detector pixel will be used to determine the corresponding line-averaged void fraction using the pre-generated void fraction – voltage curves as those shown in Fig. *2-12*(a).

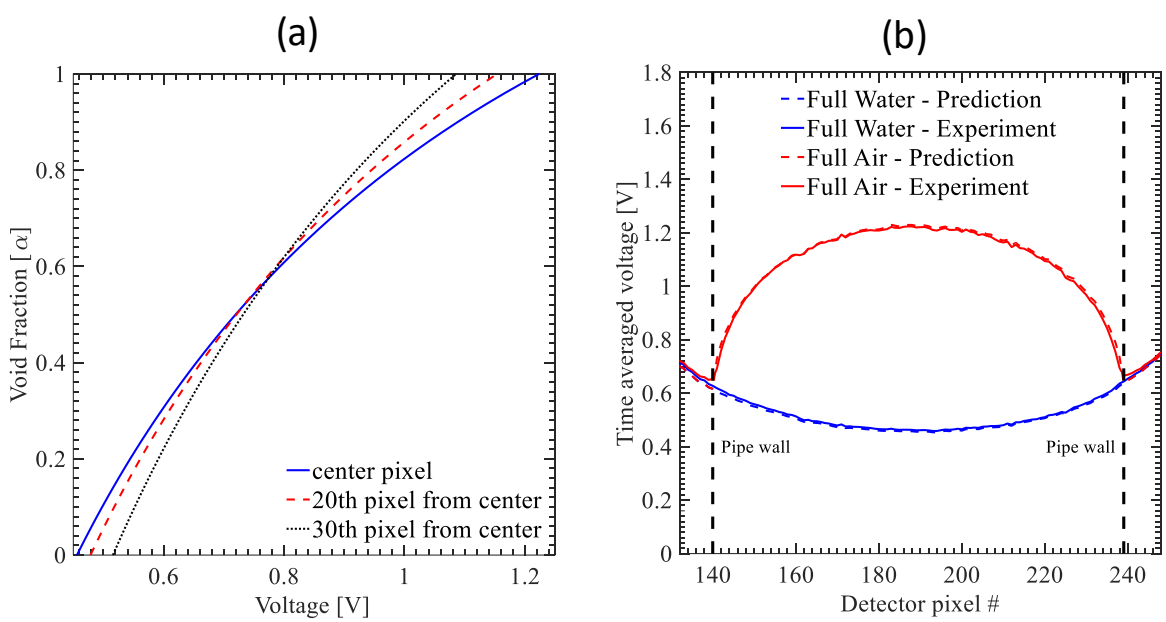

Fig. 2-12: (a) Relationship between the void fraction and detector voltage response for selected pixels for the 25.4 mm I.D. test pipe. (b) Comparison between the predicted voltage and experimental data when the 25.4 mm I.D. test section is filled with water and air.

2.5 Sample two-phase flow result

Measurements of typical two-phase flows are performed using the x-ray densitometry system in the test facility described in Section 2. Two flow conditions will be presented in this section, one bubbly flow, and one slug flow. The superficial gas and liquid velocities are j_g = 0.16, j_f = 0.69 m/s, for the bubbly flow condition, and j_g = 0.30 m/s, j_f = 0.52 m/s for the slug flow condition. These superficial gas velocities are determined based on the inlet gas flow rates and the local pressure measured at the x-ray location. During the test, voltage signals at every detector pixel are recorded for 120 seconds at 1000 fps, which results in 120,000 voltage samples for each detector pixel in a single flow condition.

Each frame of x-ray image records a 1-D distribution of chordal-averaged void fraction along the x-ray beam path. One can stack consecutive 1-D frames together to generate a synthetic 2-D image as shown in Fig. *2-13*. In this process, the bubble velocity information which is discussed later in this section has been used to determine the traveling length of the recorded bubbles within each sampling period. This length and the width of each pixel are adequately scaled in the 2-D image such that the shape and aspect ratio of the bubbles shown in Fig. *2-13* reflects the actual bubble in the flow. Considering the high frame rate of the x-ray system, a sufficient number of layers will be recorded for each bubble. Therefore, the synthetic images should be able to approximate the 2-D x-ray image taken with a film or 2-D imaging sensor on a single exposure. From Fig. *2-13*, it is seen that flow structure in both the bubbly and slug flow conditions show great similarity with conventional x-ray images. The shape of various bubbles including smaller distorted bubbles and large slug bubbles are captured in the synthetic images. It should be pointed out that the intensity of each pixel in the picture can be used to calculate the chordal-averaged void fraction corresponding to the pixel. This is different from the images obtained using visible light cameras, in which the pixel intensity cannot be directly used to calculate void fraction due to highly non-linear reflection and refraction processes.

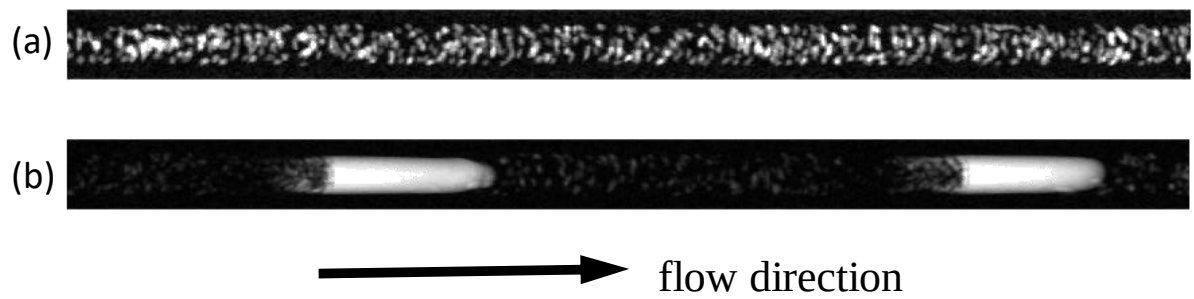

Fig. 2-13: Synthetic 2-D images from the x-ray signals obtained from the 1-D detector array for (a) bubbly flow, jg = 0.16, jf = 0.69 m/s, and (b) slug flow, jg = 0.25, jf = 0.52 m/s.

Fig. *2-14* shows the void fraction distributions along the detector pixel for the bubbly flow and slug flow conditions. The void fraction shown in the figure is obtained by averaging the instantaneous void fraction data over the entire 120 second sampling period. The time-averaged void fraction for the nth pixel, $\bar{\alpha}_n$ can be given as follows:

$$\bar{\alpha}_n = \frac{1}{\Delta T}\int_0^{\Delta T} \alpha_n(\mathrm{V}(t))\, dt \tag{2.15}$$

Two methods are used to convert the recorded voltage signal *V(t)* to void fraction value α_n, the conventional log model expressed by Eq.(2-12), and the newly developed spectrum model as given by Eq.(2-9). Near the wall, the voltage change between full liquid to full gas is small due to the short chord length in this region. The uncertainty of the void fraction measurement could be significant. Therefore, a zero void fraction is assumed at the wall boundary based on the typical void fraction profile obtained using other measuring techniques such as image processing [51]. A linear fitting is performed for the region between the wall and the third pixel to the wall. As seen in the figure, the log model generally underestimates the void fraction, particularly in the central region, where the void fraction is considerably higher than zero. This result is consistent with the calibration result obtained in the previous section, and it further demonstrates that the energy spectrum must be considered to improve the measurement accuracy of the x-ray system. The bubbly flow shows a slight wall peaking phenomenon commonly observed in the literature [51]. This wall peaking is generally attributed to the lift force effect, which acts to push small size

bubbles to the wall. The slug flow shows a center peaked void profile which is also commonly seen in the literature.

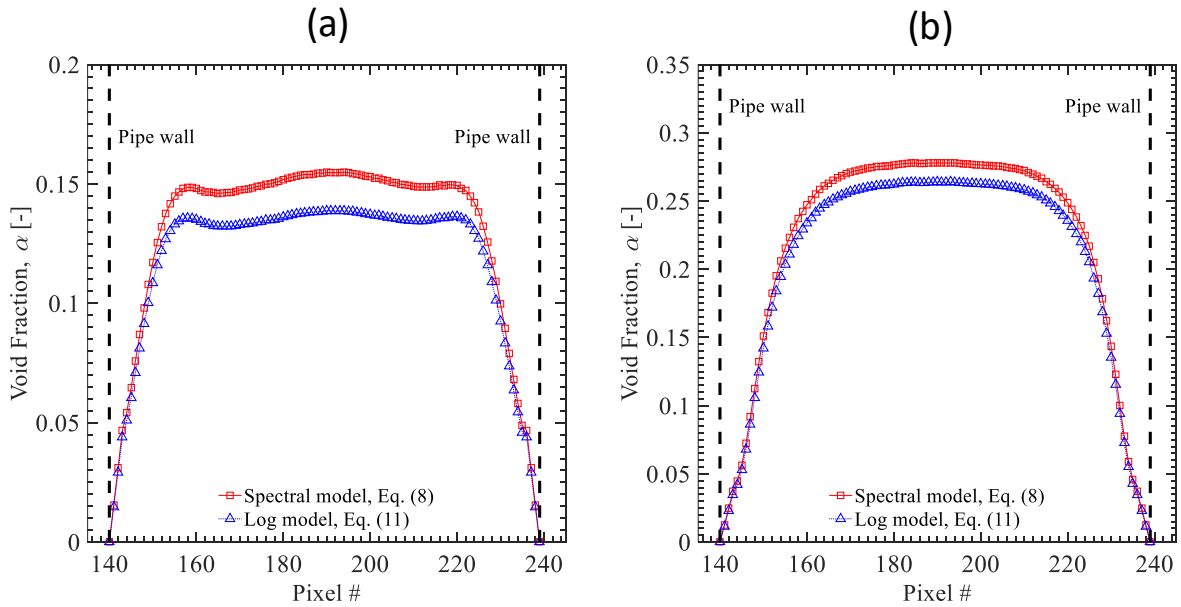

Fig. 2-14: Void fraction distribution along the pixel location. (a) Bubbly flow, jg=0.16 m/s, jf=0.69 m/s. (b) Slug flow, jg=0.30 m/s, jf=0.52 m/s.

The cross-sectional area-averaged void fraction can be calculated based on the pixel distribution discussed above. Rigorously speaking, each detector pixel has a finite area and thus measures an area-averaged void fraction as illustrated in Fig. *2-15*. The void fraction at a particular pixel should be weighted by the coverage area of that pixel (red region in Fig. *2-15*b) to obtain the cross-sectional area-averaged void fraction. Several angles are defined in Fig. *2-15*a to facilitate the calculation of coverage area. As shown in the figure, θ_1 and θ_2 represent the angles formed by the line connecting the x-ray source and the upper and lower edge of the pixel, respectively. These angles can be calculated based on the location of the x-ray source and a given detector pixel. The intersection points of an x-ray beam with the inner perimeter of the test pipe can be determined by solving the equations for the line and circle. In the figure, ξ_1 and ξ_2 represent the angles formed by the radius connecting these intersection points and the center of the test pipe. One can calculate angle ξ_1 based on angle θ_1 as follows:

$$\xi_1 = \cos^{-1}\left(\frac{x_c \cdot \sin(\theta_1)}{r}\right) \tag{2.16}$$

Here, x_c is the distance from the x-ray source to the pipe center, and r is the pipe inner radius. Once the coordinates of the intersection points and angle ξ's are determined, one can calculate the area of the arc segment formed by the x-ray beam and the test section. The coverage area of a pixel (*ABCD*) can be calculated as the difference between the two arc segment area calculated from the lower edge angle θ_1 (Area DGC) and upper edge angle θ_2 (Area AGB). The coverage area of the nth pixel shown in Fig. *2-15*b (*ABCD*) can be expressed as:

$$A_n = \left[\frac{r^2}{2}\left(2\xi_1 - \sin(2\xi_1)\right)\right] - \left[\frac{r^2}{2}\left(2\xi_2 - \sin(2\xi_2)\right)\right] \tag{2.17}$$

The cross-sectional area-averaged void fraction is then calculated as:

$$\langle \alpha \rangle = \frac{1}{\pi r^2}\sum \bar{\alpha}_n A_n \tag{2.18}$$

The above summation should be made over all the detector pixels that have a non-zero coverage area.

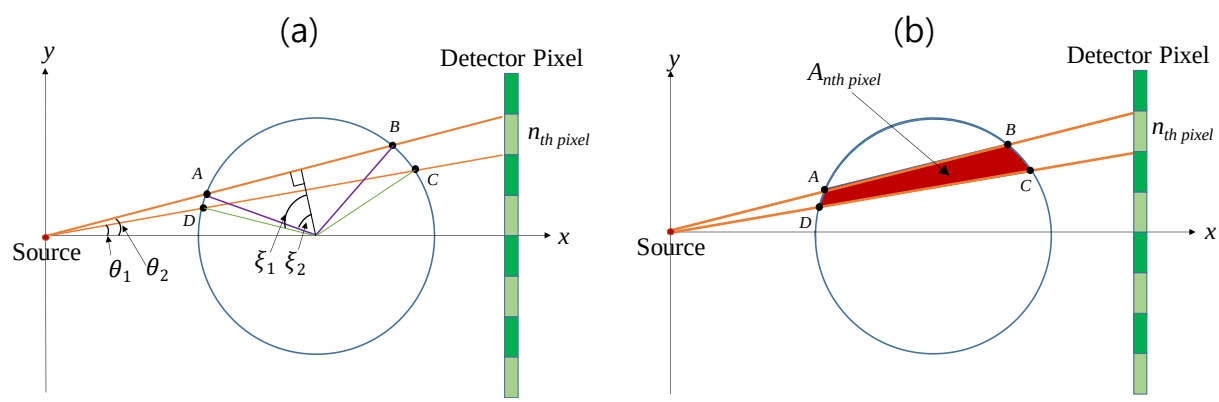

Fig. 2-15: (a) definition of the angles for the nth pixel. (b) coverage area (in red) of the nth pixel.

The x-ray detector system used in this work features two parallel linear arrays along the flow direction. When bubbles pass each detector array, a characteristic signal will be registered. Due to the finite distance between two linear arrays, there will be a time delay for each characteristic bubble signal. Sample signals from the upstream and the downstream arrays are shown in Fig. *2-16* for both the bubbly and slug flow conditions. It is seen that the delay of the bubble signals in the downstream detector array is obvious, especially for the large slug bubbles

shown in Fig. *2-16*b. The cross-correlation from the upstream and downstream signals can be used to determine the average time it takes for bubbles to travel from one detector to the other. Then the gas velocity can be calculated from a distance between the two detector arrays and the time delay obtained from cross-correlation.

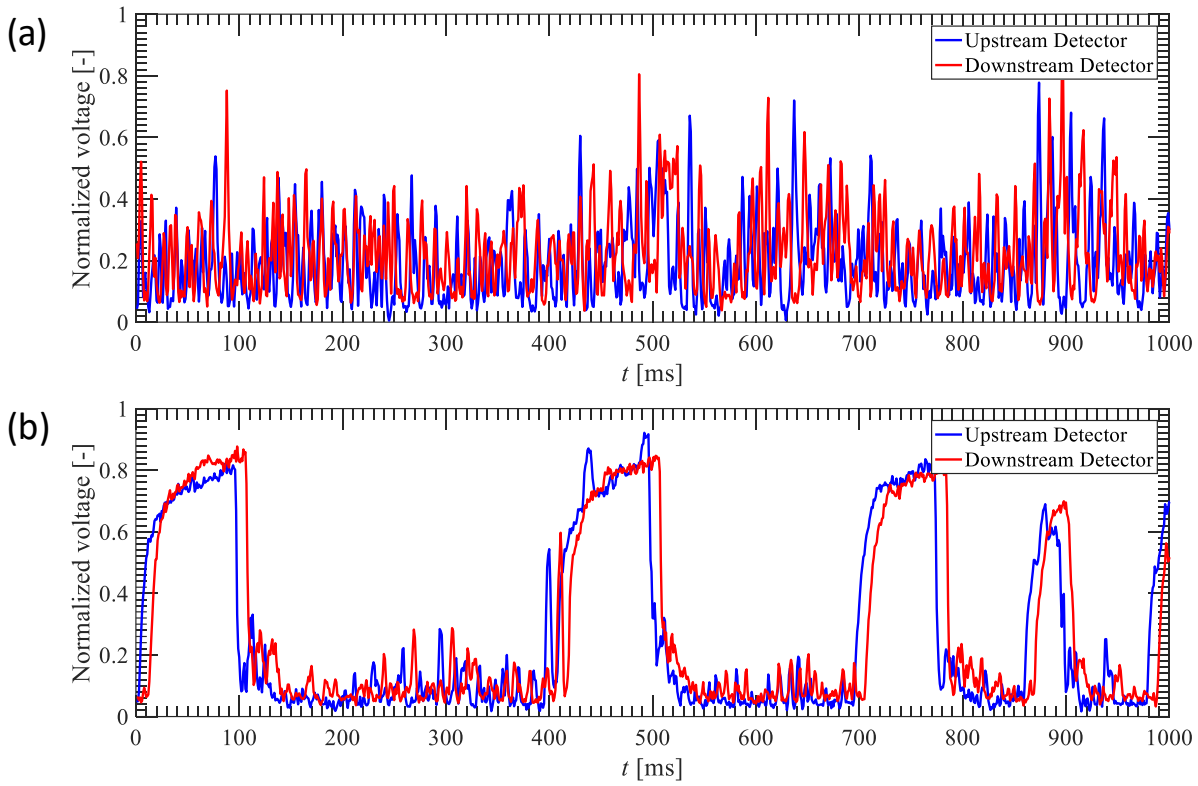

Fig. 2-16: X-ray signals obtained from upstream and downstream detector arrays, (a) bubbly flow; and (b) slug flow.

Fig. *2-17* shows the gas velocity measured at each pixel for both the bubbly and slug flows. As seen in the figure, a center peaked velocity profile appears in both flows. However, the velocity in the bubbly flow decreases faster towards the pipe wall compared with that in the slug flow. The latter has a nearly flat velocity profile in the center region of the pipe. This is anticipated for slug bubbles since each bubble occupies nearly 90% of the pipe radius and every part of the bubble moves at the same velocity. Unlike the typical near-wall velocity profile in single-phase flow, it is seen that the bubble velocity profile has a non-zero value near the wall. This indicates that bubbles have finite slip velocity near the wall, and the typical no-slip wall boundary condition

cannot be applied to bubble velocity. Similar results have been obtained in the literature using other measuring techniques such as the high-speed image processing technique [22].

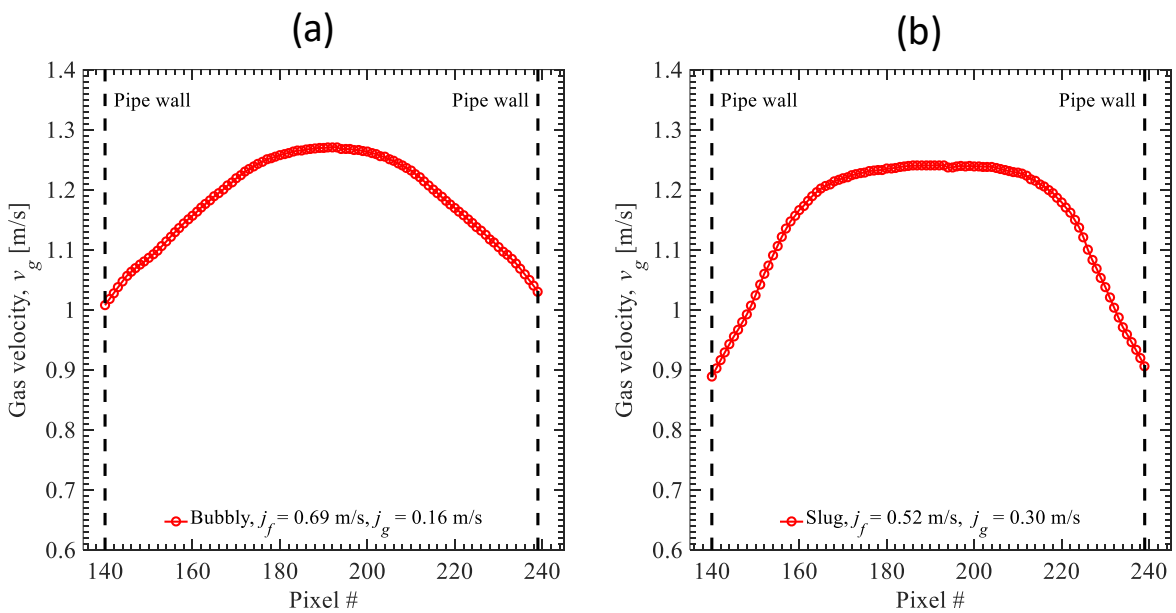

Fig. 2-17: Gas velocity distribution along the pixel, (a) bubbly flow; and (b) slug flow.

Since the voltage signal of each pixel reflects the void fraction in the coverage area, the velocity obtained from the above cross-correlation method should be considered as a void-weighted bubble velocity in the coverage area. Based on its definition, the cross-sectional area-averaged superficial gas velocity can be given as:

$$\langle j_g \rangle = \frac{1}{\pi r^2} \sum \bar{\alpha}_n v_n A_n \tag{2.19}$$

Here, the v_n stands for the velocity for the nth pixel. The void fraction α_n and coverage area A_n is given by Eqs.(2-15) and (2-17), respectively. The void weighted area-averaged gas velocity $<< v_g >>$ can be expressed by:

$$\langle\langle v_g \rangle\rangle = \frac{\langle j_g \rangle}{\langle \alpha \rangle} = \frac{\sum \bar{\alpha}_n v_n A_n}{\sum \bar{\alpha}_n A_n} \tag{2.20}$$

The area-averaged quantities from x-ray are listed in Table *2*. The superficial gas velocities have also been measured by gas flow meters which have an accuracy of ±1.0% of the actual reading. Therefore, these flowmeter readings are considered to be fairly accurate and can be used to assess the measurement accuracy of the x-ray system. The last column of the table shows the relative error of the superficial gas velocity measured by the x-ray system, which is 3.43% and -3.70% for the bubbly and slug flow, respectively. It is not shown in the table, but the relative errors of $<j_g>$ will be -6.42% and -8.73%, if the void fraction is calculated using the log model shown in Eq. (2-12).

Table 2: Area-averaged data from the x-ray and flowmeter measurement.

	$<\alpha>$ [-]	$<<v_g>>$ [m/s]	$<j_g>$ by x-ray [m/s]	$<j_g>$ by flowmeter [m/s]	x-ray $<j_g>$ error [%]
Bubbly Flow	0.140	1.211	0.170	0.164	3.43
Slug Flow	0.242	1.202	0.291	0.302	-3.70

2.6 Summary

In this chapter, the Spectral model is introduced for two-phase flow measurement. The system employs a relatively low voltage and low power x-ray tube, and a high sensitivity linear detector array based on CMOS technology. The system can measure two-phase flow with a spatial resolution of 0.4 mm per pixel and a frame rate of 1000 Hz. The small form factor of the system allows for a fast and flexible measurement at various locations in different test facilities. It is shown that a strong beam hardening effect may arise for this low energy x-ray system, due to the strong variation of attenuation coefficients in the energy range of interest. To account for the beam hardening effect, a spectral model is proposed to predict the detector response for given void fraction values. A calibration test is performed to determine the photon to electron conversion factor, which depends on photon energy and plays an important role in predicting the detector response. The newly developed spectral model has resulted in much-improved prediction accuracy compared with the conventional log model, which can only be valid when attenuation coefficients are constant or when the x-ray beam is monochromatic.

The x-ray system is used to measure the void fraction distribution of a bubbly and slug flow in a 25.4 mm I.D. test pipe. With the high frame rate, the 1-D void distribution measured by the system can be used to generate 2-D synthetic bubble images. These images could provide additional information such as bubble size, frequency, and separate distance, *etc*. The two-layer detector design also enables the measurement of bubble velocity, and thus the superficial gas velocity. Both the void fraction and velocity distributions are qualitatively consistent with the literature data measured by other techniques. The area-averaged superficial gas velocity measured by the x-ray system shows a good agreement with the gas flowmeter reading. The relative error is within ±4% for both the bubbly and the slug flow.

3 Pixel to Radial Conversion Algorithm

3.1 Introduction

The x-ray based tomography or densitometer systems are widely used in two-phase flow measurement due to its reasonable penetration capability, and insensitivity to the flow conditions, i.e., temperature, pressure, etc. [27,52,53]. However, in the one-dimensional (1-D) densitometry system, the measurement obtained from the x-ray projections are line-averaged value weighted by the absorption length, which requires further processing for the radial or local information. The concept of typical x-ray measurement is shown in Fig. *3-1*, here, the sample axisymmetric flow system using the x-ray densitometer is illustrated. The total absorption length weights the measured value at a pixel contributed by the test object placed on the path of line sight of the measurement (LOS). This 1-D tomography of axisymmetric objects has been a recurring topic among the 1-D absorption spectroscopy problem, especially in the two-phase flow measurement application. This problem has been analytically solved by Abel [54] in the early 19th century and became a useful method for reconstructing the axisymmetric flow distribution in many measurement applications such as flow analysis, combustion problem, or holographic, etc. [26,54–58]. For the axisymmetric flow system, the Abel deconvolution (three-point, two-point Abel method) [59–63], onion-peeling [54,64–67], and filtered back-projection method [27,68–70] are often used for reconstructing the radial distribution of void fraction or gas velocity. The related researches are listed in Table *3*.

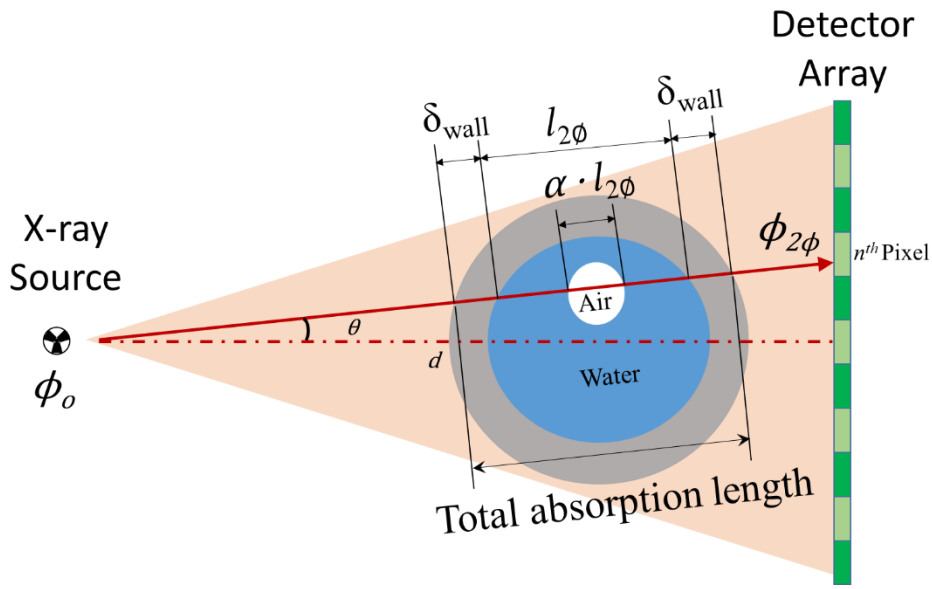

Fig. 3-1: Concept of 1-D line-averaged measurement in the axisymmetric flow system. The absorption length weights the measured value contributed by the test object placed on the path of line sight of the measurement (LOS).

In the literature, Swantek *et al.* [59] used a monochromatic synchrotron x-ray source to measure the flow distribution in a pressurized chamber. This system captures the mean flow distribution at various transverse locations. This line-averaged measurement is converted to radial distribution using the Abel inversion method. Liu and Xu [71] used the onion-peeling method to convert the pixel distribution from the fan-beam projection to radial density data. This work first converts the fan-beam projection to parallel-beam equivalent; then, axisymmetric distribution is reconstructed using the onion-peeling method. Wu *et al.* [61] investigated axisymmetric two-phase flows with a 150 kV fan-beam x-ray source using a Norelco MG 150/130 generator. In this study, the authors used Abel's inversion to convert the pixel measurement to radial distribution. In the study of Saito et al.[60], the two-phase flow experiment is conducted with high frame-rate radiography. This work reconstructs local void fraction distribution by applying the axisymmetric Abel inversion from the re-binned parallel-beam data. Cai and Kaminski [72] reviewed various beam arrangements with the CAT algorithm and investigated the phase distribution of the liquid-fuel using the tomographic absorption spectroscopy (TSA) method. During the reconstruction process, the fan-beam projection is re-sorted into parallel ray equivalent. The measured pixel

values are transformed into radial density distribution using the onion-peeling, two-point, and three-point Abel method.

Table 3: Summary of pixel to a radial flow distribution for two-phase flow application in the literature

Reference	Radiation Source	Test Section	X-ray Beam Geometry	Reconstruction Method
Duke *et al.* (2018) [73]	The monochromatic x-ray beam, 42.5 keV	0.36, 0.90 mm nozzles	Parallel-beam re-binning	Abel inversion
Swantek *et al.* (2017) [59]	Synchrotron x-ray source, 8 keV	5 mm	Parallel-beam re-binning	Abel inversion
Cai and Kaminski (2016) [72]	-	-	Parallel-beam re-binning	Abel inversion, Onion-peeling
Liu *et al.* (2014) [66]	Tunable diode laser absorption spectroscopy (TDLAS)	500 mm	Parallel-beam equivalent	Onion-peeling
Wu *et al.* (2008) [61]	X-ray, 120-150 kV	50 mm	Parallel-beam re-binning	Abel-inversion
Saito *et al.* (2005) [60]	Neutron beam	24 mm	Parallel-beam re-binning	Abel inversion
Schwierz-losefzon *et al.* (2001) [67]	-	60 mm	Parallel-beam re-binning	Onion-peeling
Verra (2000) [62]	Gamma-ray, 85.2-662 kV	20 mm	Parallel-beam re-binning	Abel inversion

From the pixel to radial conversion, there are few challenges associated with the Abel inversion before the deconvolution of the projection data set. It is noted that Abel and onion-peeling methods are intended for data that are sampled at equal intervals. Most x-ray tubes generate a cone-beam illumination where typical x-ray projections are in the form of the fan-beam projection for a linear detector array. These fan-beam projections cannot be directly integrated into an Abel or onion-peeling method. In such a case, these fan-beam projections require a re-binning process to be converted to the parallel-beam equivalent. However, the re-binning often reduces the resolution of the measured flow field; thus, proper interpolation is needed. Fig. *3-2*

illustrates the concept of the re-binning process to covert the fan-beam projection data to parallel-beam equivalent.

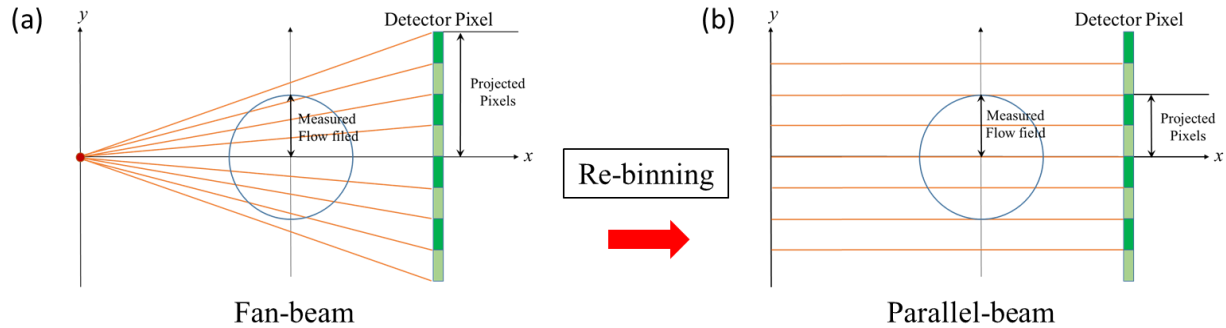

Fig. 3-2: Illustration of fan-beam to parallel-beam rebinning. (a) projected region resulted from the fan-beam projection; (b) Re-binned parallel-beam rays and the equivalent projected resolution.

To overcome the challenges discussed above and extend the pixel to the radial conversion method to the fan-beam data, an efficient and robust conversion technique is proposed to reconstruct the radial distribution in the axisymmetric flow system. The proposed algorithm has several important features, as described in the following:

1. Direct conversion from the fan-beam projection data without re-binning process,
2. The area-based measurement utilizes the local-area information in order to differentiate the specific partitioned region from the 1-D measurement; this preserves the most accurate information associated with the measured area from the line-averaged void fraction information,
3. The algorithm is capable of controlling the desired radial distribution interval without interpolation.

After obtaining the radial distribution, the reconstructed result is compared to the existing Abel and onion-peeling algorithms for conversion accuracy and computational efficiency. A general overview of the proposed method is provided in Fig. *3-3*. The goal of the newly developed method

is to reconstruct the accurate radial distribution and investigate the behavior of the algorithm under the various uncertainty factors.

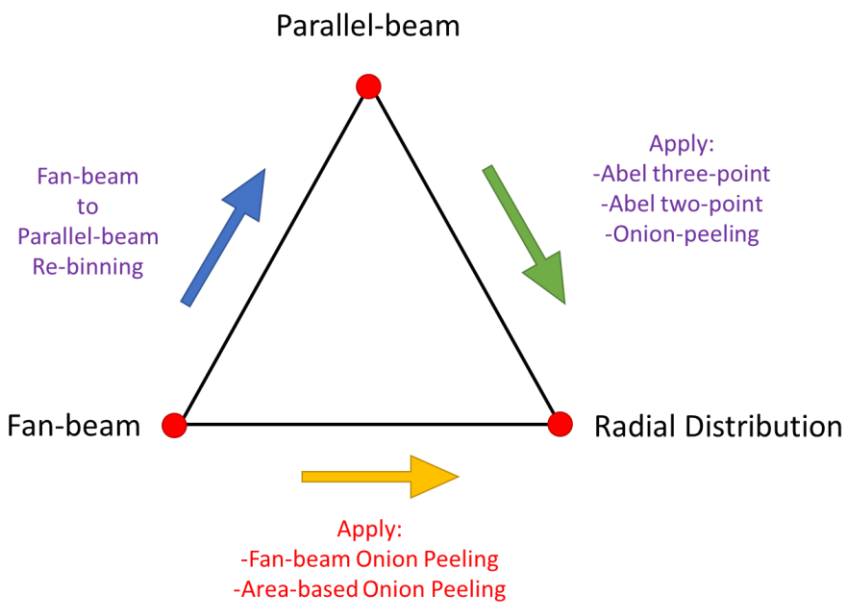

Fig. 3-3: A general overview of the proposed method.

In the following, the experimental setup of the two-phase flow facility is described. Then the details of the newly developed algorithm, the "area-based onion-peeling" (ABOP) algorithm will be presented. Also, the fan-beam based onion-peeling (FBOP), which is a modified version of the onion-peeling method is discussed. The newly developed algorithm is benchmarked by generating synthetic void distributions with added uncertainty factors (i.e., background noise, pixel resolution, off-center shift, or conversion of different void profiles). For the experimental result, the double sensor probe measurement is compared with the ABOP conversion result.

3.2 Experimental Conditions

Fig. *3-4* shows a schematic of the vertical two-phase test loop. The facility is designed to operate the adiabatic air-water two-phase flow at room temperature and near atmospheric pressure. The test section is 3 m tall, with a circular cross-section. The inner diameter (ID) of the test section

is $D_h = 25.4$ mm. A variable speed centrifugal pump (Grundfos GRNE 10-12) is used here to deliver water to the test section from a water storage tank. The building compressed airline is used to supply the airflow, which is regulated by a pressure regulator. As air-water mixture leaves the test section, water is drained back to the storage tank, and the air is vented to the atmosphere. The test loop also has a bypass line which provides additional control of the flow rate, and helps stabilize the flow in the test section.

The total water flow rate is controlled and monitored by the valves and two magnetic water flow meters (Toshiba Model LF654, 15 mm, and 50 mm), respectively. This combination can measure the water flow rate with an accuracy of less than ±1% of the actual reading over a wide range of flow rates up to 3 L/s. The gas flow is regulated by four gas flow meters (Cole-Parmer EW series) with different spans (from 0 to 640 standard liter per minute) for the accuracy of less than ±1% of the actual reading. Secondary water flow is used to shear off bubbles generated on the sparger tube in the two-phase flow injector. This flow can be controlled by a ball valve and a rotameter to ensure that the desired bubble size is generated at the test section inlet.

Three instrumentation ports are located at normalized axial distances of $z / D_h = 14.5$, 51.5, and 88.5 from the two-phase injector, where measurements of conductivity probe and X-ray densitometer system are performed. The test section is divided into a total of three-segment sections, each section contains a measurement port and pressure tap, which is connected with a high precision different pressure transducer (Yokogawa EJA110A) to measure local pressures at each instrumentation port. By controlling the air and water flow rates in the test section, various flow regimes can be measured in this facility.

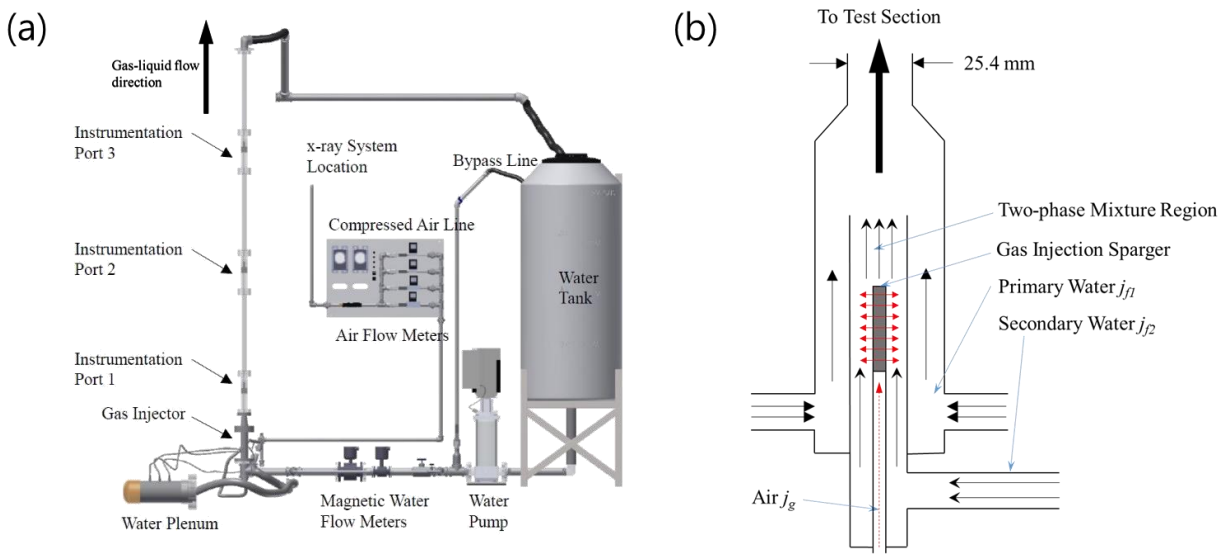

Fig. 3-4: (a) Schematic of the vertical two-phase flow test facility; (b) Two-phase flow injector design; gas-sparger and water injector at the bottom of the test loop.

The X-ray densitometry system used in this work consists of an X-ray tube (Jupiter 5000-93089 manufactured by Oxford Instruments), and two-line detector arrays (XB8804 manufactured by X-scan Imaging). In each detector system, upstream and downstream detector arrays are placed 2.54 cm apart along the flow direction. The line detector arrays have a spatial resolution of 0.4 mm per pixel width, and a total of 384 pixels for the center detector and 256 pixels for the downstream detector. The tungsten anode X-ray tube has a 127 μm thick beryllium window and 50 μm focal spot size. The x-ray tube operated at a maximum voltage of 50kV and a maximum beam current of 1 mA. This output level provides sufficiently high photon flux needed to pass through the test section pipe and two-phase mixture. At the same time, the adequate contrast in the image can be obtained due to the significant difference in attenuation coefficients of air and water. The data acquisition frequency is fixed at 1000 Hz for each detector during the test. Further details about the X-ray system can be found in reference [28].

The x-ray densitometer system records different two-phase flow patterns and shown in Fig. *3-5*. These images are recorded by the x-ray densitometer system at the three instrumentation port locations. Typical flow regimes, bubbly, slug, churn-turbulent, and annular flow are recorded. The development of the two-phase flow pattern from bottom port1 to top port3 can be identified by referring to the three-port images recorded for each flow regime.

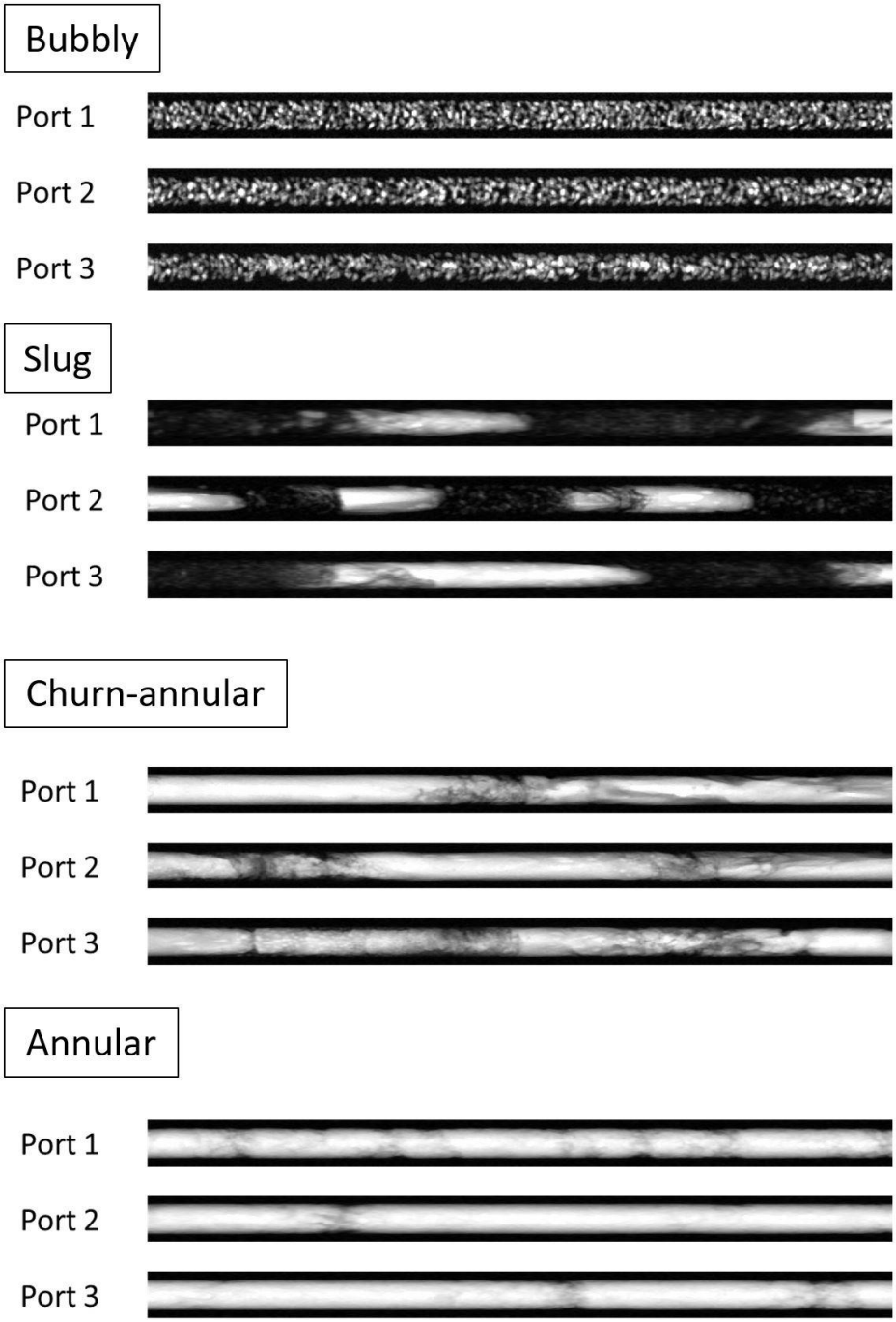

Fig. 3-5: Typical air-water two-phase flow images recorded by the x-ray system. From top to bottom, the bubbly, slug, churn-annular, and annular flow regime are visualized.

3.3 Methodology

3.3.1 Area-based onion-peeling

The line-averaged void fraction can be determined by the total absorption length contributed by the test object placed on its projection path. However, rigorously speaking x-ray projection is not a line projection because each detector pixel detects the x-ray photons with a finite measurement area. Therefore, a detector pixel measures an area-weighted void fraction at a specific pixel location; this concept is illustrated in Fig. *3-6*. Therefore, a measured line-averaged void fraction at a specific pixel location is weighted by the scanned x-ray area of that corresponding pixel (the yellow shaded area illustrated in Fig. *3-6*). Here, x-ray source and detector pixel locations are assumed to be fixed, and the circular system is placed in the global coordinate system with center position (*h*,*k*). Each ray connecting the source point and the upper edge (*UE*), and lower edge (*LE*) of the pixel has a generic line equation for the i_{th} pixel as $ax+by+c=0$. This line beam has a slope, where, $m_{i_{UE}}=(y_{i_{UE}}-y_o)/(x_{i_{UE}}-x_o)$ and $m_{i_{LE}}=(y_{i_{LE}}-y_o)/(x_{i_{LE}}-x_o)$. Here, the x-ray source is assumed to be fixed at (x_o, y_o)=(0,0), and c=0. Formulation of this i_{th} projection is:

$$y=\frac{y_i}{x_i}x \quad \rightarrow \quad \underset{a}{y_i}\,x-\underset{b}{x_i}\,y=0 \tag{3.1}$$

As shown in the figure, $r_{i_{LE}}$ and $r_{i_{UE}}$ represent the normal distance from the pipe center location (*h*,*k*) to the lower and upper edge line beam, respectively. The following equation can determine the normal distance, which is the overall distance between the center of the circular-pipe and the i_{th} projection-ray:

$$r_{i_{UE}}=\frac{|ah+bk+c|}{\sqrt{a^2+b^2}}=\frac{|y_{i_{UE}}h+x_{i_{UE}}k|}{\sqrt{{y_{i_{UE}}}^2+{x_{i_{UE}}}^2}},\quad r_{i_{LE}}=\frac{|ah+bk+c|}{\sqrt{a^2+b^2}}=\frac{|y_{i_{LE}}h+x_{i_{LE}}k|}{\sqrt{{y_{i_{LE}}}^2+{x_{i_{LE}}}^2}} \tag{3.2}$$

The interaction points between each projection ray and the circular test sections can be determined by implementing the equations for the circle and the line in the global coordinate system. In Fig. *3-6*, the variable $\beta_{i_{LE}}$ and $\beta_{i_{UE}}$ indicates the segment angles formed by the line connecting from the center of the circular test section (*h*,*k*) to the interaction points between the line formed by each projection ray and the circular test section. The variable normal distance r_i and pipe inner radius

R_s can determine the segment angle $\beta_{i_{LE}}$ and $\beta_{i_{UE}}$. This equation can be expressed in the following equation:

$$\beta_{i_{UE}} = 2 \cdot \cos^{-1}\left(\frac{r_{i_{UE}}}{R_s}\right), \quad \beta_{i_{LE}} = 2 \cdot \cos^{-1}\left(\frac{r_{i_{LE}}}{R_s}\right) \tag{3.3}$$

With the segment angle(s) and interaction points formed by the circular system and each projection ray, one can determine the portion of the segment area of the circle formed by each projection ray and the circular test section. The scanned x-ray area, which is an indication of the actual x-ray projected area of a specific pixel (*ABCD*) can be formulated by calculating the difference between the segment area formed by lower-line edge (DGC) and segment area formed by the upper-line edge (AGB), respectively. The x-ray scanned pixel area (*SPA*) for the i_{th} pixel can be determined by the difference between the segment area formed by lower and upper edge beam, this can be expressed in the following equation:

$$SPA_i = \left[\frac{R^2}{2}\left(\beta_{i_{LE}} - \sin(\beta_{i_{LE}})\right)\right] - \left[\frac{R^2}{2}\left(\beta_{i_{UE}} - \sin(\beta_{i_{UE}})\right)\right] \tag{3.4}$$

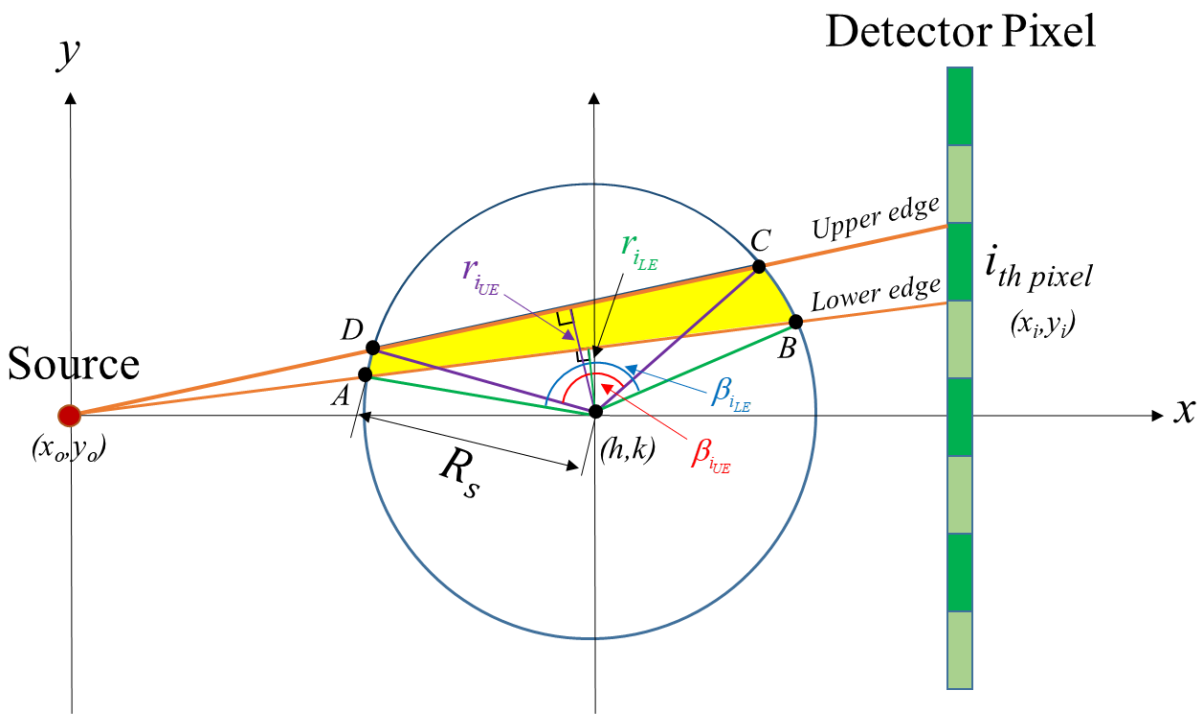

Fig. 3-6: Definition of the segment angles and the x-ray scanned pixel area (SPA) *ABCD* for the i_{th} pixel location.

Up to this point, the equation Eq.(3.4) can obtain the entire *SPA* associated with the i_{th} pixel measurement location resulted from the forward projection. The next step is to define the radial/local partitioned area associated with unknown radial/local void fraction value. Illustration of this local area (partitioned area) with a partitioned circular ring has a radius r_j are shown in Fig. *3-7*. Here, the weighted area of the local void fraction at a specific j_{th} radius can be determined by the formulating the partitioned area (*PA*) of that specific j_{th} ring (shaded red area of a specific circular ring in Fig. *3-7*). As shown in the figure, $r_{i_{LE},j}$ and $r_{i_{UE},j}$ represent the normal distance from the pipe center location (*h*,*k*) to the lower and upper edge line beam, respectively. The intersection points resulted from each projection ray, and the inner circular ring of each j_{th} radius can be determined by implementing the equations for the circle and the line in the global coordinate system for each circular sector with the j_{th} radius. In the figure, $\beta_{i_{UE},j}$ and $\beta_{i_{LE},j}$ represents the segment angles that are formed by the specific radius $r_{i,j}$ that linking intersection points and the

center of the circular test section. The next step is to calculate each segment angle $\beta_{i,j}$ with the same step for segment angle formulation by using the Eq.(3.3). This segment angle formulation is expressed in the following equation:

$$\beta_{i_{UE},j} = 2\cdot\cos^{-1}\left[\frac{r_{i_{UE},j}}{R_{s_{i,j}}}\right], \quad \beta_{i_{LE},j} = 2\cdot\cos^{-1}\left[\frac{r_{i_{LE},j}}{R_{s_{i,j}}}\right] \tag{3.5}$$

Here, the partitioned circular radius $r_{i,j}$ should be a range within $0 < r_{ij} < R_s$.

Up to here, the coordinates of the intersection points formed by each projection ray and every circular sector and segment angles are determined. With the calculated parameters in the circular system, one can determine the partitioned area formed by the forward projection and the j_{th} circular radius. The coverage area for the i_{th} pixel at the j_{th} circular radius ($A_{ij}B_{ij}C_{ij}D_{ij}$) can be calculated by subtracting between the coverage area calculated from the radius $r_{i,j}$ (Area $A_{ij}GB_{ij}$) and $r_{i,j+1}$ (Area $D_{ij}GC_{ij}$). The partitioned area *PA* (red zone shown in Fig. *3-7*) for the i_{th} pixel and j_{th} radius is:

$$\begin{aligned} PA_{i,j} &= SPA_{i,j} - SPA_{i,j+1} \\ &= \left[\frac{R_{i,j}^{\ 2}}{2}\left(\beta_{i_{LE},j} - \sin(\beta_{i_{LE},j})\right)\right] - \left[\frac{R_{i,j}^{\ 2}}{2}\left(\beta_{i_{UE},j} - \sin(\beta_{i_{UE},j})\right)\right] - \\ &\qquad \left[\frac{R_{i,j+1}^{\ 2}}{2}\left(\beta_{i_{LE},j+1} - \sin(\beta_{i_{LE},j+1})\right)\right] + \left[\frac{R_{i,j+1}^{\ 2}}{2}\left(\beta_{i_{UE},j+1} - \sin(\beta_{i_{UE},j+1})\right)\right] \end{aligned} \tag{3.6}$$

From the above equation, one can determine the *PA* for every partitioned radius r_{ij}.

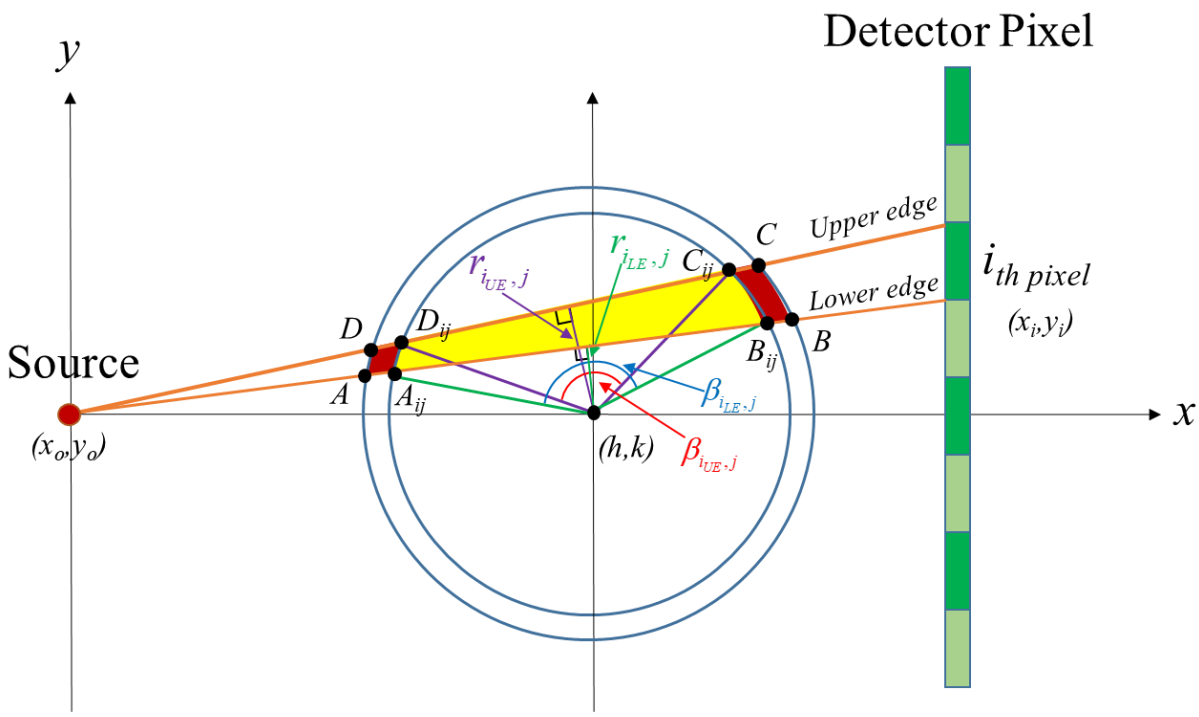

Fig. 3-7: Definition of the partitioned area (*PA*) for the i_{th} pixel and j_{th} partitioned circular ring.

Formulation from the Eq.(3.6), one can determine the *PA* for every i_{th} pixel associated with every circular sector associated with r_j. Here, one can denote the weighted area void fraction measured by the i_{th} pixel and j_{th} radius in the following equation:

$$\sum_{i,j}^{n} \alpha(r_j) \cdot \frac{PA_{i,j}}{SPA_i} = \bar{\alpha}_i \tag{3.7}$$

One may rearrange the above equation in the form of a matrix array for every pixel location and reshape the calculated matrix array into a form of an upper triangular matrix in the following form:

$$\begin{bmatrix} \frac{PA_{1,1}}{SPA_1} & \frac{PA_{1,2}}{SPA_1} & \frac{PA_{1,3}}{SPA_1} & \cdots & \frac{PA_{1,n-1}}{SPA_1} & \frac{PA_{1,n}}{SPA_1} \\ 0 & \frac{PA_{2,2}}{SPA_2} & \frac{PA_{2,3}}{SPA_2} & \cdots & \frac{PA_{2,n-1}}{SPA_2} & \frac{PA_{2,n}}{SPA_2} \\ 0 & 0 & \frac{PA_{3,3}}{SPA_3} & \cdots & \frac{PA_{3,n-1}}{SPA_3} & \frac{PA_{3,n}}{SPA_3} \\ \vdots & \vdots & \vdots & \ddots & \vdots & \vdots \\ 0 & 0 & 0 & \cdots & \frac{PA_{n-1,n-1}}{SPA_{n-1}} & \frac{PA_{n-1,n}}{SPA_{n-1}} \\ 0 & 0 & 0 & \cdots & 0 & \frac{PA_{n,n}}{SPA_n} \end{bmatrix} \cdot \begin{bmatrix} \alpha(r_1) \\ \alpha(r_2) \\ \alpha(r_3) \\ \vdots \\ \alpha(r_{n-1}) \\ \alpha(r_n) \end{bmatrix} = \begin{bmatrix} \bar{\alpha}_1 \\ \bar{\alpha}_2 \\ \bar{\alpha}_3 \\ \vdots \\ \bar{\alpha}_{n-1} \\ \bar{\alpha}_n \end{bmatrix} \tag{3.8}$$

For the convenience rewrite above equation into a reduced form:

$$\left[\frac{PA_{i's,j's}}{SPA_{i's,j's}} \right] \cdot \left[\alpha(r_{j's}) \right] = [\bar{\alpha}_i] \tag{3.9}$$

The partitioned area element $\left[\frac{PA_{i's,j's}}{SPA_{i's,j's}} \right]$ denotes the contribution of the unknown local void fraction $\alpha(r_j)$ to the measured void fraction by the i_{th} pixel location $[\bar{\alpha}_i]$. The radial void fraction can be solved as following back substitution or using Gaussian elimination method:

$$\alpha(r_j) = \left[\frac{PA_{i's,j's}}{SPA_{i's,j's}} \right]^{-1} \cdot [\bar{\alpha}_i] \tag{3.10}$$

Through the use of Eq.(3.10), the radial void fraction profile can be obtained.

3.3.3 Modified fan-beam onion-peeling method

In the fan-beam orientation, the overall cord-length cannot be mathematically solved by a single spatial variable (i.e., data spacing Δr). In the fan-beam geometry, the cord-length resulted by the LOS beam to each i_{th} pixel locations is not equivalent to the measured pixel position in the parallel-beam. Therefore, the overall cord-length for associated LOS beam needs to be calculated that varies along the fan-beam radial distance r_i (normal distance from (h,k)) for its specific i_{th} pixel location. The concept of specific cord-length contributed by the specific fan-beam projection is illustrated in *Fig. 3-8*. Here, an overall cord-length for the specific segment intervals are

determined by radial distance r_i at each i_{th} pixel location. A normal distance can describe this radial distribution from the center of the circular system (h,k) to the i_{th} pixel projection.

First, one needs to calculate the radial distance r_i for each ith pixel center and both end edges. The radial distance r_i is the normal distance between the pipe center point (h,k) and the ith projection line. Here, the x-ray source point and the detector pixel locations are assumed to be fixed in the global coordinate system. Each projection ray connecting the x-ray source and the upper-line edge (UE), centerline (CL), and lower-line edge (LE) of the pixel have a generic line equation for the ith pixel location as $ax+by+c=0$. This line beam has a slope, $m_{i_{UE}}=(y_{i_{UE}}-y_o)/(x_{i_{UE}}-x_o)$ and $m_{i_{CL}}=(y_{i_{CL}}-y_o)/(x_{i_{CL}}-x_o)$.

Here, the x-ray source is assumed to be fixed at (x_o, y_o)=(0,0), and c=0. Formulation of the i_{th} projection is:

$$y=\frac{y_i}{x_i}x \quad \rightarrow \quad \underset{a}{y_i}\,x-\underset{b}{x_i}\,y=0 \tag{3.11}$$

The normal distance r_i between the center of the system (h,k) to the i_{th} projection is::

$$r_{i_{UE}}=\frac{|ah+bk+c|}{\sqrt{a^2+b^2}}=\frac{|y_{i_{UE}}h+x_{i_{UE}}k|}{\sqrt{{y_{i_{UE}}}^2+{x_{i_{UE}}}^2}},\quad r_{i_{CL}}=\frac{|ah+bk+c|}{\sqrt{a^2+b^2}}=\frac{|y_{i_{CL}}h+x_{i_{CL}}k|}{\sqrt{{y_{i_{CL}}}^2+{x_{i_{CL}}}^2}} \tag{3.12}$$

One can rearrange above calculated arrays in the form of n by n upper triangular matrix in the following matrix form:

$$r_{i_{CL}}=\begin{bmatrix} r_{1_{CL}} & r_{1_{CL}} & \cdots & r_{1_{CL}} & r_{1_{CL}} \\ 0 & r_{2_{CL}} & \cdots & r_{2_{CL}} & r_{2_{CL}} \\ \vdots & \vdots & \ddots & \vdots & \vdots \\ 0 & 0 & \cdots & r_{n-1_{CL}} & r_{n-1_{CL}} \\ 0 & 0 & \cdots & 0 & r_{n_{CL}} \end{bmatrix},\quad r_{i_{UE}}=\begin{bmatrix} r_{1_{UE}} & r_{2_{UE}} & \cdots & r_{n-1_{UE}} & r_{n_{UE}} \\ 0 & r_{2_{UE}} & \cdots & r_{n-1_{UE}} & r_{n_{UE}} \\ \vdots & \vdots & \ddots & \vdots & \vdots \\ 0 & 0 & \cdots & r_{n-1_{UE}} & r_{n_{UE}} \\ 0 & 0 & \cdots & 0 & r_{n_{UE}} \end{bmatrix} \tag{3.13}$$

Cord-length for the specific partitioned j_{th} ring at every i_{th} pixel is:

$$CL_{i_{th},j_{th}}=2\cdot\sqrt{{r_{i_{UE}}}^2-{r_{i_{CL}}}^2} \tag{3.14}$$

Here, each partitioned j_{th} ring's radius r_i is equal to the radial distance from the center point (h,k) to the upper edge of the i_{th} pixel line beam. The radius for the j_{th} partitioned ring is:

$$r_{j_{th}} = r_{i_{UE}} \tag{3.15}$$

Cord-length for each partitioned j_{th} ring at every i_{th} pixel location can be rewritten as:

$$CL_{i_{th},j_{th}} = 2 \cdot \sqrt{r_{j_{th}}^{\ 2} - r_{i_{CL}}^{\ 2}} \tag{3.16}$$

Overall cord-length (total penetration depth) for the circular pipe measured by every i_{th} pixel location is:

$$CL_{i_{th}.sum} = 2 \cdot \sqrt{R_s^{\ 2} - r_{i_{CL}}^{\ 2}} \tag{3.17}$$

Here, R_s is the inner pipe radius. Rearrange this $CL_{i_{th}.sum}$ into n by one matrix form:

$$CL_{i_{th}.sum} = \begin{bmatrix} CL_{1.sum} \\ CL_{2.sum} \\ CL_{3.sum} \\ \vdots \\ CL_{n-1.sum} \\ CL_{n.sum} \end{bmatrix} = \begin{bmatrix} 2 \cdot \sqrt{R_s^{\ 2} - r_{1_{CL}}^{\ 2}} \\ 2 \cdot \sqrt{R_s^{\ 2} - r_{2_{CL}}^{\ 2}} \\ 2 \cdot \sqrt{R_s^{\ 2} - r_{3_{CL}}^{\ 2}} \\ \vdots \\ 2 \cdot \sqrt{R_s^{\ 2} - r_{n-1_{CL}}^{\ 2}} \\ 2 \cdot \sqrt{R_s^{\ 2} - r_{n_{CL}}^{\ 2}} \end{bmatrix} \tag{3.18}$$

Cord-length difference between the j_{th} and j_{th-1} partitioned ring at every i_{th} pixel location is:

$$CL_{i.j.differ} = \underbrace{2\sqrt{r_{j_{th}}^{\ 2} - r_{i_{CL}}^{\ 2}}}_{j_{th}} - \underbrace{2\sqrt{r_{j_{th-1}}^{\ 2} - r_{i_{CL}}^{\ 2}}}_{j_{th-1}} \tag{3.19}$$

Rearrange above calculation into n by n upper triangular matrix:

$$CL_{i,j.differ} = \begin{bmatrix} CL_{1,1.differ} & CL_{1,2.differ} & CL_{1,3.differ} & \cdots & CL_{1,n-1.differ} & CL_{1,n.differ} \\ 0 & CL_{2,2.differ} & CL_{2,3.differ} & \cdots & CL_{2,n-1.differ} & CL_{2,n.differ} \\ 0 & 0 & CL_{3,3.differ} & \cdots & CL_{3,n-1.differ} & CL_{3,n.differ} \\ \vdots & \vdots & \vdots & \ddots & \vdots & \vdots \\ 0 & 0 & 0 & \cdots & CL_{n-1,n-1.differ} & CL_{n-1,n.differ} \\ 0 & 0 & 0 & \cdots & 0 & CL_{n,n.differ} \end{bmatrix} \tag{3.20}$$

With variables obtained from the above equations, one can describe the void fraction measured by the i_{th} pixel location as:

$$\sum_{i,j}^{n} \alpha(r_j) \cdot \frac{CL_{i,j.differ}}{CL_{i_{th}.sum}} = \bar{\alpha}_i \tag{3.21}$$

Rearrange the calculated array in the form of an upper triangular matrix array:

$$\begin{bmatrix} \frac{CL_{1,1.differ}}{CL_{1.sum}} & \frac{CL_{1,2differ}}{CL_{1.sum}} & \frac{CL_{1,3.differ}}{CL_{1.sum}} & \cdots & \frac{CL_{1,n-1.differ}}{CL_{1.sum}} & \frac{CL_{1,n.differ}}{CL_{1.sum}} \\ 0 & \frac{CL_{2,2.differ}}{CL_{2.sum}} & \frac{CL_{2,3.differ}}{CL_{2.sum}} & \cdots & \frac{CL_{2,n-1.differ}}{CL_{2.sum}} & \frac{CL_{2,n.differ}}{CL_{2.sum}} \\ 0 & 0 & \frac{CL_{3,4.differ}}{CL_{3.sum}} & \cdots & \frac{CL_{3,n-1.differ}}{CL_{3.sum}} & \frac{CL_{3,n.differ}}{CL_{3.sum}} \\ \vdots & \vdots & \vdots & \ddots & \vdots & \vdots \\ 0 & 0 & 0 & \cdots & \frac{CL_{n-1,n-1.differ}}{CL_{n-1.sum}} & \frac{CL_{n-1,n.differ}}{CL_{n-1.sum}} \\ 0 & 0 & 0 & \cdots & 0 & \frac{CL_{n,n.differ}}{CL_{n.sum}} \end{bmatrix} \cdot \begin{bmatrix} \alpha(r_1) \\ \alpha(r_2) \\ \alpha(r_3) \\ \vdots \\ \alpha(r_{n-1}) \\ \alpha(r_n) \end{bmatrix} = \begin{bmatrix} \bar{\alpha}_1 \\ \bar{\alpha}_2 \\ \bar{\alpha}_3 \\ \vdots \\ \bar{\alpha}_{n-1} \\ \bar{\alpha}_n \end{bmatrix} \quad (3.22)$$

Rewrite the Eq.(3.22) into a reduced form:

$$\left[\frac{CL_{i,j.differ}}{CL_{i.sum}} \right] \cdot \left[\alpha(r_j) \right] = \left[\bar{\alpha}_i \right] \quad (3.23)$$

Here, $\left[\bar{\alpha}_i \right]$ is the measured pixel data, $\alpha(r_j)$ which is the unknown radial void fraction.

The reconstructed radial void fraction profile from the fan-beam projection can be solved as following back substitution or using Gaussian elimination:

$$\left[\alpha(r_j) \right] = \left[\frac{CL_{i,j.differ}}{CL_{i.\mathrm{sum}}} \right]^{-1} \cdot \left[\bar{\alpha}_i \right] \quad (3.24)$$

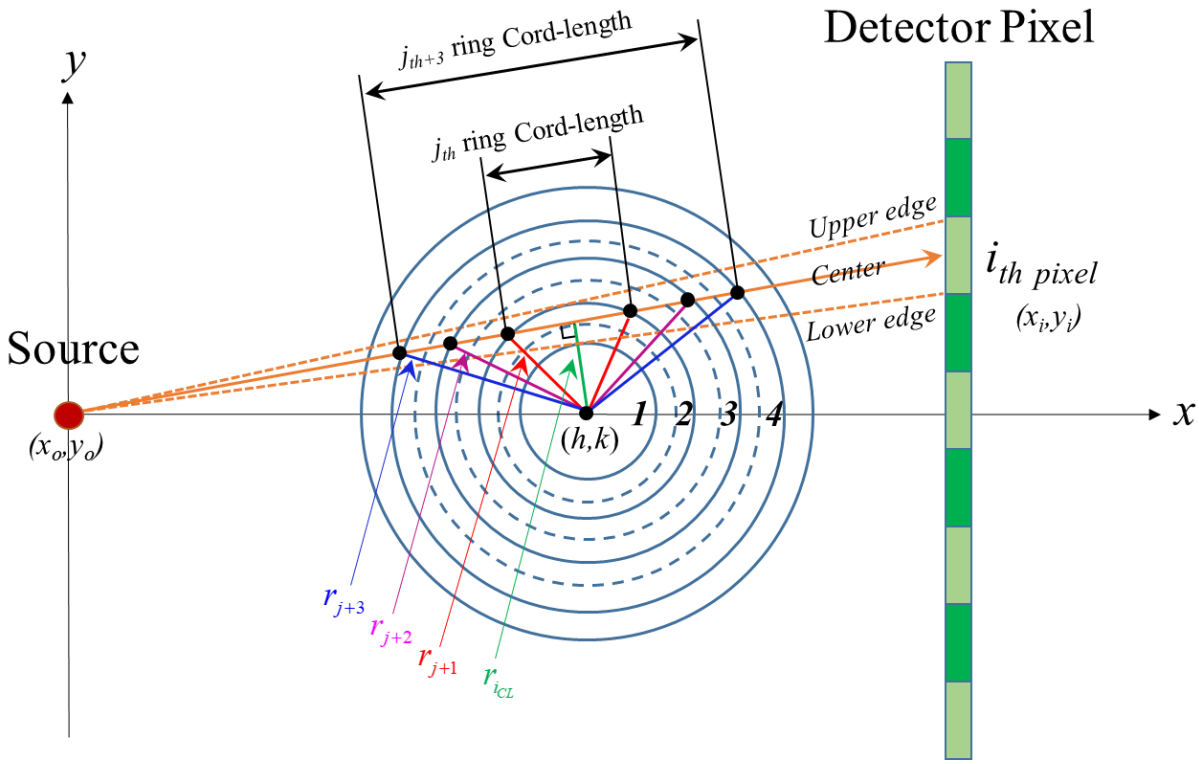

Fig. 3-8: Definition of the modified fan-beam onion-peeling (FBOP) method.

In the following section, a synthetic bubble sensitivity study is presented; the ABOP method is performed under various measurement uncertainty factors. The principal objective of this sensitivity study is to analyze how different factors of an independent variable affect the radial reconstruction quality under a given set of assumptions. The feasibility and advantages of the ABOP method are discussed over the existing method.

3.4 Algorithm Benchmark with Synthetic Bubble Sensitivity Study

In order to determine the uncertainty of the proposed method, various void fraction functions are generated within the inner test section boundary condition, which is the identical dimension used in the experimental setup for benchmarking purposes. Line-averaged void fraction information is determined based on the detector pixel response resulted from the fan-beam projection geometry. In this sensitivity study, several uncertainty factors are used to account for

the detector pixel response, these factors are, (1) pixel resolution, (2) mesh-size effect, (3) added background noise effect, (4) off-center shift effect, and (4) different void profile.

3.4.1: Pixel resolution

The pixel resolution can directly influence the data spacing. If the distance between each adjacent data point is increased or decreased, and the relative difference between them becomes relatively small or large. However, in the case of a low-resolution detector, the measured value between the two adjacent pixels can be significant. One such scenario is near the gas-film interface in the slug or annular flow. In this sensitivity study, a clean function without any added background noise is used. A total of three different resolution modes are selected, i.e., 0.1, 0.4, and 1.6 mm, which generate 428, 108, and 28 projections, respectively. Fig. *3-9* shows reconstructed radial void fraction profile using the ABOP, FBOP, and existing Abel methods. As seen in the figure, ABOP demonstrates the best fit and is able to reconstruct the sharp transition near the bubble edge (transition from gas to liquid phase). The ability to capture the sharp edge has resulted from the direct matrix inversion operation. In the Abel method, the void profile shows good agreement with the synthetic bubble profile; however, there is a significant fluctuation near the bubble edge for all three resolution modes. As expected, as resolution decreases Abel method shows less accurate radial conversion. Again, this is due to the significant difference between the two adjacent pixel values. In the case of a low-resolution detector, it is essential to consider the proper interpolation for more data points to eliminate the significant uncertainty.

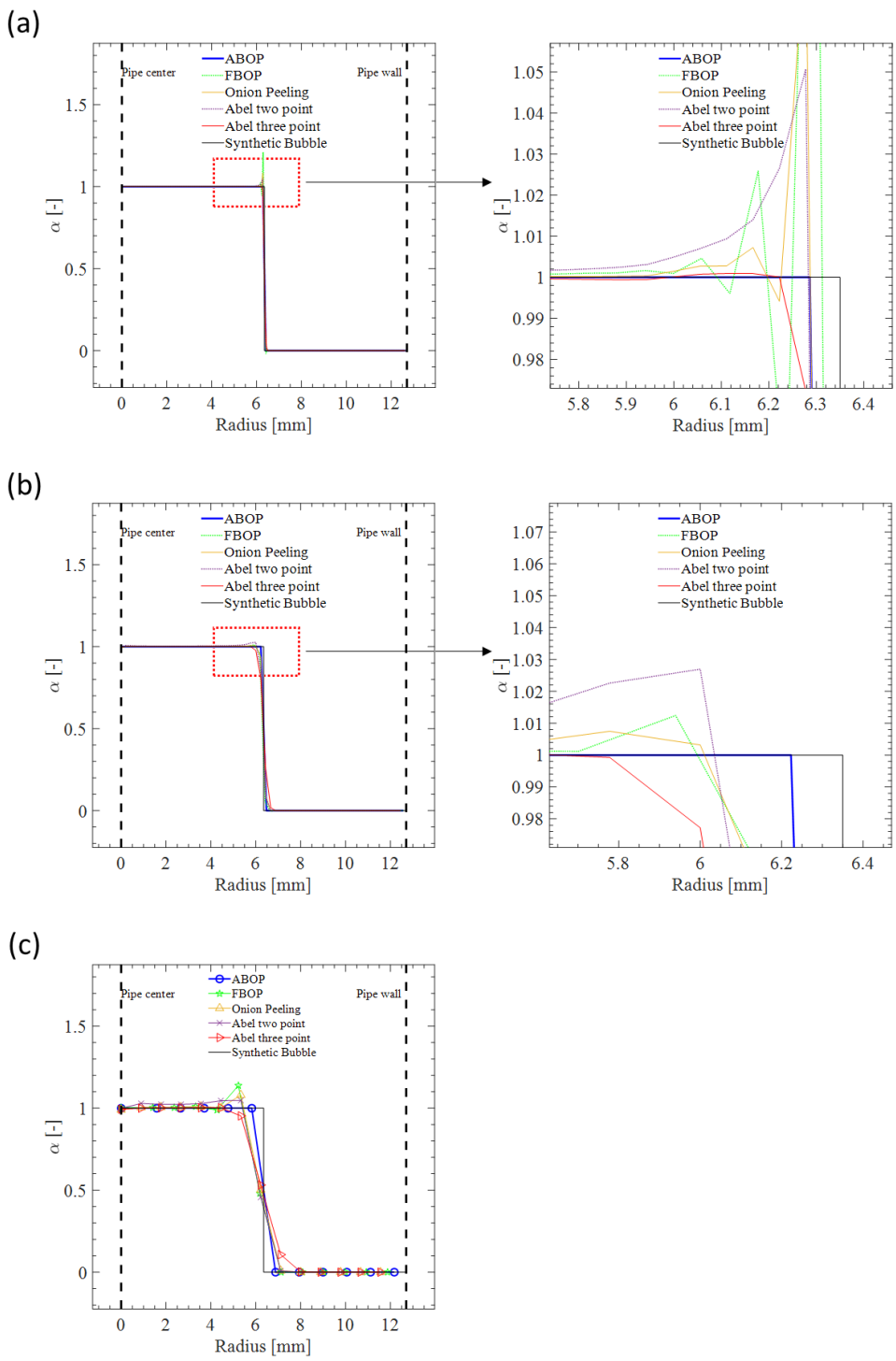

Fig. 3-9: Reconstructed radial void fraction profile for (a) 0.1mm mode; (b) 0.4mm mode; (c) 1.6 mm mode.

3.4.2 Mesh size effect

The ABOP method allows for the control of the desired number of partitioned rings of the flow field to be measured. This feature can be used to reduce the noise contribution in the measured data in case of projection data are oversampled. The distance between each mesh rings are equally spaced, and the number of mesh size can vary up to the total number of projection data points. In this sensitivity study, a clean function without any background noise is used, and a total of three different resolution modes are selected to generate detector responses. The pixel size of 0.1, 0.4, and 1.6 mm are considered with a total of 428, 108, and 28 projections are generated, respectively. Fig. *3-10* shows reconstructed radial distribution with the different mesh sizes. Since the data point does not contain any background noise, the reconstruction is an exact fit that demonstrates the inverse matrix operation. The mesh-size effect will be extended to study the added background noise effect in a later section. In conclusion, the ABOP demonstrates the exact fit and able to reconstruct the sharp transition near the bubble edge without any filter-function.

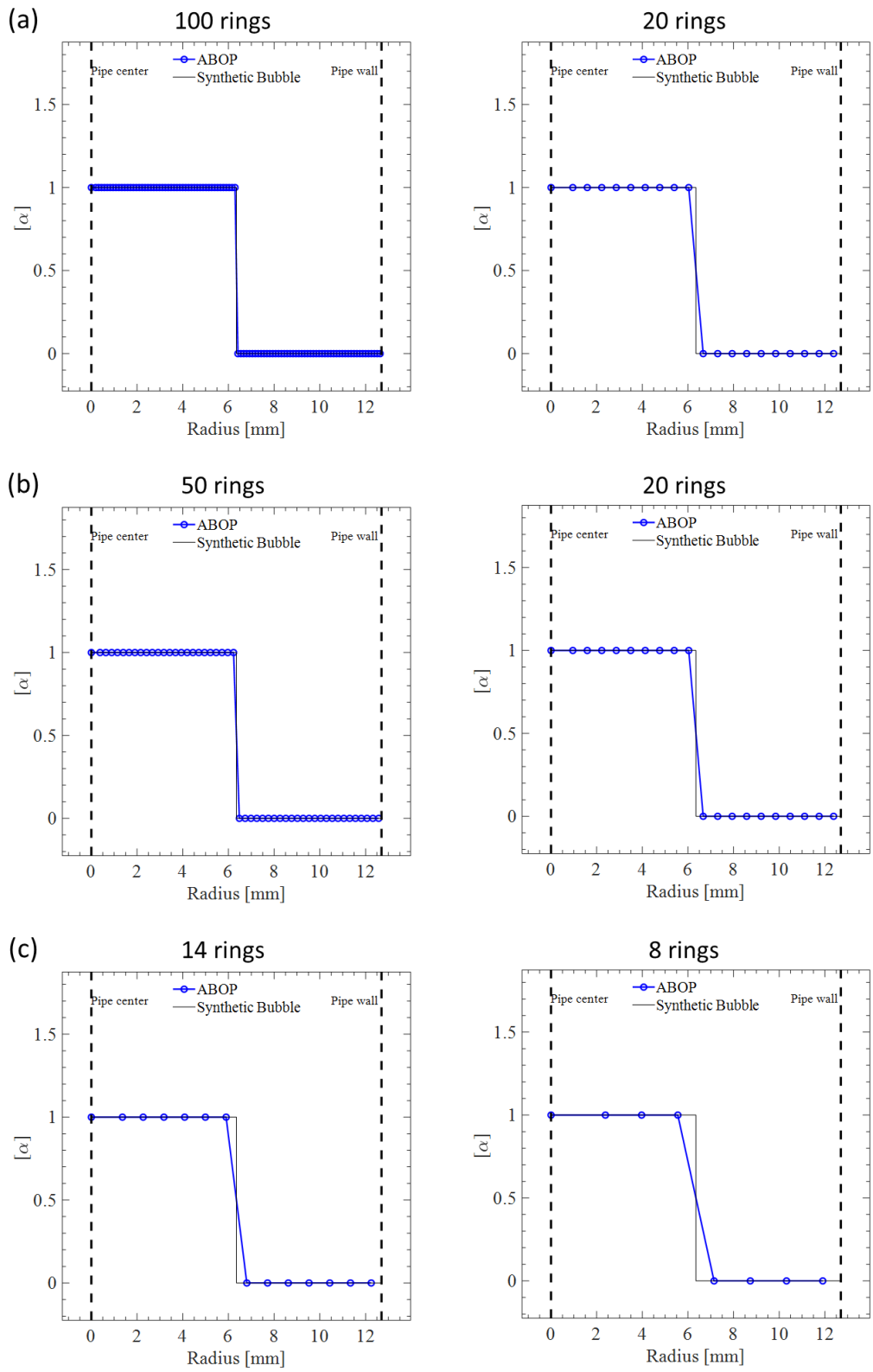

Fig. 3-10: Reconstructed radial profile from the different mesh-size interval (a) 0.1mm mode; (b) 0.4 mm mode; (c) 1.6mm mode

3.4.3 Added background noise effect

In this sensitivity study, radial reconstruction is implemented with two independent variables: the mesh size and ±1% added-background noise in the projection data set. In each resolution mode, a total of 428, 108, and 28 projections are considered for the 0.1mm, 0.4mm, and 1.6mm pixel resolution modes, respectively.

While considering the pixel size and mesh size only, the ABOP appears to perform outstandingly in apprehending the behavior of the inverse matrix operation. This result is similar to the analytic functions and the three-point Abel operation performed by the Bracewell [74] and Dasch [54]. However, when considering the maximum mesh size during the conversion, the ABOP method becomes highly unstable, which impacted by the added background noise. This behavior is similar to Abel's deconvolution method when data points are oversampled in case of noisy data. When mesh-size is overdetermined, the distance between each partitioned area is close to each other, and the difference between the weighted projection value between the adjacent area may become significant depending on the amount of the background noise impacts the magnitude of projection data. The reconstructed sample profile with the maximum allowable partitioned size is shown in Fig. *3-11*(left column). If the background noise causes instability, it is recommended to smooth the projection data before the inversion or apply the filter-function to enhance the reconstruction quality before the use of the Abel methods [54,59,64].

Instead of noise filtering or smooth the projection data, with the ABOP method, one can control the desired number of the partitioned ring in order to prevent the oversampling effect. In this sensitivity study, approximately half of the maximum allowable mesh size is chosen for the reconstruction and compared to the maximum mesh setting. Fig. *3-11* (right column) shows improved radial reconstruction quality by reducing the partition rings. As seen in the figure, the ABOP method is capable of reconstructing a smoother void profile by lowering the mesh number only, without any noise filtering.

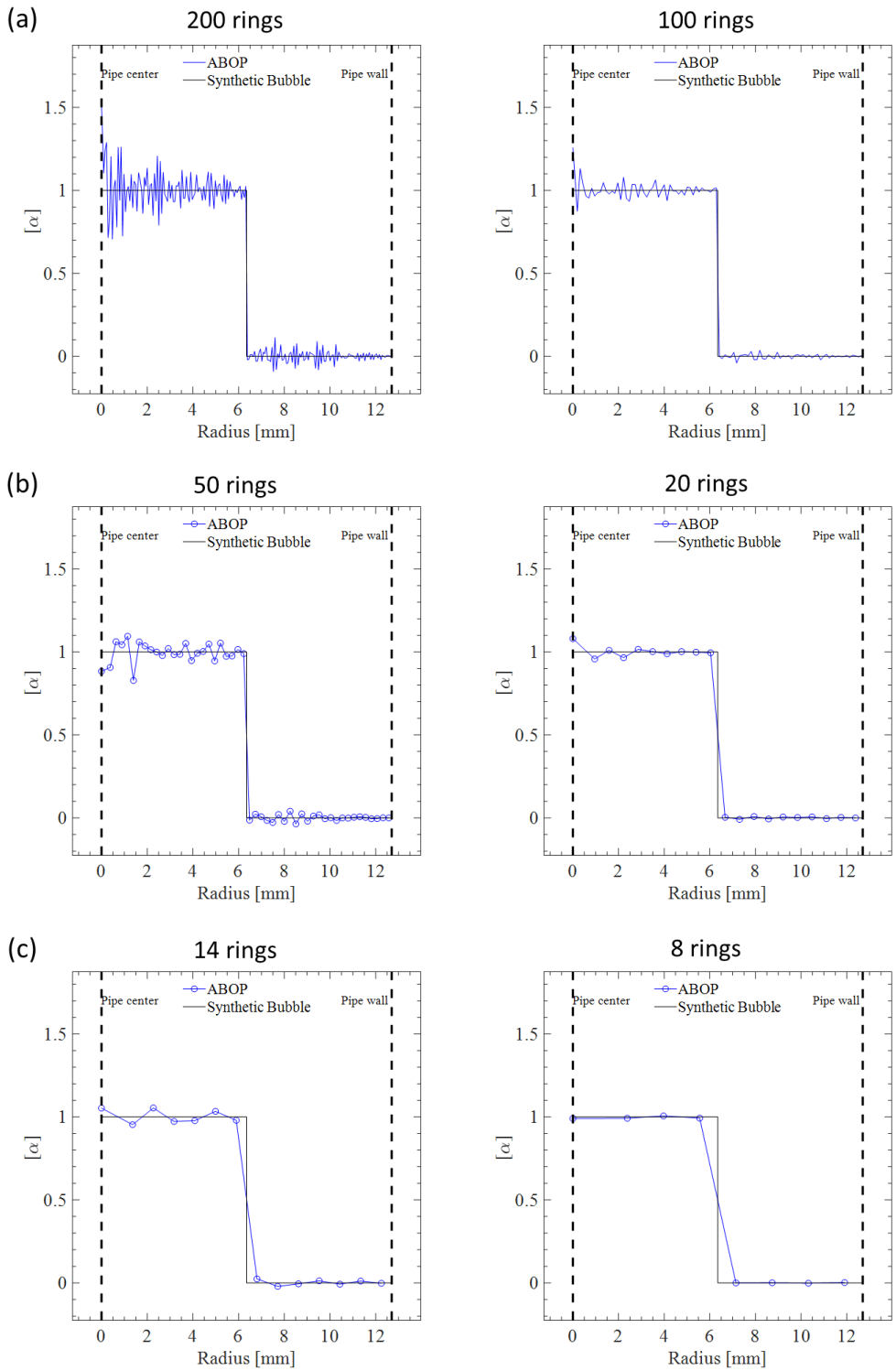

Fig. 3-11: Impact from the added background noise effect (left column) vs. improved reconstruction (right column) (a) 0.1mm mode; (b) 0.4 mm mode; (c) 1.6mm mode.

3.4.4 Off-center shift effect

In practical measurement, it is difficult to place the test section in the exact center of the x-ray measurement domain; it is crucial to investigate the reconstruction quality influenced by the off-center shift effect. The fan-beam projections are not symmetrically distributed when considering the Off-center orientation in the measurement domain. Fig. *3-12*(a) illustrates the shifted location of the test section in the global coordinate system. The detector response from the off-center shift geometry is shown in Fig. *3-12*(b). As seen in the figure, one can observe nearly 20 projections are shifted (in the 0.1mm pixel width size) to the right side of the detector pixels, even with a small shift of 0.5mm. If the exact location is not implemented in the algorithm, the difference in the partitioned area (*PA*) calculation can be significant.

In this sensitivity study, the radial conversion has been carried out using different input data as follows:

1. Input the right half of the detector response,
2. Input the left half of the detector response,
3. Input the averaged response between the left and right detectors,
4. Input the full spectrum response without center location correction,
5. Input the full spectrum response and account for the center location correction in the algorithm.

With the above conditions, the radial distribution is computed using the ABOP method, and results are shown in Fig. *3-13*. If one only uses the right half of the detector response, the void profile indicated an underestimation. On the other hand, the left half of the detector response causes an overestimation. Averaged detector response shows significant uncertainty between the transition region near the bubble edge boundary; the reconstruction fails to reconstruct the sharp transit. Therefore, averaging both sides of distribution is not a practical solution. Using the full-spectrum without the center-location correction shows a fairly reasonable radial profile. However, reconstruction still lacks accuracy and shows significant instability near the transition region. Input the full detector response with center-location correction shows exact void profile fit when the location-correction is implemented in the algorithm. Here, one can conclude that the off-center shift, even as small as 0.5 mm, plays a significant role in the measurement result. This sensitivity study shows, the pipe center-location must be identified and account for in the algorithm; otherwise, the radial conversion may cause significant uncertainty.

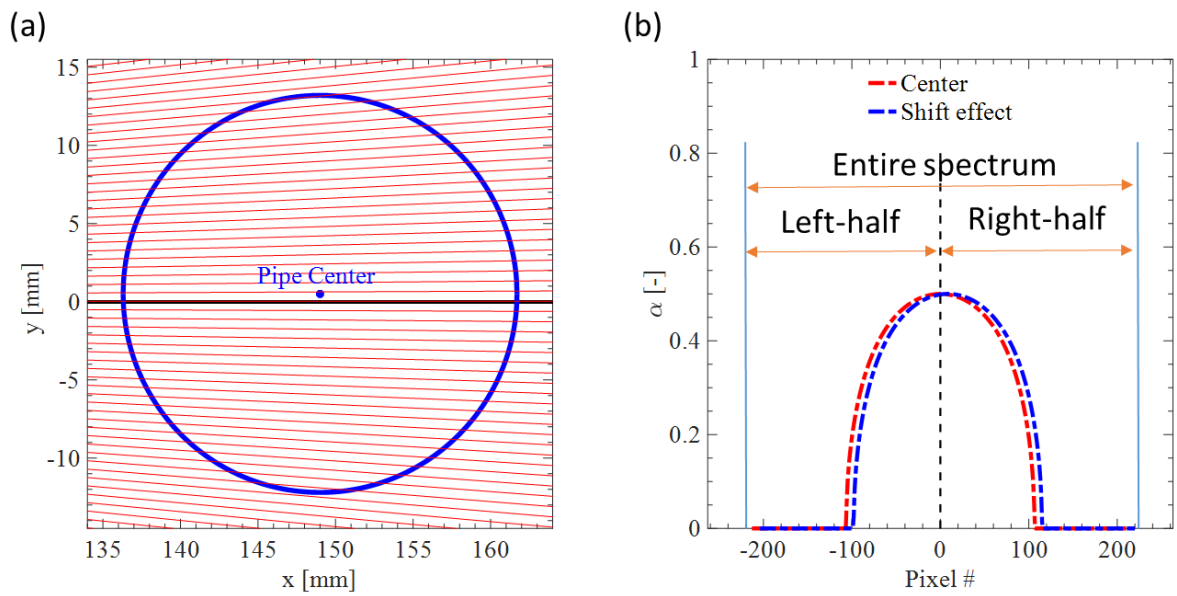

Fig. 3-12: Sample case of off-centered pipe location. (a) The test section is located 0.5 mm Off-center in the positive y-direction in the measurement domain; (b) Difference between the spectrum distribution in the detector response: centered vs. shifted geometry.

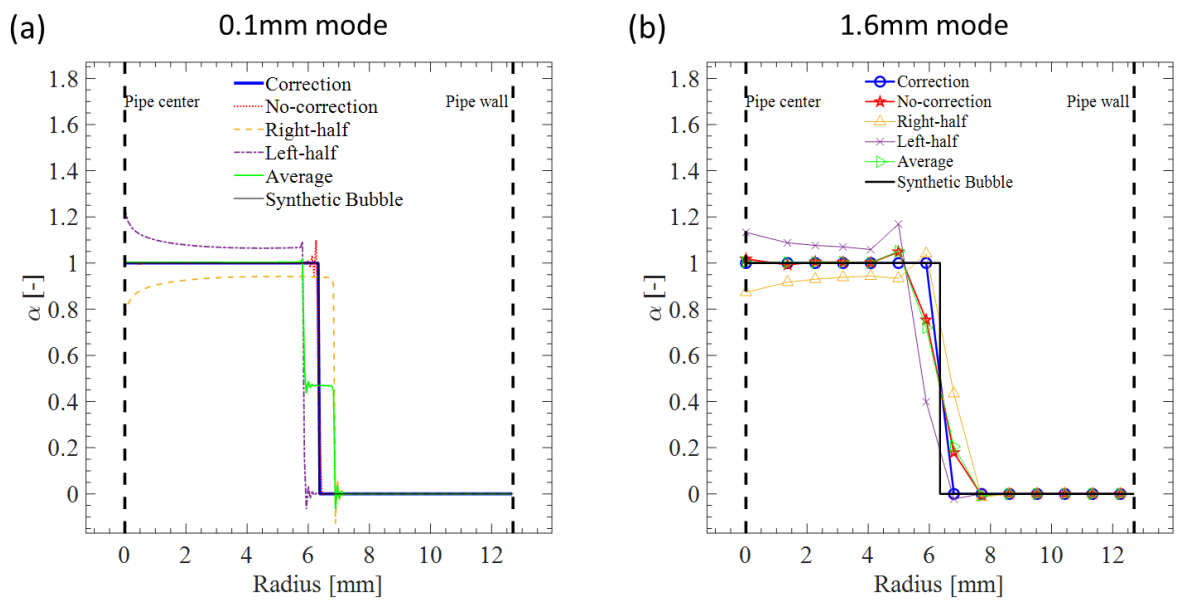

Fig. 3-13: Reconstructed radial profile influenced by the off-center shift effect, (a) 0.1mm mode; (b) 1.6 mm mode.

3.4.5 Investigate radial conversion with different void profile

In this section, five different void profiles are evaluated with ABOP, FBOP, Abel deconvolution methods including:

1. Single-step change,
2. Gaussian profile,
3. Linear decreasing profile,
4. Uniform profile, and
5. Wall peaking profile.

These profiles are computed directly from fan-beam projection data to ABOP and FBOP inversion operation. For the Able deconvolution method, fan-beam projections are converted to parallel-beam then radial profiles are reconstructed.

Fig. *3-14* shows radial reconstruction from the clean function. Both ABOP and Abel deconvolution techniques appear to accomplish in apprehending the behavior of the inverse matrix operation. Table *4* listed the mean absolute percentage error in each case of the five void profiles. In all five void profiles, ABOP and Abel three-point method performs the best. In the figure, one

can observe the deviations in the void profile transition near the bubble edge for all Abel deconvolution methods. The performance of the ABOP for is very similar to Dasch's operator function, but ABOP has advantages over the gradient capturing and smooth transition over the steep void change. The mean absolute percent errors are listed in Table *4* for all cases.

With the added random noise effect, the five void profiles are created with a ±3% random noise. A ±3% noise is the highest noise level from the experimental data. With the added random noise effect, ABOP shows the best performance among different methods. Table *4* shows the mean absolute percentage error for all three-pixel resolution modes. The least performing method is the Abel two-point and onion-peeling method.

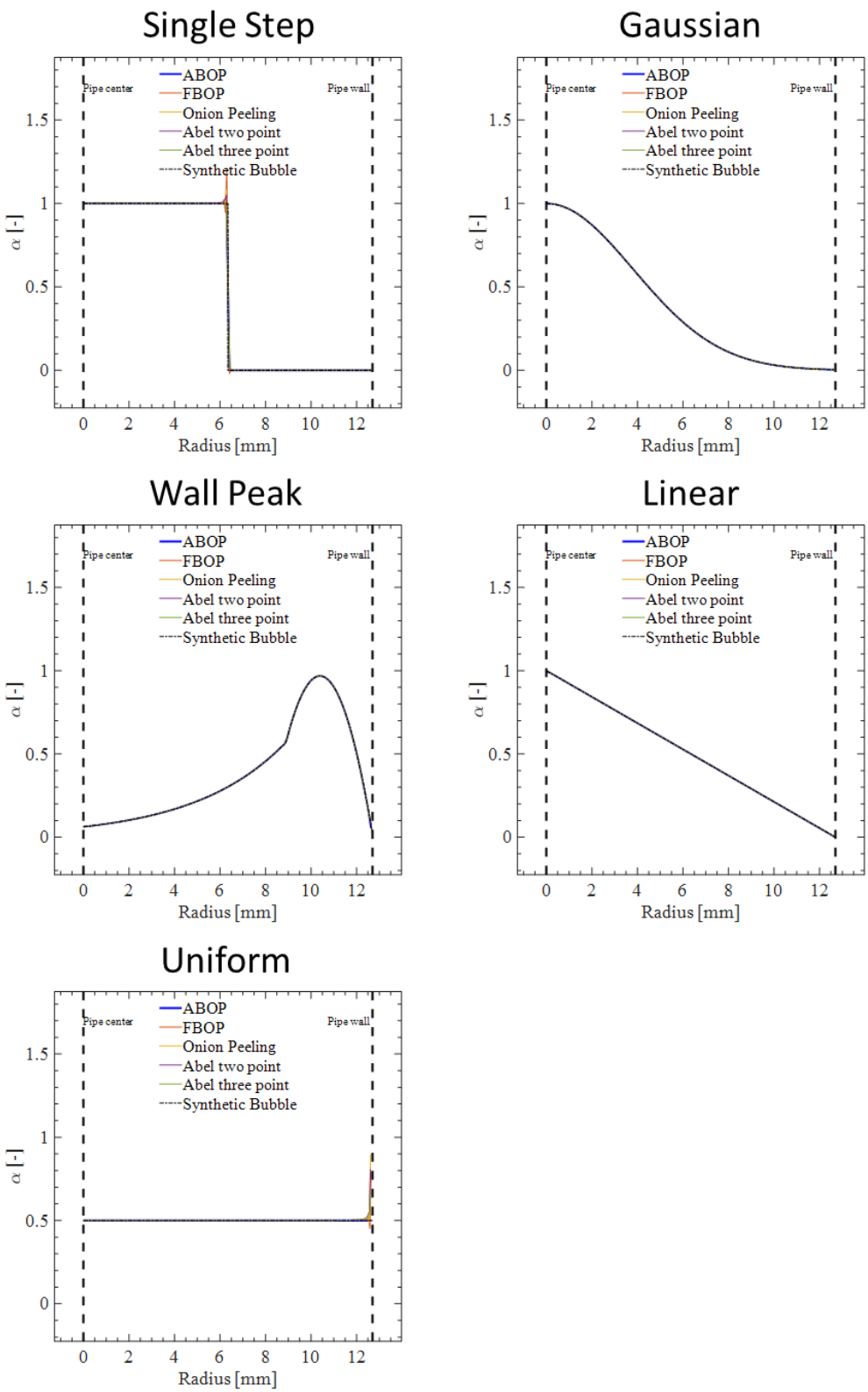

Fig. 3-14: Reconstructed radial distribution for the various void profile with clean function.

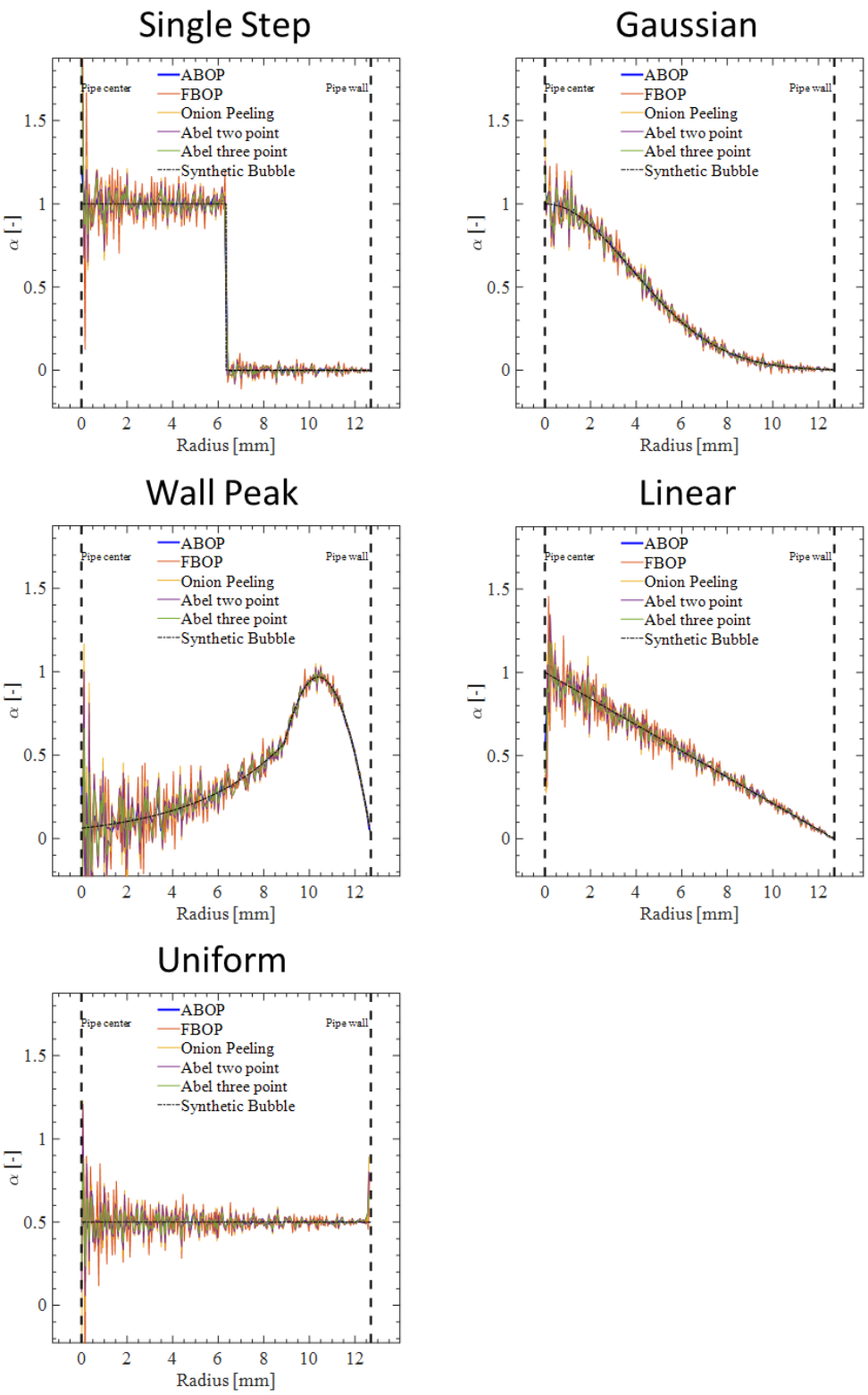

Fig. 3-15: Reconstructed radial distribution for the various void profile with added random noise effect.

Table 4: Mean absolute percent error

Mean absolute percent error			
Single Step			
	0.1mm Mode [%]	0.4mm Mode [%]	1.6mm mode [%]
ABOP	0.00	0.00	0.00
FBOP	0.67	0.63	5.05
Abel Three Point	0.20	0.50	4.10
Abel Two Point	0.25	0.77	5.10
Onion Peeling	0.19	0.49	4.06
Gaussian function			
	0.1mm Mode [%]	0.4mm Mode [%]	1.6mm mode [%]
ABOP	0.16	0.70	2.92
FBOP	0.94	1.80	1.52
Abel Three Point	0.37	0.37	3.95
Abel Two Point	0.57	1.12	3.37
Onion Peeling	0.58	1.09	3.14
Linear function			
	0.1mm Mode [%]	0.4mm Mode [%]	1.6mm mode [%]
ABOP	0.43	1.69	2.99
FBOP	0.80	0.44	1.12
Abel Three Point	0.29	0.22	1.30
Abel Two Point	0.39	0.69	1.44
Onion Peeling	0.30	0.30	1.14
Uniform Distribution			
	0.1mm Mode [%]	0.4mm Mode [%]	1.6mm mode [%]
ABOP	0.00	0.00	0.00
FBOP	0.00	0.00	0.00
Abel Three Point	0.32	0.57	2.70
Abel Two Point	0.49	1.19	5.39
Onion Peeling	0.51	1.27	5.58
Wall Peak			
	0.1mm Mode [%]	0.4mm Mode [%]	1.6mm mode [%]
ABOP	0.36	2.18	5.43
FBOP	1.00	2.78	7.09
Abel Three Point	0.28	0.62	6.84
Abel Two Point	0.39	1.00	4.69
Onion Peeling	0.38	0.58	4.35

Mean absolute percent error - Added noise effect			
Single Step			
	0.1mm Mode [%]	0.4mm Mode [%]	1.6mm mode [%]
ABOP	1.36	0.48	0.83
FBOP	5.79	2.46	5.88
Abel Three Point	2.99	1.01	4.45
Abel Two Point	4.46	1.46	5.67
Onion Peeling	5.36	1.51	4.71
Gaussian function			
	0.1mm Mode [%]	0.4mm Mode [%]	1.6mm mode [%]
ABOP	12.1	4.46	9.57
FBOP	21.94	12.98	6.01
Abel Three Point	16.52	9	4.2
Abel Two Point	24.33	14.22	4.59
Onion Peeling	26.98	15.71	5.37
Linear function			
	0.1mm Mode [%]	0.4mm Mode [%]	1.6mm mode [%]
ABOP	4.76	2.82	3.72
FBOP	10.36	5.94	2.97
Abel Three Point	6.46	2.84	2.45
Abel Two Point	10.29	4.22	3.02
Onion Peeling	11.82	5.06	3.04
Uniform Distribution			
	0.1mm Mode [%]	0.4mm Mode [%]	1.6mm mode [%]
ABOP	4.87	1.62	1.44
FBOP	11.4	6.73	1.47
Abel Three Point	6.67	3.2	3.3
Abel Two Point	10.2	5.41	5.93
Onion Peeling	11.61	6.54	6.71
Wall Peak			
	0.1mm Mode [%]	0.4mm Mode [%]	1.6mm mode [%]
ABOP	36.39	7.87	9.23
FBOP	80.81	22.69	16.45
Abel Three Point	44.95	12.02	10.93
Abel Two Point	67.68	17.02	102.91
Onion Peeling	84.17	19.16	11.48

3.5 Sample Two-phase Flow Radial Conversion result and Probe Benchmark

3.5.1 Flow measurement using the x-ray densitometer system

Two-phase flow measurement is performed with the x-ray system and the facility described in the experimental setup. A total of six flow conditions are measured, and the flow rate for each

condition is listed in Table *5*. The inlet gas flow rate is regulated by the flow meter, and the local pressure measurement is accomplished by the DP transducer, which determines the superficial gas velocity and liquid velocity at the x-ray system location. For each two-phase flow condition, a total of 180 seconds at 1000 fps are sampled, which resulted in 180,000 voltage samples for every detector pixels used in the measurement.

Fig. *3-16* shows the time- and line-averaged void fraction distribution along the pixels used for two-phase flow measurement. Equation (2-15) determines the time-averaged void fraction $\bar{\alpha}_i$ for the i_{th} pixel. Conventional void fraction calculation and spectral model are provided, which converts the measured detector signal *V(t)* to a line-averaged void fraction at a given pixel. The void fraction formulation by log model computed by the proportional energy ratio and spectral model is computed by Eq. (2-9). Void fraction near the pipe wall is assumed to be zero. This assumption is stated mainly due to the significant voltage difference from liquid to gas phase change; thus, the uncertainty of the measured voltage signal can be significant near the wall boundary. In the round pipe, zero void fraction behavior near the wall boundary can be visualized by another measuring method, such as high-speed imaging technique [17]. For the void fraction profile near the wall boundary, a total of three pixels in each end is replaced by the linear fitting where the void fraction is linearly interpolated from the pipe wall to the three pixels away from the pipe wall. In the illustration, the log model indicates an underestimation of the void distribution in the central region where the void fraction is more significant than zero value. This work is shown in the Song and Liu's calibration method [28], all six flow conditions indicate the underestimation when using the log model and demonstrate the importance of energy spectrum analysis in order to improve the measurement accuracy for the measurement system combined with polychromatic x-ray source [28].

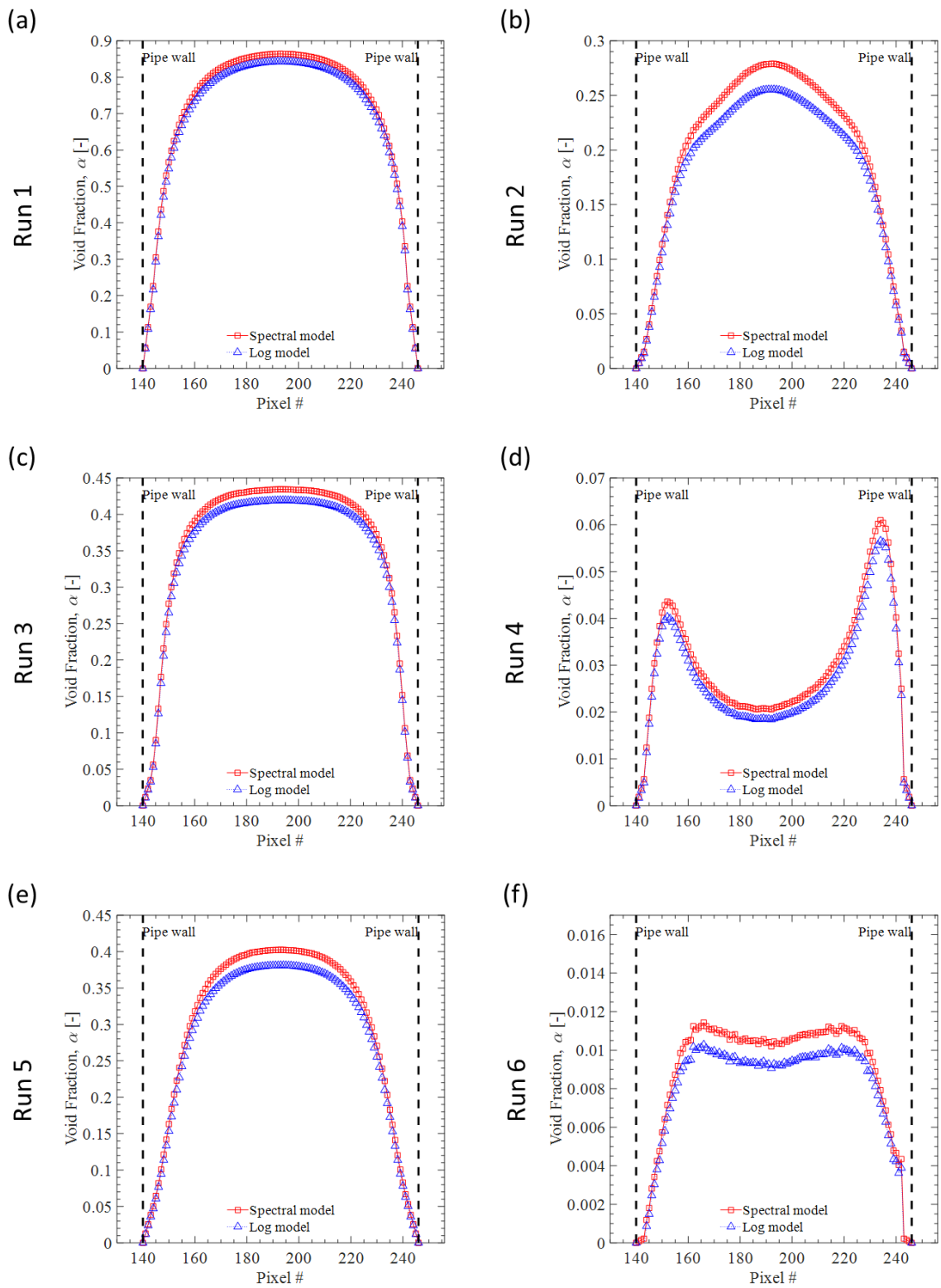

Fig. 3-16: Void fraction distribution along the pixel location (a) Run 1; (b) Run 2; (c) Run 3; (d) Run 4; (e) Run 5; (f) Run 6.

Table 5: Flow Condition

	j_f [m/s]	j_g [m/s]	Flow type
Run1	0.10	5.00	Churn-Annular
Run2	0.51	0.20	Bubbly
Run3	0.51	0.50	Slug
Run4	1.52	0.05	Bubbly
Run5	1.52	1.20	Slug
Run6	3.88	0.05	Bubbly

3.5.2 Double-sensor Conductivity Probe benchmarking

The multi-sensor conductivity probe technique has been widely used to obtain local time-averaged two-phase flow parameters in the past. The working principles are shown in Fig. *3-17*. As a bubble passing by a sensor tip, it would be registered as a voltage change, ideally a square wave. As shown in the plot, the bubble passes by the leading sensor from $t_{o,f}$ to $t_{o,r}$, and it passes by the trailing sensor from $t_{1,f}$ to $t_{1,r}$. The bubble residence time can be calculated from $t_{o,f}$ to $t_{o,r}$, or $t_{1,f}$ to $t_{1,r}$. The bubble velocity can be computed based on the time lag between $t_{o,f}$ to $t_{1,f}$ and the distance between two sensors.

The ideal probe signal should have a significant voltage difference between the gas and liquid phase, and an instantaneous transition from one phase to the other. However, actual signals are different from the ideal ones due to issues like white noise, electromagnetic interference, cross-talk (or ghosting), and finite response time of the electronics, etc. Sample probe signals obtained from the actual experiment are shown in Fig. *3-17*. As can be seen, the signal transition from one phase to the other is not instantaneous, and the exact time when the interface is at the sensor tip should be determined from these signals. Generally, a signal processing program is used to process the raw voltage signals to extract the time information needed to calculate time-averaged two-phase flow parameters such as void fraction, velocity, superficial gas velocity, etc. In the signal processing program, raw voltage signals are converted to binary signals first, then the binary signals of all sensors are input to a bubble pairing step. In this process, multiple processing

parameters such as voltage threshold values can be adjusted to yield the best processing results (Kim et al., 2000 [3], Liu et al., 2017 [4]).

In actual two-phase flow measurement, a double-sensor probe is placed on a linear stage, which could be traversed along the radius of the circular test pipe. With axisymmetric gas and liquid injections, it can be expected that the profiles of two-phase flow parameters are also axisymmetric at the measuring plane. Therefore, a conductivity probe is capable of obtaining the distribution of time-averaged parameters over the entire measuring plane.

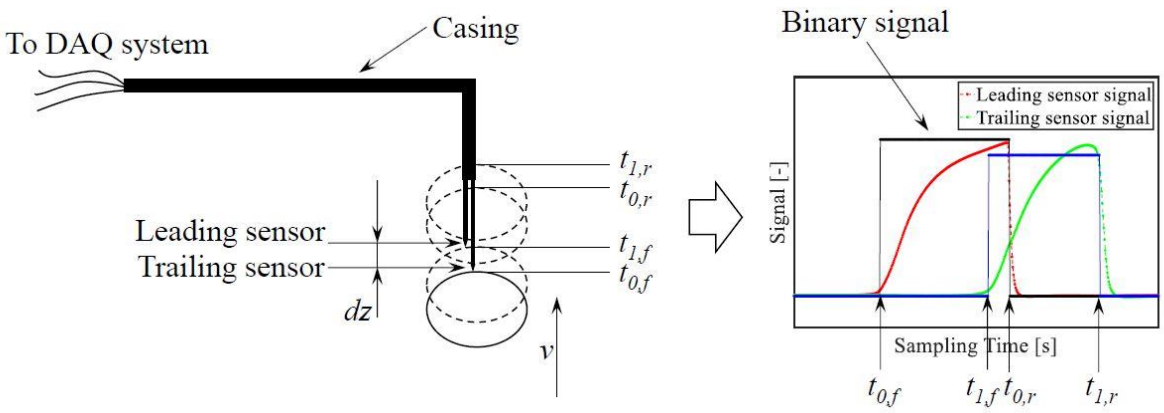

Fig. 3-17: Working principles of a double-sensor conductivity probe.

3.5.3 Pixel to Radial conversion Result

Fig. *3-18* shows the pixel to radial void fraction conversion for all six flow conditions, which initially measured by detector pixel shown in Fig. *3-16*. The radial void fraction distribution is computed by the ABOP, FBOP, and existing Abel deconvolution method. Double-sensor conductivity probe data is provided in the figure for the void profile comparison.

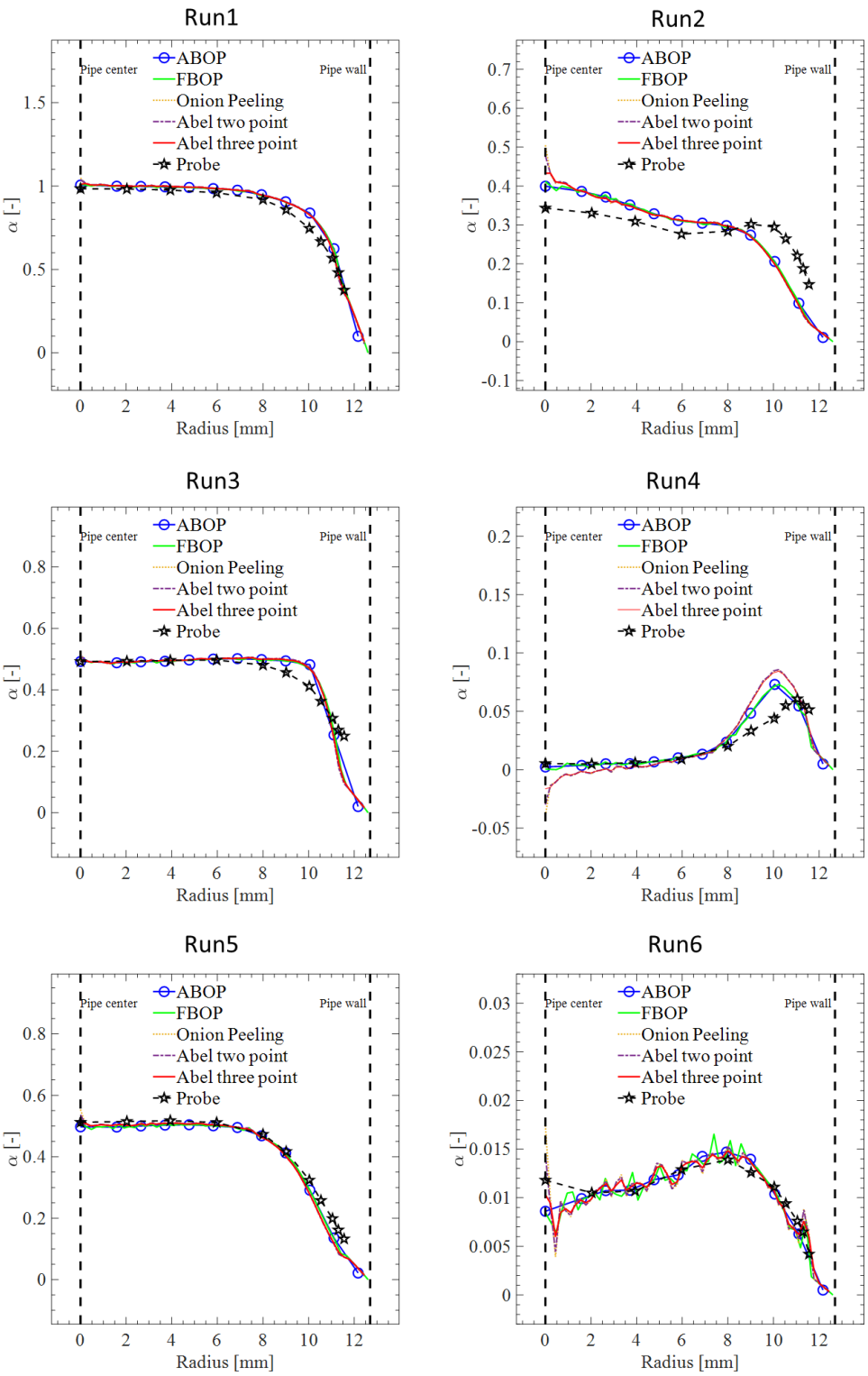

Fig. 3-18: Reconstructed radial profile from the pixel measurement using ABOP, FBOP, existing Abel deconvolution method, and probe benchmarking data.

3.5.4 Gas velocity measurement

The x-ray detector arrangement features two horizontal parallel-linear arrays along the flow direction. Each detector array records the characteristic signals when the bubble passes by the detector. When characteristic signals are recorded, there is a time delay occurred in each characteristic signal due to the distance between the two parallel array (upstream and downstream). Sample characteristic signals of the typical bubbly and slug flows are shown in Fig. *3-19*. Time delay of the two-phase flow signals is noticeable between the upstream and downstream detector array. The time delay of registered signals is evident in the slug flow signals shown in Fig. *3-19*b. For the gas velocity measurement, the cross-correlation from the upstream and downstream signals is used to calculate the average time it takes for bubbles to passing by the upstream detector to the downstream detector array. With the averaged time delay information and distance between two-parallel array, one can calculate the line and time-averaged gas velocity at each pixel location.

The traveling time of the gas-phase between upstream and downstream detector pixels is indicated by detecting the time lag, τ_m, where the cross-correlation is maximum. Since the distance between the top and center detector pixel is known, the bubble velocity, v_{gas}, can be calculated by:

$$v_{gas} = \frac{z_{i_{top}} - z_{i_{center}}}{\tau_m} \tag{3.25}$$

The following equation can calculate time delay:

$$\tau_m = \frac{\tau_{sN}}{f} \tag{3.26}$$

Here, τ_{sN} is the number of data samples the downstream signal is delayed behind the upstream signal, f which is the sampling frequency. Substitute Eq.(3.26) into equation Eq.(3.25), gas velocity determined by the two parallel linear arrays along the flow direction is:

$$v_{gas} = \frac{(z_{i_{top}} - z_{i_{center}}) \cdot f}{\tau_{sN}} \tag{3.27}$$

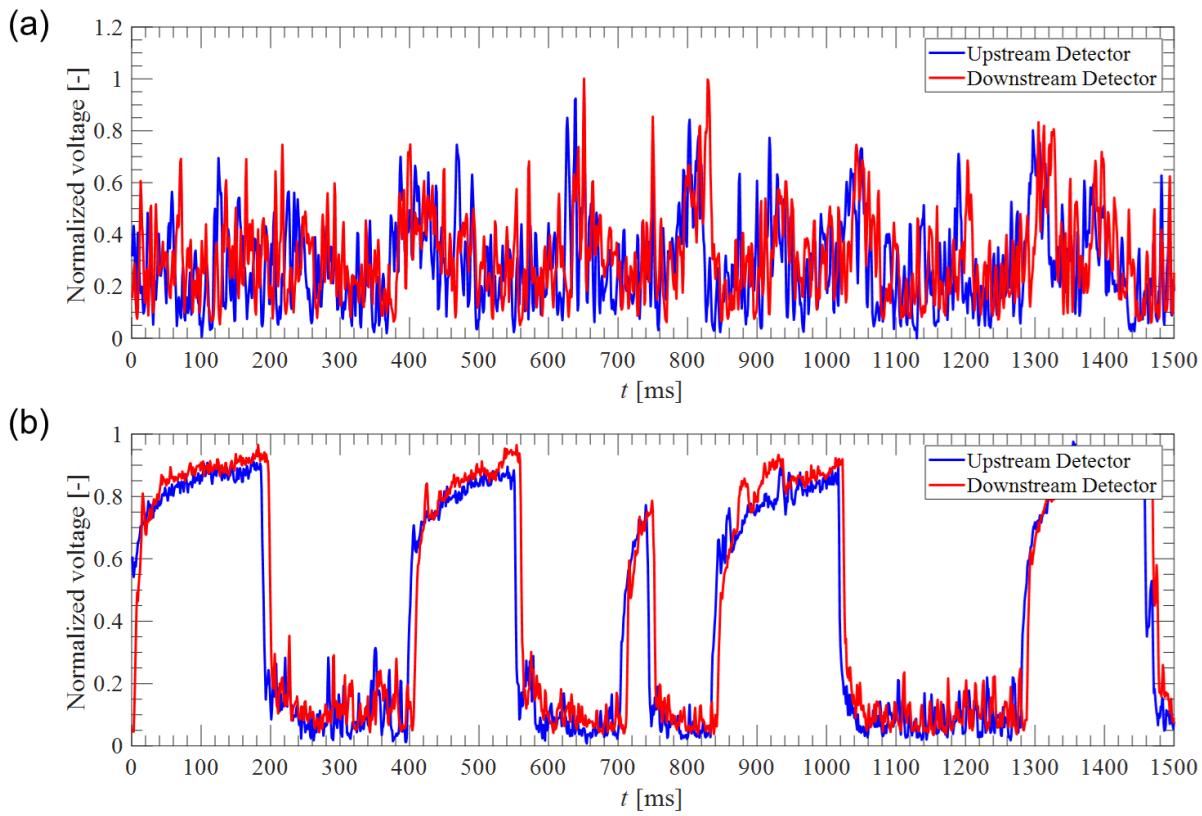

Fig. 3-19: X-ray signals obtained from the upstream and downstream detector arrays. Sample signals extracted from (a) Run2- bubbly flow; and (b) Run3-slug flow.

Fig. *3-20* illustrates the time and line-averaged gas velocity measured by each pixel of the flow condition listed in Table *5* (Run 2-6: bubbly and slug flows only). In the annular flow or churn-annular condition, the void is propagated in the test section; therefore, delay signals (characteristic signal) from the upstream to downstream detector signals are challenging to differentiate, this results in considerable uncertainty in velocity measurement in the annular flow or similar flow condition. For this reason, annular, or churn-annular flow is not suitable for the velocity measurement by the current x-ray system. Radial gas velocity distribution is converted by ABOP and Abel deconvolution method shown in Fig. *3-21*. The probe measurements are provided along the radial direction.

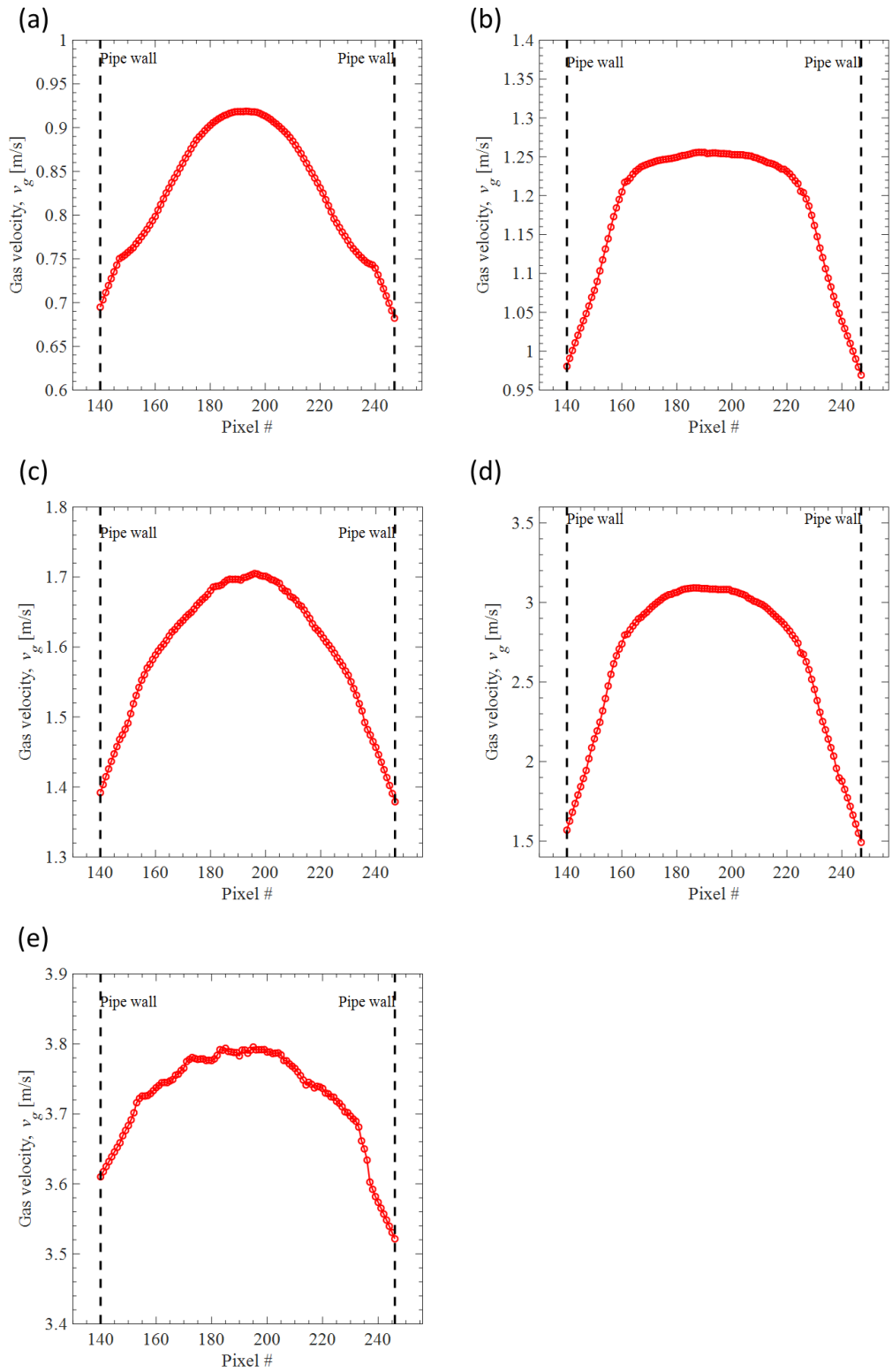

Fig. 3-20: Gas velocity distribution along the pixel, (a) Run2; (b) Run3; (c) Run4;. (d) Run5; and (e) Run6.

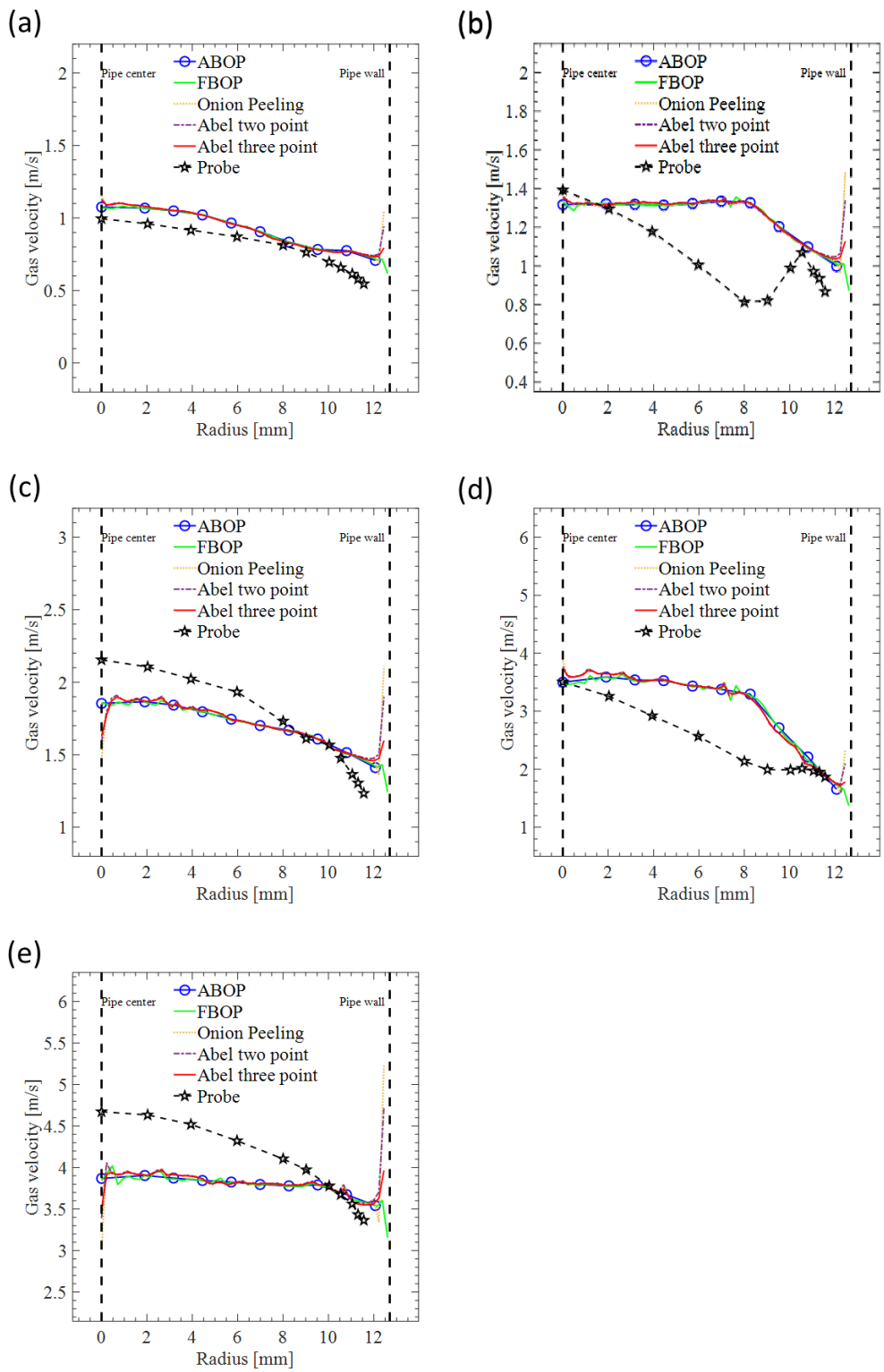

Fig. 3-21: Reconstructed radial gas velocity, (a) Run2; (b) Run3; (c) Run4;. (d) Run5; and (e) Run6.

3.5.5 Area averaged quantities: superficial gas velocity

The voltage signal recorded by a specific detector pixel mirrors the measured void fraction of the *SPA* (pixel coverage area). The time and line-averaged gas-velocity of each pixel should be considered as a void-weighted gas velocity of the *SPA*. From the definition, the cross-sectional area-averaged superficial gas velocity resulted from the time, and line-averaged information can be given as:

$$\left\langle j_g \right\rangle = \frac{1}{\pi r^2} \sum \bar{\alpha}_i \bar{v}_i SPA_i \tag{3.28}$$

Here, v_i stands for the velocity for the i_{th} pixel, $\bar{\alpha}_i$ is measured time-averaged void fraction, and SPA_i is the scanned pixel area for the i_{th} pixel, respectively.

Similar, cross-sectional area-averaged superficial gas velocity from the radial distribution can be given as:

$$\left\langle j_g \right\rangle = \frac{1}{\pi r^2} \sum \alpha_{r_j} v_{r_j} A_{ring_j} \tag{3.29}$$

Here, v_{r_j} stands for the reconstructed radial gas velocity, α_{r_j} reconstructed radial void fraction, and A_{ring_j} is the area of the circular ring for the j_{th} ring, respectively.

The area-averaged values from x-ray measurement and radial conversions are listed in Table *6* for the flow condition listed in Table *5*. Gas flow meter reading has an accuracy of ±1.0% of the actual reading, which indicates that flowmeter reading is highly accurate. For the measurement reference, the flow meter reading is used to evaluate the measurement uncertainty. Table *6* shows the relative error of the area-averaged quantities from the x-ray measurement and radial conversion.

Table 6: Area-averaged quantity and the relative error of the x-ray measurement, radial conversion

	$<j_g>$ by x-ray [m/s]	$<j_g>$ by radial conversion [m/s]	$<j_g>$ by flowmeter [m/s]	x-ray $<j_g>$ error [%]	Radial conversion $<j_g>$ error [%]

Run2	0.189	0.197	0.179	5.52	9.9
Run3	0.468	0.483	0.463	1.07	4.25
Run4	0.047	0.046	0.046	2.38	0.89
Run5	0.954	1.042	0.923	3.36	12.9
Run6	0.036	0.036	0.03	22.16	22.1

3.6 Summary

In this chapter, the newly developed ABOP method is introduced for the conversion of the pixel to radial distribution. First, pixel measurement showed good symmetry about the x-axis; thus, the axisymmetric flow assumption is reasonable. The converted radial void fraction data showed a reasonable agreement when compared with probe measurement. The synthetic bubble sensitivity study is performed to understand the impact of various uncertainty factors. The added noise effect and off-center shift effect showed a significant uncertainty in the radial reconstruction result. In order to deliver an accurate reconstruction, optimal mesh size and actual pipe center location must be accounted for in the ABOP algorithm. The newly developed ABOP method had resulted in an improved reconstruction profile compared with the existing Abel deconvolution methods, which can be a useful tool for radial conversion, mainly when raw data contains high-level background noise. In conclusion, the ABOP method is recommended for its robustness and reconstruction quality.

4 Non-axisymmetric Geometry Reconstruction

4.1 Introduction

Classical computed tomography (CT) initially introduced in the biomedical industry has been presented to other engineering applications such as nuclear energy, chemical, ocean engineering, combustion system, and multiphase flow measurement [75–77]. The computerized axial tomography (CAT) is a combined measurement technique of absorption spectroscopy with classical CT. The CAT is used in many practical engineering applications, which is capable of reconstructing the local attenuation profile from the measured data set (forward projection data set), which is taken at multiple angular views. The CAT is initially applied to investigate the axisymmetric flow system [54,56,58,78–80] and later used in many complex flow systems to reconstruct the two- or three-dimensional distribution across a transverse-plane, i.e., gas fraction distribution, local flow velocity, or temperature profile, etc. [59,71,81]. The related two-phase flow researches are summarized and listed in *Table 7*. In the CT method, there are two major steps to reconstruct the two-phase flow images. The first step is obtaining a series of angular projection data at multiple angular directions; this step is referring to the Radon transform. The second step is to reconstruct the local voxel (or pixel) elements using an analytical or algebraic iterative method.

Table 7: Summary of two-dimensional tomographic reconstruction researches for two-phase flow measurement.

Reference	Test section	Source power	Detector	Flow condition	Void fraction	Reconstruction Method
Prasser *et al.*, 2003 [27]	Pump inducer	Cs-137, 662 keV	64-scintillaion arc detectors	1500 rpm	6%	Filtered back-projection (FBP)
Wu *et al.*, 2007 [69]	Round pipe- 90 mm inner diameter	18 x-ray sources	$CdWO_4$ 2-D plane detector	N/A	Bubble column reconstruction	FBP, Algebraic Reconstruction technique (ART)
Fischer *et al.*, 2009 [82]	Vertical pipe- 60mm inner diameter	150 keV, 65 mA electron beam current	circular CZT detector- 240 pixel (1.5x1.5mm)	N/A	N/A	FBP
Bieberle *et al.*, 2009 [83]	Vertical pipe- 38mm inner diameter	150 keV	256 CZT detector array	Liquid : 20 *l/min* Gas: 2 *l/min*	N/A	ART
Wang *et al.*, 2011 [84]	Horizontal pipe- 160 mm inner diameter	^{241}Am gamma-ray source	200x200 CdZnTe photon detector	Bubbly, slug, annular flow	60%	ART

Zboray *et al.*, 2013 [85]	BWR rod bundle	Spallation Neutron Source (SNS)	1024×1024 pixels	j_g=13.39-26.55m/s, j_f=0.13-0.64m/s	N/A	FBP, ART
Liu *et al.*, 2014 [86]	Horizontal pipe-500 mm inner diameter	3-kW laser beam	8-photodiode detector	Turbulent flow regime and vortex flow	N/A	FBP
Wu *et al.*, 2014 [87]	Horizontal & vertical pipe-25.4 mm inner diameter	5 kHz pulse laser beam	750x400 pixels (max resolution)	Total of 5 flow rate condition	N/A	ART
Banowski *et al.*, 2015 [88]	Vertical pipe-54.8 mm inner diameter	150keV (max power at 10kW)	1mm spatial resolution per pixel	j_g= 0.9 m/s, j_f= 1 m/s	2.28% 11.8% 29.0%	FBP
Schafer, *et al.*, 2016 [89]	Multiple square channel inside of round pipe	150keV (max power at 10kW)	1mm spatial resolution per pixel	j_g= 0.037-0.22m/s, j_f=0.018-0.07m/s	N/A	FBP
Viggiano *et al.*, 2017 [90]	Vertical pipe-100 mm inner diameter			j_g= 0.9 m/s, j_f=0.6 m/s	N/A	Back-projection, POD
Lau *et al.*, 2018 [25]	Vertical pipe-100 mm inner diameter	150 keV	Circular ring detector- 432 pixels	Bubbly flow	10%	FBP SART(Simultaneous ART)

In the study performed by Prasser *et al.* [27], the local void fraction distribution is reconstructed by filtered back-projection (FBP) with a modified Shepp-Logan filter function [22]. In this experiment, it took a total of 7 minutes to measure the single flow condition inside of the pump structure. The detector system in this study is capable of obtaining the cross-sectional measurement at a rate of 100 fps; thus, 7 min or longer sampling time is required for the sufficient flow information. Therefore, the system used in this research provides time resolving gamma-ray tomography and capable of visualizing the time-averaged void fraction distribution inside the pump inducer and impeller. In the study of Wu, et at. [87], a fast x-ray computed tomography system is used in the air-water flow measurement. In Wu's experiment, a limited angle measurement is considered where tomography setting measured at every 15-degree angle; thus, a total of 24 projections are measured. For the reconstruction algorithm, the genetic algorithm (GA) and conventional FBP technique are used, and reconstruction methods are inter-compared for saving the computational cost. Fischer and Hampel [83] used an ultrafast x-ray CT system for adiabatic gas-liquid flow measurement. In Fischer's research, the detector system is capable of measuring two-phase flow with a maximum data acquisition rate of 1 million fps. The system arrangement with a high sampling rate and high-resolution photon detector is proficient in delivering high spatial resolution information of the two-phase flow field. Lau [25], Wang [84], and Wu [87] used iteration method (simultaneous multiplicative ART and SART) for the void fraction reconstruction to identify the two-phase flow regime. The iteration method used in these

studies generates a much better result than a minimum cross-entropy algorithm. In the study of Viggiano *et al.* [91], the proper orthogonal decomposition (POD) method is used for investigating phase fraction characteristics for the dispersed and slug flow. The phase fraction values are reconstructed by back-projecting the temporal coefficients onto POD modes.

In CT reconstruction, there are two essential variables which are required for the approximating the flow field measurement. These variables are the projection angle and the projection function (detector function). In CT reconstruction, many viewing angles are preferred for reconstructing the local distribution along with multiple angular directions. In two-dimensional tomography, the reconstruction of the measurement field can be described by a function of two spatial variables. In general, 2-D inversions can be classified into two categories, either by an analytical or algebraic iterative method. Here, the analytical method is a transform-based inversion. The filtered back-projection (FBP) is an analytical method that is broadly used in the x-ray tomography application [92].

On the contrary, the algebraic-iterative methods discretely formulate the inversion problem and solve iteratively. One of the most widely used iterative methods is called the algebraic reconstruction technique (ART) [93]. Other known algebraic-iterative methods are the Landweber algorithm [94,95], and maximum likelihood expectation maximization (MLEM) algorithm.

There are other variations of algebraic reconstruction methods available such as a level set method [96], direct inversion method for frequency domain [97], adaptive finite domain direct inversion (FDDI) reconstruction method [98], but are less commonly used in image reconstruction application. In the following, the fundamental features of most popular known algorithms are introduced.

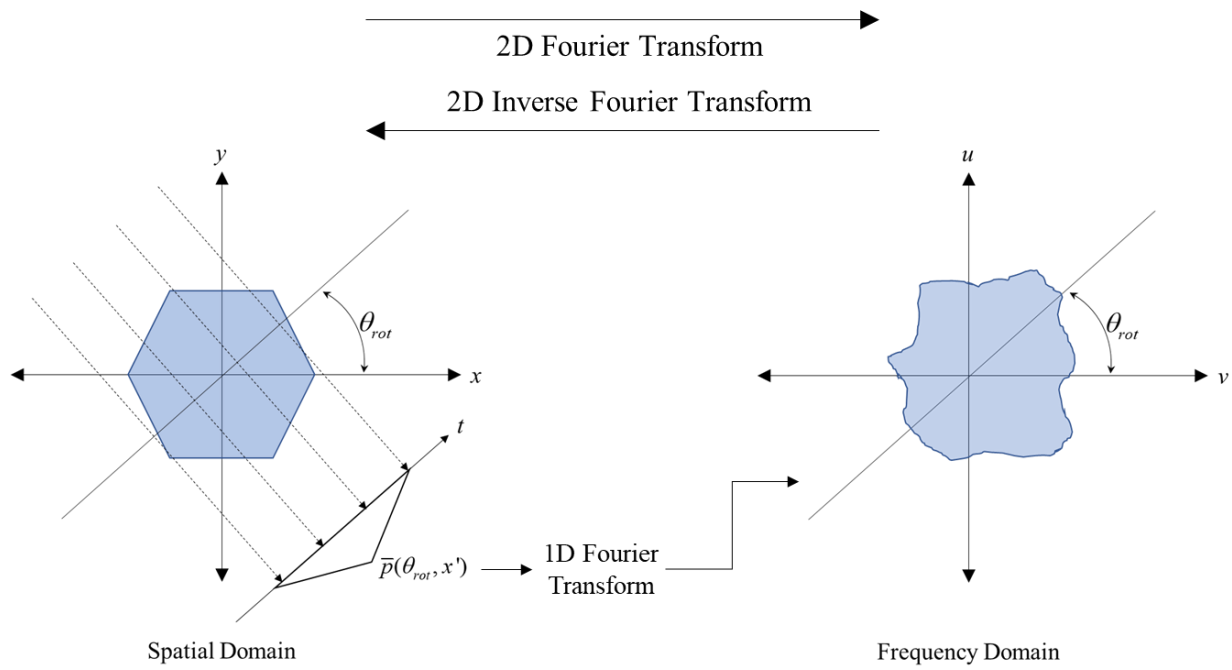

Fig. 4-1: Illustration of Radon transform (left figure) and the sinogram in the Fourier domain (right figure).

First, the FBP, which is constructed on the analytical approaching of the Radon transform [21,72,84,89], FBP is defined as:

$$\bar{p}(\theta_{rot}, x') = \int_l \mu(x, y) dl \tag{4.1}$$

Here, $\bar{p}(\theta_{rot}, x')$ is the projection function, which is assumed it is a line-averaged measurement at a rotational angle θ_{rot} concerning the rotational axis and located at a x' (detector location) from the center of rotation. This concept is illustrated in *Fig. 4-1*. Here, variable l is the overall attenuation length, and the variable $\bar{p}$ is a two-dimensional projection function. The analytical solution collects all projection data set into a two-dimensional format. This mapping procedure of local distribution function μ from the projection function $\bar{p}$ determines its classical linear tomography character. The basis of the FBP algorithm can be described by the central slice theorem.

The central slice theorem states, the Fourier transform of the specific projection data set that are projected at a specific projection viewpoint is equal to a single-shot of the two-dimensional

Fourier transform of the identical angle. Illustration of Radon transform and the sinogram in the Fourier domain is shown in *Fig. 4-1*. From the basis of the Fourier transform theorem, the FBP method can be employed into two stages:

1. First, one must yield the Fourier transform of each projection data set at a specific angle in ascending order and re-organize the projection results into a 2-D arrangement (i.e. 2-D matrix format). This rearranged data contains overall projection information (i.e. absorption length or attenuation coefficient) of the test object in the Fourier domain.
2. Second, one must take the inverse Fourier transform of the rearranged 2-D data in order to reconstruct the measured object.

However, there are a few restrictions linked with the analytical approach. Every detector pixel has a finite dimension; thus, the projection function in which line-averaged measurement has a finite sampling size. This finite sampling size ultimately causes a magnification of reconstructed voxel value associated with the low-frequency region in the Fourier domain. Implementing an inverse Fourier transform typically causes blurring even if the projection data set does not contain any background noise. In order to filtered-out resultant image blur in the reconstructed image, an additional step must be implemented. This added step is referring to the filter function (filtering of the original projection data). The following formulation denotes the entire FBP operation:

$$\mu(x,y)_{FBP} = \underbrace{\underbrace{\int_0^{\pi}\underbrace{\int_{-\infty}^{+\infty}\underbrace{\int_{-\infty}^{+\infty}\overline{p}(\theta_{rot},x')\cdot e^{-i2\pi wt}dt}_{\text{FT of a projection}}\ \left|w_{filter}\right|}_{\text{filtering function}}\ e^{i2\pi wt}dw}_{\text{inverse FT}}\,d\theta}_{\text{back-projection}} \tag{4.2}$$

Here, $\left|w_{filter}\right|$ is the high-pass filter function to suppressed the magnified low-frequency effect. The FBP method performs great if many angular projection data sets are available. One of the most significant drawbacks of the FBP is that the projections must be re-binned into a parallel-projection equivalent before performing the Fourier transformations [99]. Therefore, FBP is suggested for engineering applications in which the test object is relatively simple, and multiple projections should be obtainable along with any directions. Known sample applications are listed in the following where the FBP method is widely used and founded in many references literature [99–105]:

1. Water flux measurement in a scramjet combustor,
2. Liquid vapor distributions within the flat flame chamber,

3. Single and two-phase pipe flow,
4. Measurement of the exhaust flows from scramjet combustion-engine,
5. Reconstruction of a temperature distribution of the flame.

In the iteration based algebraic tomography, the solution is formulated in a discrete format. Illustration of discrete formulation for the CAT problem is shown in Fig. *4-2*. Due to discrete format, the measurement domain is discretized into a group of voxels which individual voxel element representing the local attenuation value. Numerous line projection beams examine these voxels. In the figure, a single line-beam is representing a specific projection index *i* is highlighted in blue, and the variable $\vec{p}_i$ is the measured projection. The attenuation coefficient of the j_{th} voxel in the measurement domain is denoted as $\vec{\mu}^v$ and which contributes the overall weighted attenuation length of the i_{th} projection ray weighted by the j_{th} voxel as W_{ij}. The total attenuation length of every projection ray contributed by every voxel is assembled into a form of $i \times j$ matrix. The following equation formulates this forward projection process:

$$\vec{p} = W_{ixj}\vec{\mu}^v \tag{4.3}$$

Here, the projection ray $\vec{p}$ is the sinogram value at a specific pixel location and the $\vec{\mu}^v$ representing the original coordinate of the attenuation coefficients, here, both of these matrix arrays are arranged in a vector format. In general, the algebraic reconstruction tomography is formed with the system of equations. For a CAT solution, the solution can be obtained by the inverse matrix operation of matrix array *W* or by the Gaussian elimination method. In the actual measurement condition, the number of available projection data set is always limited due to the limited number of detector pixels or due to the pixel resolution size. In such a case, the systems of the equation may lead to an undetermined. Also, background noise is an additional uncertainty factor during the measurement; thus, weighted matrix *W* is usually influenced by the measurement uncertainty factors.

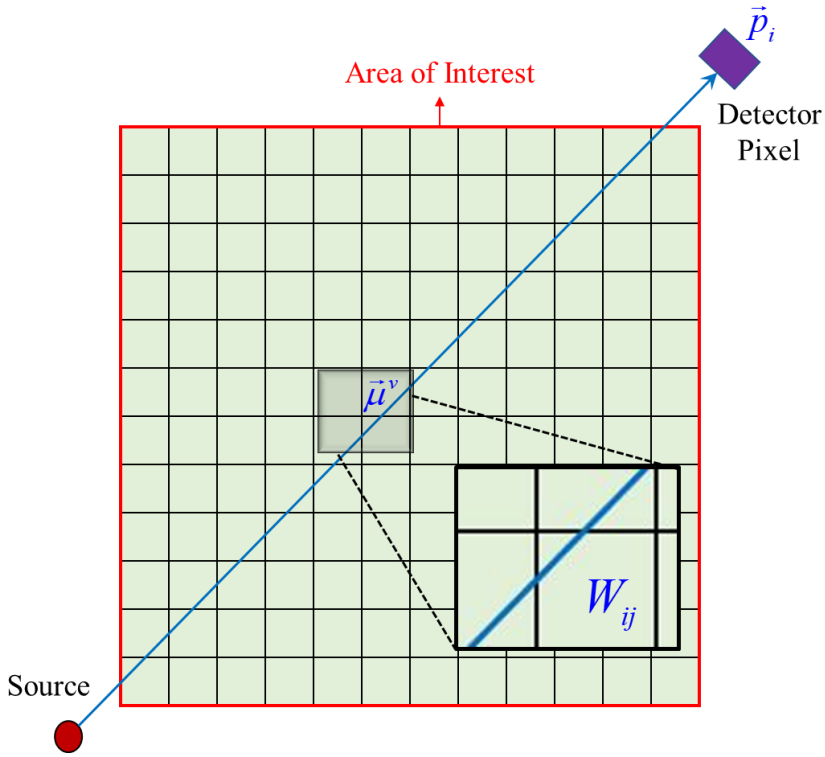

Fig. 4-2: Illustration of discrete formulation for the CAT problem. The red square represents an area of interest. The specific attenuation length of i_{th} projection-ray (blue ray) passing through specific j_{th} voxel denoted as $\vec{\mu}^v$.

Algebraic iterative based reconstruction algorithm can provide several advantages that may be suitable for harsh-conditioned of the tomographic problem, which can be encountered in the typical flow analysis or combustion application in the reference literature [106,107]. Several advantages of iteration based algorithms are:

1. Less sensitive to the presence of the background noise effect [108],
2. It is capable of reconstructing a measured object from the limited number of projections in the axisymmetric flow [109,110],
3. It is capable of integrating analytical information into the formulation to enhance reconstruction reliability [111,112],
4. The geometry of the projections does not require to be arranged in an equiangular format [52].

The ART method is considered the most suitable reconstruction method when the projection data set is ranged within 100-1000 projections. The ART algorithm is a discrete format in general [113], and there are many variations available. Known algorithms are including but not limited to simultaneous ART (SART) [114] and multiplicative ART (MART) [115], and the simultaneous iterative reconstruction technique (SIRT) [116]. These iteration-based methods have their advantages and limitations in specific research applications. Within many variations, the ART is the widely used technique.

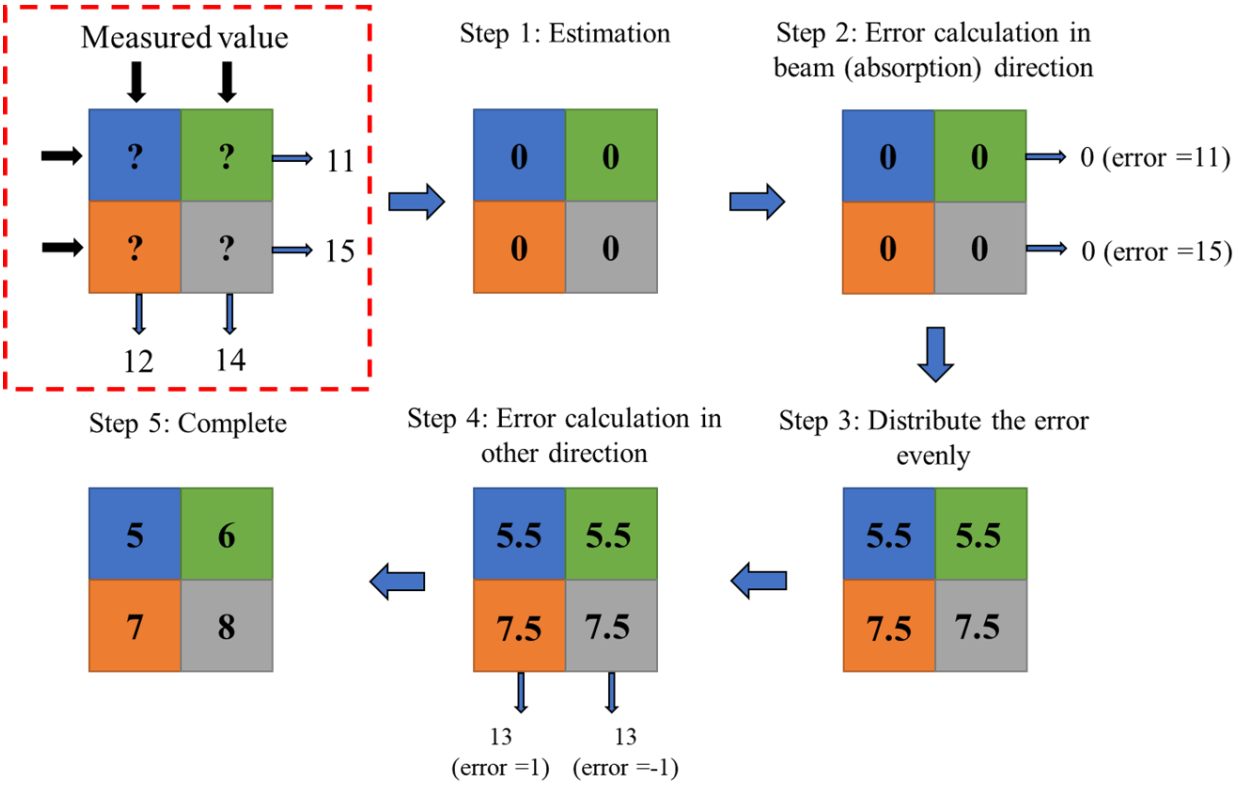

Fig. 4-3: Simple 2x2 tomography problem of the ART algorithm with one iteration.

In *Fig. 4-3*, a sample tomographic problem illustrates an operating principle of the ART algorithm with a simple two by two matrix problem, which is projected with two-line projections at two different angular view. In the upper left box (dotted red square), the sample matrix problem illustrates the tomographic problem. Here, the resultant values indicate the line-averaged value of

a specific projection. In this example, one has to determine the individual values of each voxel, which contributes to overall projection measurement. The overall steps are listed in the following order:

1. In the first step, the algorithm starts with the estimated value, here, assigning each voxel value with zero value,
2. In the second step, the algorithm subtracts the estimated value from the measured value, here, the algorithm calculates for an error value of the entire projection data set,
3. In the third step, this difference value is divided up and equally distributed to all voxels in the path of projection. This step is repeated for every LOS measurement in this direction and update the distribution value,
4. In Step 4 and 5, the same process is computed for the second projection-ray direction. This one cycle of the entire steps constitutes single-iteration in the algorithm. The iteration terminates when the iteration condition $\vec{p}_i$ is achieved. For instance, iteration can be set to terminate when the error is within the acceptable level.

Here, the solution for a simple tomographic problem is fully determined. However, in practice, the TAS measurement typically results in an underdetermined problem in some applications [108,110]. The mathematical formulation of the iteration-based algorithm is expressed in the following equation [106]:

$$\vec{\mu}_{k+1}^{v} = \vec{\mu}_{k}^{v} + \lambda \vec{a}_i \frac{\vec{p}_i - \left\langle \vec{a}_i, \vec{\mu}_k^{v} \right\rangle}{\left\langle \vec{a}_i, \vec{a}_i \right\rangle} \tag{4.4}$$

Here, the variable $\vec{\mu}_k^{v}$ is the approximated value at k_{th} current iteration step, and the variable λ is a relaxation factor which regulates the convergence rate; $\langle , \rangle$ is an inner product operation; $\vec{p}_i$ is the line-averaged attenuation of the i_{th} projection ray and $\vec{a}_i$ is the i_{th} row of the weighted matrix W_{IxJ}. The ART algorithm has been widely used for the system within 100-1000 projections are obtainable. A few example applications can be found in reference literature [92,104,117,118]. The major drawback of the ART algorithm is listed in the following:

1. The algorithm is only semi-convergent [119],
2. The computation cost in CT application is directly proportional to the available projection data set, and the total number of iterations constitute in the entire operation,

3. The ART has capable of access close to the true value in the beginning phase but diverges when iteration steps increase [120].

Alternatively, the Landweber algorithm is other variations of an iteration-based method commonly used in CAT problems [95,110,117,121–123]. The calculated values of $\vec{\mu}_k^v$ in Eq.(4.4) can be set to the initial value appropriate to the start of an operating using the equation $\vec{\mu}^v = W^T \vec{p}$, which mainly performs the linear back-projection procedure. The variable W^T is used for approximates the transpose of the W matrix array. The following equation provides the subsequent steps of the Landweber algorithm [53]:

$$\vec{\mu}_{k+1}^v = \wp\left[\vec{\mu}_k^v + \lambda W^T R(\vec{p} - W\vec{\mu}_k^v)\right] \tag{4.5}$$

Here, the subscript k refers to the current iteration step; the variable λ is a relaxation factor that regulates the convergence rate; the variable $\wp$ is a function that implements the physical constraints, such that project all negative values to zero in the voxel values. In the equation Eq.(4.5), the difference in the approximation $\vec{p} - W\vec{\mu}_k^v$ is the back-projected over matrix multiplications [53]. Advantages of the Landweber algorithm are listed in the following:

1. Useful in the application where only a limited number of projection-rays are obtainable; typically within 50-100 projections [53],
2. The algorithm is most suitable for an experiment performed in severe conditions, such as phase measurement in the pipe or measurement of the inner-chamber [121].

However, the Landweber algorithm too has its own drawbacks. The algorithm also disintegrated due to semi-convergence, in order to improve the reconstruction quality, one requires to implementing a practical termination standard [124].

Another known iterative algorithm is called the maximum likelihood expectation maximization (MLEM) method. The MLEM has been frequently used in the tomographic application for the PIV experiment [125,126]. This MLEM method is similar to the Landweber and ART method, where measured values are used for the correct initial estimated values of the voxels. In MLEM operation, the voxel information is updated one at a time throughout each iteration. Updating the corrected information for the j_{th} voxel during k_{th} iteration can be written in the following equation [127]:

$$\vec{\mu}_{k+1}^{v_j} = \vec{\mu}_k^{v_j} \sum_i \frac{\vec{p}_i}{\left\langle \vec{a}_i, \vec{\mu}_k^{v} \right\rangle} \frac{W_{ij}}{\sum_i W_{ij}} \tag{4.6}$$

Here, every projection-ray is implemented simultaneously in each iteration in order to update the correction associated with the overall attenuation length, which is an input quantity for the weighted factors. The significant advantages of the MLEM method are that MLEM is capable of determining the unequal spaced projection data points and produces significantly fewer artifacts [128]. However, a significant drawback with the MLEM method is its high computational cost, time, and prolonged convergence rate [126]. From the medical imaging application, the MLEM method demonstrated near equivalent reconstructed performance when compared with other iteration methods [127,129]. However, in terms of computational efficiency, the other available iteration methods or FBP method spends much less computational cost at a fractional cost. Therefore, the MLEM method seems suitable for the system with a large number of projections (higher than 1000 projections) where a computational cost is not limited. The example of MLEM applications is presented in the reference literature [125–127].

Lastly, the Karhun-Loeve basis (TRKB) algorithm is an alternative iteration-based technique used for the TAS application [130,131]. For the diagnostic applications with a small number of LOS measurements usually causes inversion problems to be underdetermined. In this kind of scenario, the reconstruction method using the TRKB algorithm becomes a useful tool when a limited number of projections do not contain enough spatial property of the measured domain [130,131]. In the TRKB algorithm, there is a set of information proceeds from the theoretical deduction method, which contains an extensive training set, for instance, the phase distributions in the flow field measured from the alternative experimental technique or recover from the CFD simulations [130,131]. TRKB only requires fewer projection data set for the reconstruction when compared with the other iteration-based method. This method takes advantage over where the angular measurement is limited, which makes the TRKB method is useful for when a limited number of projection data set are available. However, the TRKB method has significant drawbacks; these limitations are:

1. The TRKB method requires extensive prior information from alternative experimental methods or simulation benchmarking [72],
2. Information proceeds from the theoretical approach have limited usefulness due to the theoretical limits on the maximum acceptable compression [132].

To outline, the analytical and iteration-based algorithms are implemented methods for CAT and TSA to present date. While these techniques have applied in many engineering applications was selected instead of another. In Table *8*, algorithms that are implemented in the framework of TAS, indicate related literature, and a description of its advantages and limitations are listed.

Table 8: Summary of know algebraic iteration-based algorithms

	FBP	**ART**	**Landweber**	**MLEM**	**TRKB**
Advantages	Analytical approach Efficient, Fast	Most common iteration-based method	Improved over the ART method	Produces fewer artifacts than FBP	Requires a fewer measurement
Limits	Requires extensive angular projection sets	Fail to converge with noisy data	Requires longer computational time	Requires longer computational time	Requires extensive prior knowledge
Projection #	Below 1000	Within 100-1000	Within 30-100	Above 1000	10-30
References	[87,99–101,104,105,133]	[86,92,104,118]	[68,95,107,121–123]	[125–127]	[130,131]

In the following, the two-phase flow arrangement consisting of a tomography setting is described. Then the detail of the existing 2-D reconstruction algorithm will be presented for a two-phase flow application. The 2-D algorithm is then benchmarked by generating synthetic void profile under the various uncertainty factors implemented into the algorithm for a sensitivity study. The primary purpose of the sensitivity study is to investigate how each factor of an independent (or dependent) variable affects the 2-D reconstruction quality under a given set of assumptions. Feasibility, drawbacks, and advantages of each method are compared and discussed for its suitability in the two-phase flow application.

4.2 Experimental Setup

The schematic of the tomography setting in a two-phase flow facility is shown in Fig. *4-4*. Flow regimes in vertical, adiabatic two-phase flows spanning from bubbly to slug flow, can be generated in the test facility at room temperature and near atmospheric pressure. The 1.95 m tall

test section has a rectangular cross-section with an inner dimension of 10mm by 30mm. The hydraulic diameter of the rectangular test section is $D_h = 15\text{mm}$. The x-ray tomography measurement is performed at 0.73m above the two-phase injector, which corresponds to a dimensionless height of $z / D_h = 47.4$. A transfer pump (Hayward SP1780) is used to deliver water from a water storage tank to the test section through two major water inlets, and two water flow meters (Dwyer RMA-141 and RMA-144) are used to monitor the water flow rates for different ranges.

The airflow is supplied by the building compressed air line and regulated by a pressure regulator. Two rotameters (Dwyer VA10423 and VA10417) are used to control the airflow rates for different flow conditions. By controlling the air and water flow rates, various two-phase flows with different void fractions can be obtained in the test section. Air and water are mixed at a gas injector location, as shown in Fig. *4-4* (b), which consists of two gas opposite facing aluminum plates installed flush with the 30 mm wide walls. On each aluminum gas injector plate, there are five 200 μm holes from where the air is injected into the flow channel. This design can result in symmetric bubble distribution at the test section inlet. The gravity separates a two-phase mixture leaving the test section in the storage tank. The water and air circulate through the loop and vented to the water storage tank.

For the tomographic measurement setting, a high precision turntable (SilverThin Model: SK6-22PZ 083016) is mounted at 0.66m above the gas injector (air-inlet) location. An enlarged view of the measurement location is shown in Fig. *4-5*. The overall inner diameter of the turntable is 434±0.8mm, which is capable of rotate 360 degrees around the test section. Schematic of the tomographic setting is illustrated in Fig. *4-6*, the x-ray system is rotated around the test section and capture the time-averaged void fraction information at a given angle. The measured voltage signal has a spatial resolution of 0.4mm per pixel; the total number of detector pixels may vary depending on the angle and the distance between the source and the center of rotation. The data acquisition is rated at 1000 frames per second (fps), and the total sampling time is 60 seconds for all measured angle: a total of 37 angular directions are obtained with 5-degree increment.

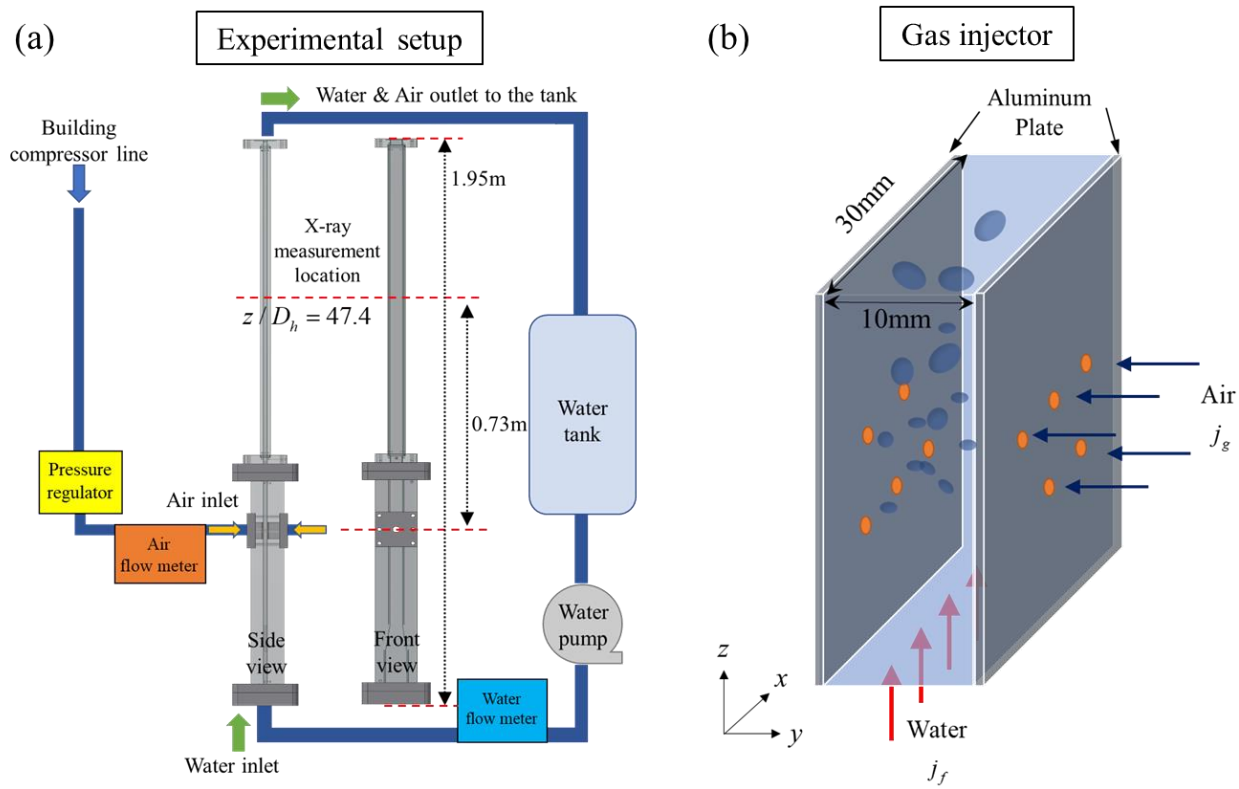

Fig. 4-4: (a) Experimental arrangement of the x-ray tomography setting, (b) Two-phase flow air injector design.

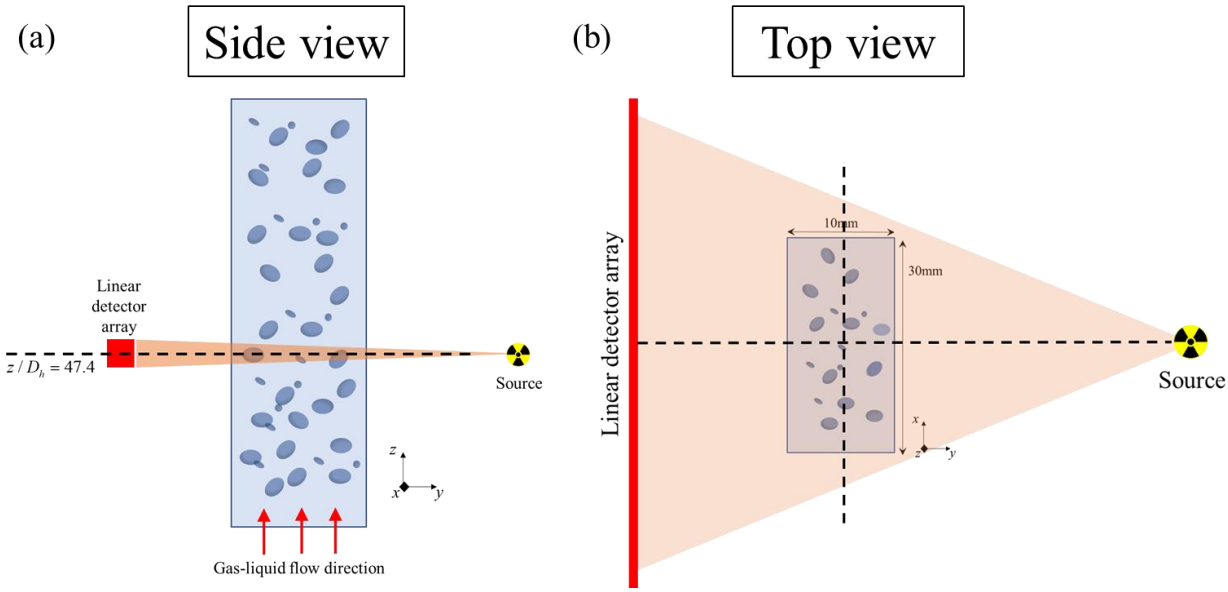

Fig. 4-5: Illustration of the x-ray fan projection and the measured location, $z / D_h = 47.4$.

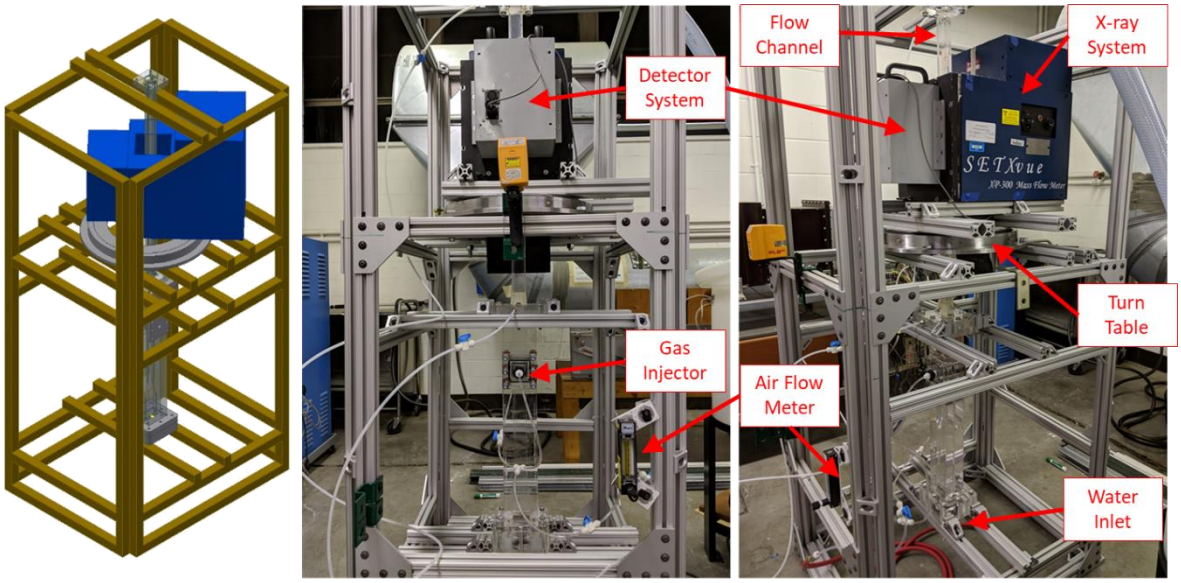

Fig. 4-6: Schematic of the x-ray system with high precision turntable tomography setting.

4.3 2-D Reconstruction Algorithm

The two-dimensional reconstruction process consists of 3 main parts, as shown in Fig. *4-7*. In Step1, the pre-processing step aims to obtain the line and time-averaged attenuation profile from the various viewing angle. Here, the integral transform, which is known as Radon transform takes a projection function on the measurement plane to the 2-D function, which defined on the 2-D space of lines in the plane. In the second step, the area-averaged void fraction is computed from the time, and line-averaged void fraction information using the Spectral Model [28] is provided for the reference data for the averaged quantity. In the third step, the algorithm divides into two groups for the 2-D reconstruction that utilizes the 2-D void fraction mapping from the reconstructed attenuation profile. The comprehensive procedures of the reconstruction process are described in the following sub-sections.

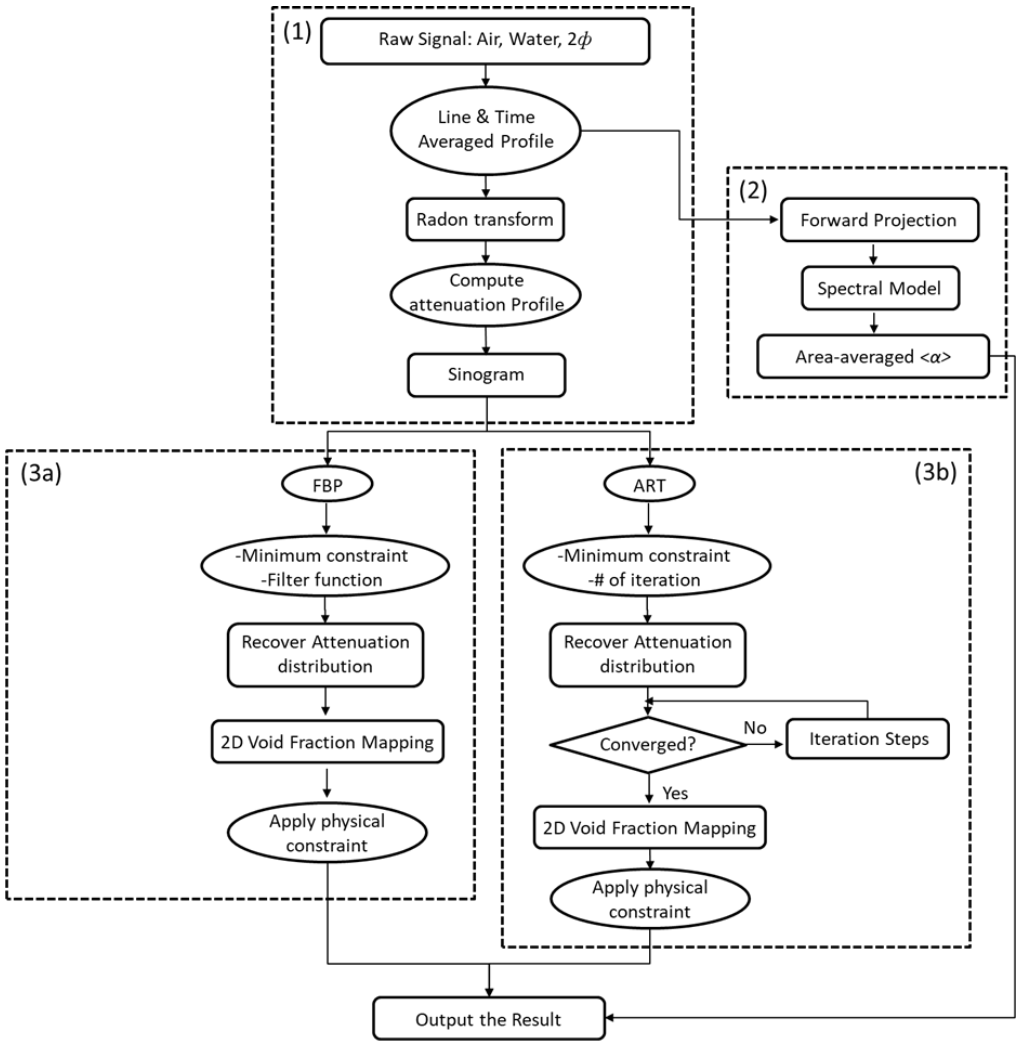

Fig. 4-7: Flowchart of the 2-D reconstruction algorithm.

4.3.1 Description of the Radon transform

To understand the behavior of the x-ray energy, one can assume that the x-ray is a form of a thin line-beam and composed of monochromatic energy photons. To describe the fundamental behavior of the x-ray interaction within the test subject, one may consider x-ray has the initial energy (denote as E_o) projected at a homogeneous test object with overall penetration depth L:

$$E(L) = E_o e^{-\mu \cdot L} \tag{4.7}$$

Here, the variable μ is the mass attenuation coefficient of the test subject. This attenuation coefficient is energy dependence following material to be examined. If the examiner has a test

object composed of heterogeneous material, one needs to replace this attenuation coefficient utilizing the integration of the attenuation coefficient over the x-ray pathway where the projection-ray is projected. For a one-dimensional x-ray projection, one can describe the x-ray energy in the following equation:

$$E(L) = E_o e^{-\int_0^L \mu(x,y)dl} \tag{4.8}$$

Here, $\mu(x, y)$ is the local-attenuation coefficient, which describes the attenuation of the initial beam energy along with the x-ray beam projection. This $\mu(x, y)$ attenuation coefficient function allows defining the spatial properties of the test object with regards to the attenuation property of its specific parts to attenuate the x-ray beam. Attenuation property is what makes it possible to distinguish the test object structures in a reconstructed tomographic image.

From the Eq.(4.8), one can formulate the initial point for describing the physical process of the x-ray attenuation characteristics. Compute the logarithm of both sides of Eq.(4.8), one can further formulate the projection function that describing the significance of the image reconstruction algorithm in the following formulation:

$$\overline{p} = -\ln\left(\frac{E(L)}{E_o}\right) = \int_0^L \mu(x, y)dl \tag{4.9}$$

Here, projection function $\overline{p}$ is the quantity relationship between the initial x-ray energy (before penetration) and measured x-ray energy at the detector pixel. This projection function is referring to the image determined by the detector pixel due to the resultant x-ray energy.

To construct the cross-sectional information of the test object in the measurement plane from the projection data set, one needs to define the parameters for the projection function, as shown in Fig. *4-8*(a). Here, the variable x' is the axis perpendicular (rotational axis) to the x-ray beam projection direction. The angle θ is the rotational angle at a specific viewing angle where the projection is obtained. Rewrite Eq.(4.9) in terms of rotational angle and rotational axis as follows:

$$\overline{p}(\theta, x') = \int_l \mu(x, y)dl \tag{4.10}$$

Here, the parameters are within the ranges $-\infty < x' < \infty$ and $0 \le \theta < \pi$. This equation is known as the Radon transform in the literature [134]. In a CT application, the Radon transform is carried

out by projecting the x-ray through the test object. Then, this attenuated x-ray energy is recorded by the detector screen located at the opposite side of the x-ray source

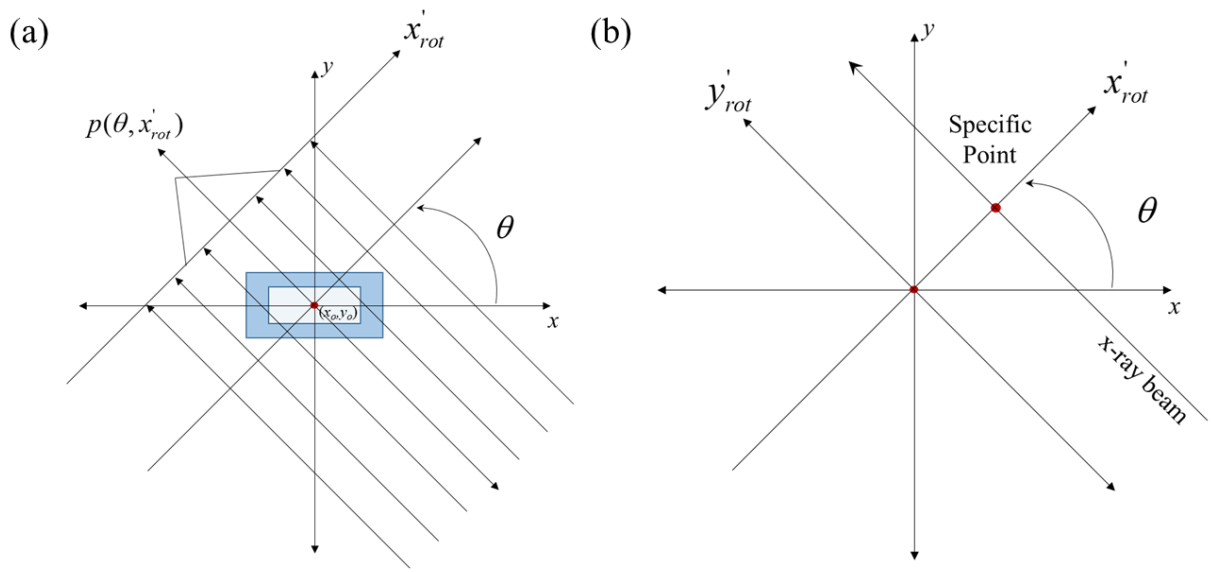

Fig. 4-8: X-ray projections in the measurement plane. (a) The set of parallel projection-rays is projected at a rotational angle θ_{rot}; (b) Geometry of the parallel-beam system.

In Fig. *4-8*(b), sample illustration shows a projection-ray at a given point, which links to the specific location of projection $\overline{p}(\theta, x')$. This projection-ray is in a parallel-beam format, this specific ray only measures the point where the test object is located in the direction of the projection-ray at a rotational angle θ. This parallel-beam projection is based on Eq.(4.10), general attenuation process of the initial energy determined by the x', where the total penetration depth is *L*. However, critical issue with the using Eq.(4.10) lies with the (*x*,*y*) spatial variable in the attenuation function. The integration with respect to a variable y' occurs pathway that the line at a distance x' from the projection axis. Here, one needs to determine the solution for converting from the frame of reference (x, y) into the rotating coordinate system (x', y'), where the projection is rotated around the test object. This rotating coordinate system is illustrated in Fig. *4-8*(b). It is essential to define the projected line along the incident x-ray line beam is projected in the rotating

coordinate system. From the illustration, one can formulate the trigonometric connection between the rotating coordinate system and the frame of reference. This trigonometric relationship is:

Table 9: trigonometric relationship

$(x, y) \rightarrow (x'_{rot}, y'_{rot})$	$(x'_{rot}, y'_{rot}) \rightarrow (x, y)$
$x'_{rot} = x\cos\theta + y\sin\theta$	$x = x'_{rot}\cos\theta + y'_{rot}\sin\theta$
$y'_{rot} = -x\sin\theta + y\cos\theta$	$y = x'_{rot}\sin\theta + y'_{rot}\cos\theta$

Using the above trigonometric relationship from *Table 9*, one can modify the Eq.(4.10) as follows:

$$\overline{p}(\theta, x'_{rot}) = \int_{-\infty}^{\infty}\int_{-\infty}^{\infty} \mu(x, y)\delta(x\cos\theta + y\sin\theta - x'_{rot})dxdy \tag{4.11}$$

This equation is describing the projection function for the specific point t and the specific rotational angle θ of the detector screen. One can visualize the projection function $\overline{p}(\theta, x')$ as an image known as a sinogram [135].

4.3.2 Geometry of the parallel-ray system

In this section, the geometry of the parallel-beam system is presented for the reconstruction from the parallel-beam projection is considered. Previously, the disadvantages of FBP is presented in the literature review. In both, the analytical or algebraic iteration based method requires equally spaced parallel projection data at a given viewing angle. Ultimately, the fan-beam projection needs to convert to the parallel-beam equivalent, then reconstruction can be achieved. In order to understand the reconstruction process from the fan-beam projection, it is essential to review the aspects of the reconstruction from the parallel-ray projection first.

Schematic of the parallel-ray system is shown in *Fig. 4-9*. Here, the detector screen and the parallel x-ray sources revolve around the test object being scanned. The test object remains stationary during the time of projection at every rotational angle. For every projection angle, x-rays are projected from the source and penetrate the test object and reach the detector pixel screen.

The detector pixel measures the resultant x-ray energy after passing through the test object being scanned. Each pixel's energy values are calculated relative to the initial x-ray energy, as defined by the Eq(4.9). This parallel projection value is denoted as $\bar{p}^{para}(\theta^{para}, x'_{rot})$. Here, the projection function parameter θ^{para} is the rotational angle at which a specific projection is performed. This angle is between the frame of reference *x*-axis and the rotating coordinate system x'-axis. The parameter x'_{rot} is the specific position of the pixel location on the detector screen. The position of the pixel screen is respect to the axis of the rotating system at the specific rotational angle where the projection is carried out.

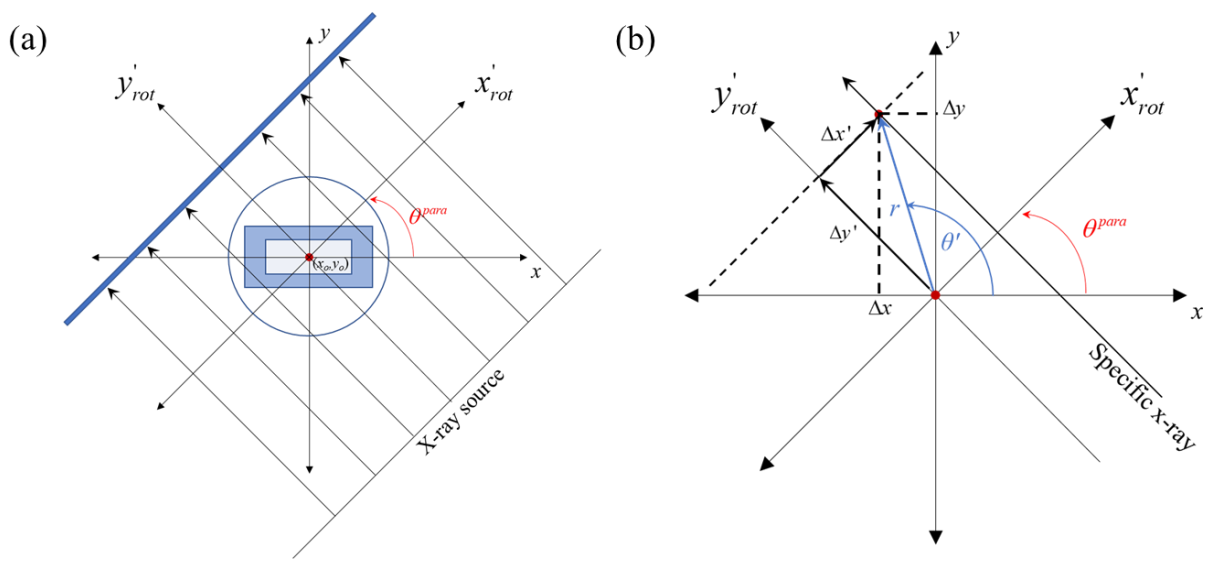

Fig. 4-9: Geometry of the parallel-ray system. (a) Parallel-ray(s) in the (*x*,*y*) coordinate system; (b) geometric relationship between the fixed system and the moving system.

Fig. 4-9 shows the parallel-beam system in the (*x*,*y*) frame of reference. The rotating coordinate system (x'_{rot}, y'_{rot}) is also illustrated in the figure. The fan-beam projection is a sample indication where rotation of the system with the specific rotational angle θ^{para}. The relationship between the frame of reference and the rotating coordinate system is presented in the earlier section. From the geometric relationship in *Table 9*, one can modify the Eq(4.11) into:

$$\overline{p}^{para}(\theta^{para}, x_{rot}^{'}) = \int_{-\infty}^{\infty} \mu(x_{rot}^{'}\cos\theta^{para} + y_{rot}^{'}\sin\theta^{para}, x_{rot}^{'}\sin\theta^{para} + y_{rot}^{'}\cos\theta^{para})dl \qquad (4.12)$$

However, for the typical image reconstruction problem, one often uses a polar coordinate system, here, denote as $(r, \theta_{rot}^{'})$ in *Fig. 4-9*(b). This relationship between the polar coordinate, frame of reference, and the rotating coordinate system is presented in *Table 10*. Illustration in *Fig. 4-9* shows a typical test object scanning in the measurement plane. Here, the parallel-beam system is rotational during the projection of the test object, and the data acquisition takes within the parallel-beam projections. The test object must be placed within the valid parallel-beam projections.

Table 10: Connection between the polar-coordinate system and the frame of reference and rotating system

$(r, \theta') \rightarrow (x, y)$	$(r, \theta') \rightarrow (x_{rot}^{'}, y_{rot}^{'})$
$x = r\cos\theta$	$x_{rot}^{'} = r\cos(\theta^{para} - \theta')$
$y = r\sin\theta$	$y_{rot}^{'} = r\sin(\theta^{para} - \theta')$

4.3.3 Description of the Fan-beam System

As illustrated in *Fig. 4-10*, the rotating fan-beam system is composed of the projection-ray, radiation (x-ray energy) source, and linear detector array. It is import to point out the relationship between the symmetry axis and the fan-beam system in order to translate the geometric relationship. The rotation axis of the rotating fan-beam system is engaged along with the fan-beam rotational angel and frame of reference. This fan-beam rotational axis is perpendicular to the center of the rotational axis. The axis of the rotating-system is engaged along the line perpendicular to the transverse of the test object, and its interaction point with this cross-section is indicated in the figure by (x_o, y_o). The center coordinate point (x_o, y_o) indicates the center of the rotational axis located at $(x_o, y_o) = (0,0)$. The rotating fan-beam system obtains the line-averaged measurement along with a given fan-beam angular projection when projecting the test object. The variable *SC* is referring to the total distance between the source and (x_o, y_o). The variable *SD* indicates the total distance between source to detector center. The entire flow domain of the test object required

to be placed within the fan-beam angle, which is a collection of series of projection-ray generated by the radiation source. Here, one can determine the individual projection-ray at a given by the angle of rotation and specific detector pixel location by the two angle parameters $(\theta_{\bar{p}_i}, \theta_{fan})$. Here, the variable θ_p is the projection-ray angle that is orientated by the projection-ray from the center ray, and the variable θ_{fan} is the fan-beam rotation angle.

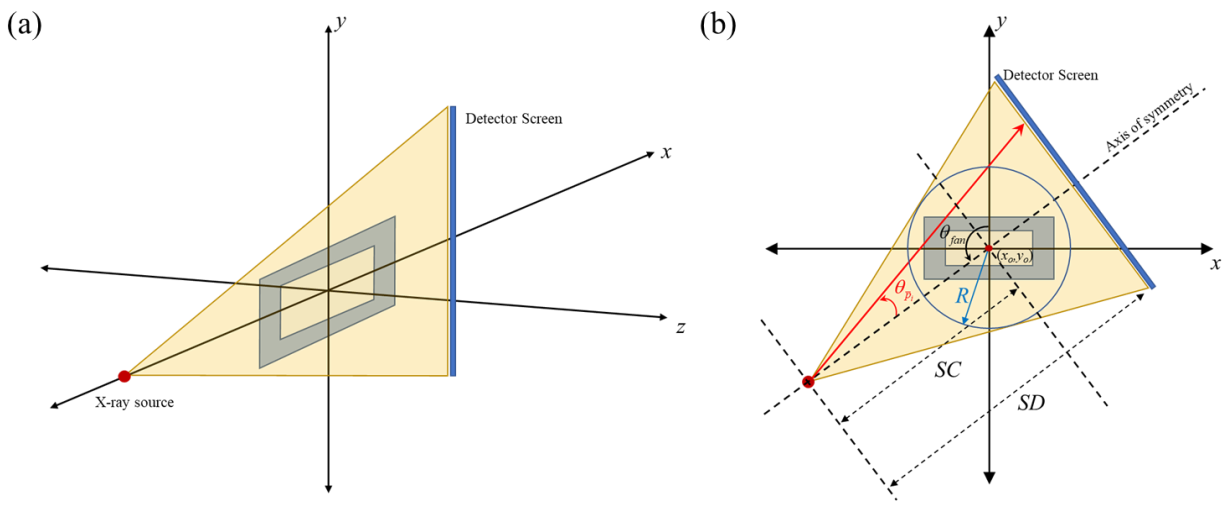

Fig. 4-10: Geometry of the fan-beam system. (a) three-dimensional illustration of the frame of the reference; (b) Basic parameters of the fan-beam geometry

Typical projections data sets are obtained within one revolution. Therefore, the angle θ_{fan} is ranged between [0,2π), which angular projections are implemented. The maximum fan-beam angle that is formed by the outer most projection-ray from the center ray is within the range $[\theta_{\bar{p}_i,\min}, \theta_{\bar{p}_i,\max}]$, this is:

$$\theta_{\bar{p}_i,\min} = \theta_{\bar{p}_i,\max} = \sin^{-1}\left(\frac{R}{SC}\right) \tag{4.13}$$

Here, variable R is the maximum allowable normal distance from the center of rotation to the outer most projection-ray. The variable SC is the overall distance between the source to the center of

rotation. Possible values for the angle $\theta_{\bar{p}_i}$ for the fan-beam system in this study lie within the range [-12°, 12°].

The Projection function obtained by the fan-beam system will be denoted as $p^{fan}(\theta_{\bar{p}_i}, \theta_{fan})$. The reconstruction process will be implemented by these parameters, $p^{fan}(\theta_{\bar{p}_i}, \theta_{fan})$, where the projection angle is ranged between $[\theta_{\bar{p}_i,\min}, \theta_{\bar{p}_i,\max}]$, and rotational angle $\theta_{fan} = [0, 2\pi)$ to reconstruct the flow field using solutions obtained from the fan-beam to parallel-beam equivalent system.

The next step is to arrange the fan-beam projection into the parallel-beam equivalent. First, one needs to define the parameters of the fan-beam projection and re-sort the fan-beam projection that corresponds to the parallel-ray system equivalent. This rearranging process is called fan-beam to parallel-beam re-binning or re-sorting.

Fan-beam sensor can be classified into two different positioning systems:

1. The arc sensors are spaced at equal angles (equiangular sampling) along the circular arc at distance SC from the center of rotation;
2. The line sensors are spaced at an equal distance (equispaced sampling) along the line that is parallel to the rotating axis (x' axis).

The detector system used in this study composed of a linear detector array; therefore, implementation is based on equispaced sampling. Individual projections are sampled at a predetermined k_{th} fan-rotational angle θ_{fan}^{k}, using the linear detector array placed on the detector screen in the shape of the line. Illustration of this fan-beam system is shown in *Fig. 4-11*.

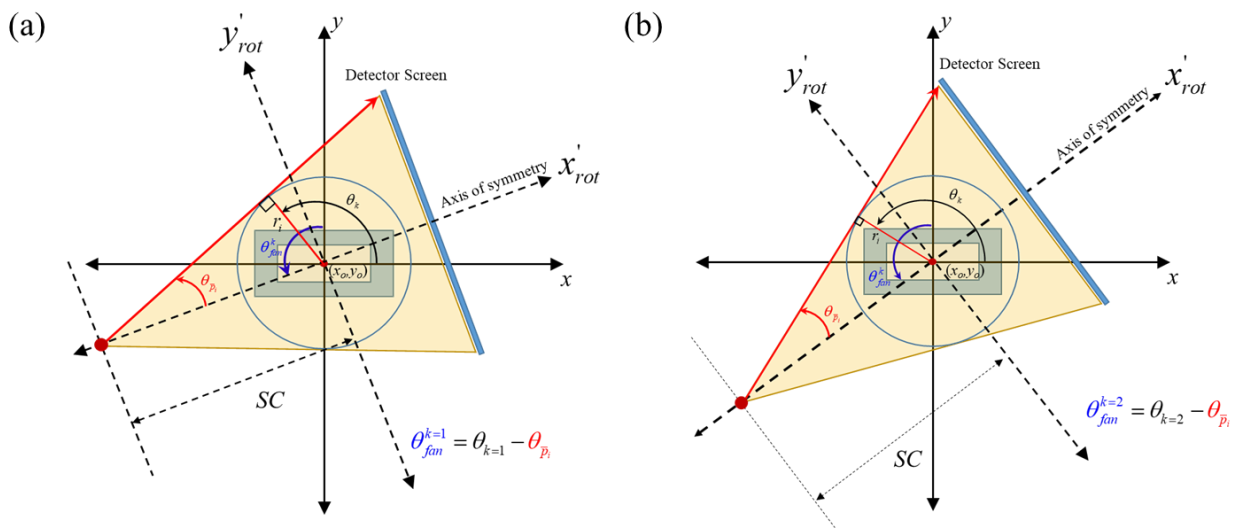

Fig. 4-11: Illustration of rotating fan-beam geometry; (a) specific fan-beam projection made at an angle $\theta_{fan}^{k=1}$; (b) a fan-beam projection is carried out at a rotational angle $\theta_{fan}^{k=2}$

The angle formed by the fan-beam projection $\theta_{\bar{p}_i}$ can be determined by the location of each detector pixel screen. The discrete rotational angels at where projections are sampled can be calculated by:

$$\theta_{fan}^{k} = \theta_k - \theta_{\bar{p}_i} \tag{4.14}$$

Here, θ_k is the angle between the x-axis and i_{th} projection ray with an angle $\theta_{\bar{p}_i}$ in which the fan-beam source is rotated after each k_{th} angular increment. The k is the sampling rotational angle index of each projection.

The angle between the specific line-beam forms from the source to detector pixel location can be defined by:

$$\theta_{\bar{p}_i} = \sin^{-1}\left(\frac{r_i}{SC}\right) \tag{4.15}$$

Here, r_i is the normal distance between the center of rotation to the i_{th} beam, and SC is the total distance between the center of rotation and the radiation source.

From the above relationship, fan-beam projection values are obtainable as follows:

$$\bar{p}^{fan}(\theta_{\bar{p}_i}, \theta_{fan}^{k}) = \bar{p}^{fan}(r_i, \theta_k) \tag{4.16}$$

Here, one can translate the parameter r_i as the total number of the line-beam that is used for the field measurement (total number of detector pixel response in the matrix) and θ_k is the number of projections made at each rotational angle.

The re-binning reconstruction method is referring to the re-sorting the fan-beam projections for the path of fan-beam that corresponds to the parallel-beam system equivalent [136,137]. The re-sorting process is under the assumption that, in one of the fan-beam in the sequence of sampling at all of the projection angle, there is a virtual line-beam that are equivalent to the parallel-beam system that is projected to the detector pixel with the rotational angle θ_{fan} and at a distance r_i from the center of rotation. One can reconstruct the image from the collection of this parallel-ray system equivalent using the back-projection method that is used in the actual parallel-ray system. The geometric of this fan-beam and virtual parallel-ray system equivalent method is illustrated in *Fig. 4-12*.

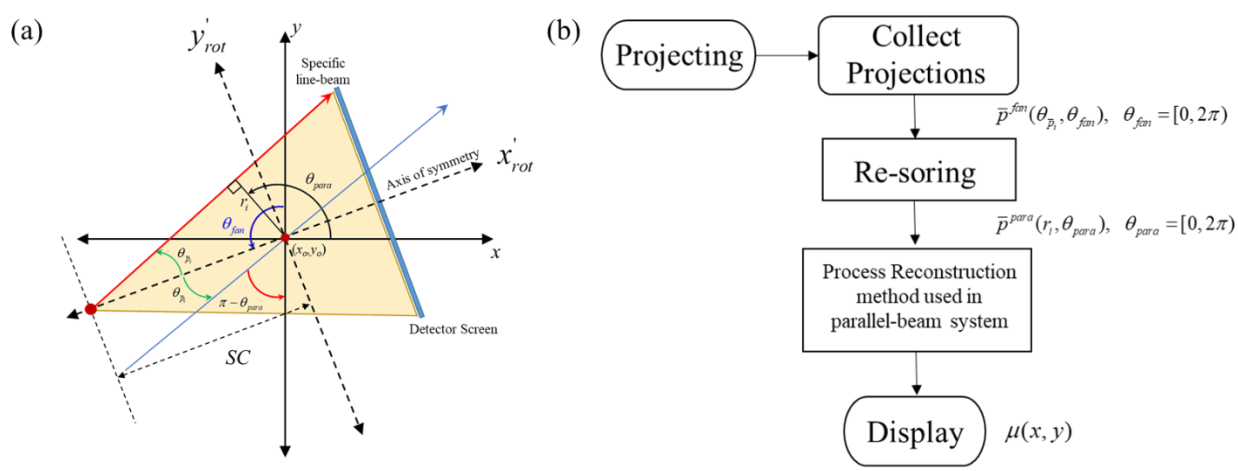

Fig. 4-12: Reconstruction method with re-sorting process; (a) Fan-beam and parallel-ray system geometrical; (b) re-sorting reconstruction method process for the fan-beam system.

There is a direct geometric connection among the basic parameters of a projection-ray of the fan-beam geometry with the equivalent projection-ray of the parallel-beam geometry. One can arrive at the following relationship:

$$\bar{p}^{fan}(\theta_{\bar{p}_i}, \theta_{fan}) = p^{para}(r_i, \theta_{para}) = \bar{p}^{para}(SC\sin\theta_{\bar{p}_i}, \theta_{fan} + \theta_{\bar{p}_i}) \tag{4.17}$$

The equation Eq.(4.17) is equivalent to:

$$\bar{p}^{para}(r_i, \theta_{para}) = \bar{p}^{fan}(\theta_{\bar{p}_i}, \theta_{fan}) = \bar{p}^{fan}\left(\sin^{-1}\left(\frac{r_i}{SC}\right), \theta_{para} - \sin^{-1}\frac{r_i}{SC}\right) \tag{4.18}$$

Form the Eq(4.18), one can determine the angular orientation of the fan projection-ray to the parallel projection-ray. A rotational angle of the fan-beam system is expressed in the following equation:

$$\theta_{fan} = \theta_{para} - \sin^{-1}\left(\frac{r_i}{SC}\right) \tag{4.19}$$

Moreover, the angle $\theta_{\bar{p}_i}$ is:

$$\theta_{\bar{p}_i} = \sin^{-1}\left(\frac{r_i}{SC}\right) \tag{4.20}$$

Every collection of the parallel-beam equivalent values becomes the input values for the reconstruction process that is designed for the parallel-beam system.

4.3.4 Description of the filtered back-projection method

The FBP involves two stages, a filtering-phase and back-projection phase. In the first stage, the back-projection operation involves the inverse of a forward-projection data set. However, when considering the projection function, measured value at a specific detector pixel records line-averaged information where projection-ray is projected, this means specific detector pixel does not determine the line integral of the measurement field. Essentially, the measured value at the detector is a resultant projection-ray that is spread out of the object domain. This is essentially the same for all the projection measurements, and measured values are basically the summation of the values of specific angular projection direction. For example, if one back-projects from one direction, one can obtain the detector function smeared out over the volume if one then add the back-projection of a second direction, two of such smears are added together. By adding multiple directions, one can obtain the outline of the object of interested. As more projections are back-projected, this object becomes clear. Reconstruction of the sample object is illustrated in *Fig. 4-13*. However, it never becomes completely sharp, and there is a critical reason for this issue. Back-

projection involves an additional problem since multiple projections are added on top of every projected angle, thus, resulted in inaccurate reconstructed local voxel value in the reconstructed image. For this reason, back-projection is not used in practical application.

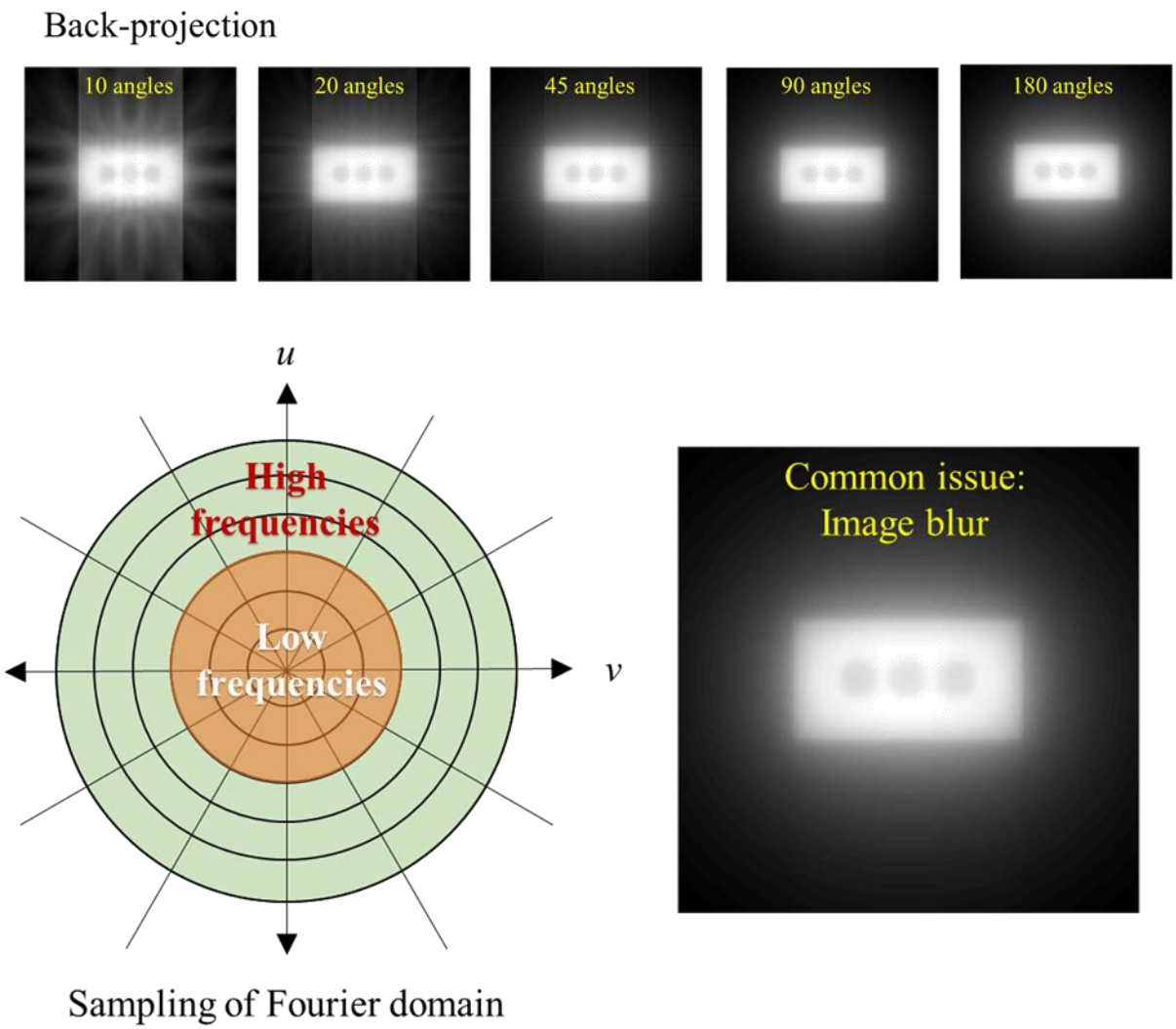

Fig. 4-13: Sample reconstructed object using the back-projection method.

In the Fourier slice theorem, one can notice that with the tomographic setup of acquiring the projections. Here, the Fourier domain of the object is sampled in such a way that the low frequencies are sampled much densely than the high frequencies. The result of that is precisely why the back projections appear to be so blurry (refer to *Fig. 4-13* top row) because an image

processing the low frequencies take care of smooth surfaces, and the high frequencies take care of the details and the sharp edges. Due to the high frequencies are underrepresented in the back-projection, the resulting back projection is indeed severely unsharp. However, by applying the high-pass filter on the detector function, the low frequencies will be suppressed, such that image will not result in an overly blurred back-projected image.

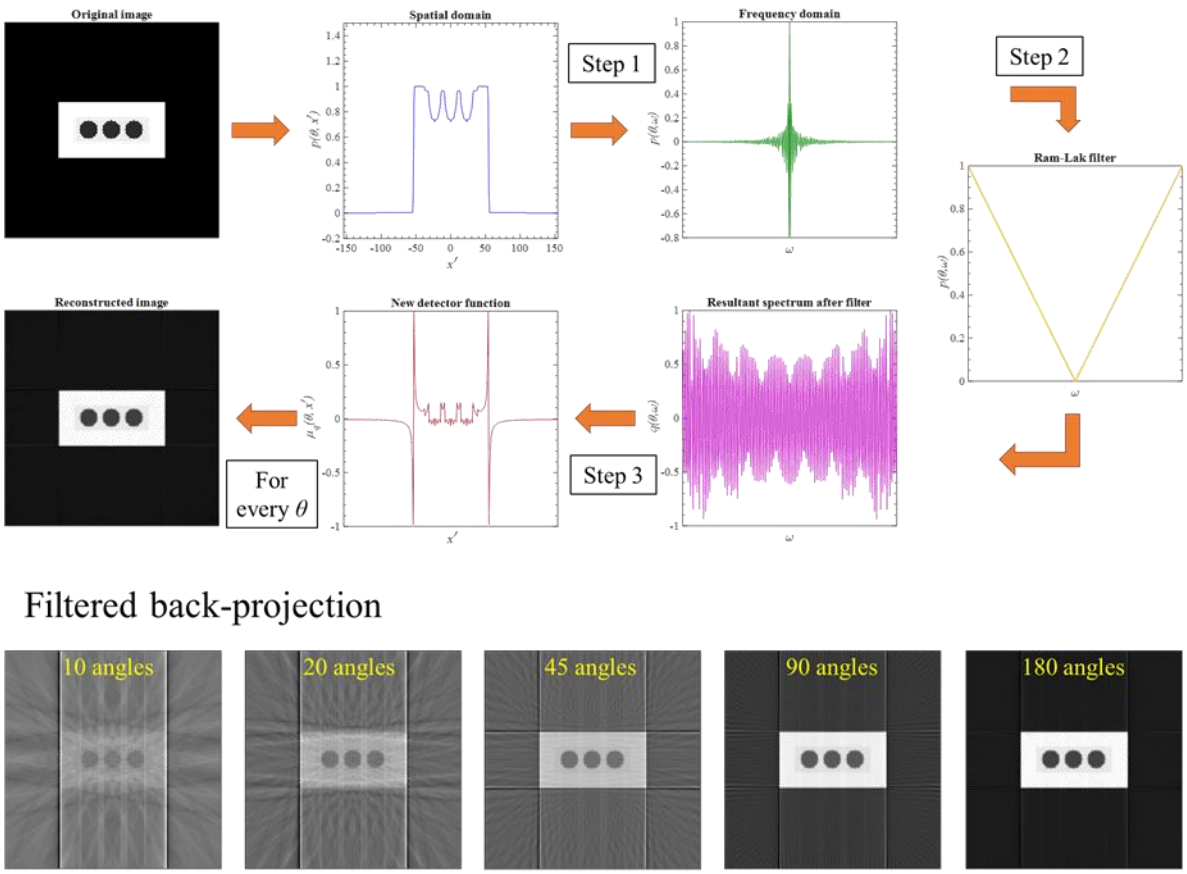

Fig. 4-14: Sample reconstructed object using a filtered back-projection method.

Fig. *4-14* shows the concept of the overall reconstruction process accomplished by the FBP method. In typical signal processing, the filter on the detector function is applied in its Fourier domain. In the first step, this function is Fourier transformed (FT) using the fast Fourier transform (FFT) method. In the second step, this resulting spectrum is then filtered by multiplying it with

what is called a high-pass filter (i.e., Ram-Lark or Shepp–Logan filter) [33]. Here, one can clearly observe that the low-frequencies are suppressed by applying the filtered function and that high frequencies gain relative importance. Also, there is a cut-off, and all frequencies higher than that are set to zero. The purpose of this operation is to suppress the noise effect in the low-frequency region. In step3, after the filtering process, the spectrum is inverse Fourier transforms (IFFT), resulting in a new detector function which denotes as μ_q. In every projection function $\bar{p}$, this is then the function that is subsequently back-projected over the domain.

From the mathematical perspective for the normal back-projection method, one can obtain the smearing out of a detector function over the lines of the x-rays as the following equation:

$$\mu(x,y)_{BP} = \int \bar{p}(\theta_{rot}, x')d\theta \tag{4.21}$$

In the FBP, back-projection on this filtered detector function μ_q , which is IFFT of the Fourier transform of the original function $\bar{p}$ multiplied by the filter function. The filtered detector function can be written as the following equation:

$$\begin{aligned} \mu(x,y)_{FBP} &= \int \mu_q(\theta_{rot}, x')d\theta \\ \mu_q(\theta, x') &= \int\int \bar{p}(\theta_{rot}, x') \cdot e^{-i2\pi wt} dt \left|w\right| e^{i2\pi wt} dw \end{aligned} \tag{4.22}$$

Repeat this process for all projection angles and back-project all the filtered detector function in the spatial domain; one can obtain the local attenuation property. The FBP can be written as the following equation:

$$\mu(x,y)_{FBP} = \underbrace{\underbrace{\int_0^{\pi}\int_{-\infty}^{+\infty}\underbrace{\int_{-\infty}^{+\infty} \bar{p}(\theta_{rot}, x') \cdot e^{-i2\pi wt} dt}_{\text{FT of a projection}} \quad \underbrace{\left|w_{filter}\right|}_{\text{filtering function}}}_{\text{inverse FT}} \quad e^{i2\pi wt} dw\, d\theta}_{\text{back-projection}} \tag{4.23}$$

If the original image is back-projected with one filtered director function, one can obtain the image where only the edges are visible. Repeating this process with more projection angles and sum them all up one can eventually obtain the sharp reconstructed image. This overall FBP process is illustrated in Fig. *4-14*.

4.3.5 Description of the algebraic tomography

Algebraic tomography is all about a system of the equation which can be written as the following equation:

$$\vec{p}_i = W\vec{\mu}^v \tag{4.24}$$

Now, in this formula, $\vec{\mu}^v$ is the one-dimensional vector of n elements each represents a voxel value of a specific single 2-D or 3-D volume, $\vec{p}_i$ is the one-dimensional vector of m elements each representing measurements taken at a specific detector in a specific projection direction. W is an m by n matrix, which is referring to the projection matrix, and it links a specific volume geometry to the specific projection geometry. Here, each row of this projection matrix corresponds to a certain projection-ray that goes through the volume to the specific detector pixel, and each column of this projection matrix corresponds to the specific voxel in the volume. Each element, W_{ij} then respectively, represents how much voxel $\vec{\mu}_j^v$ contributes to the measurements $\vec{p}_i$. This algebraic tomographic problem is illustrated in Fig. *4-15*.

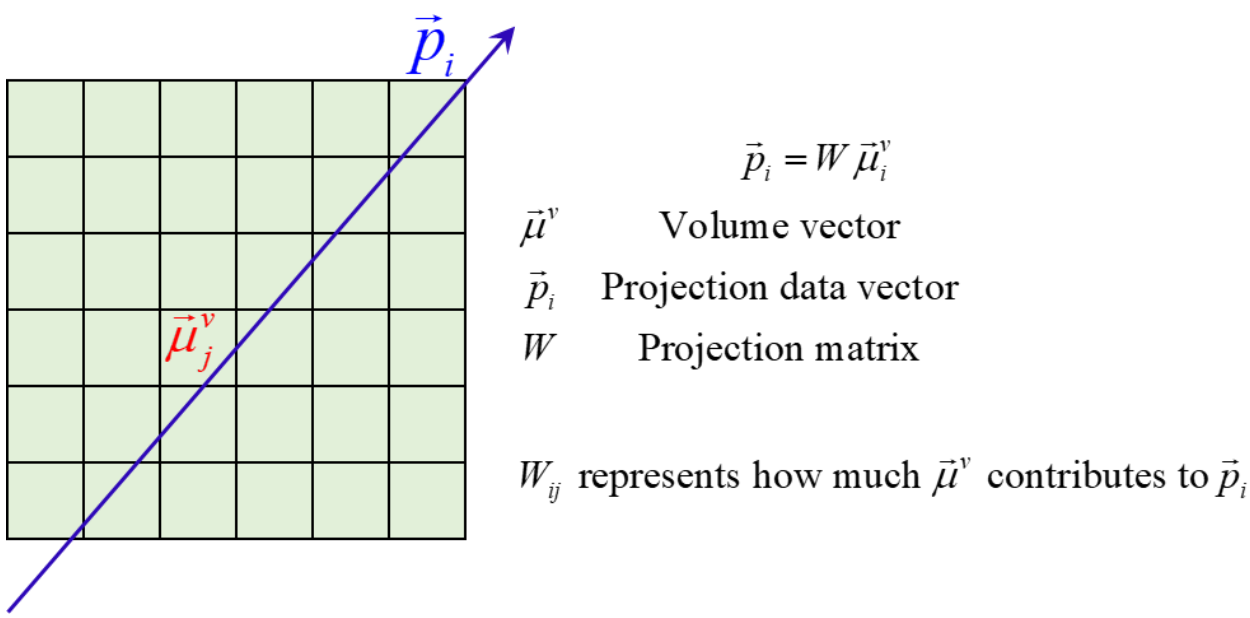

Fig. 4-15: Representation of simple algebraic tomographic problem.

First, one must understand the properties of this projection matrix. For example, one must understand what happens to the resultant matrix when one multiplies this matrix with a specific vector. Let us consider this example equation as follows:

$$p = W\mu^{v} \tag{4.25}$$

Visually this equation Eq.(4.25) would look like in the illustration shown in Fig. *4-16*(a). If one can single out a certain point of the resulting vector, one gets a linear combination of all voxels weighted with how much they contribute. Here, the projection matrix is very sparse, and most of the weights will be zero. Now, the results of this linear combination is effectively a simulation of what one would measure on the detector if the object represented by the volume μ^{v} were to be in the scanner and then if one compute this for each detector which means doing the full matrix multiplication one can obtain the full sinogram of the volume. This operation is called forward projection (FP) and is a crucial one in all algebraic reconstruction methods.

Equal importance is the multiplication of the transpose of the projection matrix. The result of this operation at a specific voxel is a linear combination of all measurements linked to that specific voxel and if one looks at all the points in the sinogram that are linked to the certain voxel one can get the line that follows a sine wave line curve which is where the term sinogram comes from. If one computes this multiplication for all the voxels, one can obtain what is called back-projection. This back-projection operation in the algebraic reconstruction method is expressed in the following equation:

$$\mu^{v} = W^{T} p \tag{4.26}$$

Visually this back-projection operation would look like in the illustration shown in Fig. *4-16*(b)

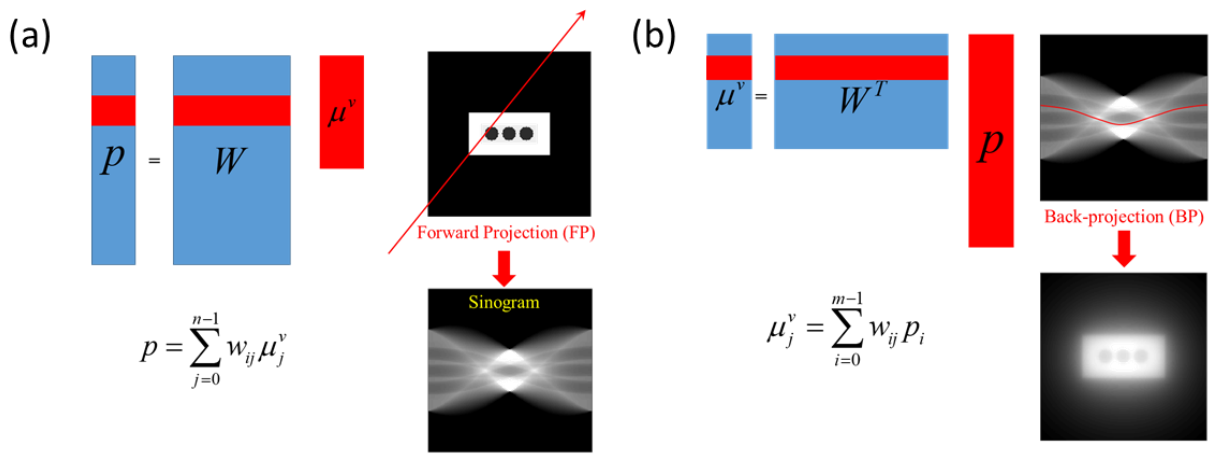

Fig. 4-16: (a) Forward projection (FP) operation in the algebraic reconstruction method; (b) Back-projection (BP) operation in the algebraic reconstruction method.

In Fig. *4-16*, one must carefully look at how the values of the projection matrix w_{ij} are defined. These values are also called projection weights. These projection weights are denoted as the following equation:

$$\sum_{j=1}^{n} w_{ij}\mu_j^v = p_i \tag{4.27}$$

Now, there is no definitive answer for this as multiple projection kernels are valid. Each method comes with its own trade-off in terms of accuracy versus efficiency to compute. Three known types can be used for reconstructing the cross-sectional image. The concept of the projection kernels is illustrated in Fig. *4-17*.

1. The first option, the projection weights are defined by the length that projection-ray p_i transverses through the voxel μ^v; this is the line projection kernel and reasonably accurate and reasonably efficient method.
2. The second projection option is called Joseph's kernel. In Joseph's kernel, for each row or each column, one finds the two voxels closest to the interaction of the ray and that row or column. Then the projection weights of both voxels are founded by linear interpolation. Joseph's kernel provides the most efficient implementation, but this is a bit less accurate, although one can say that in practice, the difference is barely noticeable.
3. The final projection method is to regard the x-ray beam not as a single line but as a strip with the width of a particular detector cell. Each projection weight is determined by the

area of interaction between the voxels and this strip of all the kernels depicted here. This concept corresponds the most to the actual x-ray detector (or scanner) thus, provides the most accurate model. The cost of this advantage, however, is a significant decrease in the time needed for each projection; therefore, in practice, this model is rarely used.

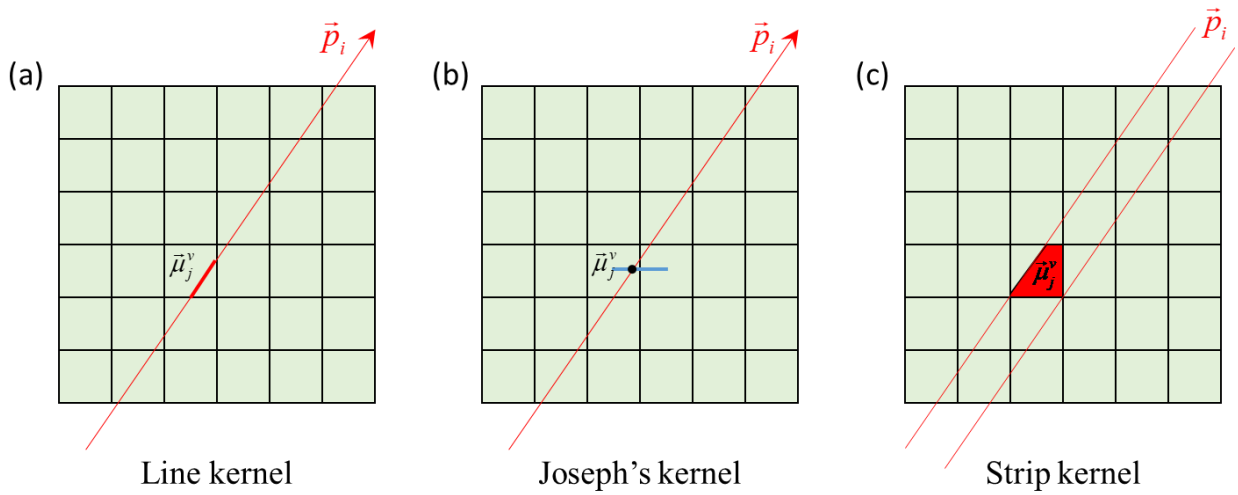

Fig. 4-17: Three different variations of projection kernels used in the algebraic tomography. (a) Line kernel; (b) Joseph's kernel; (c) Strip kernel.

4.3.6.Description of the Iterative Reconstructive Method:

When considering the tomography in its algebraic form, the reconstruction becomes equivalent to solving the system of equations:

$$\vec{p}_i = W\vec{\mu}^v \tag{4.28}$$

Here, W times $\vec{\mu}^v$ equal to $\vec{p}_i$ for the unknown vector $\vec{\mu}^v$. Ideally, solving such an equation is done by multiplying the inverse of the projection matrix W^{-1} with the projection data $\vec{p}_i$. Unfortunately, this projection matrix is not invertible because the matrix array is not a square, and it is too large to compute. Instead, this is an optimization problem and tries to find the solution vector such that the difference between the measured projection and the simulated value of the solution. This difference is also called the residual projection or the projection distance. In order to find this optimal reconstruction, one must use an iterative solver. There are two major families of such iterative solvers; there are Landweber like methods, ART, SIRT, SART, and Krylov

Subspace methods such as conjugate gradient least squares (CGLS) algorithm. The SIRT is as its name implies an iterative method that updates the reconstruction using all the available projection data simultaneously. Iteration step is denoted as the following equation:

$$\vec{\mu}_{k+1}^{v} = \wp\left[\vec{\mu}_{k}^{v} + \lambda W^{T} R(\vec{p} - W\vec{\mu}_{k}^{v})\right] \tag{4.29}$$

The first thing to spot in the iteration formula of SIRT is the computation of a weighted projection difference. It is noted, the W times, $\vec{\mu}_{k}^{v}$ which is a forward projection of the current solution is subtracted from the measured data $\vec{p}$. The result of this is then weighted by the diagonal matrix *R*, which contains the inverse row sums of the projection matrix, and this is essentially the inverse of the length that each ray passes through the volume. Shorter rays do have a higher contribution, and this weighting is required to guarantee convergence. In the second step, this weighted projection difference is back-projected by multiplying it to the transpose of the projection matrix, and the result of this is then again weighted. This time with the inverse column sums of the projection matrix. Finally, this weighted back-projection of the projection difference is then added to the current reconstruction. This can be proven by the following these updated steps the reconstruction of volume $\vec{\mu}_{k}^{v}$ converges to the weights at least square solution where the inverse row sums define the weights:

$$\vec{\mu}^{v} = argmin_{\mu^{v}} \left\| \vec{p} - W\vec{\mu}^{v} \right\|_{R} \quad \text{with} \quad \left\| x \right\|_{R} = x^{T} R x \tag{4.30}$$

In SIRT operation, every iteration step updates the solution from the forward and back-projection from each detector value, where ART only implements a single detector value to update the reconstruction. In general, this means the ART algorithm computes a solution faster than SIRT iteration, however, the ART method still suffers from the unstable convergence if the system of equation is inconsistent due to background noise or unknown uncertainty factors that causes inconsistency in the measurement. In SART operation, each iteration step updates all measured values that are associated with the single projection direction. Hence, the SART method utilizes increased performance over the ART method and offers faster computational speed than the SIRT method.

However, it is noted, the arrangement of the projection data set is critical in the SART operation, which leads to the optimization of reconstruction quality. Doing them in sequentially is a terrible idea as each subsequent projection brings relatively little new information to update. Instead,

doing them in a random order in much better in terms of accuracy and convergence speed. Another variation of SIRT is what is called order-subset SIRT (OS-SIRT), in which two or more projection directions are used in each iteration.

One of the main advantages of algebraic methods over analytical methods is that algebraic methods easily allows the exploitation of prior knowledge that one might have about the scanned object To a great extent, this is very useful if one only has a limited number of measurements available. In such a case, if the total number of a projection data element is greater than the number of voxels or unknowns in the reconstruction equation, this is known as a situation of sufficient projection data. In practice, due to the limits on radiation dose, scanning time, or due to physical constraints in the x-ray scanner, the number of measurements might be minimal compared to the number of unknowns. In this kind of scenario, the reconstruction equation is said to be underdetermined, and there is not enough projection data available to find the correct reconstruction. By exploiting prior knowledge, however, one can effectively fill up this gap of data with external or dark information. This information can come in many forms, but here, a simple case is illustrated in Fig. *4-18*.

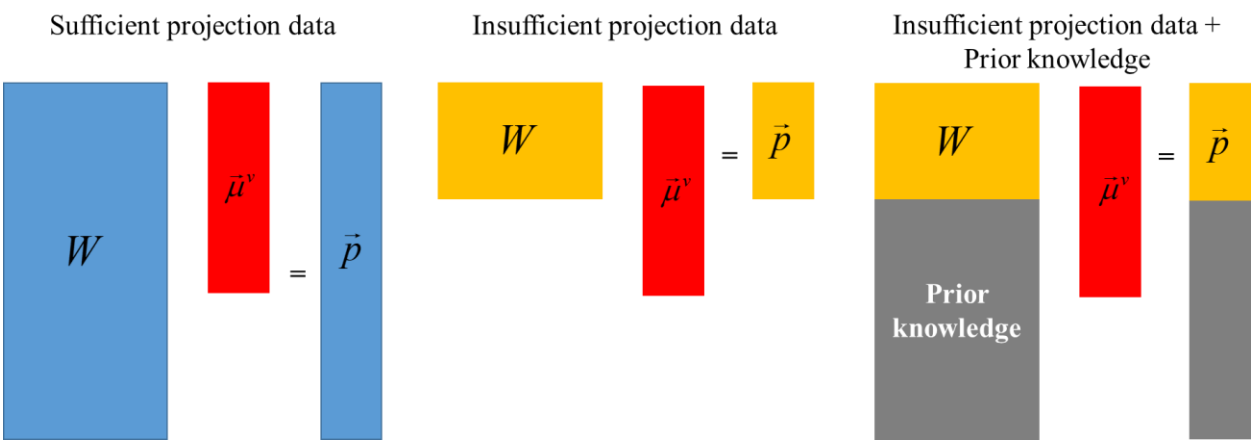

Fig. 4-18: Illustration of Ways to improve the reconstruction result by applying the minimum constraint.

In conventional x-ray tomography, the value of a specific reconstructed voxel represents the attenuation factor of the material that is present in that exact location. This attenuation factor

tells how the density of an x-ray beam will decrease when it passes through this point. Given that the beam intensities cannot increase; one can observe that negative values in the reconstructed image make no sense at all. The SIRT iteration scheme, however, it does not take this situation into account, and the negative values can and do typically pop up. A simple solution for this is to project all negative values into a zero after each SIRT or SART update.

$$\vec{\mu}_{k+1}^{v} = \wp\left[\vec{\mu}_{k}^{v} + \lambda W^{T} R(\vec{p} - W\vec{\mu}_{k}^{v})\right]$$
$$\wp(\vec{\mu}_{k+1}^{v}) = \begin{cases} \vec{\mu}_{k+1}^{v} & 0 \le \vec{\mu}_{k+1}^{v} \\ 0 & \vec{\mu}_{k+1}^{v} < 0 \end{cases} \tag{4.31}$$

Operator function is a simple, straightforward operation to perform and can be executed very efficiently during the implementation. However, doing this causes the breaks of mathematical converge theory of SIRT, but in practice, it improves the quality and results in more accurate reconstruction.

4.3.7 Attenuation images to void fraction

In one-dimensional tomography, the estimation of attenuated line-averaged x-ray energy after passing through a particular test object with a linear attenuation coefficient can be defined by Beer-Lamber energy law. Overall attenuation process of x-ray energy can be formulated in the following equation:

$$\bar{E} = \bar{E}^{o} e^{-\int_{0}^{L} \mu \, dl} \tag{4.32}$$

Here, the variable $\bar{E}$ is the line-averaged value of the attenuated x-ray, the variable $\bar{E}^{o}$ is the initial x-ray energy, and the variable μ is the linear attenuation coefficient of the test object being scanned by the x-ray beam.

Let us further express the x-ray energy attenuation process in the two-phase flow structure, the formulation of line-averaged x-ray energy after passing through the two-phase flow can be written in the following equation:

$$\bar{E}_{\theta,i}^{2\phi} = \bar{E}_{\theta,i}^{o,ref} e^{-\int_{0}^{L} \bar{\mu}_{\theta,i}^{2\phi} \, dl} = \bar{E}_{\theta,i}^{o,ref} e^{-\left[\left(\left(l_{i,\theta}\cdot\alpha\right)\mu^{air}\right)+\left(\left(l_{i,\theta}(1-\alpha)\right)\mu^{water}\right)+\left(\left(L_{i,\theta}-l_{i,\theta}\right)\cdot\mu^{pipe}\right)\right]} \tag{4.33}$$

Here, $\bar{E}_{\theta,i}^{2\phi}$ is the attenuated x-ray energy after passing through the two-phase flow mixture and $\bar{E}_{\theta,i}^{o,ref}$ is the initial x-ray energy. The subscripts i,θ are an indication of x-ray projection at specific i_{th} detector pixels and a specific angular projection. Variable μ^{air}, μ^{water}, μ^{pipe} is the attenuation coefficient of air, water, acrylic pipe wall, respectively. Variable $l_{\theta,i}$ is the absorption length of the two-phase flow, and the variable $L_{\theta,i}$ is the overall absorption of the flow structure; the overall attenuation process is shown in Fig. *4-19*.

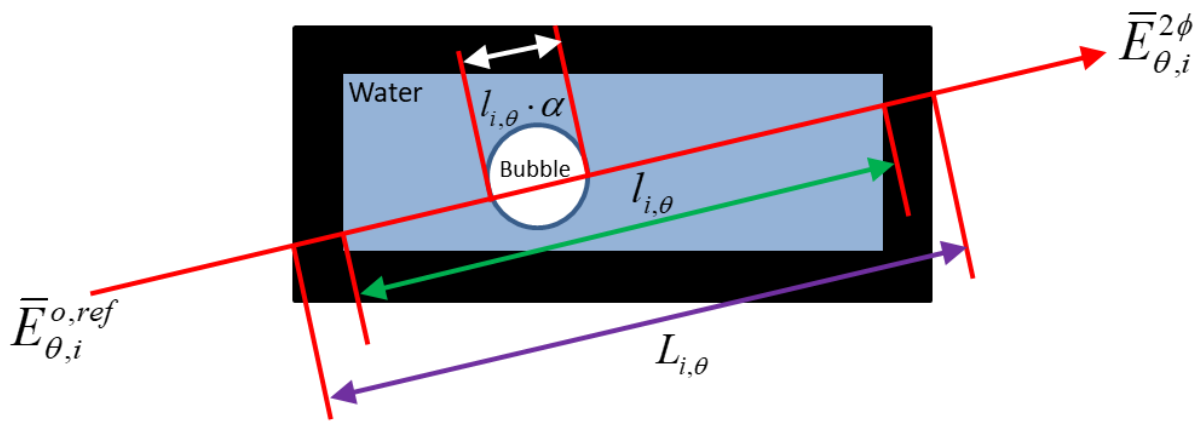

Fig. 4-19: Sample illustration of the overall attenuation process of x-ray energy before and after passing through a two-phase flow structure.

For void fraction calculation, one needs to determine the two additional reference data; line-averaged attenuation profile of single-phase water and single-phase air. The line-averaged x-ray energy passing through the test section with single-phase water is given by in the following formulation:

$$\bar{E}_{\theta,i}^{water} = \bar{E}_{\theta,i}^{o,ref} e^{-\int_0^L \bar{\mu}_{\theta,i}^{water}\, dl} = \bar{E}_{\theta,i}^{o,ref} e^{-\left[\left(l_{i,\theta}\cdot\mu^{water}\right)+\left(\left(L_{i,\theta}-l_{i,\theta}\right)\cdot\mu^{pipe}\right)\right]} \tag{4.34}$$

Here, $\bar{E}_{\theta,i}^{water}$ is the resultant x-ray energy after passing through the test section with single-phase water.

Now, dividing equation, Eq.(4.34) by Eq.(4.33), this yields into the following equation:

$$\frac{\bar{E}_{\theta,i}^{water}}{\bar{E}_{\theta,i}^{2\phi}} = \frac{\bar{E}_{\theta,i}^{o,ref} e^{-\left[\left(l_{i,\theta}\cdot\mu^{water}\right)+\left(\left(L_{i,\theta}-l_{i,\theta}\right)\cdot\mu^{pipe}\right)\right]}}{\bar{E}_{\theta,i}^{o,ref} e^{-\left[\left(\left(l_{i,\theta}\cdot\alpha\right)\mu^{air}\right)+\left(l_{i,\theta}(1-\alpha)\mu^{water}\right)+\left(\left(L_{i,\theta}-l_{i,\theta}\right)\cdot\mu^{pipe}\right)\right]}} = e^{-\left[\left(l_{i,\theta}\cdot\mu^{water}\right)-\left(\left(l_{i,\theta}\cdot\alpha\right)\mu^{air}\right)-\left(l_{i,\theta}(1-\alpha)\mu^{water}\right)\right]} \quad (4.35)$$

Rewrite the ratio of x-ray energy attenuated by the liquid and two-phase flow:

$$\frac{\bar{E}_{\theta,i}^{water}}{\bar{E}_{\theta,i}^{2\phi}} = e^{\left(l_{i,\theta}\cdot\alpha\cdot\mu^{air}\right)+\left(l_{i,\theta}\cdot\alpha\cdot\mu^{water}\right)} \quad (4.36)$$

Transform the above equation into:

$$\ln\left(\frac{\bar{E}_{\theta,i}^{2\phi}}{\bar{E}_{\theta,i}^{water}}\right) = -l_{i,\theta}\bar{\alpha}_{\theta,i}^{2\phi}\left(\mu^{air}-\mu^{water}\right) \quad (4.37)$$

Rearrange above equation into terms of void fraction, α:

$$\bar{\alpha}_{\theta,i}^{2\phi} = \frac{\ln(\bar{E}_{\theta,i}^{2\phi}/\bar{E}_{\theta,i}^{water})}{-l_{i,\theta}\left(\mu^{air}-\mu^{water}\right)} \quad (4.38)$$

Repeat the same procedure for the single-phase air in the test section. One can arrive with the following formulation:

$$\frac{\bar{E}_{\theta,i}^{2\phi}}{\bar{E}_{\theta,i}^{air}} = \frac{\bar{E}_{\theta,i}^{o,ref} e^{-\left[\left(\left(l_{i,\theta}\cdot\alpha\right)\mu^{air}\right)+\left(l_{i,\theta}(1-\alpha)\mu^{water}\right)+\left(\left(L_{i,\theta}-l_{i,\theta}\right)\cdot\mu^{pipe}\right)\right]}}{\bar{E}_{\theta,i}^{o,ref} e^{-\left[\left(l_{i,\theta}\cdot\mu^{air}\right)+\left(\left(L_{i,\theta}-l_{i,\theta}\right)\cdot\mu^{pipe}\right)\right]}} = e^{-\left[-\left(l_{i,\theta}\cdot\mu^{air}\right)+\left(\left(l_{i,\theta}\cdot\alpha\right)\mu^{air}\right)+\left(l_{i,\theta}(1-\alpha)\mu^{water}\right)\right]} \quad (4.39)$$

Now, reduce the above equation into terms of void fraction:

$$\bar{\alpha}_{\theta,i}^{2\phi} = \frac{\ln(\bar{E}_{\theta,i}^{2\phi}/\bar{E}_{\theta,i}^{air}) + l_{i,\theta}\left(\mu^{air}-\mu^{water}\right)}{-l_{i,\theta}\left(\mu^{air}-\mu^{water}\right)} = \frac{\ln(\bar{E}_{\theta,i}^{2\phi}/\bar{E}_{\theta,i}^{air})}{-l_{i,\theta}\left(\mu^{air}-\mu^{water}\right)} + 1 \quad (4.40)$$

Now, equating the Eq(4.38) and Eq(4.40), one can express the equation in terms of attenuation coefficient and energy ratio:

$$\frac{\ln(\bar{E}_{\theta,i}^{2\phi}/\bar{E}_{\theta,i}^{water})}{-l_{i,\theta}\left(\mu^{air}-\mu^{water}\right)} = \frac{\ln(\bar{E}_{\theta,i}^{2\phi}/\bar{E}_{\theta,i}^{air})}{-l_{i,\theta}\left(\mu^{air}-\mu^{water}\right)} + 1 \quad (4.41)$$

Multiplying both sides of the equation by $l_{i,\theta}\left(\mu^{air}-\mu^{water}\right)$ and rearrange the equation in terms of energy:

$$-l_{i,\theta}\left(\mu^{air}-\mu^{water}\right) = \ln\left(\frac{\bar{E}_{\theta,i}^{2\phi}}{\bar{E}_{\theta,i}^{water}}\right) - \ln\left(\frac{\bar{E}_{\theta,i}^{2\phi}}{\bar{E}_{\theta,i}^{air}}\right) = \ln\left(\frac{\bar{E}_{\theta,i}^{air}}{\bar{E}_{\theta,i}^{water}}\right) \quad (4.42)$$

Substituting above equation in Eq(4.38), one can yield a quantitative measure of void fraction in the following equation:

$$\bar{\alpha}_{\theta,i}^{2\phi} = \frac{\ln(\bar{E}_{\theta,i}^{2\phi} / \bar{E}_{\theta,i}^{water})}{\ln(\bar{E}_{\theta,i}^{air} / \bar{E}_{\theta,i}^{water})} = \frac{\ln\left(\bar{E}_{\theta,i}^{2\phi}\right) - \ln\left(\bar{E}_{\theta,i}^{water}\right)}{\ln\left(\bar{E}_{\theta,i}^{air}\right) - \ln\left(\bar{E}_{\theta,i}^{water}\right)} \tag{4.43}$$

Finally, with equation Eq(4.43), one can estimate the void fraction given by specific ray projection specific i_{th} detector pixel at a given projection angle.

However, in CAT application, each projection ray determines the line-averaged attenuation profile, not the attenuated energy ratio at the specific detector pixel. For the two-dimensional reconstruction, one must approach the 2-D inversion with the analytical or algebraic reconstruction method.

Recall, the Radon transform formulation where projection function is written in terms of the rotational angle and rotational axis:

$$\bar{p}(\theta, x') = \int_l \mu(x, y) dl \tag{4.44}$$

Here, the line-averaged projection ray $\bar{p}(\theta, x')$ is the line-averaged attenuation profile, which is a ratio of the x-ray energy before and after the penetration of a particular test object before penetration. In a typical CT problem, the projection function is referring to a line-averaged attenuation profile. The following equation can describe this ratio of the x-ray energy before and after the penetration of a particular test object:

$$E(L) = E_o e^{-\int_l \mu(x,y)\, dl} \Rightarrow -\ln\left(\frac{E(L)}{E_o}\right) = \int_l \mu(x, y)\, dl \tag{4.45}$$

One can further formulate the energy ratio that describing the projection function, which represents the attenuation dataset.

For a complete scan in the tomography setting, let us rewrite the line-averaged attenuation profile in terms of the detector pixel location i and the projection angle θ only. The representation of the line-averaged attenuation data set for the measurement at each detector pixel and a given projection angle is formulated in the following equation:

$$\bar{p}_{i,\theta} = -\ln\left(\frac{\bar{E}_{i,\theta}}{\bar{E}_{i,\theta}^{o,ref}}\right) = \int_l \bar{\mu}_{i,\theta}\, dl \tag{4.46}$$

Here, the $\bar{E}_{i,\theta}$ is the line-averaged x-ray energy response at a specific pixel location i at a given projection angle θ, $\bar{E}_{i,\theta}^{o,ref}$ is the proper reference data, which can be measured from the single

projection measurement where no object is scanned by the x-ray fan-beam (no object in the x-ray chamber). The variable $\bar{p}_{i,\theta}$ is the line-averaged projection, which indicates the ratio of the x-ray energy projected at a specific pixel location to the initial x-ray energy. The variable $\bar{\mu}_{i,\theta}$ is the line-averaged attenuation profile of a specific pixel location at a given angle. This line-averaged attenuation is the overall weighted attenuation profile, which is a contribution of the test section with water, with air or two-phase flow at a given projection point.

For the void fraction calculation, three reference data are required for the reference state, such as a test section filled with single-phase water, single-phase air, and two-phase flow. These reference data are:

$$\begin{aligned} \bar{p}_{i,\theta}^{water} &= -\ln\left(\frac{\bar{E}_{i,\theta}^{water}}{\bar{E}_{i,\theta}^{o,ref}}\right), \\ \bar{p}_{i,\theta}^{air} &= -\ln\left(\frac{\bar{E}_{i,\theta}^{air}}{\bar{E}_{i,\theta}^{o,ref}}\right), \\ \bar{p}_{i,\theta}^{2\phi} &= -\ln\left(\frac{\bar{E}_{i,\theta}^{2\phi}}{\bar{E}_{i,\theta}^{o,ref}}\right) \end{aligned} \tag{4.47}$$

Here, the variable $\bar{E}_{i,\theta}^{water}$, $\bar{E}_{i,\theta}^{air}$, $\bar{E}_{i,\theta}^{2\phi}$ is the complete CT scan of a test-section in a reference state, which, a test-section is filled with single-phase water, single-phase air, and air-water two-phase being imaged. Ultimately, this is the attenuation data set (projection function) mapping the sinogram for each reference measurement.

Recall, the Radon transform which, mathematically describes the attenuation coefficient distribution in the reconstructed 2-D image:

$$\bar{p}(\theta_{rot}, x_{rot}^{'}) = \int_{-\infty}^{\infty}\int_{-\infty}^{\infty} \mu(x,y)\delta(x\cos\theta_{rot} + y\sin\theta_{rot} - x_{rot}^{'})dxdy \tag{4.48}$$

Here, the Radon transform states that the projection function (measured line-averaged attenuation) is a line integral across the attenuation coefficient distribution in the measurement plane along a line represented by the given projection angle at θ and a detector distance x' from the center of origin. Here, one can further process this using the FBP or algebraic iteration method for reconstructing the local voxel value of three reference images.

From the three reconstructed reference image, the standard method to compute the local void fraction distributions of the flow field is [138,139]:

$$\alpha_{x,y}^{2\phi} = 1 - \frac{\mu_{x,y}^{2\phi} - \mu_{x,y}^{air}}{\mu_{x,y}^{water} - \mu_{x,y}^{air}} \tag{4.49}$$

Here, the variable $\alpha_{x,y}^{2\phi}$ is the void fraction of the local position (x, y) in the reconstructed 2-D flow image. The variable $\mu_{x,y}^{water}$ is the reconstructed attenuation coefficient in the water reference data, $\mu_{x,y}^{air}$ is the reconstructed attenuation coefficient in the air reference data, $\mu_{x,y}^{2\phi}$ is the reconstructed attenuation coefficient in the two-phase flow data at the local position, (x, y).

In the two-phase flow studies [138,139], the variable $\mu_{x,y}^{air}$ is assumed to be zero, which is neglected in the formulation, the equation Eq.(4.49) is further simplified into the following equation:

$$\alpha_{x,y}^{2\phi} = 1 - \frac{\mu_{x,y}^{2\phi}}{\mu_{x,y}^{water}} \tag{4.50}$$

However, the equation Eq.(4.50) needs to investigate further if zero attenuation assumption is valid in the 2-D reconstruction result from the polychromatic x-ray source experimental data. For example, in the diabetic flow environment, density difference due to temperature difference in the saturated steam and the gas is significant. Therefore, significant attenuation may occur in this environment. Another example is when the x-ray source is a polychromatic energy beam, which, lower level x-ray energy is attenuated in the air, and the energy spectrum is continuously modified due to the beam-hardening effect done by test-section and two-phase flow being imaged.

In the following section, detailed sensitivity studies are performed using the FBP and ART algorithm for uncertainty quantification in a two-phase flow application. A sensitivity study is to investigate the reconstruction quality influenced by the given set of uncertainty factors or assumptions which can directly impact the void fraction formulation. Details of reconstruction results are presented and discussed for each sensitivity study.

4.4 Synthetic Bubble Sensitivity Study

In the synthetic bubble sensitivity study, the x-ray energy is assumed to be constant energy, and the attenuation coefficient for the water, air, and test-section are also constants. Synthetic bubble images are generated in the resolution of 261 by 216-voxel for the 0.4mm pixel size and

108 by 108 voxel for the 0.8mm pixel size. Sample synthetic images of the three reference data (water, air, and synthetic bubble distribution in the test section) are shown in Fig. *4-20*. The following uncertainty factors are integrated into the reconstruction algorithm in the sensitivity simulation:

1. Reconstruct the 2-D void fraction image using the limited number of angular projections,
2. Investigate void fraction uncertainty with different pixel resolutions, which influence the data spacing between the adjacent projection,
3. Uncertainty of the reconstructed void fraction profile impacted by the added background noise in projection data,
4. Void fraction uncertainty influenced by the off-center shift effect,
5. Investigate the uncertainty associated with different void profiles.

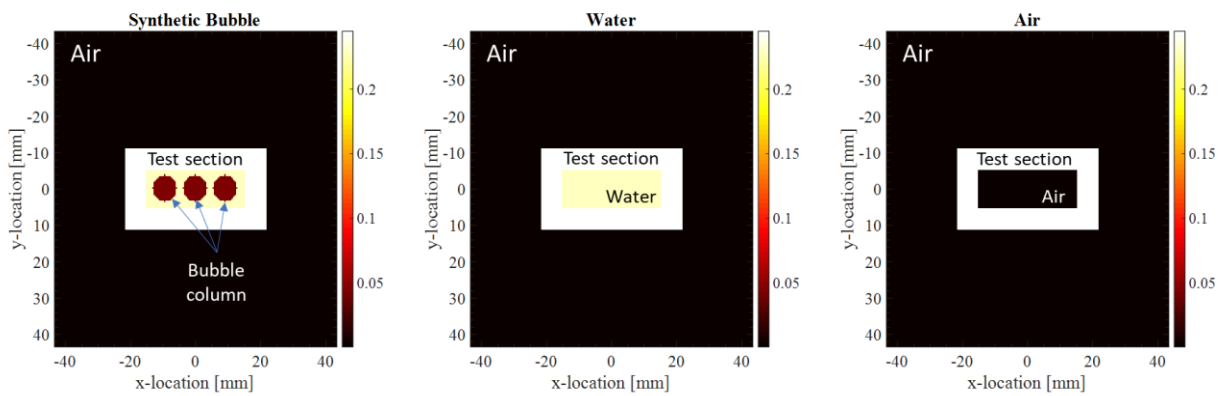

Fig. 4-20: Generated synthetic image for the three reference data for the void fraction formulation.

4.4.1 Limited viewing angle

The reconstruction is achieved with a limited number of angular projections. For the input parameter, the projection data sampled at 18 projections (10˚ increments), 36 projections (5˚ increments), and 180 projections (1˚ increment) are considered. These sampled projections are arranged in the sinogram and shown in Fig. *4-21*. In the 2-D reconstruction algorithm, the minimum constraint is applied, in which negative attenuation coefficient values are set to zero.

The reconstructed 2-D attenuation coefficient image is shown in Fig. *4-22*. It is noted, reconstruction quality is proportional to the number of angular projection data set, which quality of reconstruction image improves when extensive projection data set are available. In Fig. *4-23*, the center-line (x-axis) void fraction profile indicates reasonable void fraction distribution when compared to the actual value; however, reconstruction indicates under-estimating void fraction near the bubble edge where a sharp phase change occurs. The bubble column resembles the annular-flow characteristic; here, one can conclude that 2-D reconstruction may result in underestimating void fraction when using the FBP or algebraic iteration method. Absolute void fraction error and area-averaged void fraction errors are listed in Table *11*. It is shown in the simulation, 90 or more projections are recommended to maintain reasonable reconstruction quality. In case a limited number of angular projections are obtained, proper angular interpolation is recommended. However, reconstruction with an inadequate angular projection set, the algebraic iteration-based method is more suitable. As the number of angular projection increases, the FBP method demonstrates better performance when considering the reconstruction quality and the computational cost.

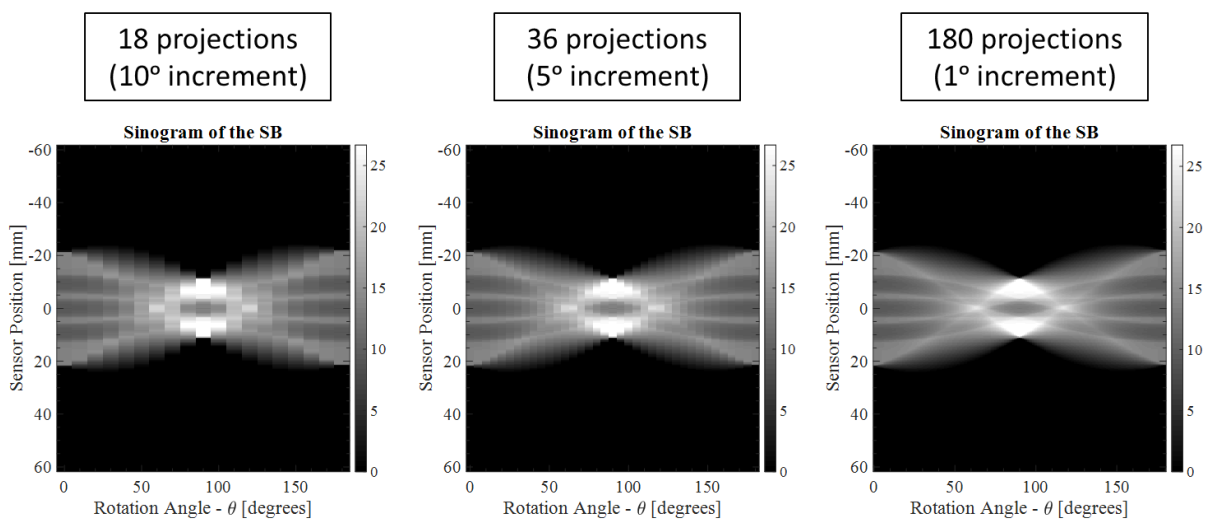

Fig. 4-21: Arranged sinogram from the limited number of viewing angles.

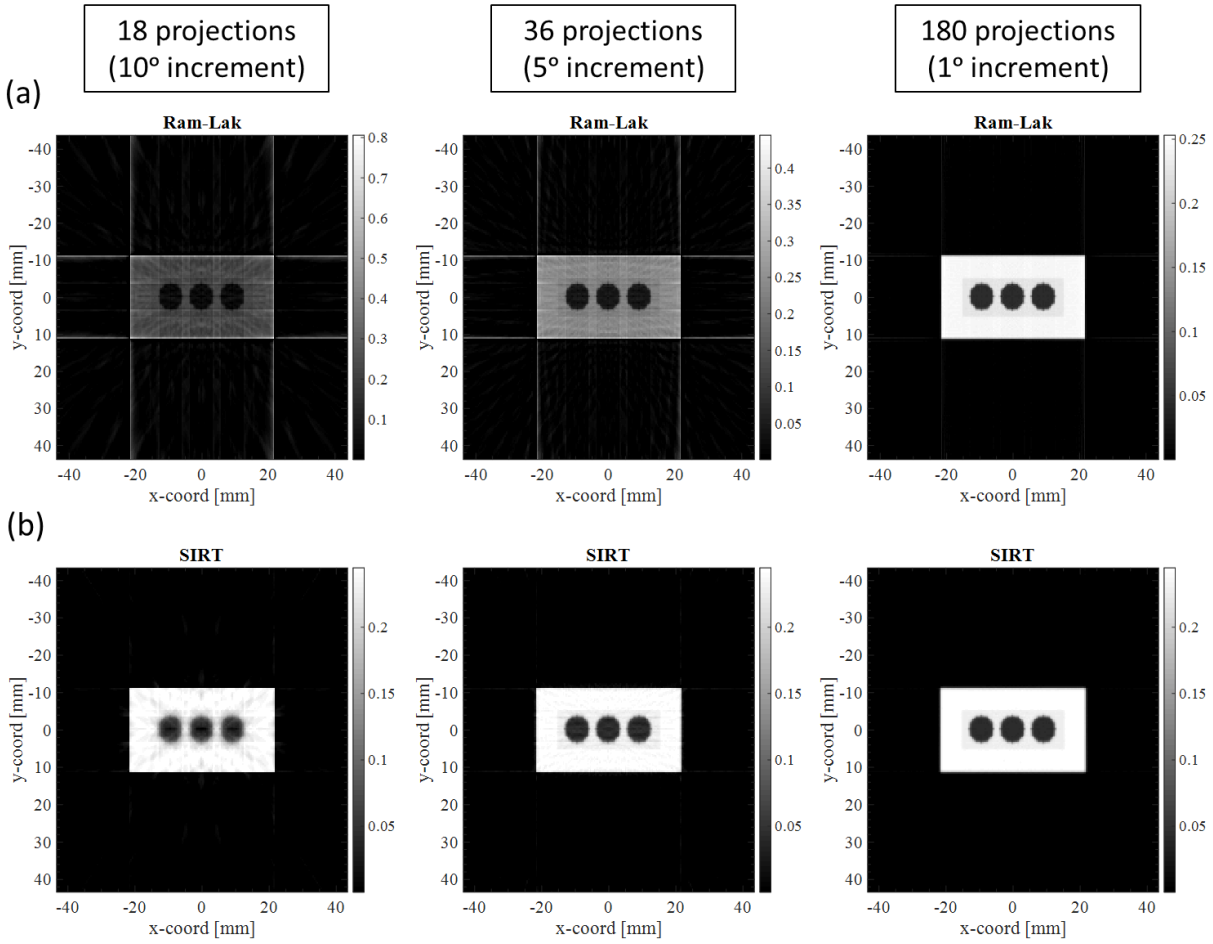

Fig. 4-22: Reconstructed 2-D void fraction image using FBP and ART method. Each column indicates the number of projection data set. (a) Reconstructed void fraction profile using the FBP method and Ram-Lark filtering; (b) Reconstructed void fraction profile using the SIRT iteration method.

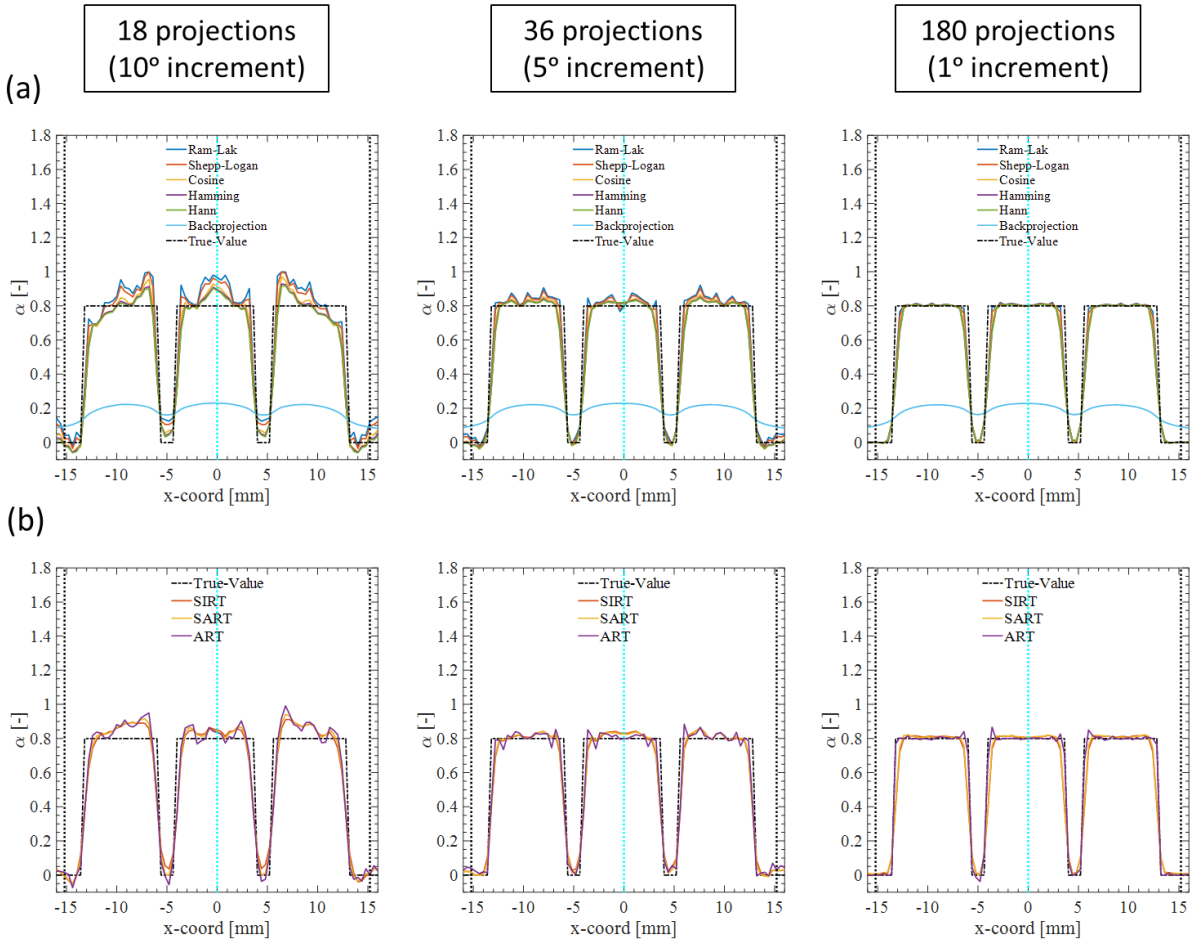

Fig. 4-23: Void fraction profile for the center-line x-axis. Each column indicates the number of projection data set used. (a) Reconstructed void fraction profile using the FBP method and Ram-Lark filtering; (b) Reconstructed void fraction profile using the various algebraic iteration methods.

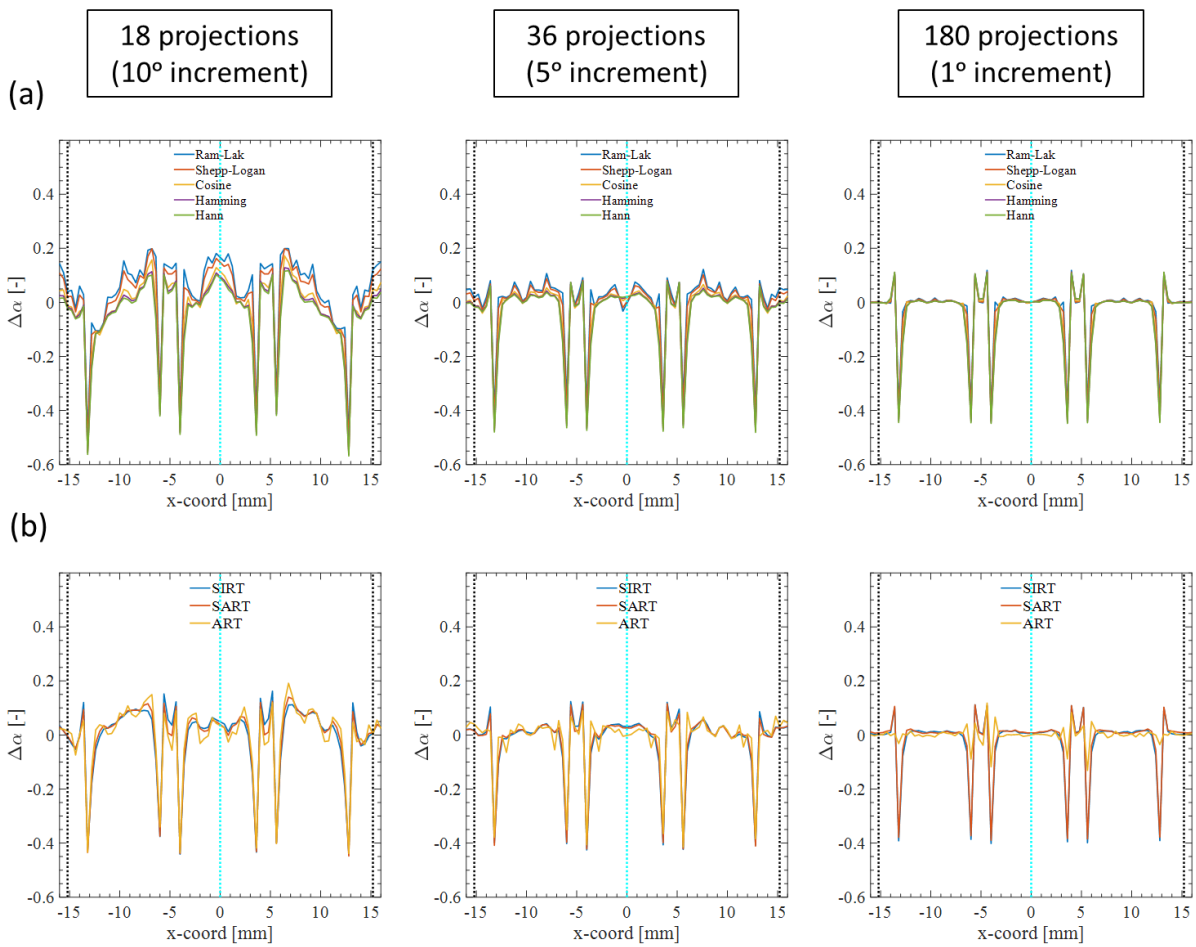

Fig. 4-24: Void fraction difference between the actual void fraction value and reconstructed profile. Each column indicates the number of projection data set. Void fraction difference resulted from (a) FBP reconstruction; (b) algebraic iteration-based method.

Uncertainty of the reconstructed void fraction profile is formulated into two categories, the absolute void error (AVE) and area-averaged error (AAE). First, the absolute void fraction error of the reconstructed image is calculated using the following equation:

$$Error_{|\alpha|} = \frac{\sum \left| \alpha_{x,y}^{rec} - \alpha_{x,y}^{True} \right|}{n_x \cdot n_y} \tag{4.51}$$

Here, the variable $\alpha_{x,y}^{rec}$ and $\alpha_{x,y}^{True}$ is the reconstructed local void fraction value and the actual void fraction value, respectively. The n is the total number of voxel elements in the x-row and y-column of the reconstructed flow region.

The area-averaged void fraction of the reconstructed image and the actual void fraction is formulated in the following equation:

$$\langle \alpha \rangle_{rec} = \frac{\sum \alpha_{x,y}^{rec} \cdot A_{voxel}}{A_{pipe}}, \qquad \langle \alpha \rangle_{True} = \frac{\sum \alpha_{x,y}^{True} \cdot A_{voxel}}{A_{pipe}} \tag{4.52}$$

Here, the bracket $\langle \alpha \rangle$ indicates area-averaged void fraction quantity, a variable A_{voxel} is the voxel area, and A_{pipe} is the cross-sectional flow area of the test section. The area-averaged error of the reconstructed profile is formulated in the following equation:

$$Error_{\langle \alpha \rangle} = \frac{\langle \alpha \rangle_{rec} - \langle \alpha \rangle_{True}}{\langle \alpha \rangle_{True}} \tag{4.53}$$

Table 11: List of the absolute void error and area-averaged quantity error resulted from the limited angular projection data set.

	Absolute void error (FBP)	Absolute void error (SIRT)	Area-averaged error (FBP) [%]	Area-averaged error (SIRT) [%]
18 projections	0.0209	0.0103	6.81	3.36
36 projections	0.0076	0.0059	2.47	1.91
180 projection	0.0013	0.0029	0.41	0.96

4.4.2 Resolution effect

In the resolution effect study, 0.4mm and 0.8mm pixels are simulated. For the input parameter, a total of 180 angular projection data sets are generated in both resolution modes. The minimum constraint is applied in the operator function, in which a negative attenuation coefficient is set to zero attenuation value. Fig. *4-25* shows the distribution of the reconstructed void fraction profile and void fraction difference $\Delta\alpha$, of the centerline x-axis. Fig. *4-25*(a) and (b) indicates a reconstructed void fraction profile resulted from the 0.4mm and 0.8mm pixel resolution mode, respectively. Fig. *4-25*(c) and (d) show the void fraction difference, $\Delta\alpha$, from the actual value. The void fraction profile indicates the reconstructed profiles tend to underestimate the void fraction when compared to the actual void fraction value in both FBP and algebraic iteration-based reconstruction. In the 0.8mm resolution mode, there is a significant void fraction uncertainty in

the liquid to gas phase transition region. For example, there is a liquid-phase region between the bubble column where reconstruction fails to capture the sharp transition and over-estimating the void fraction in the liquid-phase region which should be zero void fraction, in contrast, the reconstruction algorithm under-estimating the void fraction in the gas-phase region between the transition near the bubble wall boundary. This simulation indicates that using the low-resolution mode may cause a significant uncertainty when formulating the void fraction from the reconstructed image. When using the low-resolution detector pixel, it is recommended to incorporate the proper interpolation for increasing the number of projection data points between the pixel; thus, the reconstruction has enough projection data points to display the behavior of the sharp change between the liquid to gas-phase transit. Absolute void fraction error and area-averaged void fraction errors are listed in Table *12*.

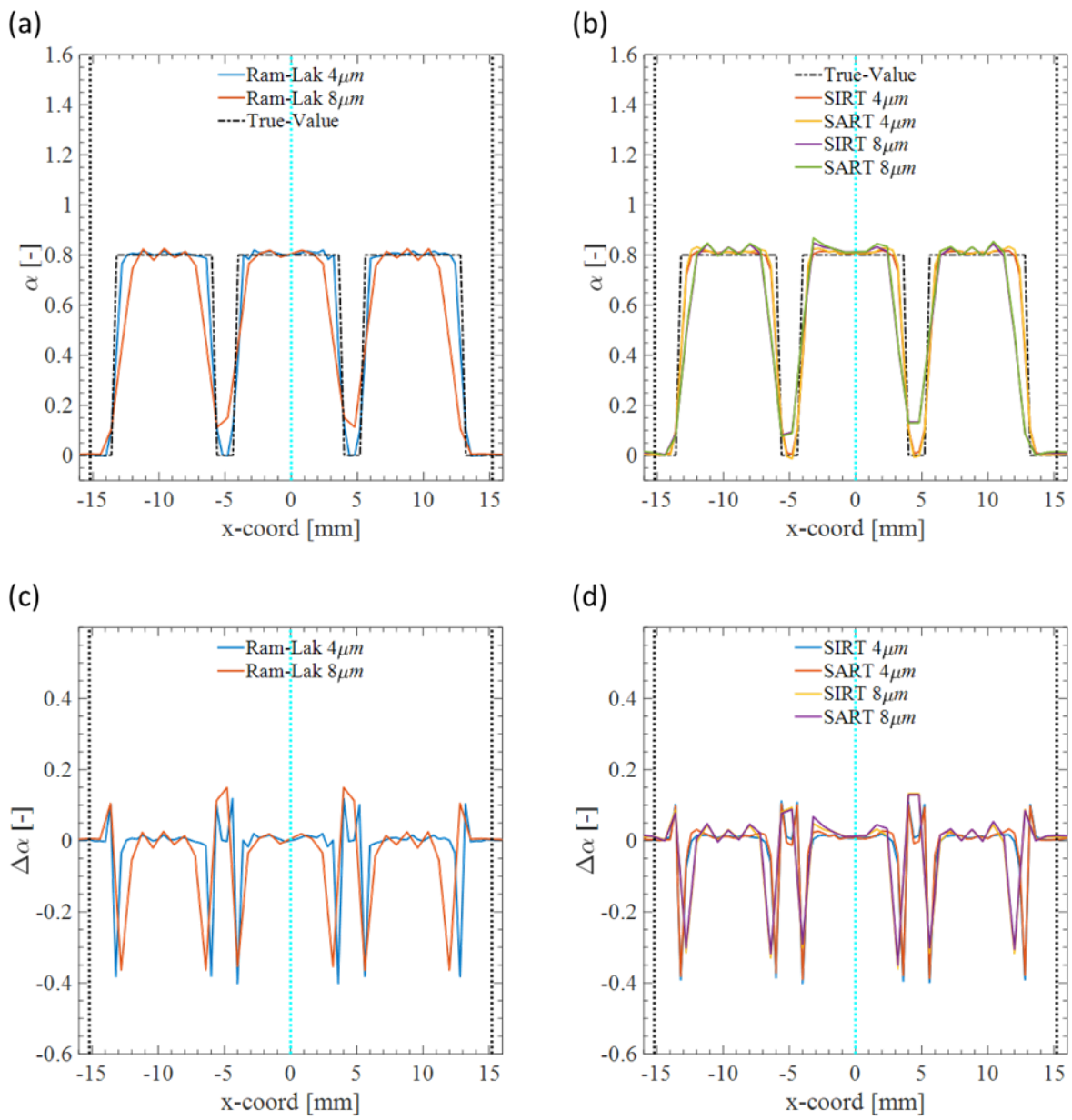

Fig. 4-25: Void fraction distribution and the void fraction difference, $\Delta\alpha$, of the centerline x-axis resulted from 0.4mm and 0.8 mm pixel resolution mode, (a) Void fraction profile of FBP method; (b) Void fraction profile of ART method; (c) $\Delta\alpha$ of FBP method; (d) $\Delta\alpha$ of ART method.

Table 12: List of the absolute void error and the area-averaged quantity errors of the 0.4mm and 0.8mm pixel resolution mode.

	Absolute void error (FBP)	Absolute void error (SIRT)	Area-averaged error (FBP) [%]	Area-averaged error (SIRT) [%]
0.4mm mode	0.0013	0.0029	0.41	0.94
0.8mm mode	0.0028	0.0059	0.92	2.29

4.4.3 Background noise effect

In this sensitivity study, the uncertainty caused by the added background noise effect is simulated. Random background noise within $\pm 3\%$ is added to the projection data set. A total of 180 angular projections are generated and the minimum constraint is applied, in which negative attenuation is set to zero attenuation value. Fig. *4-26* shows the reconstructed 2-D image of the FBP and algebraic iteration-based method. It is shown in Fig. *4-27*, added background noise effect is noticeable in both reconstruction image. In both cases, the reconstructed void profile tends to underestimate the void fraction between the bubble column and the gas to the liquid transition region. Weighted noise data values are distributed throughout the high void faction region. It is seen in the algebraic iteration-based reconstruction that the ART reconstruction is severely impacted by the added background noise, which is not a suitable reconstruction method if data contains high-level background noise. Overall, the FBP and SIRT methods performed well and delivered a reasonable reconstructed profile. FBP and SIRT are recommended for the image reconstruction if the experimental data contains significant background noise or data are taken in a severe experimental condition. The absolute void error and the area-averaged void fraction errors are listed in Table *13*.

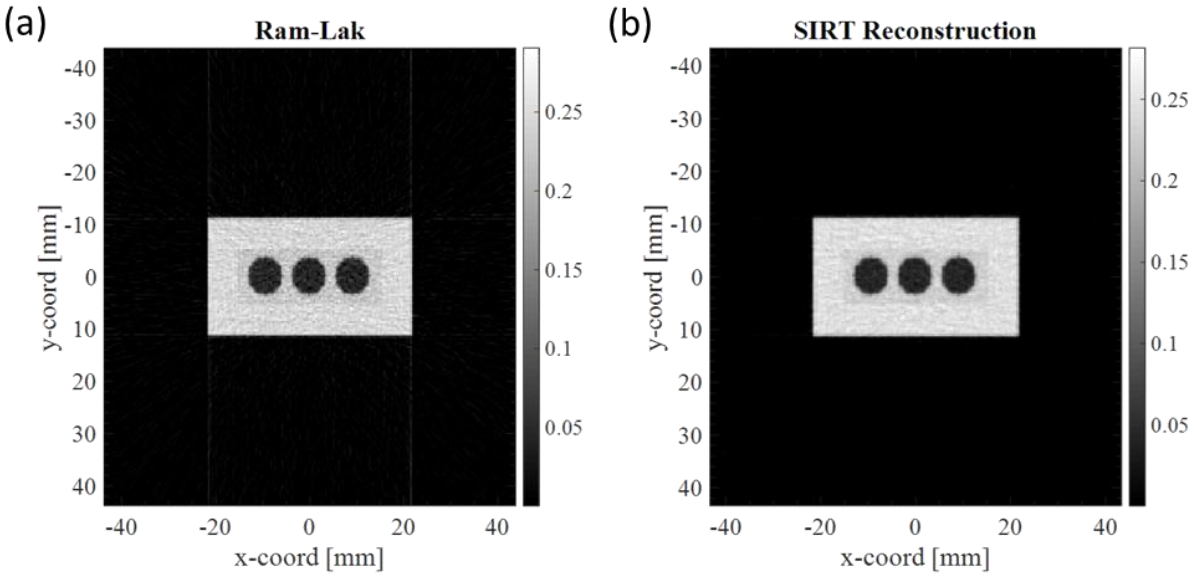

Fig. 4-26: Reconstructed 2-D image where the background noise within ±3% influences projection data. Reconstructed image of the (a) FBP method; (b) SIRT method.

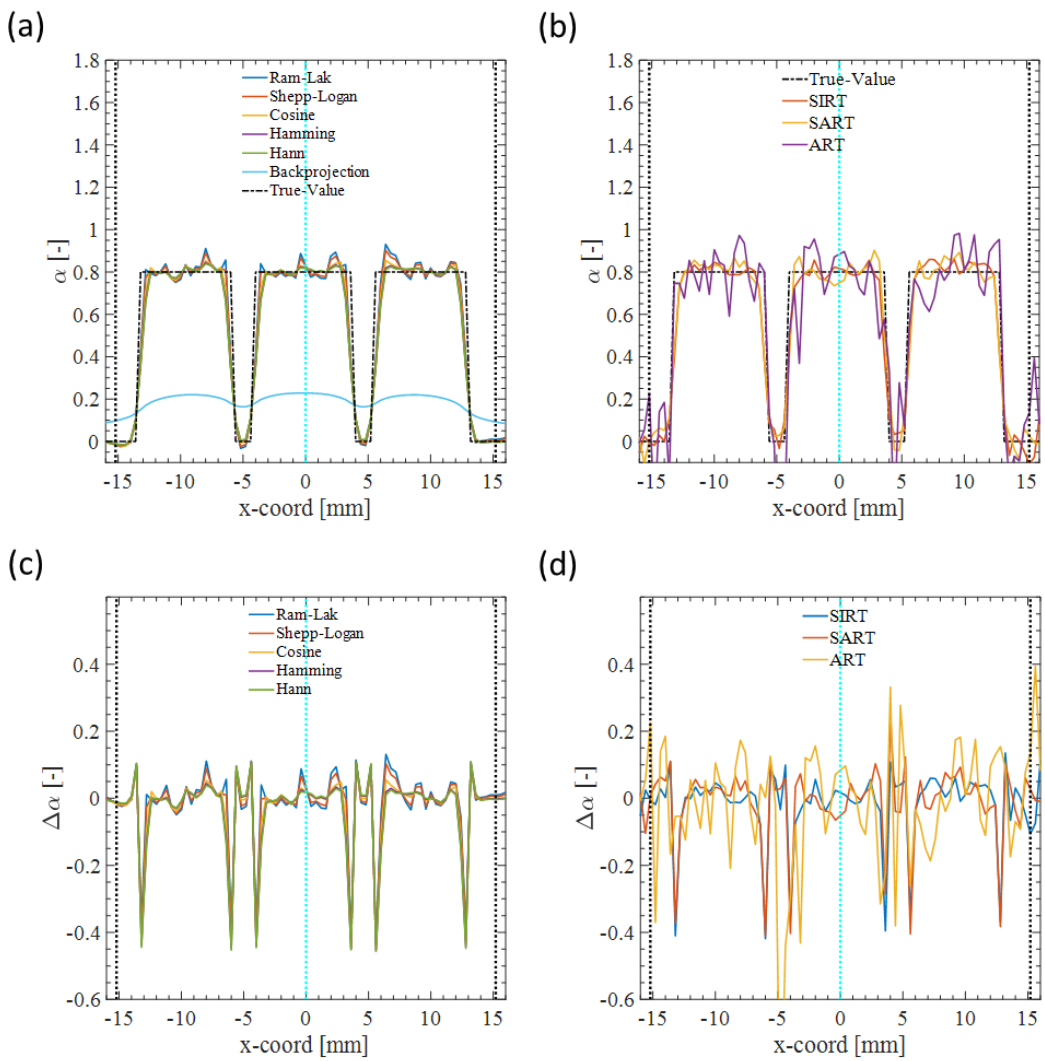

Fig. 4-27: Void fraction profile of the centerline x-axis, (a) FBP method; (b) algebraic iteration methods. Distribution of void fraction difference, $\Delta\alpha$, of the centerline x-axis, (a) FBP method; (d) algebraic iteration methods.

Table 13: List of the absolute void error and area-averaged quantity error due to the background noise effect.

	Absolute void error (FBP)	Absolute void error (SIRT)	Area-averaged error (FBP) [%]	Area-averaged error (SIRT) [%]
±3% noise	0.0037	0.012	1.19	3.79

4.4.4 Off-center shift effect

This sensitivity is investigated the reconstruction quality scenario when the source location is shifted from the center of the rotational axis. Many different factors can be considered, such as a detector array shift, turn-table uncertainty, or the slope of a test-section, which can be considered to lean in a particular direction. In this section, only one case is reviewed for a general-purpose study. Fig. *4-28* shows an example of an off-center shit in the measurement domain. In the simulation, a total distance of 0.8mm shift is implemented in the algorithm. It is shown in Fig. *4-29*, the reconstructed 2-D image shows significant distortion of the bubble column and highly affected by when considering the off-center shift. From the reconstructed image, one can conclude that the reconstruction is extremely sensitive to external uncertainty factors, which can be affecting the quality of projection data even with the small shift of 0.8mm off-centered. Fig. *4-30* illustrates the void fraction profile and void fraction difference, $\Delta\alpha$, of the centerline x-axis. It is shown in Fig. *4-30*, the reconstructed profile reveals the considerable uncertainty of the reconstruction and significant underestimation of the void fraction and fails to capture the properties of a liquid-phase region between the bubble column.

The FBP and SIRT methods tend to reconstruct the reasonable void profile where ART reconstruction fails to display the sharp transition near the bubble edge. Overall, the FBP shows the lowest error in both absolute void error and area-averaged error. The absolute and area-averaged errors are listed in Table *14*. In conclusion, this study demonstrates significant uncertainty of void fraction when the source location is shifted. During the actual experiment, the instrumentation device and x-ray system must be carefully constructed in order to reduce the measurement uncertainty. From this study, one can make an assumption which geometric orientation may affect the significant measurement error as well, which profoundly influences the reconstruction result, especially with void fraction measurement. Also, measurement uncertainty due to detector array shift, turntable uncertainty, or slant of the test-section should be further investigated.

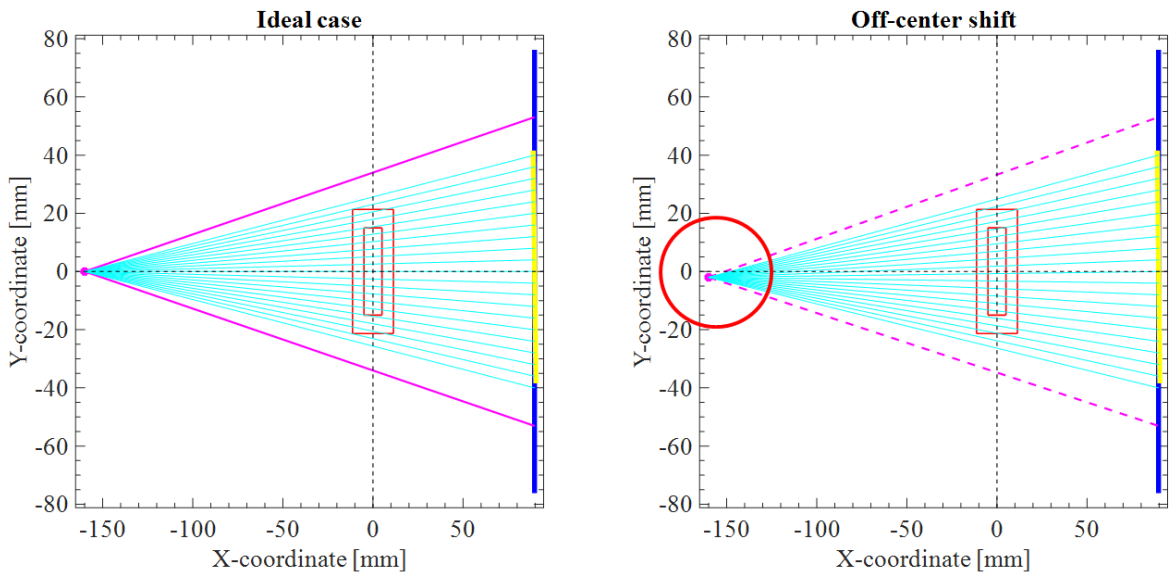

Fig. 4-28: Illustration of the Off-center source location in the global coordinate system in the measurement domain. (a) Ideal case; (b) Off-center source location shift.

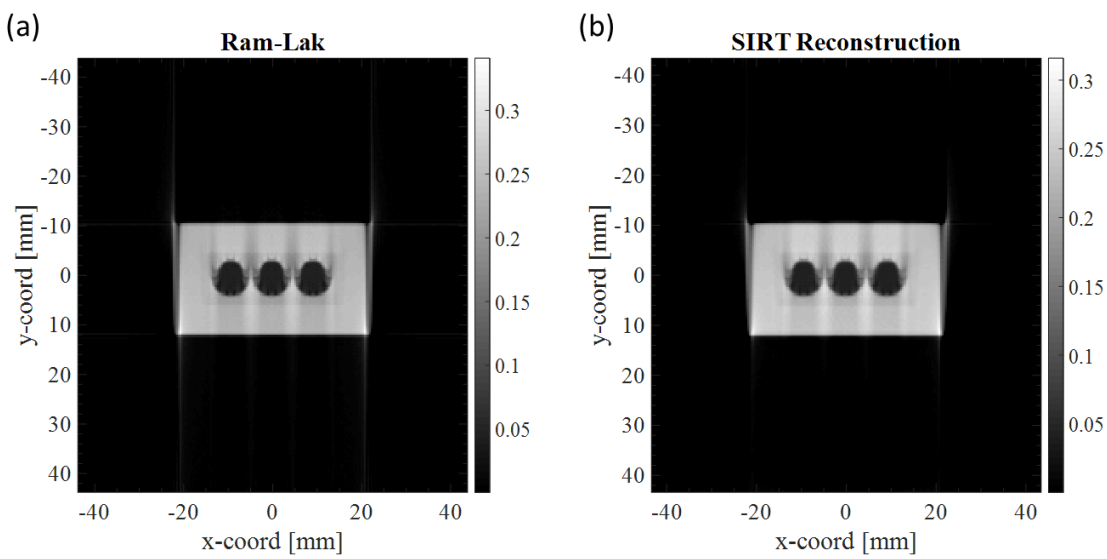

Fig. 4-29: The reconstructed 2-D image of the (a) FBP method; (b) SIRT reconstruction.

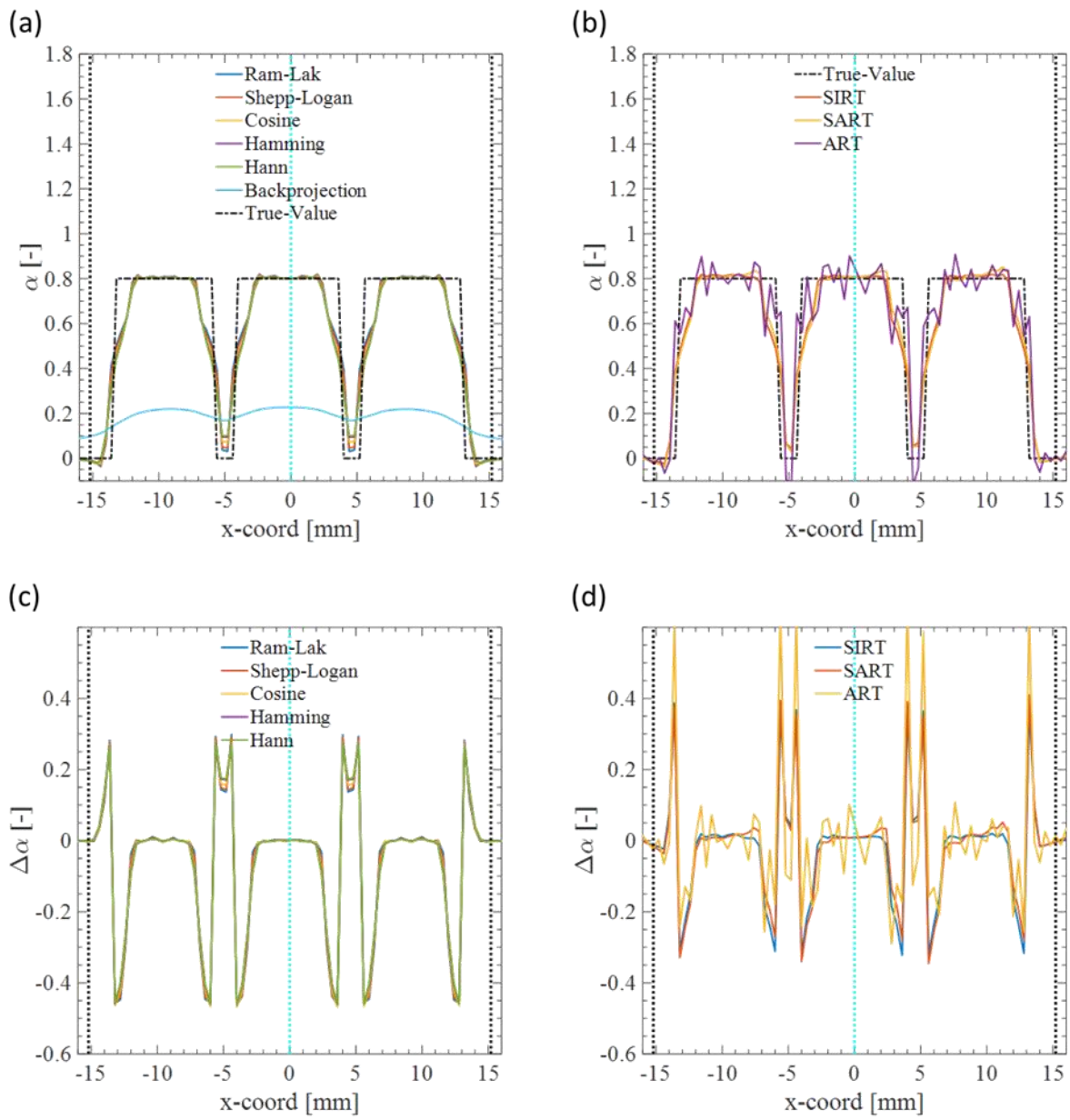

Fig. 4-30: Void fraction profile of the centerline x-axis of the (a) FBP method; (b) algebraic iteration methods. The void fraction difference, $\Delta\alpha$, of the centerline x-axis of the (c) FBP reconstruction; (d) algebraic iteration-based method.

Table 14: List of the absolute void error and area-averaged quantity error due to the off-center shift effect.

	Absolute void error (FBP)	Absolute void error (SIRT)	Area-averaged error (FBP) [%]	Area-averaged error (SIRT) [%]
Shift effect	0.037	0.041	-3.71	4.64

4.4.5 Different void profiles

In this study, different types of synthetic void profiles are benchmarked with the reconstruction algorithm. A total of four cases are reviewed and listed in Fig. *4-32*, these profiles are:

1. Single bubble column which resembles an annular flow,
2. An ellipsoid profile which can describe the slug flow like characteristic,
3. Uniform void fraction in the test-section,
4. The Gaussian profile, which might occur in bubbly flow.

In the reconstruction process, the clean functions are generated, which projection data contains no background noise or alignment shift. The synthetic image is generated in the resolution of 216 by 216 voxels The 0.4mm pixel size samples the reconstructed attenuation profiles, a total of 180 projections are imaged in the simulation, and minimum constraint is applied and set the negative attenuation coefficient to zero value. Equation (4.50) determines the local void fraction distribution of each synthetic bubble, which is shown in Fig. *4-32*. With the clean function, all techniques are performed reasonable and able to capture the characteristics of each synthetic bubble void distribution. However, in case of sharp void change near the bubble edge, the FBP tends to show an underestimating void fraction where iteration based methods are overestimating the void fraction value of the single bubble column case. Fig. *4-33* illustrates the void fraction difference, $\Delta\alpha$, for each reconstructed void profile. Overall, the FBP method shows the best result when considering the void fraction reconstruction. However, in the case of the Gaussian's function, the SIRT method shows the lowest absolute void error and area-averaged error. These results are listed in Table *15*.

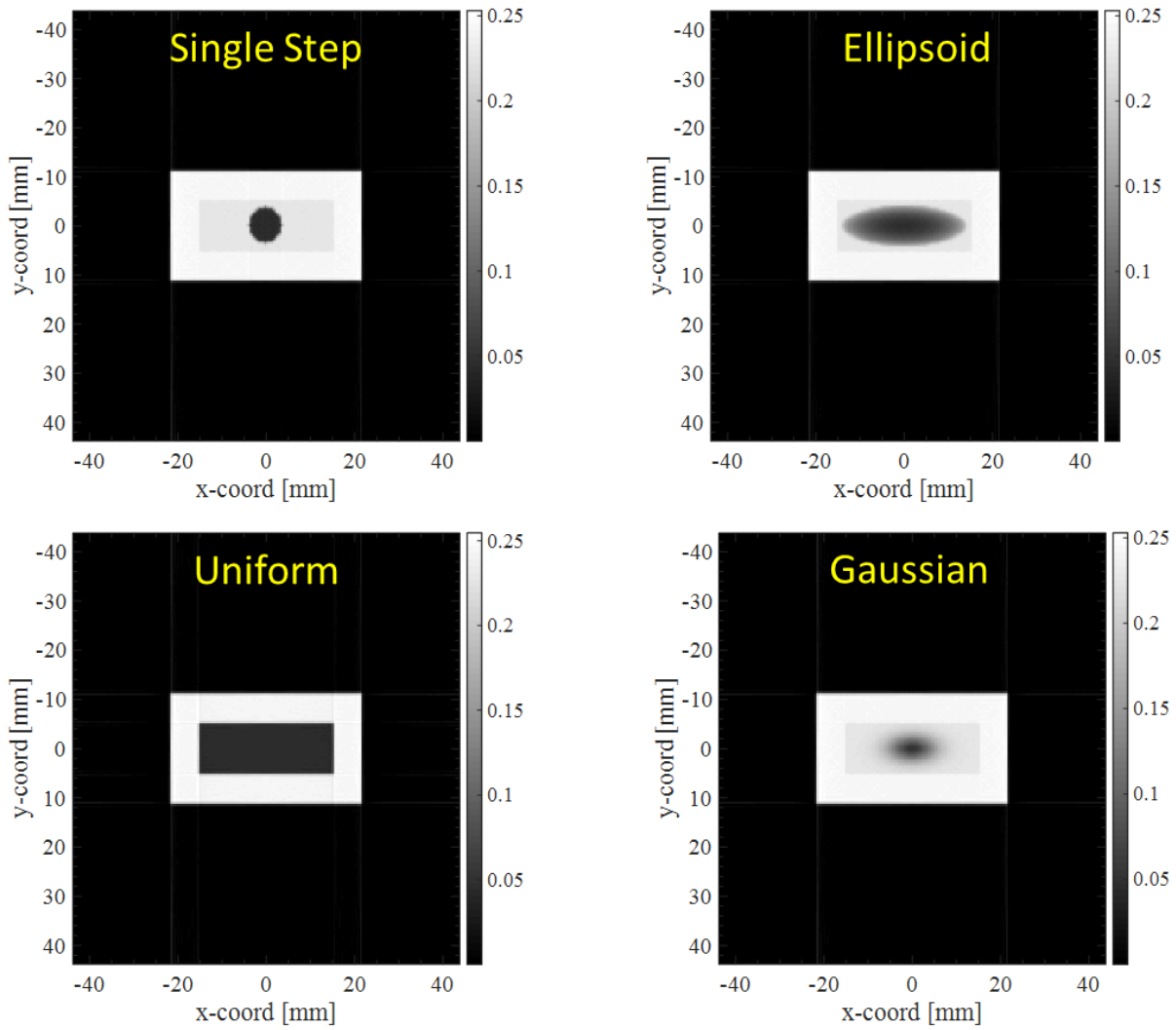

Fig. 4-31: The reconstructed 2-D image of the attenuation coefficient.

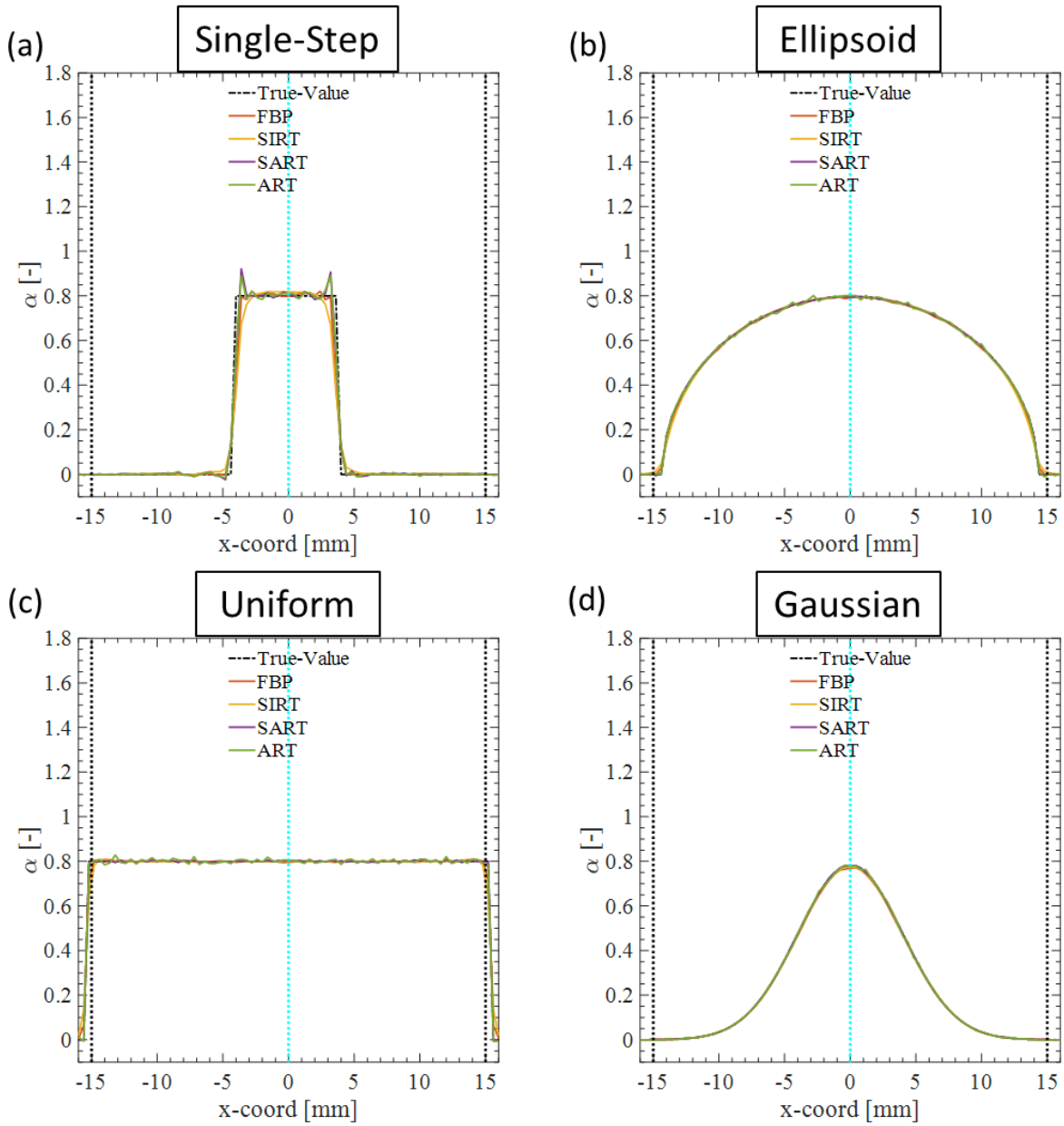

Fig. 4-32: Reconstructed void profile of the centerline x-axis, (a) Single-step; (b) Ellipsoid; (c) Uniform; (d) Gaussian distribution.

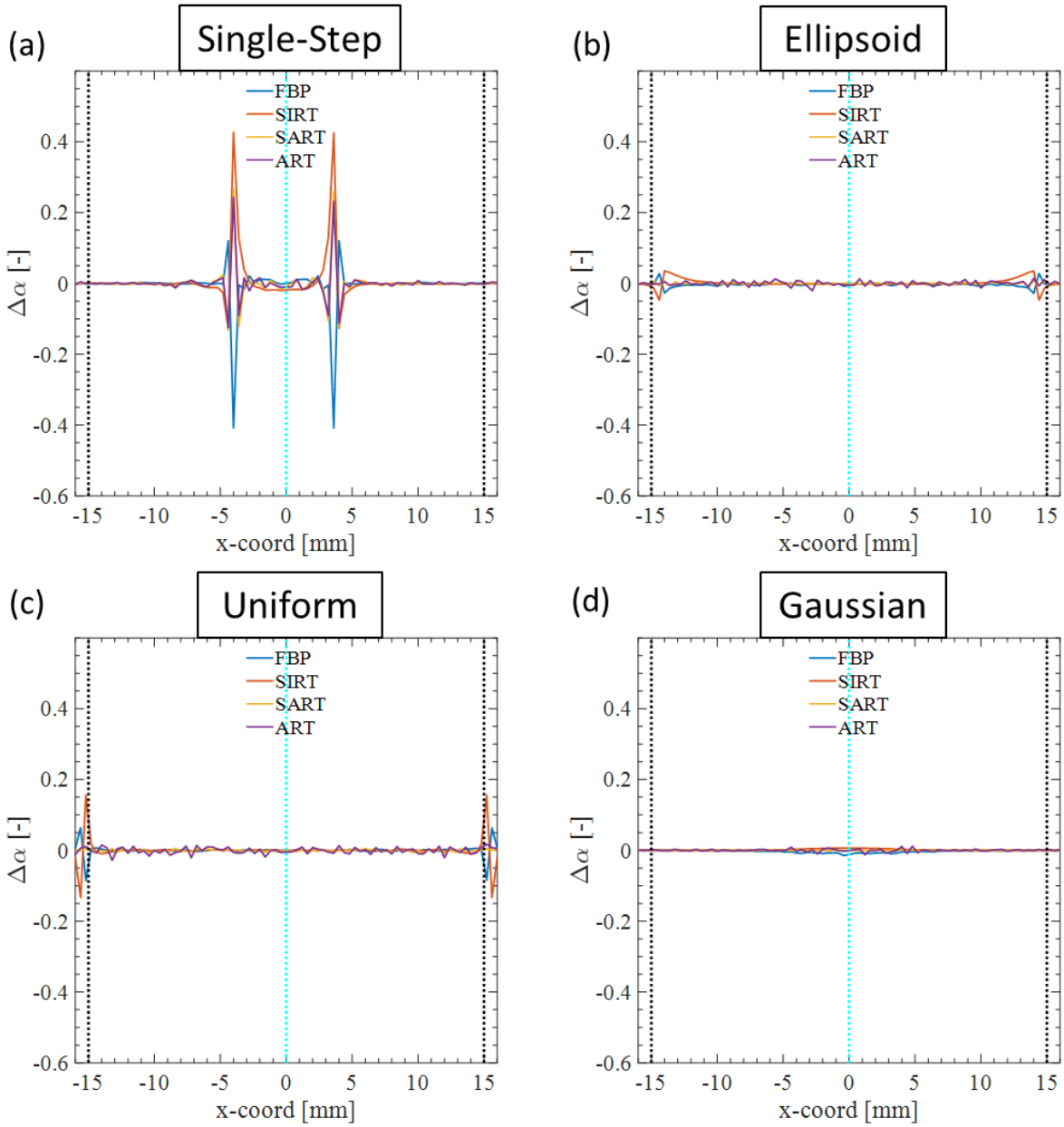

Fig. 4-33: Void fraction difference, $\Delta\alpha$, of the centerline x-axis, (a) Single-step; (b) Ellipsoid; (c) Uniform; (d) Gaussian distribution.

Table 15: List of the absolute void error and area-averaged quantity error of the different synthetic bubble void profile.

	Absolute void error (FBP)	Absolute void error (SIRT)	Area-averaged error (FBP) [%]	Area-averaged error (SIRT) [%]
Single Step	0.0006	0.0016	0.63	1.51
Ellipsoid	0.0001	0.0012	0.04	0.40
Uniform	0.0150	0.0162	-1.88	-2.02
Gaussian	0.0001	5.5e-4	-0.12	-0.03

4.5 Experimental Result

The x-ray system is installed on the high-precision turntable (slewing ring), the turntable is driven manually but controlled by a high precision pointer. First, measurements are performed at each five-degree increment to cover a 180-degree half-circle. The time and line-averaged detector signals are acquired at each angular location. In the sinogram data set, the angular projections are interpolated to every one degree to obtain a total of 180 angular projection data set. This angular interpolation of the projection data set is implemented in each of the phantom measurements and the two-phase flow experiment.

4.5.1 Phantom geometry test

A rectangular phantom with simulated bubble columns are measured for the material distribution in the flow field. The phantom is composed of the rectangular acrylic channel, which has an inner dimension of 10mm by 30mm and a 6.35mm thick wall. Three acrylic rods are installed in the flow region. Two outer rods have a diameter of 6.4mm, and the center rod has 3.2mm in diameter. Three configurations are measured:

1. The empty rectangular channel,
2. Rectangular channel with the two 6.4mm acrylic rods installed in the flow field, and
3. Rectangular channel with the two-6.4mm and one-3.2mm acrylic rods.

The reconstructed 2-D images are shown in Fig. *4-34*, Fig. *4-35*, and Fig. *4-36* for an empty channel, two acrylic-rods, and three acrylic-rods, respectively.

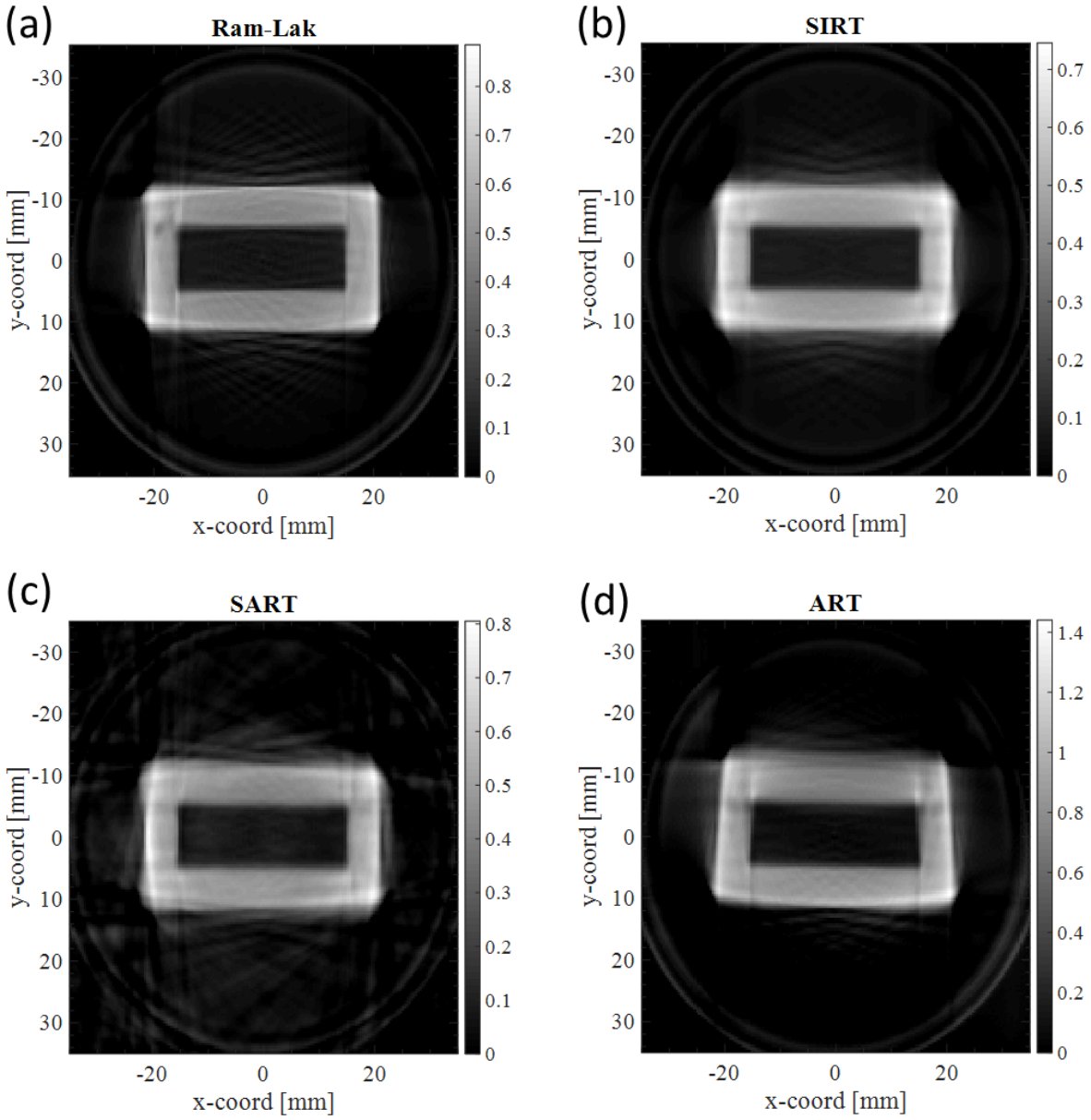

Fig. 4-34: The reconstructed 2-D image of a phantom geometry.

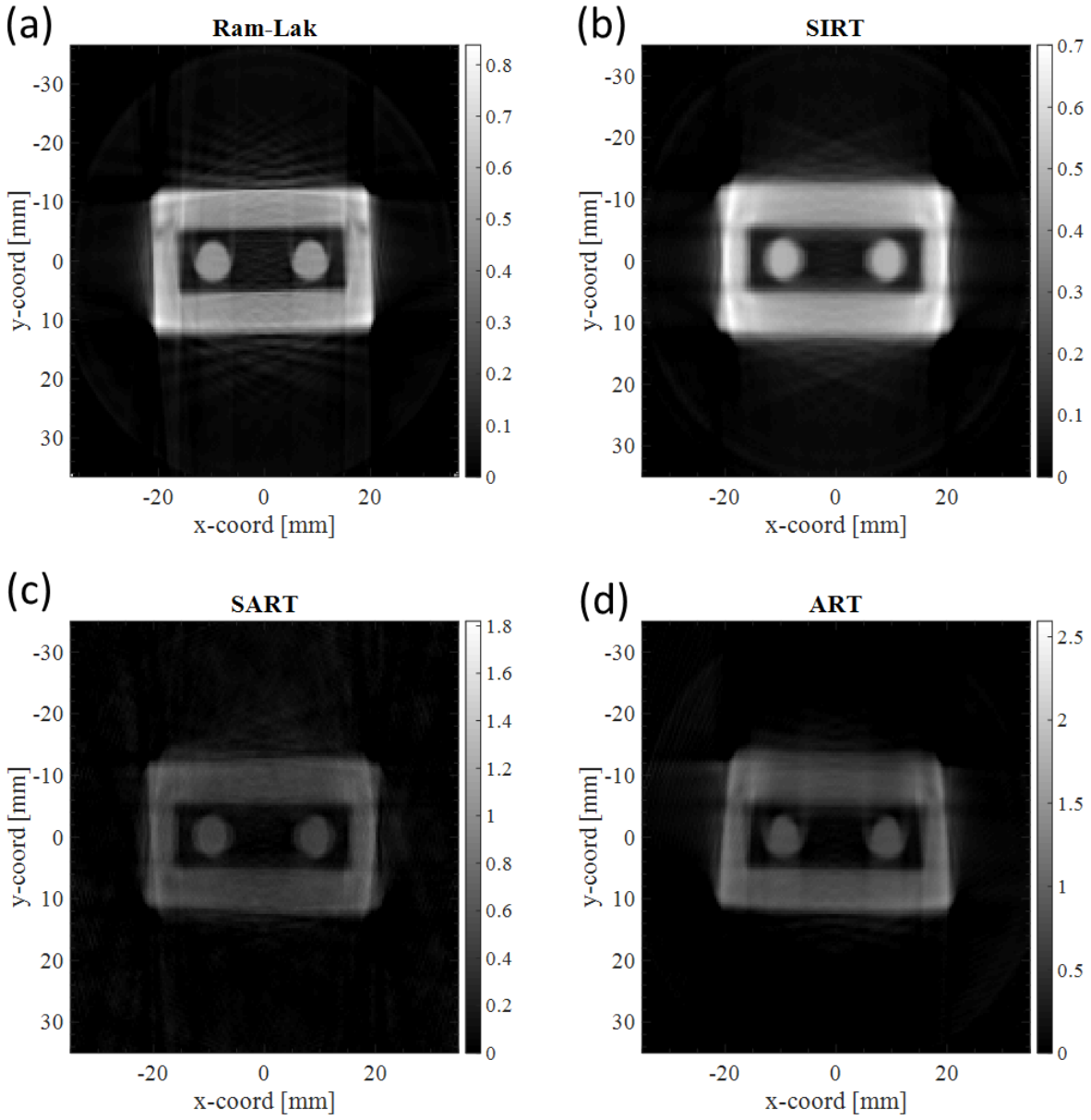

Fig. 4-35: The reconstructed 2-D image of a phantom with a two 6.3mm cylindrical rod.

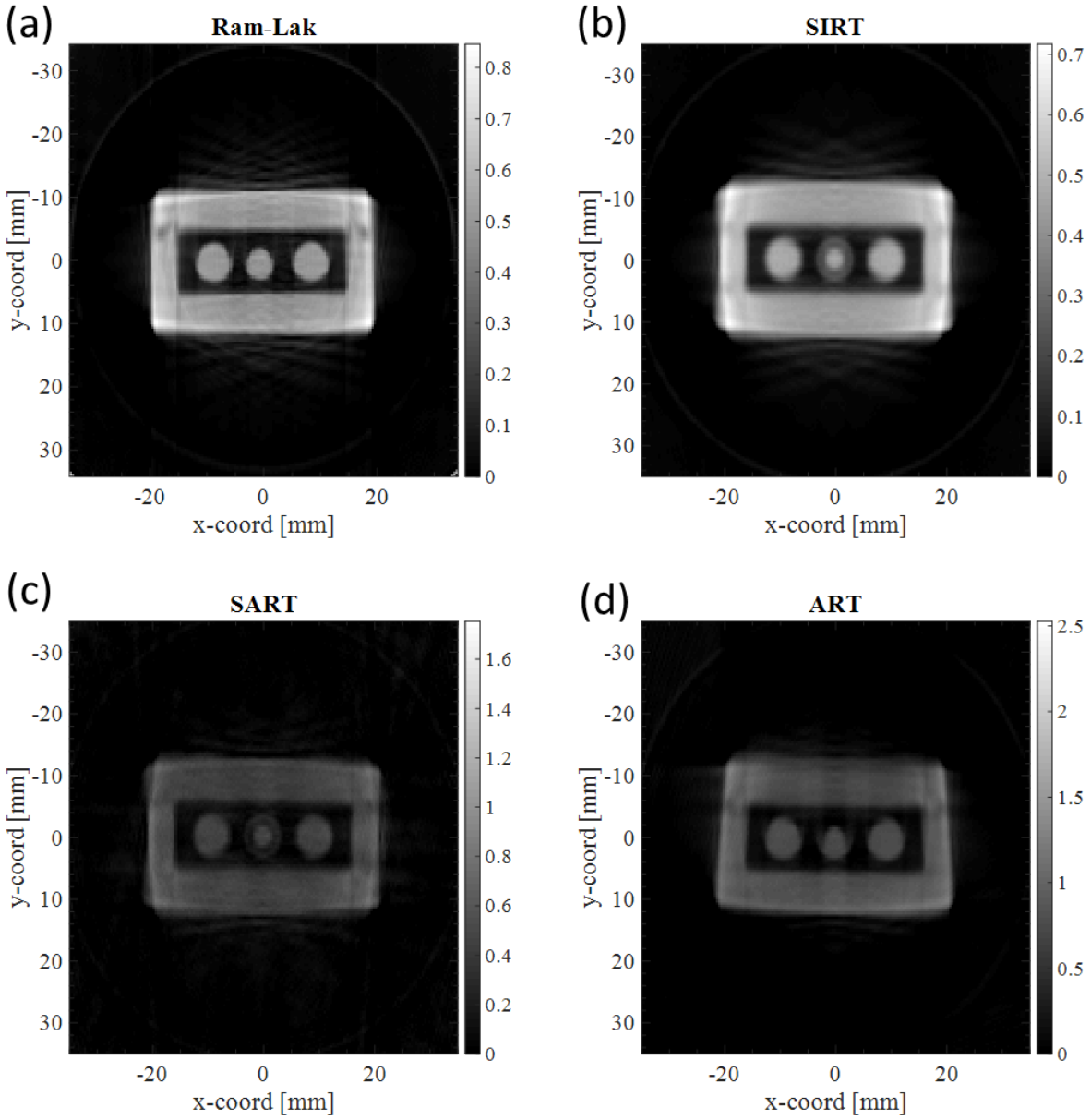

Fig. 4-36: The reconstructed 2-D image of a phantom with a two-6.3mm and one-3.2mm cylindrical rod.

Fig. *4-37* shows the centerline x-ray attenuation profile of the rectangular channel with three acrylic cylindrical rods placed inside of the test section. It is shown in Fig. *4-37*, the FBP and SIRT methods achieved the most reasonable attenuation distribution of the centerline profile, in which attenuation distribution of three acrylic rods are consistently distributed on the actual

location of where acrylic rods are installed. In the SART reconstruction, the centerline distribution is similar to the FBP and SIRT method. However, SART reconstruction lacks a smooth transition between the cylinder rods. In the ART iteration method, reconstruction never fully converged; therefore, the centerline profile is not shown in the figure.

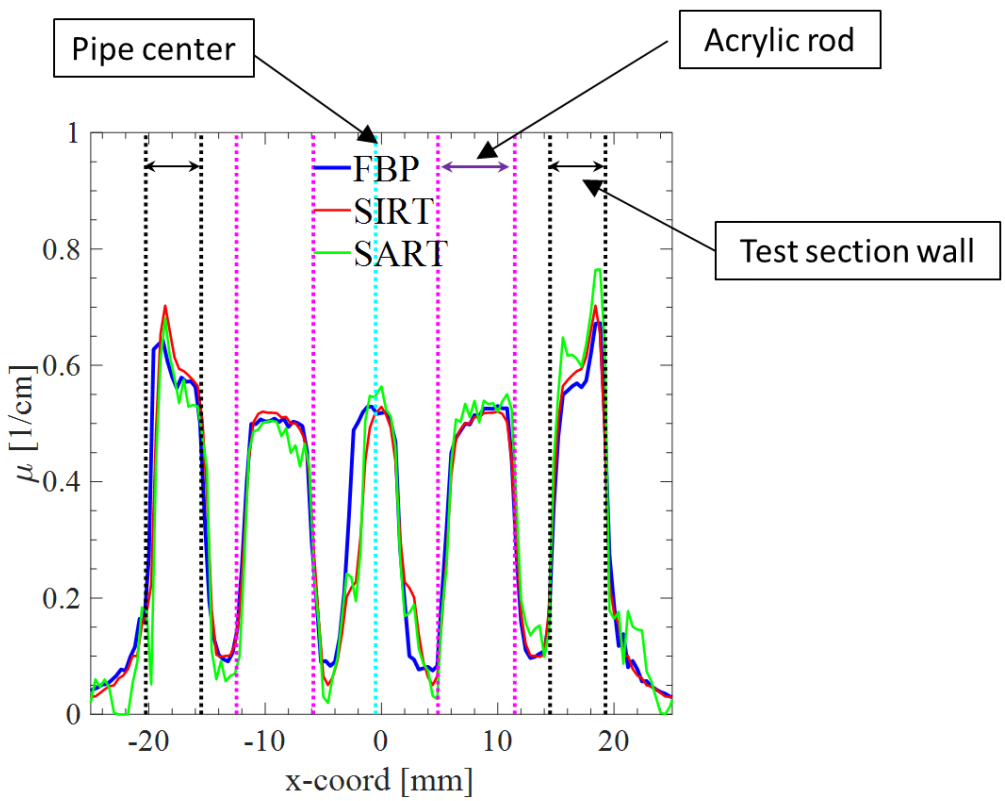

Fig. 4-37: The attenuation profile of the phantom with three acrylic cylindrical rods.

4.5.2 Two-phase flow experiment

Two-phase flow measurement is performed using the tomography system setting described in the experimental setup. A total of four flow conditions are presented, and the flow rate for each condition is listed in Table *16*. These superficial gas and liquid velocities are determined based on the inlet gas and water flow rates. At each angular location, voltage signals are recorded by every detector pixel for a total of 60 seconds at 1000 fps, which results in 60,000 samples for every pixel used for the measurement. This process is repeated for every angular projection where x-ray

images are taken every 5 degrees around a 180-degree. Thus a total of 36 projections are measured. Here, angular projections are interpolated every 1-degree angle and mapping the total of 180 projections data set. These measured values are computed to projection function $\bar{p}$ by Eq.(4.9) which is the ratio of the initial x-ray energy before projected at a given point in the two-phase flow object to the x-ray energy after the penetration through the test object.

These processes are repeated for the water and air reference data. From the two-phase flow experiment, the 2-D attenuation distribution of each reference data is accomplished by the FBP or algebraic iteration variations. Finally, the use of Eq.(4.50), one can obtain the local void fraction values from the reconstructed image.

The reconstructed attenuation coefficient distribution of the water, air, and two-phase flow data are shown in Fig. *4-38*(a). In the illustration, it is noted that the reconstructed air attenuation profile has a significant attenuation coefficient value of the reference flow region when the polychromatic x-ray source obtains projection data; thus, zero attenuation assumption of the air is not valid in this experiment. Therefore, the use of Eq.(4.50) may result in significant measurement uncertainty. It is shown in Fig. *4-38*(b), there is a significant void fraction difference in the void fraction formulation when considering the zero attenuation assumption of the air reference data. Here, it is shown in Fig. *4-38*(b), the real difference between the void fraction values formulated by Eq.(4.50) and (4.49) is 15% or higher in the center peak region. Based on the reconstructed attenuation profile, one can conclude that the air reference data must be implemented in the void fraction formulation if projection has resulted from the polychromatic x-ray source; thus, Eq.(4-49) is used for void fraction formulation.

Fig. *4-39* shows the reconstructed void fraction profile of the bubbly and slug flow listed in Table *16*. In Fig. *4-39*(a) and (b), among all variations, the ART fails to converge in the bubbly flow reconstruction where FBP, SART, and SIRT are capable of reconstructing the reasonable void fraction profile. In Fig. *4-39*(c) and (d), the slug flow indicates a center peaked reconstructed void profile, which is commonly seen in the literature. The reconstructed 2-D image of two-phase flows is shown in *Fig. 4-40*, the reconstruction image of each flow condition in this figure illustrates useful qualitative time-averaged void fraction distribution of each flow condition. In the following section, these reconstructed values are inter-compared to the DP transducer measurement and the Spectral model for void fraction benchmarking.

Table 16: Flow condition

	Flow Type	j_g [m/s]	j_f [m/s]
1	Bubbly	0.033	0.463
2	Bubbly	0.060	0.463
3	Slug	0.190	0.042
4	Slug	0.284	0.084

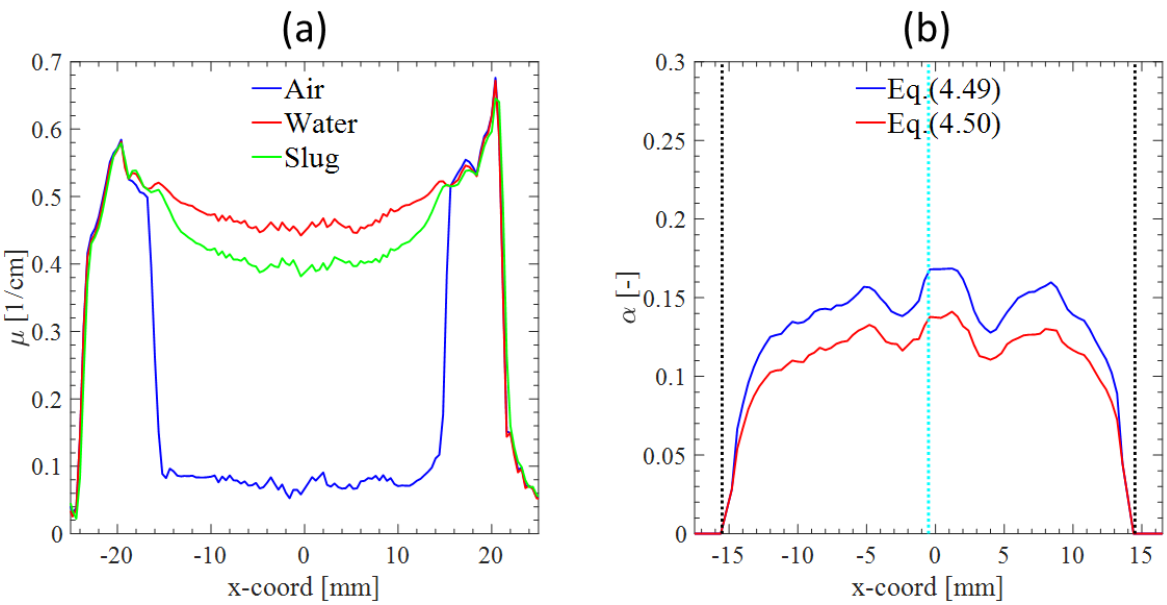

Fig. 4-38: (a) Attenuation profile of the three reference data of the centerline x-axis; (b) Illustration of measurement uncertainty if air reference data is neglected in void fraction formulation.

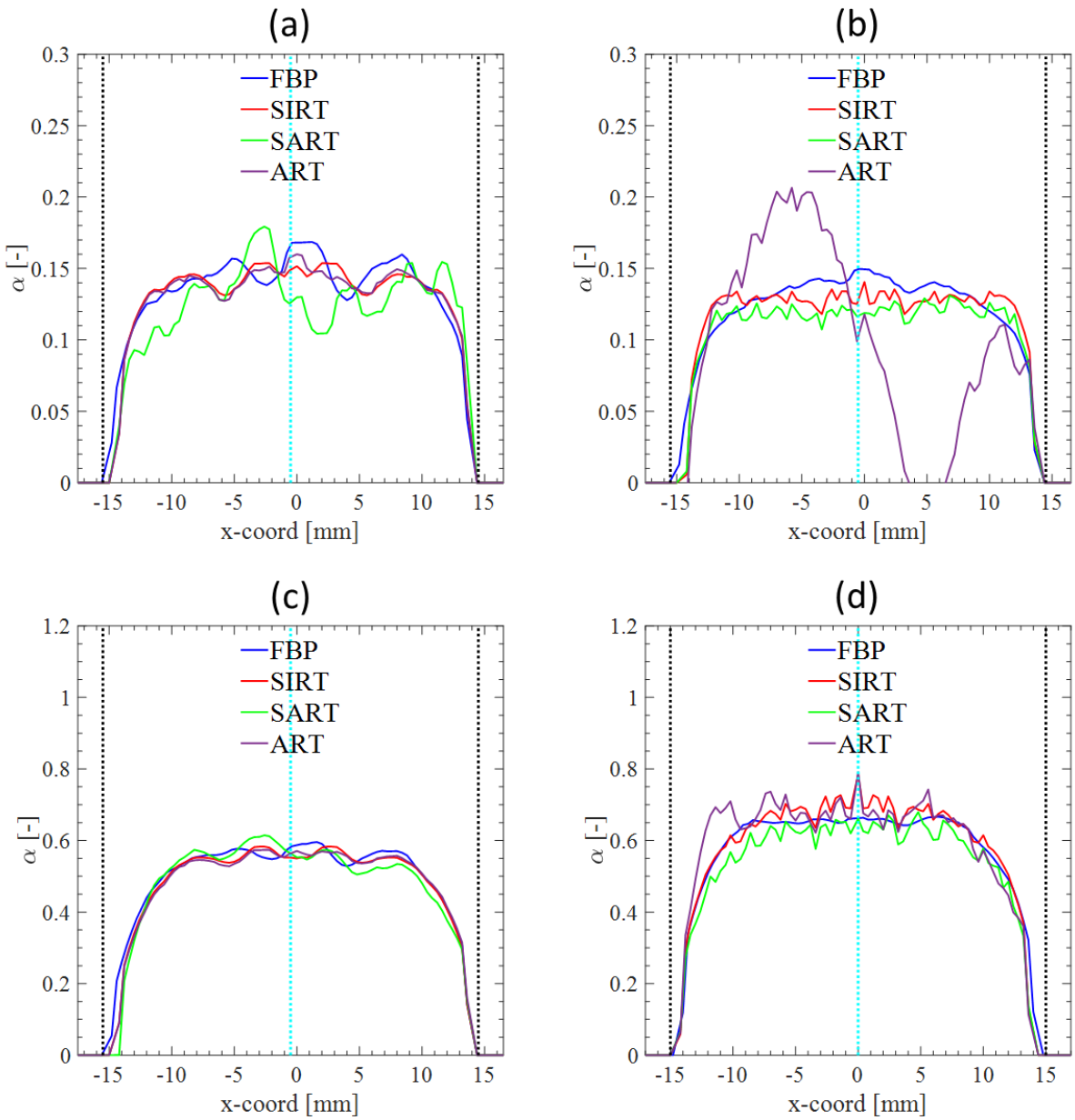

Fig. 4-39: The reconstructed void fraction distribution of each flow condition listed in Table 16. (a) Bubbly flow, j_g=0.033m/s, j_f=0.463m/s; (b) Bubbly flow, j_g=0.060m/s, j_f=0.463m/s; (c) Slug flow, j_g=0.190m/s, j_f=0.042m/s; (d) Slug flow, j_g=0.284m/s, j_f=0.084m/s;

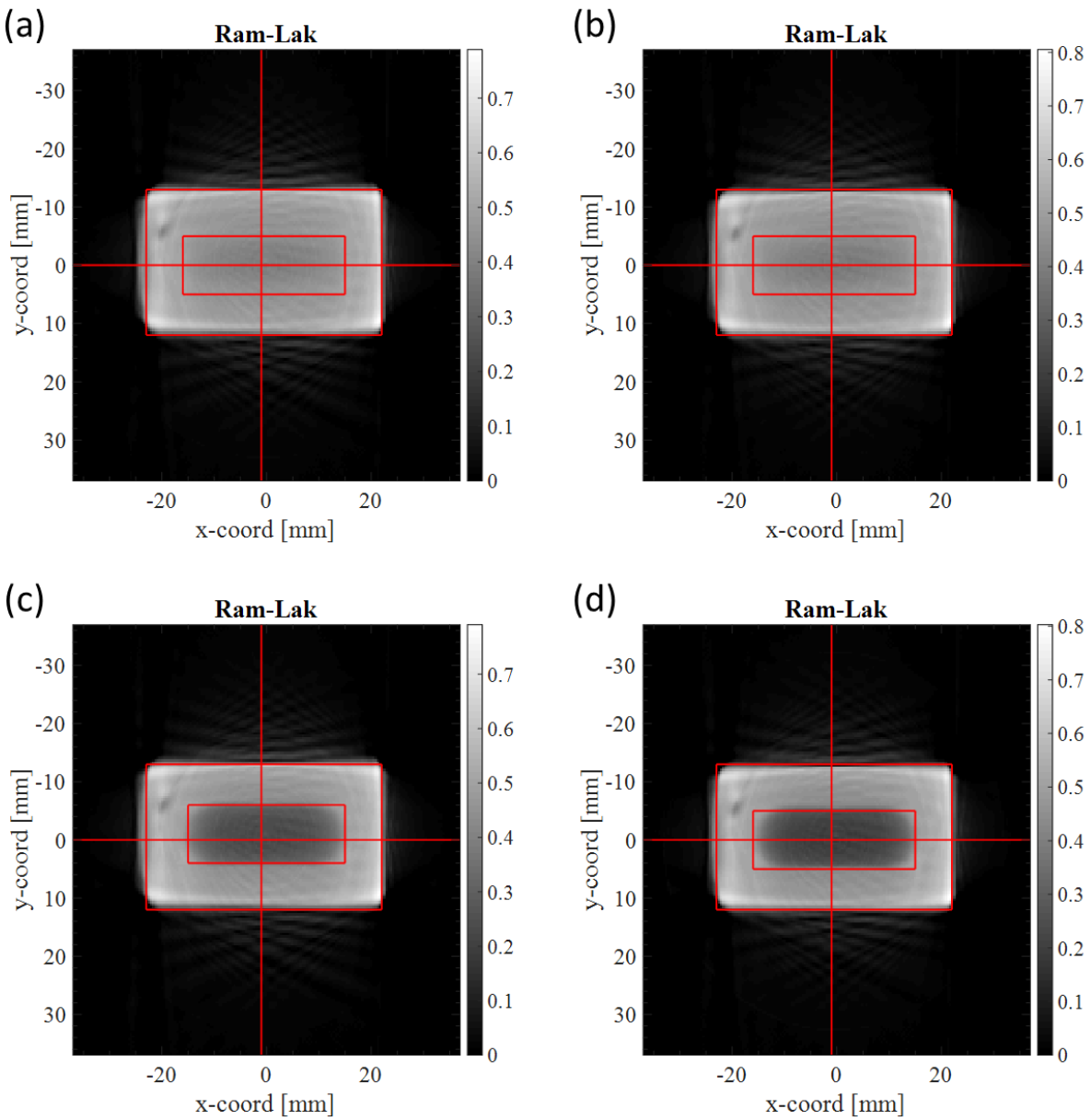

Fig. 4-40: The reconstructed 2-D void fraction image of each flow condition listed in Table 16. (a) Bubbly flow, j_g=0.033m/s, j_f=0.463m/s; (b) Bubbly flow, j_g=0.060m/s, j_f=0.463m/s; (c) Slug flow, j_g=0.190m/s, j_f=0.042m/s; (d) Slug flow, j_g=0.284m/s, j_f=0.084m/s;

4.5.3 DP transducer and Spectral model benchmark

In Fig. *4-41*, the time and line-averaged void fraction along the detector pixel are presented for all four flow conditions. This time and line averaged information is the measured value at a 0-

degree angular projection. The averaging the instantaneous void fraction from the total of 60,000 voltage samples determines all four flow conditions. Equation Eq.(2.15) determines the time-averaged void fraction $\bar{\alpha}_i$ for the i_{th} pixel. Near the wall, the void fraction is assumed to be zero. Zero void fraction behavior near the wall boundary can be visualized by another measuring method, such as high-speed imaging technique [51]. For the void fraction profile near the wall boundary, a total of three pixels in each end is replaced by the linear fitting where the void fraction is linearly interpolated from the pipe wall to the three pixels away from the pipe wall.

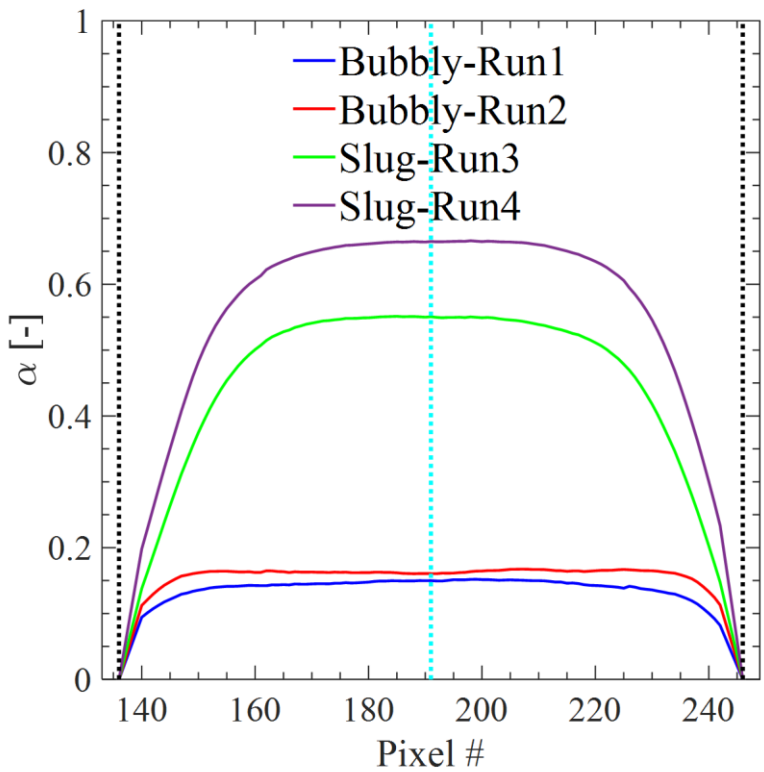

Fig. 4-41: The time and line-averaged void fraction distribution along the detector pixel determined by the Spectral model.

The cross-sectional area-averaged void fraction of the rectangular test section is calculated in the following equation:

$$\langle \alpha \rangle = \frac{1}{A_{pipe}} \sum \bar{\alpha}_n A_n \tag{4.54}$$

Here, a variable $\bar{\alpha}_n$ is the measured void fraction by each detector pixel, the variable A_n is the scanned x-ray pixel area (*SPA*) of the flow region measured by n_{th} detector pixel, and A_{pipe} is the cross-sectional area of the rectangular test section.

The relative error of the area-averaged quantities measured by different techniques is listed in Table *17*. The table shows the relative error of the area-averaged void fraction by the spectral model, which is -1.4% and 1.8% for the Run3 and Run4, respectively. When considering the area-averaged void fraction, the spectral model indicates the lowest error when compared with the differential pressure (DP) transducer measurement. The improved accuracy of the spectral model is expected since it accounts for the beam hardening effect and predicts the detector response for given void fraction values.

Table 17: Void fraction error of the area-averaged quantity measured by different measurement techniques.

	Flow Type	$<\alpha>$ by DP	$<\alpha>$ by 2-D x-ray	$<\alpha>$ Error	$<\alpha>$ by Spectral Model	$<\alpha>$ Error
Run1	Bubbly	0.066	0.080	0.014	0.120	0.054
Run2	Bubbly	0.106	0.070	-0.036	0.139	-0.073
Run3	Slug	0.409	0.390	-0.019	0.403	-0.006
Run4	Slug	0.491	0.450	-0.041	0.500	0.009

4.6 Summary

In this chapter, 2-D CAT algorithms are applied to two-phase flow imaging. A comprehensive sensitivity study using a synthetic bubble is performed to quantify the uncertainty in void fraction measurement. The reconstructed 2-D void fraction image shows significant uncertainty when projection data is influenced by each uncertainty factor addressed in the sensitivity study. From the sensitivity study, one can make a suitable choice of the reconstruction algorithm when considering the following uncertainty factors including but not limited to: the

background noise, instrumentation uncertainty, limited number of projections, speed of reconstruction algorithm, and computational cost.

Laboratory experiments have been performed using a phantom simulating the rectangular channel with "acrylic bubbles." A total of 36 angular projections (every 5-degree increment) are measured and interpolated to every one-degree angle. The FBP and different iteration based algorithms are performed to reconstruct the object domain. Due to the polychromatic source, the result of the reconstructed image shows the non-uniform attenuation distribution of the test section geometry. Two-phase flow experiment has been performed with the rectangular test section, in each projection angle, data was taken for 60 seconds with a frame rate of 1000Hz; thus, 60000 samples were measured for each angular measurement. Local void fraction distribution is obtained by the reconstructed 2-D attenuation distribution from the three reference data of the test section filled with single-phase water, air, and two-phase flow, respectively. It is noted that air attenuation coefficient data must be implemented in the void fraction formulation. From the DP transducer measurement and spectral model estimation, the uncertainty of area-averaged void fraction values is estimated. From the DP measurement, bubbly flow uncertainty is 21.3% and -33.7% for Run 1 and Run 2, respectively. From the slug flow experiment, uncertainty is -4.6% and -8.3% for Run 3 and Run 4, respectively.

5. Conclusion and Recommendations

This dissertation presents a comprehensive set of models and algorithms concerning the x-ray technique as applied to two-phase flow measurement. The developed spectral model is the fundamental tool for processing the recorded voltage information and obtain the line-averaged void fraction value. An accurate pixel to radial conversion algorithm is established with the newly developed area-based onion-peeling (ABOP) method. A series of synthetic bubble sensitivity study is performed to evaluate the robustness of the proposed algorithm. The 2-D reconstruction algorithms are investigated for suitability in the two-phase flow application, primarily void fraction measurement in the non-axisymmetric two-phase flow systems. The FBP and algebraic iteration-based methods are considered for measurement in a rectangular test section. The conclusions and recommendations are summarized as follows:

1. The spectral model is a prediction model developed for void fraction estimation in two-phase flow measurement when using the polychromatic x-ray source. The algorithm is to account for the beam-hardening effect done by the test-section and two-phase flows to predict the detector response for given void fraction values. A calibration test is performed to determine the photon to electron conversion factor, which depends on photon energy and plays a vital role in predicting the detector response. The proposed method is capable of measuring various flow conditions with a wide void fraction range.
2. The area-based onion-peeling (ABOP) method is a conversion algorithm designed for obtaining radial distributions from the line-averaged pixel measurements. The proposed algorithm is capable of converting two-phase flow parameters, such as void fraction and gas velocity of axisymmetric flow systems.
3. Uncertainty of the ABOP depends on the pixel resolution, background noise in data, the actual location of the test-section, and mesh size. The mesh size and spatial resolution should be optimized to yield good conversion accuracy. Synthetic bubble study indicated that the algorithm must implement the actual center-location of the test-section, this is one of the most sensitive factors which impacts the local area information of the partition sector associated with the radial void fraction parameter.

4. Three bubbly flows, two slug flows, and one churn-annular flow in a 25.4 mm pipe are measured with various superficial liquid and gas velocities. The radial distributions of two-phase flow parameters are presented using the ABOP conversion algorithm. The acquired data and converted parameters include void fraction, gas velocity, area-averaged void fraction, and superficial gas velocity. The lift force effect is observed in the bubbly flow experiment, which formed a wall peak void profile.
5. The modified fan-beam onion peeling (FBOP) method is provided, which converts the fan-beam measurement to a radial distribution without the rebinning process. The FBOP will provide useful information to the existing Abel or onion-peeling methods.
6. The existing 2-D tomography algorithms are reviewed for non-axisymmetric two-phase flow systems. The 2-D flow image can be reconstructed by an analytical or algebraic iteration based algorithm. Among all variations, the FBP method is the most promising method when considering the void fraction measurement due to its simplicity in implementation and high efficiency.
7. More researches can be performed in the future on the 2-D absorption tomography problem. By utilizing a non-axisymmetric onion-peeling method, the local void fraction distribution may be extracted from a single projection data set. The details of this method remain for future study.

References

[1] Oberkampf, W. L., and Smith, B., 2014, "Assessment Criteria for Computational Fluid Dynamics Validation Benchmark Experiments," (January), pp. 1–27.

[2] Smith, B. L., 2017, "The difference between traditional experiments and CFD validation benchmark experiments," Nucl. Eng. Des., **312**, pp. 42–47.

[3] Kim, S., Fu, X. Y., Wang, X., and Ishii, M., 2000, "Development of the miniaturized four-sensor conductivity probe and the signal processing scheme," **43**, pp. 4101–4118.

[4] Liu, Y., Yang, X., Zhu, Q., Ju, P., Ishii, M., and Buchanan, J. R., 2017, "Development of the droplet-capable conductivity probe for measurement of liquid-dispersed two-phase flow," Int. J. Multiph. Flow, **88**, pp. 238–250.

[5] Manera, A., Ozar, B., Paranjape, S., Ishii, M., and Prasser, H. M., 2009, "Comparison between wire-mesh sensors and conductive needle-probes for measurements of two-phase flow parameters," Nucl. Eng. Des., **239**(9), pp. 1718–1724.

[6] Bowden, R. C., Lessard, É., and Yang, S. K., 2018, "Void fraction measurements of bubbly flow in a horizontal 90° bend using wire mesh sensors," Int. J. Multiph. Flow, **99**, pp. 30–47.

[7] Prasser, H. M., Misawa, M., and Tiseanu, I., 2005, "Comparison between wire-mesh sensor and ultra-fast X-ray tomograph for an air-water flow in a vertical pipe," Flow Meas. Instrum., **16**(2–3), pp. 73–83.

[8] Roghair, I., Martínez, J., Sint, M. Van, and Kuipers, H., 2011, "International Journal of Multiphase Flow Energy spectra and bubble velocity distributions in pseudo-turbulence : Numerical simulations vs . experiments," Int. J. Multiph. Flow, **37**(9), pp. 1093–1098.

[9] Zhang, L., and Wu, X., 2006, "On the application of cross correlation function to subsample discrete time delay estimation," Digit. Signal Process., **16**, pp. 682–694.

[10] Talley, J. D., Worosz, T., and Kim, S., 2013, "Characterization of horizontal air-water two-phase flow in a round pipe part II: Measurement of local two-phase parameters in bubbly flow," Int. J. Multiph. Flow, **76**, pp. 223–236.

[11] Le Corre, J. M., Hervieu, E., Ishii, M., and Delhaye, J. M., 2003, "Benchmarking and improvements of measurement techniques for local-time-averaged two-phase flow parameters," Exp. Fluids, **35**(5), pp. 448–458.

[12] Anuar Mohd Salleh, K., Koo Lee, H., and Al-Dahhan, M. H., 2015, "Studying local liquid velocity in liquid-solid packed bed using the newly developed X-ray DIR technique," Flow Meas. Instrum., **42**, pp. 1–5.

[13] Wang, D., Song, K., and Fu, Y., "Integration of conductivity probe with optical and x-ray imaging systems for local air – water two-phase flow measurement."

[14] Wang, D., Liu, Y., and Talley, J. D., 2018, "International Journal of Multiphase Flow Numerical evaluation of the uncertainty of double-sensor conductivity probe for bubbly flow measurement," Int. J. Multiph. Flow, **107**, pp. 51–66.

[15] Warsito, W., and Fan, L., 2001, "Measurement of real-time ow structures in gas – liquid and gas – liquid – solid ow systems using electrical capacitance tomography (ECT)," **56**, pp. 6455–6462.

[16] Suard, E., Clément, R., Fayolle, Y., Alliet, M., Albasi, C., and Gillot, S., 2019, "Electrical resistivity tomography used to characterize bubble distribution in complex aerated reactors : Development of the method and application to a semi-industrial MBR in operation," Chem. Eng. J., **355**(August 2018), pp. 498–509.

[17] Fu, Y., and Liu, Y., 2016, "Development of a robust image processing technique for bubbly flow measurement in a narrow rectangular channel," Int. J. Multiph. Flow, **84**, pp. 217–228.

[18] Xin, S., and Wang, H. X., 2017, "Gamma-ray CT from incomplete projections for two-phase pipe flow," Rev. Sci. Instrum., **88**(2), p. 025106.

[19] Bieberle, A., Hoppe, D., Schleicher, E., and Hampel, U., 2011, "Void measurement using high-resolution gamma-ray computed tomography," Nucl. Eng. Des., **241**(6), pp. 2086–2092.

[20] Kendoush, A. A., 1992, "A comparative study of the various nuclear radiations used for void fraction measurements," Nucl. Eng. Des., **137**(2), pp. 249–257.

[21] Banowski, M., Hampel, U., Krepper, E., Beyer, M., and Lucas, D., 2018, "Experimental investigation of two-phase pipe flow with ultrafast X-ray tomography and comparison with state-of-the-art CFD simulations," Nucl. Eng. Des., **336**, pp. 90–104.

[22] A.C. Kak, M. S., 1988, Principles of Computerised Tomographic Imaging, IEEE Press, New York.

[23] Khashehchi, M., and Harun, Z., 2019, "Accuracy of tomographic particle image

velocimetry data on a turbulent round jet," Int. J. Heat Fluid Flow, **77**(March), pp. 61–72.

[24] Hanus, R., Petryka, L., and Zych, M., 2014, "Velocity measurement of the liquid – solid fl ow in a vertical pipeline using gamma-ray absorption and weighted cross-correlation," Flow Meas. Instrum., **40**, pp. 58–63.

[25] Lau, Y. M., Hampel, U., and Schubert, M., 2018, "Ultrafast X-ray tomographic imaging of multiphase flow in bubble columns - Part 1: Image processing and reconstruction comparison," Int. J. Multiph. Flow, **104**, pp. 258–271.

[26] Khan, A. H., and Chaudhuri, R. A., 2014, "Fan-beam geometry based inversion algorithm in computed tomography (CT) for imaging of composite materials," Compos. Struct., **110**(1), pp. 297–304.

[27] Prasser, H. M., Baldauf, D., Fietz, J., Hampel, U., Hoppe, D., Zippe, C., Zschau, J., Christen, M., and Will, G., 2003, "Time resolving gamma-tomography for periodically changing gas fraction fields and its application to an axial pump," Flow Meas. Instrum., **14**(3), pp. 119–125.

[28] Song, K., and Liu, Y., 2018, "A compact x-ray system for two-phase flow measurement," Meas. Sci. Technol., **29**(2).

[29] Schlegel, J., Hibiki, T., and Ishii, M., 2010, "Development of a comprehensive set of drift-flux constitutive models for pipes of various hydraulic diameters," Prog. Nucl. Energy, **52**(7), pp. 666–677.

[30] Stutz, B., and Legoupil, S., 2003, "X-ray measurements within unsteady cavitation," Exp. Fluids, **35**(2), pp. 130–138.

[31] N. N. Clark, R. L. F., 1985, "Predicting the holdup in two-phase bubble upflow and downflow using the Zuber and Findlay drift-flux model," AIChE J., **31**(3), pp. 500–503.

[32] Kennedy, W. M. and R. J., 1956, "Attenuation of 86- and 176-Mev Synchrotron X-Rays in Concrete and Lead," Radiat. Res. Soc., **4**(5), pp. 360–366.

[33] Cierniak, R., ed., 2011, X-Ray Computed Tomography in Biomedical Engineering, Springer London Dordrecht Heidelberg New York.

[34] Boone, J. M., Fewell, T. R., and Jennings, R. J., 1997, "Molybdenum, rhodium, and tungsten anode spectral models using interpolating polynomials with application to mammography.," Med. Phys., **24**(12), pp. 1863–1874.

[35] Poludniowski, G. G., 2007, "Calculation of x-ray spectra emerging from an x-ray tube.

Part II. X-ray production and filtration in x-ray targets," Med. Phys., **34**(6), p. 2175.

[36] Inoue, A., 1995, "Void fraction distribution in BWR fuel assembly and evaluation of subchannel code," J. Nucl. Sci. Technol., **640**(July), pp. 629–640.

[37] Coutier-Delgosha, O., Stutz, B., Vabre, A., and Legoupil, S., 2007, "Analysis of cavitating flow structure by experimental and numerical investigations," J. Fluid Mech., **578**, p. 171.

[38] Mudde, R. F., 2011, "Bubbles in a Fluidized Bed: A Fast X-Ray Scanner," AIChE J., **57**(10), pp. 2684–2690.

[39] Fischer, F., and Hampel, U., 2015, "Ultra fast electron beam X-ray computed tomography for two-phase flow measurement," Int. J. Therm. Sci., **90**(9), pp. 311–322.

[40] Mäkiharju, S. A., Gabillet, C., Paik, B. G., Chang, N. A., Perlin, M., and Ceccio, S. L., 2013, "Time-resolved two-dimensional X-ray densitometry of a two-phase flow downstream of a ventilated cavity," Exp. Fluids, **54**(7).

[41] Barthel, F., Bieberle, M., Hoppe, D., Banowski, M., and Hampel, U., 2015, "Velocity measurement for two-phase flows based on ultrafast X-ray tomography," Flow Meas. Instrum., **46**, pp. 196–203.

[42] Hori, K., Fujimoto, T., Kawanishi, K., and Nishikawa, H., 2000, "Development of an ultrafast X-ray computed tomography scanner system: Application for measurement of instantaneous void distribution of gas-liquid two-phase flow," Heat Transf. - Asian Res., **29**(3), pp. 155-165*.

[43] Hubers, J. L., Striegel, A. C., Heindel, T. J., Gray, J. N., and Jensen, T. C., 2005, "X-ray computed tomography in large bubble columns," Chem. Eng. Sci., **60**(22), pp. 6124–6133.

[44] Li, W., Batteux, F., Araujo, S., Delpouve, N., Saiter, J. M., Tan, L., and Negahban, M., 2016, "Measurement of Beer-Lambert Attenuation Coefficient and Curing Kinetics Power Order: A Method Based on Rapid-Scan FTIR During Laser Curing on an ATR," Macromol. Symp., **365**(1), pp. 173–179.

[45] Hubbell, J. H., and Seltzer, S. M., 1996, "Tables of X-Ray Mass Attenuation Coefficients and Mass Energy-Absorption Coefficients from 1 keV to 20 MeV for Elements Z = 1 to 92 and 48 Additional Substances of Dosimetric Interest Title" [Online]. Available: https://www.nist.gov/pml/x-ray-mass-attenuation-coefficients.

[46] Boone, J. M., and Seibert, J. a, 1997, "An accurate method for computer-generating tungsten anode x-ray spectra from 30 to 140 kV," Med Phys, **24**(11), pp. 1661–1670.

[47] Poludniowski, G., Landry, G., DeBlois, F., Evans, P. M., and Verhaegen, F., 2009, "SpekCalc: a program to calculate photon spectra from tungsten anode x-ray tubes.," Phys. Med. Biol., **54**(19), pp. N433–N438.

[48] Nikl, M., 2006, "Scintillation detectors for x-rays," Meas. Sci. Technol., **17**(4), pp. R37–R54.

[49] Ludwig, G. W., 1971, "X-Ray Efficiency of Powder Phosphors," J. Electrochem. Soc., **118**(7), p. 1152.

[50] Liu, Y., Roy, T., Lee, D. Y., Ishii, M., and Jr, J. R. B., 2013, "Experimental study of non-uniform inlet conditions and three-dimensional effects of vertical air – water two-phase flow in a narrow rectangular duct," Int. J. Heat Fluid Flow, **39**, pp. 173–186.

[51] Fu, Y., and Liu, Y., 2016, "Experimental study of bubbly flow using image processing techniques," Nucl. Eng. Des., **310**, pp. 570–579.

[52] Salem, K., Tsotsas, E., and Mewes, D., 2005, "Tomographic measurement of breakthrough in a packed bed adsorber," Chem. Eng. Sci., **60**(2), pp. 517–522.

[53] Zeng, G. L., 2012, "A filtered backprojection algorithm with characteristics of the iterative landweber algorithm," Med. Phys., **39**(2), pp. 603–607.

[54] Dasch, C. J., 1992, "One-dimensional tomography: a comparison of Abel, onion-peeling, and filtered backprojection methods," Appl. Opt., **31**(8), p. 1146.

[55] Scarcelli, R., Powell, C. F., Kastengren, A. L., and Matthias, N. S., 2018, "ICEF2012-92137," pp. 1–9.

[56] Kalal, M., and Nugent, K., 1988, "Abel inversion using fast Fourier transforms," Appl. Opt., **27**(10), p. 1956.

[57] Villarreal, R., and Varghese, P. L., 2005, "Frequency-resolved absorption tomography with tunable diode lasers.," Appl. Opt., **44**(31), pp. 6786–6795.

[58] Dribinski, V., Ossadtchi, A., Mandelshtam, V. A., and Reisler, H., 2002, "Reconstruction of Abel-transformable images: The Gaussian basis-set expansion Abel transform method," Rev. Sci. Instrum., **73**(7), p. 2634.

[59] Swantek, A. B., Duke, D. J., Kastengren, A. L., Sovis, N., Powell, C. F., Bartolucci, L., Scarcelli, R., and Waller, T., 2017, "An experimental investigation of gas fuel injection with X-ray radiography," Exp. Therm. Fluid Sci., **87**, pp. 15–29.

[60] Saito, Y., Mishima, K., Tobita, Y., Suzuki, T., Matsubayashi, M., Lim, I. C., and Cha, J.

E., 2005, “Application of high frame-rate neutron radiography to liquid-metal two-phase flow research,” Nucl. Instruments Methods Phys. Res. Sect. A Accel. Spectrometers, Detect. Assoc. Equip., **542**(1–3), pp. 168–174.

[61] Wu, C., Cheng, Y., Liu, M., and Jin, Y., 2008, “Measurement of axisymmetric two-phase flows by an improved X-ray-computed tomography technique,” Ind. Eng. Chem. Res., **47**(6), pp. 2063–2074.

[62] Parasu Veera, U., 2001, “Gamma ray tomography design for the measurement of hold-up profiles in two-phase bubble columns,” Chem. Eng. J., **81**(1–3), pp. 251–260.

[63] Asaki, T. J., Campbell, P. R., Chartrand, R., Powell, C. E., Vixie, K. R., and Wohlberg, B. E., 2006, “Abel inversion using total variation regularization: Applications,” Inverse Probl. Sci. Eng., **14**(8), pp. 873–885.

[64] Hammond, K. C., Diaz-Pacheco, R., Kornbluth, Y., Volpe, F. A., and Wei, Y., 2016, “Onion-peeling inversion of stellarator images,” (1), pp. 1–5.

[65] Manzhos, S., and Loock, H. P., 2003, “Photofragment image analysis using the Onion-Peeling Algorithm,” Comput. Phys. Commun., **154**(1), pp. 76–87.

[66] Liu, C., Xu, L., Cao, Z., and McCann, H., 2014, “Reconstruction of axisymmetric temperature and gas concentration distributions by combining fan-beam TDLAS with onion-peeling deconvolution,” IEEE Trans. Instrum. Meas., **63**(12), pp. 3067–3075.

[67] Schwierz-Iosefzon, T., Notea, A., and Deutsch, M., 2002, “Radiography of nonaxisymmetric objects: An onion-peeling inversion method,” Appl. Phys. Lett., **81**(11), pp. 2121–2123.

[68] Liu, J. N., Wang, B. X., Cui, Y. Y., and Wang, H. Y., 2015, “Ultrasonic tomographic velocimeter for visualization of axial flow fields in pipes,” Flow Meas. Instrum., **41**, pp. 57–66.

[69] Wu, C., Cheng, Y., Ding, Y., Wei, F., and Jin, Y., 2007, “A novel X-ray computed tomography method for fast measurement of multiphase flow,” Chem. Eng. Sci., **62**(16), pp. 4325–4335.

[70] Horbelt, S., Liebling, M., and Unser, M., 2002, “Discretization of the radon transform and of its inverse by spline convolutions,” IEEE Trans. Med. Imaging, **21**(4), pp. 363–376.

[71] Liu, C., Xu, L., Cao, Z., and Li, F., 2014, “One-dimensional tomography of axisymmetric temperature distribution with limited TDLAS data by using three-point Abel

deconvolution," IST 2014 - 2014 IEEE Int. Conf. Imaging Syst. Tech. Proc., pp. 432–435.

[72] Cai, W., and Kaminski, C. F., 2017, "Tomographic absorption spectroscopy for the study of gas dynamics and reactive flows," Prog. Energy Combust. Sci., **59**, pp. 1–31.

[73] Duke, D. J., Kastengren, A. L., Matusik, K. E., and Powell, C. F., 2018, "Hard X-ray fluorescence spectroscopy of high pressure cavitating fluids in aluminum nozzles," Int. J. Multiph. Flow, **0**, pp. 1–11.

[74] Bracewell, R., 1965, "The Fourier Transform and Mis Applications."

[75] Ginat, D. T., and Gupta, R., 2014, "Advances in Computed Tomography Imaging Technology," Annu. Rev. Biomed. Eng., **16**(1), pp. 431–453.

[76] Minto, J. M., Hingerl, F. F., Benson, S. M., and Lunn, R. J., 2017, "X-ray CT and multiphase flow characterization of a 'bio-grouted' sandstone core: The effect of dissolution on seal longevity," Int. J. Greenh. Gas Control, **64**(July), pp. 152–162.

[77] Li, L., Zhao, T., and Chen, Z., 2018, "First Dual MeV Energy X-ray CT for container inspection: Design, algorithm, and preliminary experimental results," IEEE Access, **6**, pp. 45534–45542.

[78] Pretzler, G., Jäger, H., Neger, T., Philipp, H., and Woisetschläger, J., 1992, "Comparison of Different Methods of Abel Inversion Using Computer Simulated and Experimental Side-On-Data," Zeitschrift für Naturforschung. A, A J. Phys. Sci., **47**(9), pp. 955–970.

[79] Kolhe, P. S., and Agrawal, A. K., 2009, "Abel inversion of deflectometric data: comparison of accuracy and noise propagation of existing techniques.," Appl. Opt., **48**(20), pp. 3894–902.

[80] Fulge, H., Knapp, A., Wernitz, R., Eichhorn, C., Herdrich, G., Fasoulas, S., and Lohle, S., 2011, "Improved Abel Inversion Method for Analysis of Spectral and Photo-Optical Data of Magnetic Influenced Plasma Flows," 42nd AIAA Plasmadynamics Lasers Conf., (June), pp. 1–11.

[81] Joseph A. Ranalli, 2009, "Spatially Resolved Analysis of Flame Dynamics for the Prediction of Thermoacoustic Combustion Instabilities," Ph.D Diss.

[82] Fischer, F., and Hampel, U., 2010, "Ultra fast electron beam X-ray computed tomography for two-phase flow measurement," Nucl. Eng. Des., **240**(9), pp. 2254–2259.

[83] Bieberle, M., Fischer, F., Schleicher, E., Koch, D., Menz, H. J., Mayer, H. G., and Hampel, U., 2009, "Experimental two-phase flow measurement using ultra fast limited-

angle-type electron beam X-ray computed tomography," Exp. Fluids, **47**(3), pp. 369–378.

[84] Wang, Q., Wang, H., Hao, K., and Dai, P., 2011, "Two-phase flow regime identification based on cross-entropy and information extension methods for computerized tomography," IEEE Trans. Instrum. Meas., **60**(2), pp. 488–495.

[85] Zboray, R., and Prasser, H., 2013, "Optimizing the performance of cold-neutron tomography for investigating annular flows and functional spacers in fuel rod bundles," Nucl. Eng. Des., **260**, pp. 188–203.

[86] Liu, J., Wang, B., Cui, Y., and Wang, H., 2015, "Ultrasonic tomographic velocimeter for visualization of axial fl ow fi elds in pipes," Flow Meas. Instrum., **41**, pp. 57–66.

[87] Wu, Y., Lei, Q., and Ma, L., 2014, "Experimental demonstration of 4D imaging in two-phase flows based on computed tomography at 5 kHz," Appl. Opt., **53**(24), p. 5547.

[88] Banowski, M., Lucas, D., and Szalinski, L., 2015, "International Journal of Thermal Sciences A new algorithm for segmentation of ultrafast X-ray tomographed gas e liquid fl ows," Int. J. Therm. Sci., **90**, pp. 311–322.

[89] Schäfer, T., Meitzner, C., Lange, R., and Hampel, U., 2016, "A study of two-phase flow in monoliths using ultrafast single-slice X-ray computed tomography," Int. J. Multiph. Flow, **86**, pp. 56–66.

[90] Viggiano, B., Skjæraasen, O., Schümann, H., and Tutkun, M., 2018, "International Journal of Multiphase Flow Characterization of flow dynamics and re duce d-order description of experimental two-phase pipe flow," Int. J. Multiph. Flow, **105**, pp. 91–101.

[91] Viggiano, B., Skjæraasen, O., Schümann, H., Tutkun, M., and Cal, R. B., 2018, "Characterization of flow dynamics and reduced-order description of experimental two-phase pipe flow," Int. J. Multiph. Flow, **105**, pp. 91–101.

[92] Wei, Y., Wang, G., and Hsieh, J., 2005, "Relation between the filtered backprojection algorithm and the backprojection algorithm in CT," IEEE Signal Process. Lett., **12**(9), pp. 633–636.

[93] Herman, G. T., Lent, A., and Rowland, S. W., 1974, "ART: Mathematics and applications a report on the mathematical foundations and on the applicability to real data of the algebraic reconstruction techniques," J. Theor. Biol., **45**(2), p. 597.

[94] Wright, P., Terzija, N., Davidson, J. L., Garcia-Castillo, S., Garcia-Stewart, C., Pegrum, S., Colbourne, S., Turner, P., Crossley, S. D., Litt, T., Murray, S., Ozanyan, K. B., and

McCann, H., 2010, “High-speed chemical species tomography in a multi-cylinder automotive engine,” Chem. Eng. J., **158**(1), pp. 2–10.

[95] Al, N. T. et, 2008, “Image optimization for chemical species tomography with an irregular and sparse beam array,” Meas. Sci. Technol., **19**(1), pp. 19–23.

[96] Twynstra, M. G., Daun, K. J., and Waslander, S. L., 2014, “Line-of-sight-attenuation chemical species tomography through the level set method,” J. Quant. Spectrosc. Radiat. Transf., **143**, pp. 25–34.

[97] Chung, K. B., Gouldin, F. C., and Wolga, G. J., “Distribution of a Nonreacting Flow With E E.”

[98] Edwards, J., Gouldin, F., and MacDonald, M., 2013, “High Speed Absorption Tomography with Advanced Reconstruction Algorithms,” (January).

[99] Terzija, N., and McCann, H., 2011, “Wavelet-based image reconstruction for hard-field tomography with severely limited data,” IEEE Sens. J., **11**(9), pp. 1885–1893.

[100] Mohamad, E. J., Rahim, R. A., Ibrahim, S., Sulaiman, S., and Manaf, M. S., 2006, “Flame imaging using laser-based transmission tomography,” Sensors Actuators, A Phys., **127**(2), pp. 332–339.

[101] Schleicher, E., Da Silva, M. J., Thiele, S., Li, A., Wollrab, E., and Hampel, U., 2008, “Design of an optical tomograph for the investigation of single- and two-phase pipe flows,” Meas. Sci. Technol., **19**(9).

[102] Bryner, E., Busa, K., McDaniel, J., Goyne, C., and Diskin, G., 2012, “Spatially Resolved Temperature and Water Vapor Concentration Distributions in a Flat Flame Burner by Tunable Diode Laser Absorption Tomography,” (January).

[103] Busa, K., Ellison, E., McGovern, B., McDaniel, J., Diskin, G., DePiro, M., Capriotti, D., and Gaffney, R., 2013, “Measurements on NASA Langley Durable Combustor Rig by TDLAT: Preliminary Results,” pp. 1–13.

[104] Xia, H., Kan, R., Xu, Z., He, Y., Liu, J., Chen, B., Yang, C., Yao, L., Wei, M., and Zhang, G., 2017, “Two-step tomographic reconstructions of temperature and species concentration in a flame based on laser absorption measurements with a rotation platform,” Opt. Lasers Eng., **90**(September 2016), pp. 10–18.

[105] Peng, D., Jin, Y., Zhai, C., and Yang, J., 2018, “Numerical simulations to improve the performance of tunable diode laser absorption tomography in a harsh combustion

environment," Spectrosc. Lett., **51**(1), pp. 7–16.

[106] Cai, W., and Ma, L., 2010, "Comparison of approaches based on optimization and algebraic iteration for binary tomography," Comput. Phys. Commun., **181**(12), pp. 1974–1981.

[107] Zhou, B., Li, Q., He, Y., Petersson, P., Li, Z., Aldén, M., and Bai, X. S., 2015, "Visualization of multi-regime turbulent combustion in swirl-stabilized lean premixed flames," Combust. Flame, **162**(7), pp. 2954–2958.

[108] Hindle, F. P., 2001, "Measurement of gaseous hydrocarbon distribution by a near-infrared absorption tomography system," J. Electron. Imaging, **10**(3), p. 593.

[109] Liu, C., Xu, L., Cao, Z., and Yang, Y., 2012, "Fan-beam TDLAS tomography for gas concentration distribution with limited data," IST 2012 - 2012 IEEE Int. Conf. Imaging Syst. Tech. Proc., pp. 117–120.

[110] Song, J., Hong, Y., Wang, G., and Pan, H., 2013, "Algebraic tomographic reconstruction of two-dimensional gas temperature based on tunable diode laser absorption spectroscopy," Appl. Phys. B Lasers Opt., **112**(4), pp. 529–537.

[111] Zhang, Z., Sun, P., Pang, T., Xia, H., Cui, X., Li, Z., Han, L., Wu, B., Wang, Y., Sigrist, M. W., and Dong, F., 2016, "Reconstruction of combustion temperature and gas concentration distributions using line-of-sight tunable diode laser absorption spectroscopy," Opt. Eng., **55**(7), p. 076107.

[112] Xia, H. H., Kan, R. F., Liu, J. G., Xu, Z. Y., and He, Y. B., 2016, "Analysis of algebraic reconstruction technique for accurate imaging of gas temperature and concentration based on tunable diode laser absorption spectroscopy," Chinese Phys. B, **25**(6).

[113] Casey, R. G., and Nagy, G., 1971, Advances in Pattern Recognition.

[114] Prun, V. E., Nikolaev, D. P., Buzmakov, A. V., Chukalina, M. V., and Asadchikov, V. E., 2013, "Effective regularized algebraic reconstruction technique for computed tomography," Crystallogr. Reports, **58**(7), pp. 1063–1066.

[115] Cengiz, K., and Kamasak, M., 2014, "Comparison of algebraic reconstruction techniques for Tomosynthesis system," IWSSIP 2014 Proc., (May), pp. 2142–2145.

[116] Wellander, R., Richter, M., and Aldén, M., 2014, "Time-resolved (kHz) 3D imaging of OH PLIF in a flame," Exp. Fluids, **55**(6).

[117] Wang, F., Wu, Q., Huang, Q., Zhang, H., Yan, J., and Cen, K., 2015, "Simultaneous

measurement of 2-dimensional H2O concentration and temperature distribution in premixed methane/air flame using TDLAS-based tomography technology," Opt. Commun., **346**, pp. 53–63.

[118] Gillet, B., Hardalupas, Y., Kavounides, C., and Taylor, A. M. K. P., 2004, "Infrared absorption for measurement of hydrocarbon concentration in fuel/air mixtures (MAST-B-LIQUID)," Appl. Therm. Eng., **24**(11–12), pp. 1633–1653.

[119] "2016_Leitao_On projective Landweber–Kaczmarz methods for.pdf."

[120] Elfving, T., Hansen, P. C., and Nikazad, T., 2014, "Semi-convergence properties of Kaczmarz's method," Inverse Probl., **30**(5).

[121] Tsekenis, S. A., Wilson, D., Lengden, M., Hyvönen, J., Leinonen, J., Shah, A., Andersson, and McCann, H., 2017, "Towards in-cylinder chemical species tomography on large-bore IC engines with pre-chamber," Flow Meas. Instrum., **53**, pp. 116–125.

[122] Pal, S., Ozanyan, K. B., and McCann, H., 2008, "A computational study of tomographic measurement of carbon monoxide at minor concentrations," Meas. Sci. Technol., **19**(9).

[123] Wood, M. P., and Ozanyan, K. B., 2013, "Concentration and temperature tomography at elevated pressures," IEEE Sens. J., **13**(8), pp. 3060–3066.

[124] Elfving, T., and Nikazad, T., 2007, "Stopping rules for Landweber-type iteration," Inverse Probl., **23**(4), pp. 1417–1432.

[125] Todd, L. A., and Bhattacharyya, R., 1997, "Tomographic reconstruction of air pollutants: evaluation of measurement geometries," Appl. Opt., **36**(30), p. 7678.

[126] Verkruysse, W., and Todd, L. A., 2005, "Novel algorithm for tomographic reconstruction of atmospheric chemicals with sparse sampling," Environ. Sci. Technol., **39**(7), pp. 2247–2254.

[127] D., Y., L., W., D., C., C., Y., X., H., and J., L., 2018, "Filtered maximum likelihood expectation maximization based global reconstruction for bioluminescence tomography," Med. Biol. Eng. Comput., pp. 1–15.

[128] Chuang, K. S., Jan, M. L., Wu, J., Lu, J. C., Chen, S., Hsu, C. H., and Fu, Y. K., 2005, "A maximum likelihood expectation maximization algorithm with thresholding," Comput. Med. Imaging Graph., **29**(7), pp. 571–578.

[129] Herman, G. T., and Meyer, L. B., 1993, "Can Be Made Computationally Efficient," October, **12**(3).

[130] Chojnacki, A. M., Sarma, A., Wolga, G. J., Torniainen, E. D., and Gouldin, F. C., 1996, "Infrared tomographic inversion for combustion and incineration," Combust. Sci. Technol., **116**–**117**(1–6), pp. 583–606.

[131] Torniainen, E. D., Gouldin, F. C., and Hinz, A. K., 1998, "Tomographic analysis of unsteady, reacting flows: Numerical investigation," AIAA J., **36**(7), pp. 1270–1278.

[132] Williams, K. E., Van Sinh, N., Unnikrishnan, R., Bagnell, J. A., Huber, D., Taubin, G., Klein, R., Gumhold, S., Cai, R., Bergstrom, J. C., Mullen, J. D., Wetzstein, M. E., Shurley, W. D., Dony, R. D., and Jolliffe, I. T., 2001, "R. D. Dony 'Karhunen-Loève Transform,'" Encycl. Stat. Behav. Sci., **30**(3), pp. 1–37.

[133] Busa, K., Bryner, E., McDaniel, J., Goyne, C., Smith, C., and Diskin, G., 2012, "Demonstration of Capability of Water Flux Measurement in a Scramjet Combustor using Tunable Diode Laser Absorption Tomography and Stereoscopic PIV," (January), pp. 1–14.

[134] Bashore, T., 2001, "Fundamentals of X-ray imaging and radiation safety," Catheter. Cardiovasc. Interv., **54**(1), pp. 126–135.

[135] Hiriyannaiah, H. P., 1997, "X-ray computed tomography for medical imaging," IEEE Signal Process. Lett., **97**(March), pp. 42–52.

[136] Herman, G. T., 1980, "RECONSTRUCTION FROM DIVERGENT BEAMS : A COMPARISON OF ALGORITHMS WITH AND WITHOUT REBINNING," **I**(2), pp. 131–139.

[137] Bonnet, S., Member, F. P., Turjmani, F., Member, R. P., and Cedex, G., 2001, "Multiresolution Reconstruction in Fan-Beam Tomography," pp. 105–109.

[138] Banowski, M., Lucas, D., and Szalinski, L., 2015, "A new algorithm for segmentation of ultrafast X-ray tomographed gas-liquid flows," Int. J. Therm. Sci., **90**, pp. 311–322.

[139] Bieberle, A., Hoppe, D., Schleicher, E., and Hampel, U., 2011, "Void measurement using high-resolution gamma-ray computed tomography," **241**, pp. 2086–2092.